

---

# X-Ray Observations of Neutron Stars with XMM-Newton & Chandra

Hui Chung Yue

---



München 2007



---

# **X-Ray Observations of Neutron Stars with XMM-Newton & Chandra**

**Hui Chung Yue**

---

Dissertation  
an der Fakultät für Physik  
der Ludwig-Maximilians-Universität  
München

vorgelegt von  
Hui Chung Yue  
aus Hong Kong

München, den 6 November 2007

Erstgutachter: Priv. Doz. Dr. Werner Becker

Zweitgutachter: Prof. Dr. Harald Lesch

Tag der mündlichen Prüfung: 27 November 2007

# Contents

Summary	xiii
<b>1 Introduction</b>	<b>1</b>
1.1 A Brief History of Neutron Stars . . . . .	1
1.2 The Physics of Neutron Stars . . . . .	4
1.2.1 Formation . . . . .	4
1.2.2 Global structure . . . . .	5
1.2.3 Composition . . . . .	7
1.2.4 Thermal evolution . . . . .	9
1.2.5 Pulsar magnetosphere and high energy radiation . . . . .	11
1.3 Manifestations of Isolated Neutron Stars . . . . .	18
1.3.1 Rotation-powered pulsars . . . . .	19
1.3.2 Soft $\gamma$ -ray repeaters/Anomalous X-ray pulsars . . . . .	19
1.3.3 Central compact objects in supernova remnants . . . . .	20
1.3.4 Dim thermal isolated neutron stars . . . . .	21
1.3.5 Rotating RADIO Transients (RRATs) . . . . .	21
1.4 Studying Neutron Stars with XMM-Newton & Chandra . . . . .	22
1.4.1 Chandra . . . . .	22
1.4.2 XMM-Newton . . . . .	23
<b>2 X-ray observations of RX J0822-4300 and Puppis-A</b>	<b>25</b>
2.1 Introduction . . . . .	25
2.2 Observations . . . . .	27
2.2.1 XMM-Newton Observations . . . . .	27
2.2.2 Chandra Observations . . . . .	28
2.3 Data Analysis . . . . .	29
2.3.1 Spatial Analysis . . . . .	29
2.3.2 Spectral Analysis . . . . .	31
2.3.3 Timing Analysis . . . . .	33
2.4 Discussion & Conclusion . . . . .	35

<b>3</b>	<b>Probing the Proper Motion of the Compact Object in Puppis-A</b>	<b>51</b>
3.1	Introduction . . . . .	51
3.2	Observation and data analysis . . . . .	52
3.3	Results and Discussion . . . . .	55
<b>4</b>	<b>XMM-Newton Observations of the Compact Object in RX J0852.0-4622</b>	<b>59</b>
4.1	Introduction . . . . .	59
4.2	Observations & Data Reduction . . . . .	61
4.3	Data Analysis . . . . .	62
4.3.1	Spatial Analysis . . . . .	62
4.3.2	Spectral Analysis . . . . .	63
4.3.3	Timing Analysis . . . . .	64
4.4	Discussion . . . . .	65
<b>5</b>	<b>Radio and X-ray Nebulae associated with PSR J1509-5850</b>	<b>75</b>
5.1	Introduction . . . . .	75
5.2	Observations and data analysis . . . . .	76
5.3	Discussion & Conclusion . . . . .	78
<b>6</b>	<b>Discovery of an X-ray Nebula associated with PSR J2124-3358</b>	<b>87</b>
6.1	Introduction . . . . .	87
6.2	Observations and data analysis . . . . .	88
6.3	Discussion & Conclusion . . . . .	90
<b>7</b>	<b>X-ray emission properties of the old pulsar PSR B2224+65</b>	<b>97</b>
7.1	Introduction . . . . .	97
7.2	Observations and data analysis . . . . .	98
7.3	Discussion & Conclusion . . . . .	101
<b>8</b>	<b>Chandra observation of the old pulsar PSR B1929+10</b>	<b>113</b>
8.1	Introduction . . . . .	113
8.2	Observations and data analysis . . . . .	114
8.2.1	Spatial analysis . . . . .	115
8.2.2	Spectral analysis . . . . .	116
8.3	Discussion . . . . .	118
<b>9</b>	<b>Searches for X-ray counterparts of millisecond pulsars in M28</b>	<b>127</b>
9.1	Introduction . . . . .	127
9.2	Observations and Data Analysis . . . . .	128
9.3	Discussion . . . . .	130

---

<b>10 Conclusions &amp; Discussions</b>	<b>135</b>
10.1 The nature of central compact objects in supernova remnants . . . . .	135
10.2 Emission mechanism of non-recycled old pulsars . . . . .	137
10.3 High energy emission of pulsar wind nebulae . . . . .	138
10.4 Millisecond pulsars in globular clusters . . . . .	139
10.5 Future prospects . . . . .	140
<b>Bibliography</b>	<b>147</b>
<b>Acknowledgments</b>	<b>155</b>
<b>Curriculum Vitae</b>	<b>156</b>





# List of Figures

1.1	Illustration of the structure of the neutron star interior . . . . .	7
1.2	Illustration of the pulsar magnetosphere . . . . .	12
2.1	MOS1/2 false color X-ray image of the central region of Puppis–A. . . . .	39
2.2	RASS false color image of Puppis–A and parts of the Vela SNR . . . . .	40
2.3	XMM PN False color image of the $4.4' \times 4.4'$ region around RX J0822-4300 . . . . .	41
2.4	Chandra HRC-I brightness profile for RX J0822-4300 . . . . .	42
2.5	X-ray images of Puppis–A with radio contour lines . . . . .	43
2.6	Energy spectrum of RX J0822-4300 . . . . .	45
2.7	Components of the model fitted to the spectral data of RX J0822–4300 . . . . .	46
2.8	Error contours for the best-fit model to the spectrum of RX J0822–4300 . . . . .	47
2.9	Energy spectrum of the rim emission underneath RX J0822–4300 . . . . .	48
2.10	Pulse profiles of RX J0822–4300 and the $Z_1^2$ -distribution . . . . .	50
3.1	Part of the HRC-I image of Puppis–A as observed in April 2005 . . . . .	57
3.2	The best-fit positions of RX J0822–4300 in two HRC-I observations . . . . .	58
4.1	RASS image of Puppis–A and RX J0852.0-4622 . . . . .	67
4.2	MOS1/2 false color image of RX J0852.0-4622 . . . . .	69
4.3	Energy spectrum of CXOU J085201.4-461753 . . . . .	71
4.4	Error contours for the best-fitted spectral model for CXOU J085201.4-461753 . . . . .	72
5.1	ACIS image of the field around PSR J1509–5850 . . . . .	82
5.2	Energy spectrum of the X-ray trail of PSR J1509–5850 . . . . .	83
5.3	Radio image of the field around PSR J1509–5850 . . . . .	84
5.4	X-ray image of PSR J1509–5850 with radio contour lines . . . . .	85
6.1	MOS1/2 and ACIS images of PSR J2124–3358 . . . . .	93
6.2	Energy spectrum of the X-ray trail of PSR J2124–3358 . . . . .	94
7.1	ACIS image of the field around PSR B2224+65 . . . . .	104
7.2	Brightness profile of the extend feature associated with PSR B2224+65 . . . . .	105
7.3	Energy spectrum of PSR B2224+65 . . . . .	107
7.4	Temperature upper limits of the polar cap of PSR B2224+65 . . . . .	108

---

7.5	Energy spectrum of the extended feature associated with PSR B2224+65 . . . . .	109
7.6	Variation of $f(r_{in}, \alpha)$ with the magnetic inclination angle . . . . .	111
8.1	ACIS images of the field around PSR B1929+10 . . . . .	120
8.2	Radial profile of PSR B1929+10 . . . . .	121
8.3	Comparison between Chandra and XMM images . . . . .	122
8.4	Energy spectra of PSR B1929+10 . . . . .	124
8.5	Error contours for the best-fit model to the spectra of PSR B1929+10 . . . . .	125
8.6	Energy spectra of the arc-like structure associated PSR B1929+10 . . . . .	126
9.1	ACIS-S3 image of the central region of M28 . . . . .	132
10.1	ROSAT PSPC image of G67.7+1.8 . . . . .	144
10.2	ACIS-I false color image of G67.7+1.8 . . . . .	145

# List of Tables

2.1	Details of the XMM-Newton and Chandra observations of RXJ0822-4300 . . . . .	38
2.2	Spectral parameters of RX J0822-4300 . . . . .	44
2.3	Observed fluxes of RX J0822-4300 . . . . .	49
3.1	X-ray properties of serendipitous sources around RX J0822-4300. . . . .	58
4.1	Details of XMM-Newton observations of CXOU J085201.4-461753 . . . . .	68
4.2	Faint X-ray sources detected serendipitously within RX J0852.0-4622. . . . .	70
4.3	Spectral parameters of CXOU J085201.4-461753 . . . . .	73
5.1	Pulsar parameters of PSR J1509-5850 . . . . .	81
6.1	Ephemeris of J0030+0451, J2124-3358, J1024-0719 and J0437-4715 . . . . .	92
6.2	Identifications of the stars around the X-ray trail of PSR J2124-3358. . . . .	94
6.3	Properties of rotation-powered pulsars with X-ray/ $H_{\alpha}$ bow shocks. . . . .	95
7.1	Proper-motion corrected ephemeris of PSR B2224+65 . . . . .	103
7.2	Spectral parameters of PSR B2224+65 and the X-ray feature . . . . .	106
7.3	The theoretical outer-gap sizes of old pulsars . . . . .	110
8.1	Ephemerides of PSR B1929+10 . . . . .	120
8.2	Spectral parameters of PSR B1929+10 and its compact nebula . . . . .	123
8.3	Energetics of PSR B1929+10 . . . . .	123
9.1	PSR J1824-2452A positions (J2000) . . . . .	131
9.2	Properties of the millisecond pulsars in M28 . . . . .	133
10.1	Physical properties of non-recycled old pulsars . . . . .	143



# Summary

Utilizing the state-of-art X-ray telescopes — XMM-Newton and Chandra, I have carried out detailed studies covering a wide range of topics on the X-ray emission from young neutron stars in supernova remnants, pulsar wind nebulae, old non-recycled pulsars as well as millisecond pulsars.

I have observed two neutron star candidates located in the supernova remnants, Puppis-A and RX J0852.0-4622, with XMM-Newton and Chandra. X-ray spectroscopy suggested that the X-ray emission from these objects is of thermal origin and is emitted from high temperature hot spots on the stellar surfaces. Searching for the possible pulsations from these objects revealed an interesting periodicity candidate of  $\sim 0.22$  s from the compact object in Puppis-A. Utilizing the superior spatial resolution of Chandra, the point source nature of the compact object in Puppis-A was constrained to an accuracy of sub-arcseconds. No compact nebula is detected around this object. Moreover, making use of two Chandra observations with an epoch separation of somewhat more than five years, I measured the proper motion of this compact object. I found that the transverse velocity of this object is at the order of  $\sim 1000$  km/s to the southwest. Both the magnitude and the direction of the proper motion are in agreement with the birth place of the object in the supernova remnant being near to its optical center. This is the first case that a proper motion of a central compact object in the supernova remnant was measured directly.

In searching for diffuse X-ray emission around pulsars, trail-like nebulae associated with PSRs J2124–3358 and J1509–5850 were discovered. Examining the diffuse emission suggested that the observed X-rays are non-thermal in nature. Modeling the nebular emission with a standard shock model, the observed X-rays were found to be in line with the emission originating from the accelerated particles in the post shock flow. The X-ray nebula of PSR J2124–3358 is the first found near a solitary millisecond pulsar. In contrast to a typical bow-shock morphology, the X-ray nebula of PSR J2124-3358 appears to be highly asymmetric and significantly deviated from the direction of the pulsar’s proper motion direction. Searching for radio counterparts, a radio nebula associated with PSR J1509–5850 which is apparently longer than its X-ray counterpart was discovered. The later is consistent with the scenario of synchrotron cooling.

I have explored the non-recycled old pulsars PSR B2224+65 and PSR B1929+10 and their environments with Chandra. Through the spectral analysis, the X-ray emission from these pulsars is found to be mostly non-thermal. This is well-consistent with the picture inferred from the independent studies of other non-recycled old pulsars which suggests that the observed X-rays of these old pulsars are originating from their magnetosphere. I further discussed a possible origin of their non-thermal pulsar emission. I have also examined the extended feature which seems to be associated with PSR B2224+65. Its orientation is entirely misaligned with the pulsar’s proper motion direction which makes its formation difficult to be understood in terms of simple bow-shock emission. In the case of PSR B1929+10, in addition to the X-ray trail already seen in previous observations

by ROSAT and XMM-Newton, an arc-like nebula surrounding the pulsar was discovered. Assuming a synchrotron nature for the emission of this nebula, a high compression factor in this compact shock region is suggested.

We have revisited the archival Chandra data on the globular cluster M28 to evaluate whether the newly discovered millisecond pulsars find a counterpart among the various X-ray sources detected in M28 previously. Radio position of PSR J1824–2452H is found to be in agreement with the position of CXC 182431-245217 while some faint unresolved X-ray emission near to the center of M28 is found to be coincident with the millisecond pulsars PSR J1824-2452G, J1824-2452J, J1824-2452I and J1824-2452E.

# Chapter 1

## Introduction

### 1.1 A Brief History of Neutron Stars

Shortly after the discovery of the neutron by Chadwick (1932), Baade & Zwicky (1934) proposed the existence of the neutron stars. Their conclusion was resulted from their investigation of the explosive endpoint of massive stars — *Supernovae*. In view of the tremendous energy release in supernovae, Baade & Zwicky had speculated that the release of the gravitational energy when a massive stellar core collapsed to form a neutron star can possibly power supernova. They envisioned that supernovae represent the transitions from “normal” stars into neutron stars, which would be at an ultra high density and with a small radius (cf. Baade & Zwicky 1934). This is the *first* precise prediction that neutron stars can be formed in core-collapsed supernova explosion.

Since the gravity of a neutron star is extremely strong, general relativistic effects have to be taken into account in calculating the stellar structure. Theoreticians had derived the equations of hydrostatic equilibrium from Einstein field equation and presented the first relativistic calculations of neutron star models (Tolman 1939; Oppenheimer & Volkoff 1939). These calculations had shown the existence of stable equilibrium stars which are much more dense than white dwarfs (see Oppenheimer & Volkoff 1939). There were predictions that neutron stars can be rapidly rotating compact objects with strong magnetic field (Hoyle, Narlikar, & Wheeler 1964). In 1962, the most powerful persistent extra-solar X-ray source, Scorpius X-1, had been discovered with the X-ray detector on an Aerobee rocket (Giacconi et al. 1962). This discovery had motivated people to speculate that neutron stars could be observable in X-rays. Zel’dovich & Guseynov (1965) and Hayakawa & Matsouka (1964) had independently predicted that binary systems which comprise a compact object, either a neutron star or a white dwarf and a massive normal stars could generate X-ray emission. When a compact star is accreting matter from its main sequence companion star, thermal X-rays would be generated. Despite the theoretical speculations, there was no conclusive evidence for the existence of neutron stars. Neutron stars were still just the dream of theoreticians.

The most remarkable breakthrough of neutron star study came in November 1967. At

the Mullard Radio Astronomy Observatory, Antony Hewish and his collaborators had build a large radio telescope array to study interplanetary scintillation of compact radio sources at 81.5 MHz. Soon after the instrument started operating, it had been noticed a series of weak sporadic signals. Observing with this transit telescope, these fluctuating signals appeared four minutes each day which indicated their celestial origin. In November, systematic investigations of these signals were initiated by adopting a recorder with a faster response time. The first sequence of clearly distinguishable pulses with periodicity of  $\sim 1.337$  s were firstly recorded on November 28, 1967. This is the *first* detected pulsar — PSR B1919+21 (Hewish, Bell, Pilkington, Scott, & Collins 1968). The absence of any parallax  $\geq 2$  arcmin showed that the source is located further than  $10^3$  A.U. away. Also, the rapidity of the pulsation placed the upper limit of the source size to  $\sim 5 \times 10^3$  km. This insight led the authors to suggest that the source could be a compact object, either a neutron star or a white dwarf. They have further speculated that the observed phenomena were associated with the oscillations of the compact star.

The discovery of PSR B1919+21 exerted an enormous impact on the international astronomical community. This can be reflected by the fact that more than 100 papers about pulsars were published in 1968. As a new class of objects appeared, the identification of their physical nature was badly needed. Actually, the correct path in explaining the origin of pulsar emission had already been published just before the discovery of PSR B1919+21. Adopting an oblique magnetic dipole rotator, Pacini (1967) had shown that the rotational energy of a neutron star can be converted into electromagnetic radiation. The author also specifically pointed out the possibility that a large amount of energy and momentum can be pumped from a rotating neutron star to the supernova remnant such as the Crab Nebula. Without knowing the work by Pacini (1967), Gold (1968) independently suggested that the observed pulsars were in fact rotating neutron stars which have magnetic fields as high as  $10^{12}$  G. The author had also pointed out that neutron stars can explain many observed properties of pulsars such as the short and the high accuracy of the observed periodicities. Moreover, directional beam rotating like a lighthouse beacon was proposed to explain the sub-structure of the observed pulses. The author had also precisely predicted that the pulsar period should increase slowly as it radiates at the expense of the star's rotational energy. Shortly after the publication of Gold (1968), a radio pulsar was discovered in the Crab Nebula which had a period as short as  $\sim 33$  ms (Staelin & Reifenstein 1968). Such short period can only be achieved by either the rotation or vibration of a neutron star. This discovery had intimately connected supernovae, neutron stars and pulsars. Later, Richard & Comella (1969) discovered the increase in the period of the Crab Pulsar which was in agreement with the prediction by Gold (1968). Since the slowdown of the period can only be resulted from the rotation and not from vibration. This leaves a rotating neutron star as the most plausible model to explain all the observational facts. Furthermore, Gold (1969) demonstrated that the implied energy loss by the Crab Pulsar was approximately equal to the energy requires to power the Crab Nebula. At this time, the identification of pulsars as rotating neutron stars was generally accepted. The discovery of pulsars had eventually made a theoreticians' dream come true!

Many experiments were then designed to investigate neutron stars in the high energy



regime. By acquiring data during an Aerobee rocket flight, Fritz et al. (1969) had observed the Crab Nebula in X-rays and found X-ray pulsations in the nebula at a frequency identical with that of the Crab Pulsar. This led to the discovery of the first X-ray rotation-powered pulsar. While Fritz et al. (1969) observed the Crab Pulsar in the soft X-ray band ( $\sim 1 - 13$  keV), Fishman, Harnden & Haymes (1969) had observed the pulsed hard X-rays ( $> 35$  keV) from the pulsar with the data obtained during a balloon-borne measurement. In 1970, a milestone in X-ray astronomy was established when the UHURU (means “freedom” in Swahili words) satellite was launched on 12 December 1970. This was the first X-ray astronomical satellite in orbit which allowed observations of a single target with a long exposure time, which cannot be achieved by a rocket. Soon after the launch of UHURU, two new pulsating X-ray sources were discovered by the satellite which were designated as Hercules X-1 and Centaurus X-3 (Giacconi et al. 1971). These sources are believed to be neutron stars accreting gas from their main sequence companions in the binary systems.

The next big leap in X-ray pulsar astronomy was initiated by the launch of the EINSTEIN observatory in 1978 which carried the first imaging X-ray telescope. Systematic searches for X-ray emission from  $\sim 40$  pulsars had been performed by EINSTEIN (see Seward & Wang 1988). This study had shown that X-rays from 10 pulsars were firmly detected, including two Crab-like pulsars (age  $< 10^4$  yrs) PSRs B0540-69 and B1509-58 (Seward, Harnden & Helfand 1984; Seward & Harnden 1982). It is interesting to notice that these two pulsars were discovered in X-rays before their radio counterparts were found. Apart from pulsars, the imaging capability of EINSTEIN also allowed the other class of neutron stars be revealed. Young neutron stars, which appear to be compact X-ray sources, had been found close to the centers of supernova remnants like RCW 103 (Touhy & Garmire 1980), Puppis-A (Petre et al. 1982) and PKS 1209-51 (Helfand & Becker 1984).

In 1990s, our knowledge about X-ray pulsars was significantly improved by the observations with ROSAT, ASCA and BeppoSAX. There were 33 radio pulsars detected in X-rays during this new era of X-ray astronomy (see Becker 2008). One triumph of ROSAT is the discovery of the radio quiet X-ray pulsar, Geminga (Halpern & Holt 1992; Bertsch et al. 1992). Also, the improved sensitivity and spectral resolution enabled detailed spectral studies of the enlarged sample of X-ray pulsars. It was found that the X-ray properties of rotation-powered pulsars correlate with age (see Becker & Trümper 1997). For the young pulsars with age less than  $\sim 10^4$  yrs, their spectra can be well-modeled by a single power-law model. The non-thermal nature suggests the X-rays from these pulsars are dominated by magnetospheric emission. On the other hand, neither a single power-law nor a single blackbody is found to fit the observed spectra of the middle-aged pulsars ( $\sim 10^5 - 10^6$  yrs). This class of pulsars is characterized by composite spectra consisting of a soft thermal component, a harder thermal component from the hot polar caps as well as some non-thermal contribution. For the millisecond pulsars ( $P \leq 20$  ms), they had been studied exclusively in the radio domain before the era of ROSAT. Thanks to the significantly higher sensitivities compared with previous X-ray satellites, ROSAT had detected X-ray emission from the millisecond pulsars PSR B1957+20 in early 1990s (Kulkarni et al. 1992; Fruchter et al. 1992). Soon after came the discovery of X-ray pulsations from PSR J0437-4715 (Becker & Trümper 1993). Apart from the rotation-powered pulsars, the improved angular resolution

also allow the astronomers to better resolve the compact X-ray sources from the supernova remnants and confirmed the neutron star candidates detected by EINSTEIN. In view of all the aforementioned triumphs, it is fair enough to state that the 1990s was a golden era of X-ray neutron star astronomy which provided a solid ground for further studies.

## 1.2 The Physics of Neutron Stars

Neutron stars are one of the most dense objects in the Universe. These compact objects provide us with ideal laboratories for testing gravitational physics, nuclear and particle physics and high energy physics in extreme conditions. In this section, the basic physical properties of neutron stars will be briefly reviewed.

### 1.2.1 Formation of neutron stars

At the end of the life of a massive star (i.e.  $> 8M_{\odot}$  when it is on the main sequence), a Type II supernova explosion will be triggered and a proto-neutron star will be created during the collapse of the iron core of the progenitor. The uncontrolled core collapse is driven by two possible energy absorbing processes: nuclear photodisintegration and electron capture.

The core temperature will increase as the stellar core contracts. The thermal photons will eventually become energetic enough to disintegrate the tightly bound nuclei into less tightly bound nuclei with energy absorbed in this process. For example, at a high enough core temperature ( $T \sim 10^{10}$  K), a large fraction of the tightly bound iron nuclei can be dissociated via the process:



At even higher temperatures, helium nuclei are also expected to be dissociated via the process:



A neutron in the free space will decay into a proton, an electron and a neutrino with a half life of 10.25 min via the process



However, such process will be suppressed in the core contents a degenerate electron gas. The upper limit of the energy of the electron is given by the mass difference between the proton and neutron,  $(m_n - m_p)c^2 = 1.293$  MeV, which is well below the Fermi energy of the electron gas in the core. While the production the electron via the process 1.3 is forbidden by Pauli exclusion principle, the neutron will not be able to decay.

On the other hand, the process of electron capture is not suppressed in the core:



The process of converting protons to neutrons is usually referred as neutronization. It is this process makes the core become neutron rich.

When the central density of the star reaches  $n_0$ , the core collapse will be halted and a shock wave will be triggered as the collapsing gas bounce off the outer edge of the core. During this shock wave propagates outward, it will dissipate its energy via nuclear dissociation of the material that it plows through and to the neutrinos. This energy dissipation has limited the shock to propagate only  $\sim 100-200$  km before it halts (Lattimer & Prakash 2004). Although the mechanism is poorly understood, it is believed that the neutrinos emitted from the proto-neutron star play an important role in resuscitating the shock and eventually expelling the mantle of the progenitor (Lattimer & Prakash 2004). This has left the proto-neutron star behind.

One main difference between the proto-neutron star matter and the neutron star matter is whether the neutrinos are trapped (Weber, Negreiros & Rosenfield 2008). Right after its formation, a proto-neutron star is believed to have a radius larger than 20 km (Lattimer & Prakash 2004). While the typical cross section of a neutrino in the proto-neutron star matter is estimated to be  $\sigma_\nu \sim 10^{-40}$  cm<sup>2</sup>, a very short mean free path  $\lambda = (\sigma_\nu n)^{-1} \sim 10$  cm is implied at a baryon number density of  $n \sim 2-3n_0$  (Lattimer & Prakash 2004) where  $n_0 \sim 0.16$  fm<sup>-3</sup> is the nuclear saturation density. This suggests that the neutrinos will be trapped within the proto-neutron star.

Neutrino emission is still possible in the periphery of a proto-neutron star. Therefore, the star will further contract because of the pressure loss. The loss of neutrinos has also increased the electron capture rate and made that matter become more neutron rich. Since  $\sigma_\nu$  is found to be scaled with the square of the mean neutrino energy,  $\lambda$  will become larger as the star cools down. After  $\sim 10-20$  s after the collapse, the neutrinos start to cool the interior. At  $\sim 50$  s,  $\lambda$  becomes larger than the stellar radius of the star ( $\sim 10$  km). The star hence becomes transparent to the neutrinos and a standard notion of neutron star is established (cf. Lattimer & Prakash 2004).

### 1.2.2 Global structure of neutron stars

The structure of a neutron stars depends sensitively on its state of matter which is usually described as a pressure-density relation,  $P(\rho)$ , namely the equation of state (EOS). The adopted EOS has significant impact on global aspects of a neutron star (e.g. mass, radius). Stellar structure is determined by solving the equations of hydrostatic equilibrium. Owing to the strong gravity of neutron stars, general relativity has to be taken into account. In the time independent and spherically symmetric case, the metric at the star's interior is described by (with the convention  $G = c = 1$ ):

$$ds^2 = -e^{2\Theta(r)} dt^2 + \frac{dr^2}{1 - \frac{2m(r)}{r}} + r^2 d\theta^2 + r^2 \sin\theta d\phi^2 \quad (1.5)$$

The metric function  $e^{2\Theta(r)}$  and the global properties of the neutron star is then obtained by solving the following hydrostatic equation set:

$$\frac{dm}{dr} = 4\pi r^2 \rho \quad (1.6)$$

$$\frac{dP}{dr} = -\frac{\rho m}{r^2} \left(1 + \frac{P}{\rho}\right) \left(1 + \frac{4\pi P r^3}{m}\right) \left(1 - \frac{2m}{r}\right)^{-1} \quad (1.7)$$

$$\frac{d\Theta}{dr} = -\frac{1}{\rho} \frac{dP}{dr} \left(1 + \frac{P}{\rho}\right)^{-1} \quad (1.8)$$

Equation 1.7 usually called as Tolman-Oppenheimer-Volkoff (TOV) equation. The mass continuity equation 1.6 provides the quantity  $m(r)$  which is the mass enclosed inside a sphere of radius  $r$ . One should notice that there are four quantities to be solved, however, there are only three equations here. The extra equation is provide by the adopted EOS  $P(\rho)$ .

The boundary condition at  $r = 0$  is given by selecting a central density  $\rho_c$  and  $m(0) = 0$ . Integrating the equations outward until  $P(r = R) = 0$ , then the mass and radius of the star is given by  $M = m(R)$  and  $R$ . One exact boundary condition is imposed on the metric function:

$$\Theta(R) = \frac{1}{2} \ln \left(1 - \frac{2M}{r}\right) \quad (1.9)$$

which ensure the function with match smoothly with the Schwarzschild metric that describe the spacetime at  $r > R$ .

The first neutron star structure was calculated by Tolman (1939) and Oppenheimer & Volkoff (1939). They adopted an EOS of non-interacting relativistic neutron gas which is extremely soft. At an unreasonably high central density of  $\sim 17n_0$ , such EOS predicts a maximum mass of  $0.7M_\odot$ . Such low value obviously contradicts the measured masses of neutron stars in the binaries which has an average value of  $1.5M_\odot$  (cf. Prakash 2007 and references therein).

It has been found that the stiffness of the EOS for neutron gas can be increased drastically by taking the interaction of the neutrons into account (see Fig. 2 in Weber, Negreiros & Rosenfield 2008). However, such stiff EOS results in a very large radius ( $\sim 20$  km). This results in a fact that the Keplerian frequency,  $\Omega_K \propto R^{-3/2}$ , which is considerably smaller than that of the fast rotating pulsars. For examples, PSR J1748-2446ad with  $\Omega = 716$  Hz (Hessels et al. 2006) and B1937+21 with  $\Omega = 630$  Hz (Backer et al. 1982). This suggests that this EOS provide us a tighter upper bound of the stiffness than the condition of causality,  $(dP/d\rho)^{1/2} = c$ , (Weber, Negreiros & Rosenfield 2008).

These have demonstrated that measurements of masses, radii as well as the rotation of the neutron stars can provide constraints in the neutron star matter and help in discriminating among the different EOS candidates.

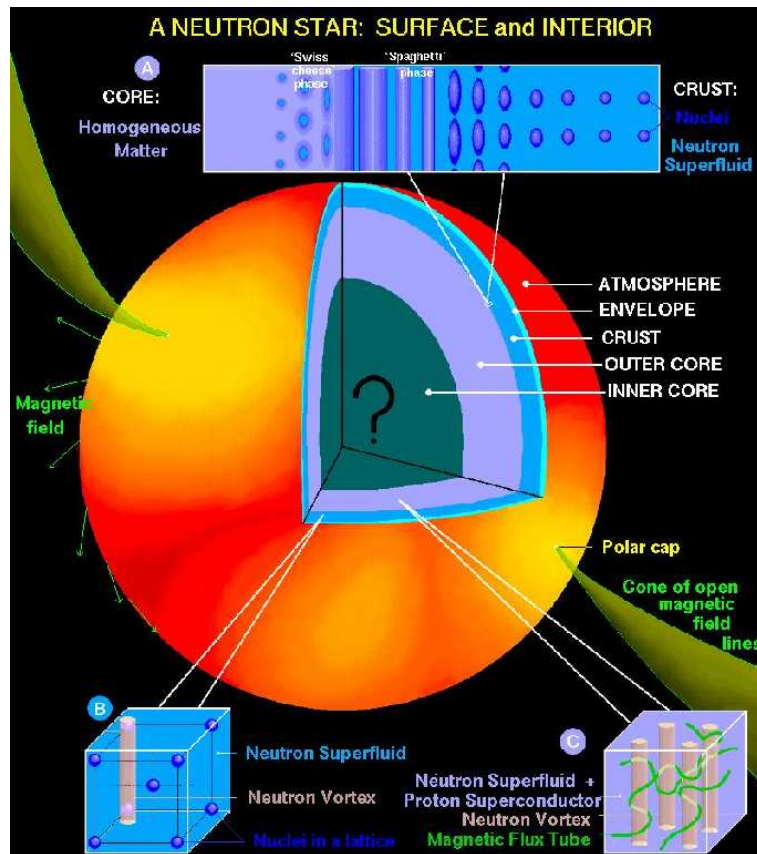


Figure 1.1: Illustration of the structure of the neutron star interior. *Figure Courtesy: Dany Page*

### 1.2.3 Composition of neutron stars

The structure of a neutron star can be divided into four major regions: the core, the crust, the envelope and the atmosphere. In this section, we are going to review the basic properties from the stellar surface to the inner core.

#### Envelope & Atmosphere

Although the atmosphere only has a thickness at the order of magnitude of a few centimeter, it can possibly alter the emergent photon spectrum from that of a perfect blackbody. However, modeling the spectrum requires knowledge of many physical properties of the atmosphere (e.g. the abundance, magnetic field) which are still not well understood. This makes the atmospheric modeling is still subjected to many unknown parameters. While the degenerated core can be well-described with an isothermal model, the envelope (i.e.  $\rho \leq 10^{10} \text{ g cm}^{-3}$ ) can sustain a significant temperature gradient which crucially affects the thermal transport inside a neutron star (see the following section for a more detailed

review).

## Crust

The crust has a thickness of  $\sim 1 - 2$  km below the stellar surface (see Fig. 1.1). The main components of the crust are nuclei. The dominant nuclei are found to vary with the crust density (Lattimer & Prakash 2004). At a density of  $\leq 10^6$  g cm $^{-3}$ ,  $^{56}\text{Fe}$  are the dominant nuclei. While at the core-crust interface ( $n \sim n_0/3$ ), the nuclei can have a mass number of  $A \sim 200$  and a high isospin asymmetry which has a proton fraction of  $\sim 0.1 - 0.2$ .

At the neutron drip density (i.e.  $4 \times 10^{11}$  g cm $^{-3}$ ), the chemical potential of the neutrons is zero which implies that the neutrons can freely leak out of the nuclei. As the density goes beyond this value, more neutrons leak out and form a fluid rather than residing in the nuclei. If the temperature in the crust is low enough (i.e.  $< 0.1$  MeV), the neutron fluid can form a  $^1S_0$  superfluid (Baym & Pethick 1975, 1979). Superfluid can have profound effects on the neutron star cooling (see the following section).

Furthermore, a novel state of matter within the crust has been speculated by Pethick & Ravenhall (1995) (see Fig. 1.1). Beginning at the subnuclear density ( $\sim 0.1n_0$ ), there can be a continuous change of the dimensionality of the matter: from 3D nuclei (meatballs) to 2D cylindrical nuclei (spaghetti) and 1D slab-like nuclei (lasagna). Such state of nuclear matter is usually referred as nuclear “pasta” (Lattimer & Prakash 2004). If this state of matter actually exists, it could have impact on many transport properties, such as neutrino propagation through star (e.g. Horowitz et al. 2005).

## Core

The core of a neutron star consists of  $\sim 99\%$  of the stellar mass. It can be divided into two region, namely the outer core and the inner core (see Fig. 1.1). In the outer core, the neutrons and protons can form a  $^3P_2$  superfluid and a  $^1S_0$  superconductor, respectively. The presence of superfluid has a significant effect in the thermal history of a neutron star (see the following section). In the inner core, the density can be up to an order of magnitude higher than  $n_0$ . At such high density, the chemical potential of neutrons can exceed the effective masses of certain exotic particles. Hence, it is speculated that strangeness-carrying hyperons and/or meson condensates can exist in the inner core (e.g.  $K^-$ ,  $\pi^-$ ,  $\Lambda$ ). Apart from affecting the stiffness of the EOS, these exotic particles also play an important role in neutron star cooling (see the following section). Also, it has been shown that  $K^-$  condensates can possibly turn the neutron star core to become a more isospin symmetric composition (Brown 1996). Thus the meson condensates can alter the stellar structure through the symmetric energy of the neutron star matter.

Without the presence of exotic particles, as mentioned in the formation of neutron stars, the core is consisted of a highly isospin asymmetric matter (i.e. the number of neutrons is much larger than that of protons). Any acceptable model of the EOS has to take the symmetric energy of neutron star matter into account and its value has to be reduced to the limit of 32.5 MeV for infinite symmetric nuclear matter at the saturation density  $n_0$

(Weber, Negreiros & Rosenfield 2008). The symmetric energy of neutron star matter is highly uncertain. This provides a freedom in varying the model of EOS. Such uncertainty can result in a variation of the pressure at  $n_0$  by a factor of 6 and consequently leads to a  $\sim 50\%$  variation in the inferred neutron star radius (Lattimer & Prakash 2001).

Under the enormous pressure in the core, nucleons can be brought extremely close to each other. Considering a simple picture of a characteristic nucleon radius  $r_N \sim 0.5 - 1$  fm, nucleons can start to touch each other at the density of  $(4\pi r_N^3/3)^{-1} \sim 2 - 10n_0$ . It has been suggested that the constituent quarks of nucleons can be deconfined. Therefore, a neutron star might contain a quark core (see Weber, Negreiros & Rosenfield 2008 and references therein). However, until now there is no convincing observational evidence for its existence (see Trümper 2008).

### 1.2.4 Thermal evolution of neutron stars

Apart from being compact, neutron stars are also very hot since they are generally believed to be formed at very high temperatures in the core-collapsed supernovae (see section 1.2.1). After the epoch when the star becomes transparent to the neutrinos, electrons play the role of energy carriers and become the primary agent of energy transport. Because of the extreme degeneracy of the electrons, a very large thermal conductivities in the interior are resulted which lead to an approximately isothermal core.

Thermal study of neutron stars has long been proposed to be a promising probe to unravel the interior structure and the physics of neutron star matter (see Tsuruta 2008). This is due to the fact that the thermal evolution calculations are highly sensitive to physics inputs, in particular the EOS. The stiffness of the adopted EOS will significantly affect the structure of a neutron star. For a given mass of a neutron star, the stiffer the EOS, the lower the central density, the thicker the crust and the larger the radius will be. Moreover, the density distribution of interior, on which many other physics inputs such as, thermal conductivity, heat capacity and neutrino emission rely, also depends on the adopted EOS. All the aforementioned factors will definitely affect the heat transport inside a neutron star and hence the cooling rate.

By the law of conservation of energy, a neutron star cooling scenario can be obtained by equating the time derivative of the total internal energy  $U$  and the negative of the total luminosity  $L_{tot}$ :

$$\frac{dU}{dt} = -L_{tot} \quad (1.10)$$

$L_{tot}$  consists of surface photon emission  $L_\gamma = 4\pi R^2 \sigma T_{eff}^4$ , neutrino emission  $L_\nu$  and the internal heating mechanism  $H$ :

$$L_{tot} = L_\gamma + L_\nu - H \quad (1.11)$$

where  $H$  is included as a negative energy sink. Internal heating can be as a result of several mechanisms which includes the energy deposited by pulsar glitches (Hui & Cheng 2004).

It is not certain how long the thermal emission from a neutron star surface can remain visible to observers. This is mainly due to our poor knowledge of the actual neutrino cooling reactions in the neutron star interior. These reactions produce neutrinos or anti-neutrinos which continuously carry out energy. The most efficient cooling mechanisms are the direct URCA processes (cf. equations 1.3 & 1.4). However, such processes are only permitted if the proton fraction exceeds a certain critical value. Assuming a neutron star consists of only nucleons and electrons, the critical proton fraction can be estimated as followings.

From equations 1.3 & 1.4, conservation of momentum is expressed as the equality of the particle Fermi momenta:  $k_{F_n}^{\vec{}} = k_{F_p}^{\vec{}} + k_{F_e}^{\vec{}}$ . With the triangular inequality, this implies the magnitude of the momenta to be  $k_{F_n} \leq k_{F_p} + k_{F_e}$ . In addition, charge neutrality requires  $n_p = n_e$ . The particle number density  $n$  can be expressed in terms of the Fermi momentum as  $n = k_F^3/3\pi^2$ . Therefore the charge neutrality can be expressed as  $k_{F_p} = k_{F_e}$ . Putting all these together, the triangular inequality becomes  $k_{F_n} \leq 2k_{F_p}$  or  $n_n \leq 8n_p$ . Assuming the total baryon number density  $n_{tot} = n_p + n_n$ , a proton fraction,  $n_p/n_{tot} \geq 1/9$ , is required to conserve both energy and momentum simultaneously in the direct URCA processes.

If neutrons and protons are the only baryons in the star and the proton fraction is not high enough, direct URCA process will be forbidden. In this case, a so-called standard cooling scenario will take place with modified URCA process as the cooling mechanism:

$$n + n \rightarrow n + p + e^- + \bar{\nu}_e \quad (1.12)$$

$$e^- + p + n \rightarrow n + n + \nu_e \quad (1.13)$$

In these processes, bystander nucleons are present to absorb momentum and thus both momentum and energy can be conserved. Comparing with the direct URCA process, the cooling rate of modified URCA process is considerably slower. Therefore, within the context of a standard cooling scenario, the surface thermal emission of a neutron star is expected to remain observable for a few million years.

As discussed above, the question of whether the direct URCA processes can occur is of key importance for neutron star cooling. The proton fraction depends on the symmetric energy and generally increases with density (Lattimer & Prakash 2004). Hence, direct URCA processes might occur when the central density is above certain threshold. However, since the symmetric energy of neutron star matter is highly uncertain, the threshold density at which the nucleonic direct URCA process occur is not well-determined. On the other hand, if exotic particles such as hyperons exist in the inner core, other direct URCA processes can be triggered. For example:

$$\Sigma^- \rightarrow \Lambda + e^- + \bar{\nu}_e \quad (1.14)$$

$$e^- + \Lambda \rightarrow \Sigma^- + \nu_e \quad (1.15)$$



Comparing with the nucleon direct URCA process, the ones involving hyperons are generally less efficient (Weber, Negreiros & Rosenfield 2008).

Superfluidity can further modify the cooling rates in several ways. First, the heat capacity is affected. The heat capacity will undergo a discontinuous increase at the phase-transition temperature followed by an exponential decline as the temperature drops. Hence, the cooling rate decreases immediately above the transition temperature and increases at lower temperature. Furthermore, since the phase spaces of the nucleonic neutrino production processes are suppressed in a superfluid, the cooling rate decreases. However, an additional way of cooling which involves the formation and breaking of nucleonic Cooper pairs has been suggested (Flowers, Ruderman, & Sutherland 1976). This can increase the cooling rate from the modified URCA process.

Despite the interior can be well approximated as in an isothermal state, the envelope (i.e.  $\rho \leq 10^{10} \text{ g cm}^{-3}$ ) can sustain a very large temperature gradient which results in a surface temperature about 100 times smaller than that at the base of the envelope (Gudmundsson, Pethick & Epstein 1983). The composition of this layer gives one more uncertainty affecting the cooling trajectories of a neutron star. The light elements (H or He) in the envelope can have a smaller photon opacity. For a give temperature at the base, the presence of light elements can result in a higher surface temperature. This effect will strongly affect the conclusions drawn by comparing the theoretical models with the observational data.

### 1.2.5 Pulsar magnetosphere and high energy radiation

Goldreich & Julian (1969) had firstly pointed out that a vacuum solution for the region surrounding a rotating magnetized neutron star cannot be stable, since the strong electric field parallel to the stellar surface will rip off charged particles and develop a magnetosphere around the pulsar. While the charged particles in the magnetosphere are threaded by the magnetic field lines, it is expected that they must corotate with the neutron star. Nevertheless, the corotation must break down at certain large distance as a result of the finite inertia of the particles. The exact place for this to happen is not well-known yet, but it is certain that the corotation region cannot past the light cylinder radius (the distance at which the corotation velocity equal to the speed of light  $c$ ) given by:

$$R_{LC} = \frac{c}{\Omega} = 5 \times 10^9 P \text{ cm} \quad (1.16)$$

where  $P$  is the rotation period of the pulsar in units of seconds. In this view, the magnetosphere can be divided into two regions (see Fig. 1.2): 1) The corotating closed field-lines region with the last closed field touching the light cylinder, and 2) the open field-line region with the last open field-line defining the conventional polar cap size on the stellar surface:

$$R_{PC} = R \sqrt{\frac{2\pi R}{cP}} \quad (1.17)$$

Assuming the charge supply creates a force-free condition (i.e.  $E + v \times B/c = 0$ ), Goldreich & Julian (1969) had calculated the corotation charge density (usually dubbed

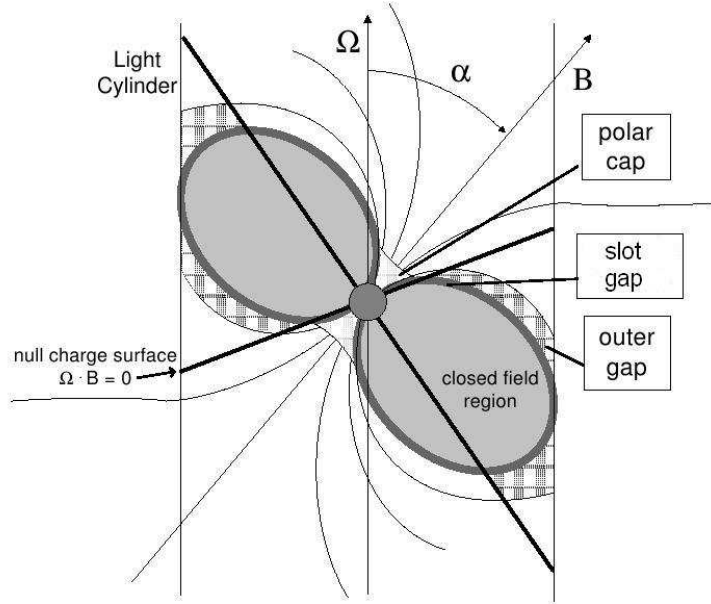


Figure 1.2: Illustration of the pulsar magnetosphere and some suggested acceleration regions. *Figure Courtesy: Alice Harding*

as Goldreich-Julian density) developed in the magnetosphere which is given as:

$$\rho_{GJ} = -\frac{1}{2\pi c}\Omega \cdot B \quad (1.18)$$

Since pulsars are rotating and highly magnetize celestial objects, they behave as natural unipolar inductors and are expected to generate huge electric field in vacuum. However, if the charge density is described by  $\rho_{GJ}$  everywhere in the magnetosphere, the electric field parallel to the magnetic field will be shorted out (i.e.  $E \cdot B = 0$ ). This leads to the speculation that the charged particles can only be accelerated in the regions with the charge density deviated from  $\rho_{GJ}$  which result in an electric field along  $B$ .

Various emission models had been proposed. Despite the fact that these models are fundamentally different from each other, they do incorporate acceleration of electron/positron in the charge depletion regions (or gaps) of certain forms. High energy photons are produced when the charged particles are accelerated in these regions. According to the location of the accelerating regions, these models can be divided into two main classes: a) *Polar cap models*, which have the high energy emission originated near the magnetic poles in the inner magnetosphere. b) *Outer-gap models*, which have the radiation processes taking place in the outer magnetosphere (see Fig. 1.2).

### Polar cap model

The earliest polar cap models are proposed by Sturrock (1971) and Ruderman & Sutherland (1975). There are a number of variations and modifications of this class of model. These models can be divided into two sub-classes depending on whether there is free emission of particles from the neutron star surface. In this consideration, the nature of the acceleration region is governed by the surface temperature  $T_s$  and the thermal emission temperature of ions/electrons at the crust  $T_{ion,e}$ . If  $T_s < T_{ion,e}$ , there will be no free emission of charges and a vacuum gap will develop from the surface as the acceleration region (e.g. Ruderman & Sutherland 1975, Usov & Melrose 1995). On the other hand, if  $T_s > T_{ion,e}$ , there will be free emission of charged particles of either sign from the surface. The flow of these particles is limited by space charge and usually called as space charge limited flow models (Arons & Scharlemann 1979; Muslimov & Tsygan 1992).

In the space charge limited flow model, the charge density at the surface is  $\rho_{GJ}$  (see Harding 2008) and hence  $E \cdot B = 0$  at the surface. However, the flow of particles along each open-field line above the surface is unable to supply the corotation charge to short out the electric field parallel to the magnetic field. Hence, an acceleration region is developed just above the stellar surface due to the charge deficit (Arons & Scharlemann 1979; Muslimov & Tsygan 1992). The acceleration region will extend until the parallel component of the electric field is screened at a height where the accelerated particles radiate high energy photons that subsequently produce pairs. Such locus is usually called pair formation front (PFF).

There are two radiative mechanisms that can take place in the gap in determining the PFFs. For the accelerated particles at a Lorentz factor  $\gamma \sim 10^2 - 10^6$ , high energy photons will be produced by inverse Compton (IC) scattering of thermal X-rays from the stellar surface. If the accelerated particles have a Lorentz factor  $\gamma \geq 10^6$ , curvature photons will be radiated (Kaspi, Roberts & Harding 2004). The lower values of Lorentz factor required in producing pairs through IC emission implies that the IC PFF will form first and closer to the stellar surface. Since it has been found that the IC PFF cannot produce sufficient pairs to completely screen the parallel electric field, acceleration can continue beyond IC PFF and up to a Lorentz factor of  $\sim 10^7$  to form a curvature PFF (see Harding 2008). The curvature photons are able to produce secondary electron/positron pairs via magnetic pair production in the strong magnetic field. These pairs are generally created in excited transverse (to the field) momentum states, namely Landau states. De-excitations will subsequently radiate synchrotron radiation which is energetic enough to create more pairs and successive generations of photons (Daugherty & Harding 1996). While transverse portion of the energy of the pairs goes to synchrotron radiation, the parallel portion of energy probably loses through ICS with the thermal X-rays from the stellar surface (Zhang & Harding 2000). A full cascade that comprises non-thermal emission of curvature, synchrotron and ICS radiation is thus formed. The soft tail of the spectrum resulting from ICS of higher order generation pairs has provided a non-thermal X-ray component to model the observed properties in soft X-ray band (Zhang & Harding 2000).

Thermal X-rays in polar cap models are produced from surface heating as a result of the

screening of the parallel electric field (Harding & Muslimov 2001,2002). As aforementioned, the screening region starts beyond the IC PFF. In this region, a fraction of positrons will decelerate and turn around. Then they will subsequently be accelerated towards the stellar surface and give rise to the polar cap heating emission (Harding & Muslimov 2001,2002). For the X-ray luminosity of the polar cap heating by positrons trapped in the curvature PFF, if the rotation period satisfies  $P \leq 0.1B_{s,12}^{4/9}$  sec, then

$$L_+^{CR} = 4 \times 10^{30} P^{6/7} \tau_6^{-1/7} \text{erg s}^{-1} \quad (1.19)$$

where  $B_{s,12}$  is the surface magnetic field in units of  $10^{12}$  G and  $\tau_6$  is the pulsar age in units of  $10^6$  years. On the other hand, if  $P > 0.1B_{s,12}^{4/9}$  sec, then

$$L_+^{CR} = 10^{31} P^{1/2} \text{erg s}^{-1} \quad (1.20)$$

For the polar cap heating from the positron returning from the IC PFF, the X-ray luminosity can be expressed as

$$L_+^{ICS} = 2.5 \times 10^{27} P^{-3/2} \text{erg s}^{-1} \quad (1.21)$$

Since the curvature PFF can produce sufficient pairs to completely screen off the parallel electric field, this PFF determines the upper limit of the acceleration voltage and hence the luminosity of high energy radiation (Kaspi, Roberts & Harding 2004). The polar cap model predicts a very sharp high energy cut-off in the pulsar spectrum. This is determined by the highest energy at which the photons can escape the magnetosphere without any pair production attenuation. The cut-off energy at a radius  $r$  from the star is estimated as (Kaspi, Roberts & Harding 2004)

$$E_{cutoff} \sim 2P^{1/2} \left(\frac{r}{R}\right)^{1/2} \max \left[ 0.1, B_{s,12}^{-1} \left(\frac{r}{R}\right)^3 \right] \text{GeV} \quad (1.22)$$

In conventional polar cap models, a hollow cone of cascade radiation is produced within a few stellar radii above the magnetic pole (Kaspi, Roberts & Harding 2004). The opening angle of the cone is thus given by the polar cap half angle at the location of the emission region  $r$ :  $\theta_{PC} = (2\pi r/cP)^{1/2}$ . However, many X-ray and  $\gamma$ -ray pulsars (like Crab, Vela and Geminga) are observed to have wide double-peaked pulse profiles. To reproduce such profiles in the context of a polar cap model would require to place the gap artificially at large distances above the surface without any physical reason. This is one drawback of polar cap models in describing the high energy emission of pulsars. One proposed remedy for this problem is to reconsider the parallel electric field along the last-open field lines (Harding 2008). Assuming the last-open field lines to be a conducting boundary, this would imply the electric field parallel to these field lines to be zero. This would result in a slower acceleration in the gap so that the particles need a longer distance to accelerate to the requiring Lorentz factors to produce pairs. As a result, the PFFs are pushed to a higher altitude. With this consideration, it was found that the PFF asymptotically approach the the last-open field lines (Arons 1983) which forms a pair-free zone (see Fig. 1.2) usually called as a slot gap (cf. Harding 2008 and references therein).

### Outer gap model

The outer gap model was firstly proposed by Cheng, Ho, Ruderman (1986) in order to explain the  $\gamma$ -ray emission observed from the Crab and Vela pulsars. The acceleration regions in this model are located along the last closed field-line and above the null charge surface which is defined by  $\Omega \cdot B = 0$ . Since charged particles on each side of the null charge surface have opposite charges (see equation 1.18), charge depletion regions can be developed from the fact that the charged particles escaping along the open field-lines above the null charge surface cannot be replaced by the charges from below.

The gaps are sustained self-consistently (Zhang & Cheng 1997). The size of the outer gaps are controlled by the electron/positron pairs produced in the photon-photon pair production resulting from collisions between the curvature photons with energy  $E_{\gamma_{cur}}$  emitted by the primary electron/positron accelerated in the gaps and the soft thermal X-rays emitted from the stellar surface. These soft X-rays with energies  $E_{X_{soft}}$  are produced by the collision of the backflow of the primary electron/positron. One should notice that both  $E_{X_{soft}}$  and  $E_{\gamma_{cur}}$  are functions of the gap size. With this consideration, the size of the outer gap is determined by the criteria that the center of mass energy of the soft X-rays and the curvature photons at least matches the threshold for electron/positron pair production (i.e.  $E_{X_{soft}}E_{\gamma_{cur}} \sim (m_e c^2)^2$ ). Zhang & Cheng (1997) quantified the gap size by:

$$f_0 = 5.5 P^{26/21} B_{12}^{-4/7} \quad (1.23)$$

which is the ratio of the mean vertical separation of the gap boundaries in the plane spanned by the rotation axis and the magnetic axis to the light cylinder radius. Zhang et al. (2004) have incorporated the effect of the magnetic inclination angle in calculating the gap size. The effect is found to be profound in the cases of old pulsars (for further discussion, please see Chapter 7).

In the outer gap model, the observed thermal/non-thermal X-ray emission is related to the backflow current (Cheng & Zhang 1999). The electron/positron leaving the inner boundary of the outer gap emit curvature photons with a characteristic energy of

$$E_\gamma = \frac{3}{4\pi} h \frac{c}{s} \gamma(x)^3 \quad (1.24)$$

where  $x = s/R_{LC}$ ,  $s$  is the local radius of the curvature and  $\gamma(x) \propto x^{-3/4}$  is the Lorentz factor of the electron/positron at the inner boundary. Some of these high energy photons will be converted into secondary electron/positron pairs, if the magnetic field is strong enough that the pair production condition is satisfied, i.e.

$$\frac{E_\gamma}{2m_e c^2} \frac{B(r_s)}{B_g} = \frac{1}{15} \quad (1.25)$$

where  $E_\gamma$  is given by equation 1.24,  $B(r_s)$  is the magnetic field at position  $r_s$ , and  $B_g = 4.4 \times 10^{13}$  G. Assuming the local field is a simple dipole field, equation 1.6 implies the first generation of secondary pairs will be generated as the distance  $r_s$  from the star:

$$r_s = \left( \frac{15E_\gamma B_s}{2m_e c^2 B_g} \right)^{1/3} R \quad (1.26)$$

where  $R$  is the neutron star radius and  $B_s$  is the surface magnetic field. These secondary pairs will subsequently lose their energy by emitting synchrotron photons with a characteristic energy of  $E_{syn} = E_\gamma/20$ . These synchrotron photons will keep traveling towards the star. If these photons are energetic enough and/or they encounter a strong magnetic field, they will further convert into a new generation of pairs which will again lose their energy through synchrotron radiation. As a result, a cascade is developed and responsible for the production of non-thermal X-rays.

The production of thermal X-rays in the outer gap model is through the bombardment of the return current onto the neutron star surface (Cheng & Zhang 1999). The X-ray luminosity can be written as

$$L_X^{therm} = E_e(R) \dot{N}_e \quad (1.27)$$

where  $E_e(R) = m_e c^2 \gamma(R)$  is the residual energy deposit on the stellar surface by each particle and  $\dot{N}_e = f_0 \dot{N}_{GJ}$  is the return particle flux with  $\dot{N}_{GJ}$  is the Goldreich-Julian particle flux (see Goldreich & Julian 1969):

$$\dot{N}_{GJ} = \frac{B_s \Omega^2 R^3}{Z e c} \quad (1.28)$$

in which  $Ze$  is the ion charge. However, if the magnetic field of the neutron star is strong enough, only a fraction of these X-rays can escape from the neutron star surface through a narrow window with opening angle  $\leq 10^\circ$  and the others are reflected back to the stellar surface in the closed-field lines (see Cheng & Zhang 1999 for further details). Their energy will then be transferred to the whole stellar surface and subsequently be reradiated as softer thermal X-rays.

In the previous sub-section, the high energy cut-off in the pulsar spectrum has been mentioned. While a very sharp cut-off at a few GeV is expected by the magnetic pairs attenuation in the context of polar cap model, outer gap model predicts a different high energy cut-off (cf. Smith 2008 and references therein). Instead of magnetic pairs creation, the cut-off is determined by photon-photon pair production (as described in this sub-section) in outer gap model. It has been found that the photon-photon pair production has a weaker energy dependence than magnetic pair production (cf. Smith 2008), a higher cut-off energy (at a few tens of GeV) is thus expected.

One particular drawback of the conventional outer gap model (e.g. Cheng & Zhang 1999) is found in the pulse profile modeling. Since no outward emission originates below the null charge surface, the edges of the profiles produced by the conventional outer gap model fall very abruptly (cf. Cheng 2008). This contradicts the observed leading and trailing wings in many pulsars including the Crab, Vela and Geminga. One proposed remedy is to allow a large current flow through the outer gaps which can alter the inner boundary and

thus possibly produce an extended emission region from the null charge surface nearly to the stellar surface (cf. Hirotani 2005; Cheng 2008).

### Pulsar wind nebulae

The aforementioned models are applied to explain the high energy radiation within the light cylinder which contribute to the pulsed component of the observed emission. For the non-thermal non-pulsed component, it is produced in a wind region beyond the light cylinder (Kaspi, Roberts & Harding 2004). While the pulsed component only consume a small fraction of the rotational energy from a pulsar, most of the energy leaves the magnetosphere via the magnetized wind consisting of high energy particles (Hui & Becker 2007b and references therein). The basis of the pulsar wind is provided by  $\dot{N}_{GJ}$ . To characterize the wind, a magnetization parameter,  $\sigma$ , is commonly used which is defined as the ratio between the Poynting flux,  $F_{E \times B}$ , and the particle energy flux  $F_{particle}$ :

$$\sigma = \frac{F_{E \times B}}{F_{particle}} = \frac{B^2}{4\pi\rho\gamma_w c^2} \quad (1.29)$$

where  $\rho$  is the mass density of the wind particles and  $\gamma_w$  is the corresponding Lorentz factor. Almost all pulsar emission models predict that  $F_{E \times B}$  is many orders of magnitude larger than  $F_{particle}$  (cf. Gaensler & Slane 2006). When the wind flows through the light cylinder,  $\sigma$  is typically  $> 10^4$ . However, modeling the structure of the Crab Nebula requires  $\sigma \leq 0.01$  just behind the termination shock (Kennel & Coroniti 1984; Rees & Gunn 1974). This implies the wind particles must be dramatically accelerated in a region between the light cylinder and the termination shock. Although there are many attempts in establishing the connection between the magnetosphere and the wind zone (e.g. Contopoulos et al. 1999), there is no generally accepted model.

In the termination shock, the relativistic wind particles interact with the shocked interstellar medium and radiate synchrotron radiation across the electromagnetic spectrum. Physical models for describing pulsar wind nebular emission can be divided into two main classes, depending on whether the pulsar is moving subsonically or supersonically (see Cheng, Taam, & Wang 2004). For a subsonic pulsar motion, the shock termination radius  $R_s$  is determined by the balance between the wind ram pressure and the total magnetic and particle pressure within the nebula (Rees & Gunn 1974):

$$R_s \simeq \left( \frac{\dot{E}}{B^2 c} \right)^{1/2} \quad (1.30)$$

where  $\dot{E}$  is the spin-down power the pulsar. This will result in a wind bubble with the pulsar located at the center.

In the case of supersonic motion, a bow shock nebula will be formed.  $R_s$  is then determined by the balance between the wind particles and the interstellar medium (ISM) at the head of the shock:

$$R_s = \left( \frac{\dot{E}}{2\pi\rho_{ISM}v_p^2c} \right)^{1/2} \quad (1.31)$$

where  $\rho_{ISM}$  is the density of the ISM and  $v_p$  is the pulsar velocity.

The energy distribution of the radiating particles in the postshock,  $N(\gamma) \propto \gamma^{-p}$ , is determined by the balance between the particle injection rate, and the synchrotron loss which is expressed in a differential equation as (Chevalier 2000):

$$\frac{\partial N(\gamma)P(\gamma)}{\partial\gamma} = m_e c^2 \dot{N}(\gamma) \quad (1.32)$$

where  $P(\gamma)$  is the synchrotron power of an electron with a Lorentz factor  $\gamma$ . By solving the above equation, the luminosity of radiating particles in the range of  $\gamma$  to  $\gamma + d\gamma$  can be calculated as  $N(\gamma)P(\gamma)$ . Since this model implicitly assumes that a single distribution of electrons have been injected evenly throughout the pulsar wind nebula, it is usually referred as one-zone model (Chevalier 2000; Cheng, Taam, & Wang 2004). For a further description of the model and its applicability in actual X-ray observations, please see Hui & Becker (2006a, 2007b).

Apart from the non-thermal emission, some fast-moving pulsars have produced a forward shock which are observable in the  $H\alpha$  line. The  $H\alpha$  emission is resulted from the collisional excitation and charge exchange of the neutral hydrogen atoms in the ISM which is a thermal process indeed. One classic example for this is the Guitar nebula which is powered by the pulsar PSR B2224+65 which is moving through the space at a velocity of  $\sim 1000$  km/s (Hui & Becker 2007a and references therein).

Many pulsar wind nebulae have been discovered in TeV regime recently (de Jager 2008). It is generally believed that the TeV photons from these nebulae are resulted from IC scattering of soft photons field by the relativistic electrons and positrons emitted by the pulsars. The seed soft photons for the IC processes are possibly contributed by the cosmic microwave background, interstellar dust, starlight and the synchrotron photons emitted by the accelerated particles (see Gallant et al. 2006). Apart from the leptonic model, a hadronic model, which involves neutral pion decay, has also been proposed for the TeV emission from the pulsar wind nebulae (for recent review, see Cui 2006 and references therein).

### 1.3 Manifestations of Isolated Neutron Stars

We now know that neutron stars can reveal themselves in a number of different ways. The “family” of isolated neutron stars includes: rotation-powered pulsars, soft  $\gamma$ -ray repeaters, anomalous X-ray pulsars, central compact objects in the supernova remnants, dim thermal isolated neutron stars as well as the recently discovered rotating radio transients (RRATs). In this section, the main observational properties of these “family members” will be briefly reviewed.



### 1.3.1 Rotation-powered pulsars

Pulsars is the first class of celestial objects be identified as rotating neutron stars. Because of many successful pulsar surveys (cf. Manchester 2004 and references therein), the sample size of pulsars is now known to be as large as  $\sim 1800$ . The most remarkable characteristics of pulsars is their highly periodic pulse train. Pulsars can be divided into two main categories: non-recycled pulsars and millisecond pulsars. Non-recycled pulsars are characterized by the typical periods of  $\sim 1$  s and the period derivatives of  $\sim 10^{-15}$  s s $^{-1}$ . Dipolar surface magnetic fields of  $\sim 10^{12}$  G are implied from spin parameters. Millisecond pulsars are the pulsars with periods less than  $\sim 20$  ms. Their short periods are believed to be the results of a recycling process in which mass and angular momentum are transferred to a slowly rotating pulsar from its binary companion (cf. Bhattacharya & van den Heuvel 1991). The spin-down rates of millisecond pulsars are found to be smaller than those of non-recycled pulsars by four to six orders of magnitudes (Manchester et al. 2005). These imply their ages and surface magnetic field to be  $\sim 10^{9-10}$  yrs and  $10^{8-9}$  G respectively.

Through the spectral and temporal analysis of the X-rays detected from rotation-powered pulsars, the emission is found to comprise thermal and non-thermal components. The non-thermal component is characterized by a power-law spectrum. It can further be separated into two different contributions, namely the pulsed and non-pulsed non-thermal emission. Pulsed non-thermal emission is originated from the charged relativistic particles accelerated in the pulsar magnetosphere. For the non-pulsed contribution, it is originated outside the light cylinder and arise from the interaction between the pulsar wind and the surrounding medium. For more details of pulsars' non-thermal emission, please see section 1.2.5. Thermal emission from the pulsar can possibly have two components: a soft thermal component contributed by the cooling emission from the hot stellar surface and a harder component from the hot polar caps.

The relative contribution from each components in the observed pulsar X-ray emission depends on the age of the pulsar, the structure and the orientation of the magnetic field, the viewing geometry as well as the surrounding interstellar medium.

### 1.3.2 Soft $\gamma$ -ray repeaters/Anomalous X-ray pulsars

While the canonical pulsars typically have a dipolar surface magnetic field of  $\sim 10^{12}$  G, it has been suggested that neutron stars can have magnetic fields as high as  $\sim 10^{15}$  G (cf. Thompson & Duncan 1996). These highly magnetic neutron stars are usually called magnetars. Thompson & Duncan (1996) suggested that such high magnetic field can be formed through the amplification by a convection-driven dynamo during the first  $\sim 10$  s of the proto-neutron star phase. If the rotation of a proto-neutron star is compatible with the typical convection period of  $\sim 10$  ms, the convection currents are able to operate globally and transfer a significant amount of their kinetic energy into magnetic field strength.

It is now widely accepted that magnetars can manifest themselves into at least two forms: anomalous X-ray pulsars (AXPs) and soft gamma-ray repeaters (SGRs). AXPs are X-ray sources that have been detected through their persistent X-ray pulsations. Their

periods lie in the range between  $\sim 5 - 12$  s (Popov 2006). Their spin-down rates are orders of magnitudes larger than the canonical pulsars. Modeling their X-ray spectra usually require a blackbody of  $kT \sim 0.4$  keV plus a steep power-law tail of photon index  $\sim 2.5 - 4$  (Kaspi 2004). For SGRs, the most remarkable characteristic is the repeating short soft  $\gamma$ -ray bursts with typical durations of  $\sim 0.1$  s and typical energies of  $\sim 10^{41}$  erg (Kaspi 2004). Occasionally, SGRs can produce giant  $\gamma$ -ray bursts at energies  $> 10^{44}$  erg (Kaspi 2004). The spin periods of SGRs span a range of  $\sim 5 - 8$  s which is similar to that of AXPs. Also, the similarity between X-ray spectra of SGRs in quiescence and those of AXPs suggests that they both belong to the same class (see Popov 2006 and references therein). Furthermore, the connection between AXPs and SGRs is supported by the ability of AXPs 1E 1048.1-5937 and 1E 2259+586 to produce SGR-like bursts (cf. Kaspi 2004 and references therein).

Neither the thermal energy and the rotational energy is sufficient to explain observed X-ray luminosities of SGRs and most AXPs. The most accepted model to explain their observed properties is the magnetar model which takes the magnetic field as the main energy source (Duncan & Thompson 1992). Within the context of this model, the normal bursting and the energetic flare are due to the energy released by the crust-crackings caused by the diffusion of magnetic field through the stellar core and the magnetic reconnection respectively. For the persistent X-ray emission, it is explained as a result of magnetic field decay.

### 1.3.3 Central compact objects in supernova remnants

Thanks to the sensitive spectro-imaging observations with the state-of-art X-ray observatories, the sample size of a class of X-ray point sources usually dubbed as central compact objects (CCOs) is constantly growing. The nature of CCOs is still not well understood. They are characterized by their locations near to the expansion centers of supernova remnants. Such association suggests that they are the compact stellar remnants formed in the supernova events. Since supernova remnants can be detected only for a few tens of thousands of years before they fade into the interstellar medium, CCOs are thus considered to be the promising young neutron star candidates. They are usually identified by their high X-ray to optical/radio ratios which rule out many types of X-ray sources (e.g. AGNs) as the possible counterparts. Their X-ray spectra can be typically modeled with a double blackbody model of  $T \sim (3 - 7) \times 10^6$  K with small emitting regions  $R \sim 0.3 - 3$  km or a blackbody plus power-law model with photon indices  $> 3$  (see Hui & Becker 2006b; Becker, Hui, Aschenbach & Iyudin 2006). For the temporal behaviour, most of the CCOs show no long-term variability except for the one in RCW 103. A 6.7 hour period is confirmed for the CCO in RCW 103 (de Luca et al. 2006). However, the origin of the period is not yet clear. In a short time-scale, searches for X-ray pulsations from the CCO in Puppis-A have suggested an interesting periodicity candidate. If confirmed, the pulsations are likely from the hot spots on the rotating neutron star surface (Hui & Becker 2006b). Another interesting result related to the CCO in Puppis-A is its large possible proper motion (Hui & Becker 2006c). Both the magnitude and the direction of the proper

motion are in agreement with the birth place of the CCO in the supernova remnant being near to the optical expansion center (see Chapter 3 for more details).

### 1.3.4 Dim thermal isolated neutron stars

In the ROSAT era, seven radio-quiet isolated neutron stars with very similar properties were found. They are usually dubbed as “Magnificent Seven” (cf. Haberl 2008). The first source of this class, RX J1856.4-3754, was discovered a decade ago (Walter et al. 1996). The X-ray emission of all seven neutron stars are found to be very soft and characterized by a blackbody-like continuum. For three of them, relatively high proper motions have been detected (cf. Haberl 2008). This makes the accretion from the interstellar medium highly ineffective and thus favors the interpretation of isolated cooling neutron stars. Comparing with the standard cooling model, the ages of these neutron stars are in the bracket of  $\sim 10^5 - 10^6$  years (Tsuruta 2008). Photo-electric absorptions by the interstellar medium for these neutron stars are found to be very small which indicate that they are close-by objects (i.e. less than few hundred parsec).

Periodicities have been observed from the “Magnificent Seven”, though some of these periodicities still need further confirmation (Harbel 2008; Tiengo & Mereghetti 2007). The most recent discovered low-amplitude pulsations comes from RX J1856.4-3754 (Tiengo & Mereghetti 2007). The spin periods of these neutron stars span a range of  $\sim 3 - 13$  s which is similar to the case of magnetars. This indicates that the “Magnificent Seven” might have strong magnetic fields as well. Broad absorption features have been detected in the 0.1 – 1 keV band from several members in this class (see Haberl 2008 and references therein). The origin of these features is not yet clear. If the interpretation of these features as cyclotron lines is correct, this will imply the magnetic field of these neutron stars to be in the range of  $\sim 10^{10} - 10^{11}$  G or  $\sim 10^{13} - 10^{14}$  G for electron cyclotron resonance absorption and proton cyclotron resonance absorption respectively.

### 1.3.5 Rotating RAdio Transients (RRATs)

Very recently, a new manifestation of neutron stars is characterized by repeated dispersed short bursts of radio waves has been discovered in searches for transient radio sources (McLaughlin et al. 2006). These sources are dubbed as Rotating RAdio Transients (RRATs). Unlike normal radio pulsars, RRATs cannot be detected through the standard Fourier analysis of their emission. So far 11 RRATs have been discovered. Their the periods span a range of 0.4 – 7 s. These sources are located at distances of  $\sim 2 - 7$  kpc (McLaughlin et al. 2007). Although there are many speculations on the nature of RRATs, no consensus has yet been achieved (see McLaughlin et al. 2007 and references therein). One interesting speculation is that they are transient X-ray magnetars. Such possibility is suggested by the recent detection of transient radio pulsations from the anomalous X-ray pulsar XTE J1810-197 (Camilo et al. 2006).

One of the RRATs, J1819-1458, has been detected in X-ray (Reynolds et al. 2006; McLaughlin et al. 2007). The spin parameters of this source imply a surface dipole

magnetic field as high as  $5 \times 10^{13}$  G. X-ray pulsations at the period predicted by the radio ephemeris are identified (McLaughlin et al. 2007). Its X-ray spectrum is rather soft and can be well fitted with a blackbody model. An absorption feature has been suggested at  $\sim 1$  keV but the nature is not yet clear (McLaughlin et al. 2007).

## 1.4 Studying Neutron Stars with XMM-Newton & Chandra

Observatories in the last decade, including BeppoSAX, ASCA, ROSAT and RXTE, had helped us to make a big leap in X-ray neutron star astronomy. However, none of these facilities possessed the capability of wide energy bandwidth, large collecting area and high spatial and temporal resolution at the same time. This made the identification of the nature of neutron stars being difficult. This aspect can be illustrated with a few examples.

While ROSAT had allowed observers to study the soft thermal emission from the neutron star surface, its limited bandwidth of 0.1 – 2.4 keV precluded any broadband study. Therefore, the non-thermal contributions from the magnetosphere which characterized by hard power-law tails could not be conclusively identified. On the other hand, ASCA and BeppoSAX were sensitive up to 10 keV. They had allowed successful discoveries of young neutron stars in supernova remnants by their hard X-ray emission. However, their poor angular resolutions forbidden observers to resolve the central compact X-ray sources from their surrounding nebulae and/or their host supernova remnants. Despite there are a few bright Crab-like pulsars, neutron stars are generally known to be relatively faint X-ray emitters. This is especially true for the old neutron stars. None of the previous X-ray observatories was sensitive enough to constrain the nature of these faint sources. Moreover, even though the spectro-imaging analysis can put constraints on the nature of the pulsars' emission, the most strong argument that the X-ray sources are indeed the counterparts of the pulsars comes from the detection of X-ray pulsations which requires the detectors to have sufficiently good temporal resolution. With the advent of the Chandra X-ray Observatory and the X-ray Multi-Mirror Mission XMM-Newton, overcoming the aforementioned technical difficulties has become possible.

### 1.4.1 Chandra

The Chandra X-ray Observatory was launched into a 63.5 hours orbit on July 23, 1999 by the ill-fated Space Shuttle Columbia. Its X-ray telescope is made of four nested paraboloid-hyperboloid (Wolter-I) mirrors. The on-axis point spread function (PSF) of the telescope has a full width half maximum (FWHM) of  $\sim 0.5$  arcsec. Comparing with ROSAT, the mirror effective area of Chandra is about two times larger. Chandra has two focal plane instruments: Advanced CCD imaging spectrometer (ACIS) and High Resolution Camera (HRC).

ACIS has two CCD detector arrays, namely the ACIS-I and ACIS-S. ACIS-I is a  $2 \times 2$  CCD array which are optimized for direct image and ACIS-S is a  $1 \times 6$  CCD array which

are optimized for imaging X-rays that are dispersed by the High Energy Transmission Grating (HETG). The spatial resolution for on-axis imaging with the ACIS instrument is limited by the pixel size (0.492 arcsec). ACIS-I is designed to operate in the energy band of 0.5 – 8 keV. ACIS-S includes two back-illuminated CCDs with one at the best focus position. These devices cover a wider bandwidth than the front-illuminated CCDs and have superior quantum efficiency at the soft band (i.e. below 1 keV). In a full-frame mode, the typical exposure time is 3.24 s. Faster readout can be possible in the timed-exposure mode by utilizing only a portion of the CCD (i.e. sub-frame). In this mode, exposure times can be commanded from 0.1 to 10.0 s. For a even faster timing response, CCDs can be used in a continuous-clocking mode with the charges in the image condensed into one row to be readout. A fast temporal resolution of 2.85 ms is thus achieved at the expense of the loss of the information in one spatial dimension.

Similar to ACIS, HRC also has two detectors, namely the HRC-I and HRC-S. HRC-I is a microchannel plate designed for direct X-ray imaging. Its pixel size of 0.132 arcsec oversamples the PSF by a factor of  $\sim 5$ . Therefore, it has the superior spatial response among all the detectors on-board. HRC-S is a  $1 \times 3$  microchannel plate arrays designed as a readout detector of Low Energy Transmission Grating (LETG). Although HRC can offer a timing resolution of 16  $\mu$ s, the device is mis-wired so that the time of the event associated with the  $j^{\text{th}}$  trigger is that of the previous  $(j - 1)^{\text{th}}$  trigger. If all the events are telemetered, this anomaly can be corrected by simply reassigning the time-tag. This can be accomplished by operating HRC-S in a special mode with the outer two segments of the microchannel plate disable in order to keep the total count rate below the telemetry saturation limit. Therefore, all events can be assigned with accurate time and the HRC timing anomaly can be minimized. For detailed and updated information of Chandra, please refer to the user's guide at <http://xc.harvard.edu/proposer/POG/html/>.

### 1.4.2 XMM-Newton

XMM-Newton was placed into a 48 hours orbit on December 10, 1999 by the launcher Ariane-5. There are three identical X-ray telescopes on-board. Each of these telescopes consists of 58 nested Wolter-I mirrors. This design enables a large collecting area over a wide energy band of 0.3 – 10 keV. Although the spatial resolution is about ten times worse than that of Chandra (i.e FWHM of the telescope's PSF is  $\sim 5$  arcsec), the mirror effective area of XMM-Newton is about a factor of six larger than that of Chandra. Therefore, XMM-Newton is well suited for detailed spectral studies with moderate angular resolution. X-ray CCD cameras, EuroPeAn Imaging Camera (EPIC), are installed in the focal plane of each telescopes. EPIC consists of two Metal Oxide Semiconductor (MOS 1/2) CCD cameras and a third Postive-Negative depleted Silicon CCD cameras (PN). The pixel size of the MOS and PN CCDs is  $\sim 1$  arcsec and  $\sim 4$  arcsec.

Halves of the beams from two of the three X-ray telescopes are reflected to MOS 1/2. The other two halves of these beams are intercepted by the Reflection Grating Spectrometers (RGS 1/2) which diffract the X-rays to two dedicated detectors. Each of the MOS cameras consists of seven CCD chips. The orientation of the chips in MOS 1 and MOS

2 are orthogonal to each other so that the gaps between the chips of one camera can be covered by the other. When the MOS CCDs are operated in a full window mode, the frame time is  $\sim 2.6$  s. Faster frame time can be achieved by limiting the window size for readout (i.e. partial-window mode).

The third of the three telescope is dedicated to expose the PN CCD solely. While the MOS camera comprises front-illuminated CCDs, PN camera is made of twelve back-illuminated CCDs which provide the camera to have a better spectral response at the soft band. PN camera can be operated in the small-window mode which is most suitable for neutron star studies. It can provide spectro-imaging information with a temporal resolution of  $\sim 6$  ms. This is most suitable for the timing studies of neutron stars in a crowded environments or supernova remnants in order to avoid source confusion. For even faster rotating neutron stars, the fast-timing mode of PN CCD can be utilized with a temporal resolution of  $\sim 0.03$  ms by collapsing the 2-dimensional image down into a 1-dimensional array at the expense of the loss of the spatial information in the Y-direction. For detailed and updated information of XMM-Newton, please refer to <http://xmm.vilspa.esa.es>.

Combining the enormous collecting power of XMM-Newton and the sub-arcsecond resolution of Chandra, we have conveyed a series of researches which covered a wide range of topics on studying the X-ray emission from the young neutron stars in the supernova remnants, pulsar wind nebulae, old non-recycled pulsars as well as millisecond pulsars. This is the theme of the thesis. Here we present the results and the discussions from the explorations of neutron stars and their environments with these two state-of-art X-ray telescopes.

# Chapter 2

## X-ray observations of RX J0822-4300 and Puppis-A

This chapter is adopted from the refereed paper entitled “X-ray observations of RX J0822-4300 and Puppis-A” published in *Astronomy & Astrophysics* (Hui & Becker 2006b).

### 2.1 Introduction

For many years, it has been generally believed that all young neutron stars have similar properties as those observed in young rotation-powered pulsars, i.e. emitting strongly pulsed plus powerful plerionic radiation caused by non-thermal emission processes in the neutron star’s magnetosphere. Many recent observations of compact X-ray sources in supernova remnants (SNRs), however, suggest that this picture is incomplete and no longer justified. Apart from appearing as rotation-powered pulsars, it has been shown that there are other manifestations of young neutron stars, e.g. with no radio counterpart identified. There are slowly rotating ( $P \sim 6 - 12$  s) compact objects which possibly have an ultra strong ( $B \sim 10^{14} - 10^{15}$  G) magnetic field. These neutron stars are dubbed as magnetars, which include the *anomalous* X-ray pulsars (AXPs) and the soft gamma-ray repeaters (SGRs), depending on whether bursts of strong  $\gamma$ -ray emission is detected from them (e.g., Mereghetti 1998; Thompson 2000). The other class of objects are the “radio-quiet neutron stars” (e.g. Brazier & Johnston 1999). Most of them were identified by their high X-ray to optical flux ratios, others simply by their locations near to the expansion centers of SNRs (e.g. Becker & Pavlov 2001, Kaspi et al. 2004), strongly suggesting that they are indeed the compact stellar remnants formed in the supernova events. The group of SNRs which are known to host a radio-quiet but X-ray bright central compact object is a slowly growing one. Thanks to more sensitive X-ray observatories it currently includes Cas-A (Tananbaum 1999), the Vela-Jr. remnant (RX J0852.0–4622; Aschenbach 1998), RX J1713.7–3946 (Pfeffermann & Aschenbach 1996), RCW 103 (Tuohy & Garmire 1980), Puppis-A, (Petre et al. 1982), PKS 1209-51/52 (Helfand & Becker 1984) and Kes 79 (Seward et al. 2003; Gotthelf et al. 2005).

The discovery of the X-ray point source, RX J0822–4300, in Puppis-A, was initially made in one of the EINSTEIN HRI images of the SNR G260.4–3.4 (Petre et al. 1982). RX J0822–4300, appeared in this data as a faint *X-ray feature*. With ROSAT, it became strongly evident that RX J0822–4300 is the compact stellar remnant which was formed in the SN event (Petre, Becker & Winkler 1996; hereafter PBW96), although the positional offset from the SNR’s optical expansion center is 6.1 arcmin (cf. Winkler & Kirshner 1985, Winkler et al. 1988). The age of Puppis-A, estimated from the kinematics of oxygen-rich filaments is  $\sim 3700$  years. The remnant’s kinematic distance estimated from an HI study of the interstellar medium along the line of sight towards Puppis-A, is  $\sim 2.2 \pm 0.3$  kpc (Reynoso et al. 1995; 2003). The space velocity of RX J0822–4300, required to travel to its observed position thus is  $\sim 1000$  km/s. This is very high if compared with the mean proper motion velocity observed in ordinary field pulsars but still comparable with what is observed in several of the other young supernova/pulsar associations (Manchester et al. 2005).

RX J0822–4300 has not been detected as a radio pulsar. Limiting radio flux densities at 436 MHz, 660 MHz and 1520 MHz are 1.5 mJy, 1.3 mJy and 0.3 mJy, respectively (Kaspi et al. 1996). For comparison, the limiting flux density in the Parkes Multi Beam Survey along the galactic plane was  $\approx 0.2$  mJy (Manchester et al. 2001) and the typical limiting sensitivity in deep searches for young radio pulsars in SNRs is  $50 \mu\text{Jy}$  (Camilo 2003). Gaensler, Bock & Stappers (2000) searched for a radio nebula around RX J0822–4300, with a resolution of  $27 \times 17$  arcsec. Their non-detection of any extended plerionic radio emission up to a scale of 30 arcmin prompted them to conclude that if RX J0822–4300, is a rotation-powered pulsar, e.g. with the radio beam not intersecting with the observer’s line of sight, then it must be less powerful than other typical young radio pulsars located in SNRs. All young radio pulsars which are associated with a SNR have a spin-down power in excess of  $\sim 10^{36}$  ergs/s and are observed to power a X-ray/radio bright pulsar-wind nebula.

RX J0822–4300 has no optical counterpart down to a limiting magnitude of  $B \leq 25.0$  and  $R \leq 23.6$  (PBW96). This limit yields an X-ray-to-optical flux ratio  $f_X/f_B \leq 5000$  (PBW96). Together with the radio upper limits this rules out many types of X-ray sources as a likely counterpart of RX J0822–4300, except a neutron star.

PBW96 fitted the ROSAT PSPC spectrum with a blackbody model and obtained a temperature of  $(3.2 \pm 1.2) \times 10^6$  K and a column density of  $(4.1 \pm 0.2) \times 10^{21}$  cm $^{-2}$ . The radius of the corresponding blackbody emitting area in their fits is only  $\sim 2$  km. Zavlin, Trümper, & Pavlov (1999; hereafter ZTP99) tested whether a hydrogen atmosphere model could bring this result in better agreement with the predictions of standard cooling models. They fitted a temperature which is about half that found by PBW96 though with an increased radius of 10 km for the emitting area. However, as atmosphere models are seen not to be in agreement with the spectral fits from the cooling neutron stars Geminga, PSR B0656+14 and PSR B1055-52 (e.g. De Luca et al. 2005), the applicability of those models which in most cases use non-magnetic opacities only, is restricted.

EINSTEIN and ROSAT data do not show any evidence for short or long term flux variations. Although a marginal detection of X-ray pulses at a period of  $\sim 75.3$  ms was claimed by Pavlov, Zavlin, & Trümper (1999; hereafter PZT99), it could not be confirmed



so far (Pavlov et al. 2002; Becker & Aschenbach 2002).

In order to put tighter constraints on the emission properties of RX J0822–4300, various observations with the new generation X-ray satellites XMM-Newton and Chandra were targeted to it in the past few years. Making use of XMM-Newton’s huge collecting power and high spectral resolution as well as of Chandra’s sub-arcsecond angular resolution we have performed a sensitive broadband spectro-imaging analysis of RX J0822–4300 and its environment using all XMM-Newton and Chandra data taken from this source so far. This is the subject of this chapter which is organized as follows. In Section 2.2 we give a brief description of the relevant XMM-Newton and Chandra observations. In Section 2.3, we present the methods and results of our data analysis which are discussed in Section 2.4 in the context of a number of physical models for the nature of RX J0822–4300.

## 2.2 Observations

In total, five observations have been targeted with XMM-Newton and Chandra on RX J0822–4300. All data have been taken between December 1999 and November 2001. We summarize the basic information of these observations in Table 2.1 and give a more detailed description in the following subsections.

### 2.2.1 XMM-Newton Observations

Two of the five data sets reported here were obtained with the **E**uropean **P**hoton **I**maging **C**amera (EPIC) aboard XMM-Newton (Jansen et al. 2001). EPIC consists of two Metal Oxide Semiconductor (MOS1/2) CCD detectors (Turner et al. 2001) of which half of the beam from two of the three X-ray telescopes is reflected to. The other two halves of the incoming photon beams are reflected to a grating spectrometer (RGS) (den Herder et al. 2001). The third of the three X-ray telescopes is dedicated to expose the EPIC-PN CCD detector solely (Strüder et al. 2001). The April 2001 XMM-Newton observation (hereafter XMM1) was taken with a total exposure time of  $\sim 28.8$  ksec. The November 2001 observation (hereafter XMM2) had an exposure time of  $\sim 24.3$  ksec. The EPIC-PN CCD was operated in both observations in small-window mode with a thin filter to block optical stray light. This data provide imaging, spectral and temporal information. All recorded events are time tagged with a temporal resolution of 5.7 ms. The MOS1/2 CCDs were setup to operate in full-window mode with a medium filter in the April 2001 observation and a thick filter in the November 2001 observation. The MOS1/2 cameras provide imaging, spectral and timing information, though the later with a temporal resolution of 2.6 s only.

For both XMM-Newton observations, the satellite was pointed to RA=08<sup>h</sup>21<sup>m</sup>56<sup>s</sup> and Dec=−43°00′19″ [J2000]) which places RX J0822–4300 at the optical axis in the EPIC-PN CCDs. The raw data from the EPIC instruments were processed with version 6.0.0 of the XMM Science Analysis Software. Examining the raw data from the EPIC-PN CCD for both XMM1 and XMM2, we did not find any timing anomaly observed in many of the XMM-Newton data sets (cf. Becker & Aschenbach 2002; Kirsch et al. 2004). This provides

us with opportunities for an accurate timing analysis. We created filtered event files for the energy range 0.3 keV to 10 keV for all EPIC instruments. A small fraction of X-ray events might be split between CCD pixels. In order to correct for this effect only those events were accepted for which the corresponding X-ray generated pattern was between 0 – 12 in MOS cameras and between 0 – 4 in the EPIC-PN camera<sup>1</sup>. We further cleaned the data by accepting only the good times when sky background was low and removed all events potentially contaminated by bad pixels. The *effective* exposure times after data cleaning are summarized in column 7 of Table 2.1.

In order to correct for the non-uniformity across the detector and the mirror vignetting, exposure map is needed to rescale all parts of the image to the same relative exposure. This is created by using XMM-SAS task EEXPMAP.

RX J0822–4300 is located in a patchy SNR environment. This makes the extraction of its source and background spectrum difficult. In order to maximize the signal-to-noise ratio for RX J0822–4300, we extracted its source spectrum from circles with 18 arcsec radii in both, the MOS1/2 and EPIC-PN cameras. About 70% of all point source events are located within the selection region. Annular regions with radii between 20 – 35 arcsec, centered at RX J0822–4300, were used to extract the background spectra. The background corrected count rates are listed in column 8 of Table 2.1. Response files were computed for all data sets by using the XMM-SAS tasks RMFGEN and ARFGEN.

### 2.2.2 Chandra Observations

Three of the five data sets on RX J0822–4300 were taken with the Chandra satellite (e.g. Weisskopf 2004). One observation was performed by using the Advanced CCD Imaging Spectrometer (ACIS; Burke et al. 1997) whereas the other two exposures were done by using the High Resolution Camera (HRC; Zombeck et al. 1995; Murray et al. 1997). For the data reduction we used CIAO 3.0.2.

The Chandra HRC data were taken on 1999 December 21 and 2001 January 25 for HRC-I and HRC-S, respectively, with RX J0822–4300 placed  $\sim 0.3$  arcmin off-axis. In order to determine the event positions accurately, we started the analysis with level-1 event files and corrected for the tap-ringing distortion in the HRC event position reconstruction. Apart from this, we also performed the de-gap correction to the event files so as to compensate the systematic errors introduced in the event positions by the algorithm used to determine the centroid of the charge cloud exiting the rear micro-channel plate of the HRC. Furthermore, aspect offset was corrected for the event files.

The ACIS observation was performed on 2000 January 1 using the front-illuminated (FI) ACIS-S2 chip with a frame time of 0.84 s. RX J0822–4300 is located  $\sim 2.7$  arcmin off-axis in this ACIS observation. In order to correct for possible pileup effects, we started our analysis again with level-1 files as those have preserved a number of source events which could have been misidentified as afterglows of cosmic ray events in the standard processing

---

<sup>1</sup>For a detailed description of EPIC event grade selection, please see the XMM-Newton Users' Handbook.

of level-2 data (cf. Davis 2002). The sub-arcsecond resolution of Chandra allows to extract the counts for the spectral analysis from a circle with radius 2.6 arcsec (encircled energy  $\sim 99\%$  for on-axis point sources). This selection radius minimizes the contamination from the supernova background emission. An annular region with radii between  $\sim 2.6 - 5.3$  arcsec, centered at RX J0822–4300 was chosen to extract the background spectrum. Response files were created using the tools MKRMF and MKARF of CIAO. The background corrected HRC and ACIS count rates of RX J0822–4300 are given in column 8 of Table 2.1.

From the ACIS-S2 and XMM-Newton data we found that the energy of the central source peaks at  $\sim 1.5$  keV. With the peak energy and for the off-axis angle of  $\sim 0.3$  arcmin we extracted the desired point spread function (PSF) model images from CALDB 2.26 standard library files (F1) by interpolating within the energy and off-axis angle grids by using CIAO tool MKPSF. Exposure maps for the corresponding images were generated by the tool MKEXPMAP.

## 2.3 Data Analysis

### 2.3.1 Spatial Analysis

Composite images of the supernova remnant Puppis–A and its central region around RX J0822–4300, as seen by the ROSAT HRI, by XMM-Newton’s MOS1/2 CCDs and by the Chandra HRC-I, are shown in Figure 2.1. RX J0822–4300 is located at the center of these images. From Figure 2.1b it can be seen that the hardest X-ray emission in the remnant is mainly contributed by the central compact object RX J0822–4300. Apart from this, we observed two more hard X-ray sources in the XMM-Newton MOS1/2 images. Their locations as indicated by circles in Figure 2.1b are RA=  $08^{\text{h}}22^{\text{m}}26.70^{\text{s}}$ , Dec=  $-43^{\circ}10'25.99''$  (J2000) for the source located in the south and RA=  $08^{\text{h}}22^{\text{m}}24.25^{\text{s}}$ , Dec=  $-42^{\circ}58'00.82''$  (J2000) for the northern source. The location of the northern source is close to the region which was suggested by Winkler et al. (1989) to be a second supernova within Puppis–A. These authors have observed an unusual swirl-like structure in optical images and interpreted this as a possible second supernova remnant. The center coordinate of this structure is at about RA=  $08^{\text{h}}22^{\text{m}}39^{\text{s}}$ , Dec=  $-42^{\circ}59'41''$  (J2000). The left box in Figure 2.1b illustrates the field of view in their observations. The angular separation between the northern hard X-ray source and the center of the swirl-like structure is  $\sim 3.2$  arcmin. From the spectral analysis of optical filaments, Winkler et al. (1989) estimated that the kinematic age of the proposed second SNR is  $< 800$  years. If the northern hard X-ray source is correlated with this structure and this age estimate is correct it would require a space velocity  $> 2000$  km/s (for an assumed distance of 2.2 kpc) in order to travel to its observed location. An association thus would be unlikely due to this high space velocity. For the southern hard X-ray source its correlation with Puppis–A is unspecified though most likely this is a background source. The photon statistics does not support a detailed spectral analysis for these two sources.

The XMM-Newton MOS1/2 false color image (Figure 2.1b) demonstrates nicely that the south-western part of the remnant as well as the region near RX J0822-4300 comprise mainly hard X-ray photons. This is different from other parts of the image which consist of soft X-rays from the hot supernova ejecta. As Puppis-A is located at the edge of the Vela supernova remnant (distance  $\sim 0.25$  kpc), and is located behind it, we speculate that there is intervening absorbing material from Vela along the line of sight which absorbs most of the soft X-ray photons of the south-western part of Puppis-A. This view is supported by Figure 2.2 which shows a belt of absorbing material crossing the whole Puppis-A supernova remnant from the south-western to the north-eastern direction (Aschenbach 1994 and discussion therein).

The high resolution X-ray image from HRC-I allows for the first time to examine the spatial nature of RX J0822-4300 with sub-arcsecond resolution. However, we have found that the full width half maximum (FWHM) of the point spread function (PSF) ( $\sim 0.4$  arcsec) generated from the library files is narrower than expected. This can be ascribed to the fact that the PSF library files are derived by a ray-tracing program instead of obtained directly from the calibration data. Due to this caveat, it is legitimate to fit the image with the convolution of a 2-dimensional Gaussian function instead of a delta function. The radial profile of RX J0822-4300 is depicted in Figure 2.4. The solid curve represents the best-fit Gaussian model with the modeled PSF at 1.5 keV as a convolution kernel. The best-fit results yield a FWHM of  $0.59 \pm 0.01$  arcsec which is very close to the expected width of the Chandra PSF. This result appears as the first evidence for the point source emission nature of RX J0822-4300. Moreover, we were also able to narrow down the position of this compact object to the smallest region that has never been obtained before. The best-fit gives us a position for RX J0822-4300 which is RA=  $08^{\text{h}}21^{\text{m}}57.40^{\text{s}}$  and Dec=  $-43^{\circ}00'16.69''$  (J2000). The statistical error of the position introduced by the image-fitting is found to be 0.01 arcsec ( $1 - \sigma$ ). The predominant uncertainty of the source position is given by the finite width of the PSF ( $\sim 0.5$  arcsec) and the average pointing accuracy of the satellite ( $\sim 0.6$  arcsec). The same position is obtained from the analysis of the HRC-S data. The position and point source character of RX J0822-4300, deduced by using Chandra, are in agreement with what we found in the XMM-Newton data (PSF  $\sim 5$  arcsec FWHM).

From observations of the neutral hydrogen surrounding RX J0822-4300, Reynoso et al. (2003) found a depression in the  $\lambda 21$ -cm line emission near to RX J0822-4300. According to their interpretation this structure could be connected to the compact stellar remnant because of its symmetric appearance as well as because of its alignment with the remnants optical expansion center and the position of RX J0822-4300. In order to search whether there is an X-ray structure near to RX J0822-4300 which correlates with this radio structure we have overlaid the radio contours from Reynoso et al. (2003) on the XMM-Newton and Chandra HRC-I image (cf. Figure 2.5). No clear correlation between the radio and X-ray structures is seen, though the patchy supernova environment makes any conclusion uncertain.

### 2.3.2 Spectral Analysis

We estimated the effects of pileup in both XMM1 and XMM2 data by using the XMMSAS task EPATPLOT. Our results showed that all the EPIC data were not affected by CCD pileup. Using the spectral parameters of RX J0822–4300 inferred from XMM-Newton, we estimated with the aid of PIMMS (version 3.6a) that the ACIS-S2 data are piled-up by a fraction of  $\sim 11\%$ . We applied adequate correction by incorporating a pileup model in the spectral fitting (Davis 2001). Chandra data were also corrected for the degradation of quantum efficiency.

In order to constrain the spectral parameters tightly, we fitted XMM1, XMM2, as well as the ACIS-S2 data simultaneously. In order to obtain spectra from different observations and instruments with compatible significance, the energy channels were grouped dynamically with respect to the photon statistics in the analyzed data sets. For the MOS1/2 data of XMM2, we grouped the data to have at least 50 counts per bin. For the MOS1/2 data of XMM1 as well as the ACIS-S2 data we applied a grouping so as to have at least 100 counts per spectral bin. For the EPIC-PN data from XMM1 and XMM2 a grouping of 200 cts/bin was used. All spectral fits were performed in the 0.3 – 10 keV energy range by using XSPEC 11.3.1.

Various model spectra like single blackbody, double blackbody, power-law, combinations of blackbody and power-law, broken power-law, as well as thermal bremsstrahlung were fitted to the data. Independent of the fitted spectral models we found that the fits improve if the spectrum extracted from the Chandra data was not included in the analysis. Since the spectra extracted from XMM-Newton data supersedes the Chandra data in photon statistics, we excluded the later from the spectral analysis without loss of generality. The parameters of all fitted model spectra are summarized in Table 2.2. The quoted errors are conservative and are  $1\sigma$  for 2 parameters of interest for single component spectral models and for 3 parameters of interest for multi-component model.

Fitting the spectral parameters of RX J0822–4300 as inferred from ROSAT PSPC data by PBW96 we found that these parameters ( $T = 3.2 \times 10^6\text{K}$ ,  $N_H = 4.1 \times 10^{21}\text{cm}^{-2}$ ,  $R = 2$  km) yield no acceptable description of the XMM-Newton observed spectrum ( $\chi^2_\nu = 21.17$  for 467 dof). In general, spectral fitting with a single component blackbody or power-law model did not model the data beyond  $\sim 3$  keV (cf. Table 2.2). Testing multi-component models we found that a two component blackbody with  $N_H = 4.54^{+0.49}_{-0.43} \times 10^{21}\text{cm}^{-2}$ ,  $T_1 = 2.61^{+0.30}_{-0.26} \times 10^6\text{K}$ ,  $T_2 = 5.04^{+0.28}_{-0.20} \times 10^6\text{K}$  and  $R_1 = 3.29^{+1.12}_{-0.74}$  km,  $R_2 = 0.75^{+0.12}_{-0.15}$  km for the blackbody temperatures and emitting areas, respectively, yields the best description of the observed spectrum. The reduced- $\chi^2$  of this fit is 1.20 for 465 dof. We note that the apparent deviation of the reduced- $\chi^2$  from one, indicating an acceptable fit, is due to the fact that the data from different instruments and different epochs are modeled simultaneously. The benefit of combining all spectral data in simultaneous fits is the higher photon statistics and thus the ability to better discriminate between competing model spectra.

Figure 2.6 and 2.7 shows the spectral fit for an absorbed double blackbody model and the corresponding spectral components respectively. In order to properly constraint the parameter space for the best-fitting model, we calculated the contour plots in the  $T_1 - R_1$ ,

$T_1 - N_H$  and  $T_2 - R_2$ ,  $T_2 - N_H$  planes, respectively. These plots are depicted in Figure 2.8. For a consistence check we modeled the Chandra ACIS-S2 spectrum with the best fitting double blackbody model and found all parameters in agreement with those fitted for the XMM-data.

Both  $R_1$  and  $R_2$  inferred from the double blackbody fit are inconsistent with the size of a canonical neutron star (i.e.  $R \sim 10$  km). It is therefore instructive to redo the fitting for this model with  $R_1$  fixed at 10 km. This model still yields acceptable values of  $N_H = 6.38_{-0.13}^{+0.21} \times 10^{21} \text{cm}^{-2}$ ,  $T_1 = 1.87_{-0.02}^{+0.02} \times 10^6 \text{K}$ ,  $T_2 = 4.58_{-0.07}^{+0.03} \times 10^6 \text{K}$ , and  $R_2 = 1.09_{-0.04}^{+0.04}$  km with  $\chi^2_\nu = 1.28$  (for 466 dof) only a slightly larger than leaving  $R_1$  unconstrained.

For a model combining a blackbody and a power-law, the goodness-of-fit is compatible with that for the double blackbody model ( $\chi^2_\nu = 1.21$  for 465 dof). The inferred slope of the power-law component is  $\Gamma = 4.67_{-0.05}^{+0.14}$ . Although this is steeper than the photon-index,  $\Gamma = 1 - 3$ , observed for rotation-powered pulsars (cf. Becker & Trümper 1997), the model cannot be rejected simply based on this as it is not a priori applicable for central compact objects. However, the column density is much higher than the expected level. When  $N_H$  is fixed to  $4 \times 10^{21} \text{cm}^{-2}$ , which is consistent with the values obtained by PBW96, ZTP99 and Winkler et al. (1981), it results in a parameter set of  $\Gamma = 2.51_{-0.13}^{+0.11}$ ,  $T = 3.80_{-0.05}^{+0.06} \times 10^6 \text{K}$ ,  $R = 1.59_{-0.06}^{+0.06}$  km, though with a large  $\chi^2_\nu$  of 1.42 for 466 dof.

It is necessary to examine whether a broken power law model can describe the spectra. This implies a purely non-thermal emission with spectral steepening at high energy after an energy break which is due to the deficit of energetic emitting charged particles. From Table 2.2 it is obvious that the broken power law model does not yield any photon index that is consistent with that of a typical pulsar. We also fitted the data with a thermal bremsstrahlung model which physically implies that the central compact object would be surrounded by a hot plasma. From the normalization constant inferred from the spectral analysis, we can calculate the extent of the plasma. Following Iaria et al. (2001), we assume the bremsstrahlung normalization to be  $N_{brems} = 3.02 \times 10^{-15} N_e^2 V / 4\pi D^2$ , where  $D$  is the distance to the source in cm,  $N_e$  is the electron density ( $\text{cm}^{-3}$ ), and  $V$  is the volume of the bremsstrahlung emitting region. Assuming  $N_e$  is comparable with the average density  $\sim 1 \text{cm}^{-3}$  of Puppis-A (Petre et al. 1982), the radius of the assumed spherical emitting region is estimated to be  $\sim 2.7$  pc for an adopted distance of 2.2 kpc. This implies that the source should be extended (at a level of  $\sim 4.2$  arcmin assuming a distance of 2.2 kpc), in contradiction to the results from the spatial analysis.

From both, the XMM-Newton MOS1/2 and the Chandra HRC-I images, some faint and diffuse hard X-ray emission around RX J0822-4300 seems to be present (cf. Figures 2.1 & 2.3). Its nature can be determined by examining its spectrum. We extracted the events in the X-ray filament near to RX J0822-4300 from the MOS1/2 cameras of XMM1 from a  $80 \text{ arcsec} \times 30 \text{ arcsec}$  box centered at RA=08<sup>h</sup>21<sup>m</sup>57.077<sup>s</sup>, Dec=-43°01'15".42 (J2000). We found that its spectrum is consistent with an absorbed non-equilibrium ionization collisional plasma model (XSPEC model: VNEI) with goodness-of-fit of  $\chi^2 = 151.08$  for 142 dof. The energy spectrum as fitted to this model spectrum is displayed in Figure 2.9. Line emission is easily recognized in this plot. The most obvious feature is the O VII and O VIII line complex at 0.662 keV and 0.651 keV respectively. Parameters inferred from the best-

fitted model are the column density  $N_H = 3.70_{-0.12}^{+0.12} \times 10^{21} \text{cm}^{-2}$ , the plasma temperature  $T = 7.62_{-0.21}^{+0.10} \times 10^6 \text{K}$ , the ionization timescale  $\tau = 2.33_{-0.11}^{+0.15} \times 10^{11} \text{s cm}^{-3}$ , and the metal abundances with respect to the solar values (O:  $17.83_{-1.56}^{+1.58}$ , Ne:  $4.00_{-0.68}^{+0.67}$ , Si:  $2.25_{-1.32}^{+1.33}$ , S:  $6.58_{-4.81}^{+4.85}$ , Fe:  $2.24_{-0.21}^{+0.20}$ ) (quoted errors are  $1\sigma$  for 2 parameters of interest). These parameters imply a relative abundance ratio O:Fe to be about 6 – 9 times its solar value which strongly suggest an enhancement of oxygen in Puppis–A. This is in agreement with the conclusion drawn by Canizares & Winkler (1981). For the other elements, including H, He, C, Mg, Ar, Ca and Ni, we do not find any sign of enhancement and their abundances are in agreement with the solar values. We have performed the spectral fitting with different selected backgrounds. Provide that the backgrounds are selected from low count regions, all the best-fitted values are found to be within the quote  $1\sigma$  errors above. Since the remnant environment is patchy and inhomogeneous, abundance ratios from different regions are not expected to be comparable. A detailed modeling of the variation of chemical abundance is beyond the scope in this paper. A further detailed analysis of Puppis–A is in preparation and will be published elsewhere.

Although the rim emission appears to be a part of the structure of Puppis–A, we also exam whether there is any non-thermal contribution in the emission by adding a Crab-like power-law component (i.e. with photon index of 2) in the spectral fit. The additional component does not improve the goodness-of-fit at all ( $\chi^2 = 150.95$  for 141 dof). A  $3\sigma$  upper bound of the power-law model normalization is estimated to be  $6 \times 10^{-5}$  photons  $\text{keV}^{-1} \text{cm}^{-2} \text{s}^{-1}$ . This implies a limiting flux of non-thermal plerionic emission, if any, to be  $3.06 \times 10^{-13}$  ergs  $\text{cm}^{-2} \text{s}^{-1}$  and  $2.88 \times 10^{-13}$  ergs  $\text{cm}^{-2} \text{s}^{-1}$  in 0.1–2.4 keV and 0.5–10 keV respectively.

### 2.3.3 Timing Analysis

#### Search for long-term variabilities

To check whether the energy fluxes measured from RX J0822–4300 by XMM-Newton and Chandra are consistent with each other or whether there are significant long-term deviations observed in the different data sets we computed the flux for the best fitting double blackbody model from all available data. In order to compare the XMM-Newton and Chandra results with the existing ROSAT flux we restricted this computation to the energy range 0.1 – 2.4 keV. As shown in Table 2.3, all observed energy fluxes, from ROSAT to XMM-Newton are consistent with a constant energy flux of  $f_x(0.1\text{-}2.4 \text{ keV}) \sim 3 \times 10^{-12}$  ergs  $\text{cm}^{-2} \text{s}^{-1}$ . The same conclusion can be drawn from comparing the broadband fluxes from Chandra, XMM1 and XMM2. The observed flux of these three observations are found to be  $\sim 4 \times 10^{-12}$  ergs  $\text{cm}^{-2} \text{s}^{-1}$  in the range of 0.5–10 keV.

#### Search for coherent pulsations

Although the lack of long-term variability and the spectral analysis eliminates some highly improbable models and hence helps us to put constraints on the properties of the central

compact object, the most strong argument that this object is indeed a neutron star would come from the detection of X-ray pulsations. Since the small-window mode was setup for the EPIC-PN camera in both XMM1 and XMM2 observations, the 5.7 ms temporal resolution of this data is sufficient to search for coherent short-term pulsations.

The arrival times in both event files were barycentric corrected using the XMMSAS task BARYCEN. In order to minimize the systematic errors induced in the barycentric correction, we use the position inferred from the Chandra HRC-I image fitting (c.f. §3.1) for correcting the arrival times in both data sets. The initial period searches were performed by applying a fast Fourier transformation (FFTs) on both sets of photon arrival times separately. The advantage of having multiple data sets from different epochs supports to cross-check any periodicity candidates easily and prevents wrong identifications. FFTs were calculated for each time series with 20 different binnings. Searches in the frequency domain were limited at  $0.01 \text{ Hz} \leq f \leq 100 \text{ Hz}$ . Promising frequency peaks appearing in the power spectra of both observations were cross-correlated and selected for subsequent searches using standard epoch-folding analysis.

PZT99 reported the detection of a periodic signal with  $P = 75.2797300 \text{ ms}$  and  $\dot{P} = 1.49 \times 10^{-13} \text{ s s}^{-1}$  in their ROSAT analysis. We searched for coherent pulsations in a period range extrapolated to these spin parameters in XMM-Newton data. The photon statistics of this data, compared to the ROSAT data, is about a factor 25 higher. A similar analysis as reported in the present work was already performed by Becker & Aschenbach (2002) who could not confirm the existence of a pulsed signal in an extrapolated period range, neither in the ROSAT nor in the XMM-Newton data. We herewith fully confirm their result in our independent analysis.

Taking peaks in the power spectra as initial candidates, we made a more detailed search using  $Z_m^2$  test where  $m$  is the numbers of harmonics (Buccheri et al. 1983). We have detected periodicities of  $P = 0.218749 \pm 0.000001 \text{ s}$  in XMM1 (MJD 52014.4634390827268 days)<sup>2</sup> and  $P = 0.222527 \pm 0.000002 \text{ s}$  in XMM2 (MJD 52221.8938398198225 days) which both have very similar properties. The quoted uncertainties indicate the Fourier resolution  $P^2/T$  in the corresponding observation, where  $T$  is the time span in the data set. Using the  $H$ -test (De Jager, Swanepoel, & Raubenheimer 1989), we found that  $H$  is maximized for the first harmonic. The calculated  $Z_1^2$  for the detected signals in XMM1 and XMM2 are 28.10 and 28.92, respectively. The nominal probabilities for the identification of these signals by chance are  $8 \times 10^{-7}$  and  $5 \times 10^{-7}$ , respectively. The pulse profiles and  $Z_1^2$  distribution is given in Figure 2.10. Both lightcurves are similar to each other and share the same sinusoidal characteristics. Following Becker & Trümper (1999), we calculated the pulsed fraction of this signal by the bootstrap method proposed by Swanepoel, de Beer, & Loots (1996) and obtained  $P_f = 5 \pm 1\%$  in both, the XMM1 and XMM2 data sets. The period time derivative calculated from the separation of the epochs of the two data sets is  $\dot{P} = (2.112 \pm 0.002) \times 10^{-10} \text{ s s}^{-1}$ .

Taking the number of  $10^5$  trials into account, the probabilities for finding these signals by chance is  $(5 - 8) \times 10^{-2}$ . However, given the similarity in period, pulse shape, signal

<sup>2</sup>The mean epoch of the observation in TDB at the solar system barycenter (SSB)



strength and pulse fraction together with the detection of the signal in two independent XMM-Newton data sets makes this signal a very promising candidate to test and search for in future observations.

In order to minimize the probability of a false detection we have investigated the possibility that the signals are induced from the readout processes in the detector CCDs or other cyclic processes operating during data acquisition. For this we have extracted events from Puppis–A in both, the XMM1 and XMM2 data sets from a location near to RX J0822–4300, i.e. from CCD columns located at the same level in the readout direction as RX J0822–4300. The same procedure of timing analysis was applied on these events as applied to the events from RX J0822–4300. However, we did not detect any cyclic signal at a period near to  $\sim 0.22$  s. We therefore can rule out that the detected pulsations are due to periodic systematics in the on-board data processing during data acquisition.

To further cross-check this periodicity detection, we utilized an independent data set from Chandra HRC-S. Since the observation with HRC-S was performed in “imaging” mode where the outer segments of the micro-channel plate were disabled, the total count rate is below the telemetry saturation limit, so that all events can be assigned with accurate time and the HRC timing anomalies are minimized. This enables us to perform an accurate timing analysis on this data set, though the photon statistics is a factor of  $\sim 6$  lower than in the XMM-Newton data. The event file of HRC-S was firstly barycentric corrected (with the position given in the HRC-I image fit) by CIAO tool AXBARY. With the  $P$  and  $\dot{P}$  estimated from XMM-Newton data, we extrapolated the period to the epoch of HRC-S observation as an initial starting point. A detailed search around this period gives a promising candidate at  $P = 0.217303 \pm 0.000002$  s in the Chandra HRC-S data (MJD 51934.6266560833901 days). The  $H$ -test indicates the highest probability for  $Z_7^2 = 45.94$  which yields a nominal chance probability of  $3 \times 10^{-5}$ . This is not strong enough to conclude a significant signal in the HRC-S data though we point out that there are only  $\sim 6000$  counts available for this test. For a 5% pulsed fraction as indicated in the XMM-Newton data only  $\sim 300$  counts would contribute to the pulsed component. The low significance of the signal found in the Chandra data thus would be in line with a low significance of the periodic signal. Archival ROSAT and ASCA data of RX J0822–4300 are of small photon statistics so that we did not include this data in order to search for a pulsed signal near to 0.22 s.

## 2.4 Discussion & Conclusion

The lack of any detectable long term variability together with the high X-ray/optical flux ratio and the observed spectral characteristics makes it very unlikely that RX J0822–4300 is something else but the compact stellar remnant formed in the core collapsed supernova which was left behind Puppis–A. Our image analysis shows that the compact object is the hardest X-ray source in the 30 arcmin central region of Puppis–A. Chandra and XMM-Newton data do not show any extended X-ray emission which could be plerionic emission powered by the compact remnant, though this is difficult to quantify given the patchy

environment in which RX J0822–4300 is located.

From the spectral fitting, we found that the point-source spectrum is compatible with a two component blackbody model. The best-fit model yields  $N_H = 4.54_{-0.43}^{+0.49} \times 10^{21} \text{cm}^{-2}$ , temperatures of  $T_1 = 2.61_{-0.26}^{+0.30} \times 10^6 \text{K}$  and  $T_2 = 5.04_{-0.20}^{+0.28} \times 10^6 \text{K}$  for the projected blackbody emitting areas with radii  $R_1 = 3.29_{-0.74}^{+1.12} \text{km}$  and  $R_2 = 0.75_{-0.15}^{+0.12} \text{km}$ , respectively. Compared to standard cooling curves (e.g. Yakovlev et al. 2004)  $T_1$  is a little higher than  $\sim 1.8 \times 10^6 \text{K}$  which would be expected for a  $1.35 M_\odot$  neutron star with a stiff equation of state (Prakash et al. 1988).  $R_1$  is not quite consistent with the size of a typical neutron star. This was already found by ZTP99 who attempted to obtain a set of reasonable neutron star parameters by modeling the ROSAT data with spectral models which take the presence of a hydrogen atmosphere into account, though the applicability of these models are restricted.

In the present work we have shown that a parameter set which is consistent with a standard cooling neutron star model can be obtained by fixing  $R_1$  at 10 km. This yields a column density of  $6.38_{-0.13}^{+0.21} \times 10^{21} \text{cm}^{-2}$ , temperatures of  $T_1 = 1.87_{-0.02}^{+0.02} \times 10^6 \text{K}$  and  $T_2 = 4.58_{-0.07}^{+0.03} \times 10^6 \text{K}$  for a projected blackbody emitting area with radius  $R_2 = 1.09_{-0.04}^{+0.04} \text{km}$ .

The results of our analysis suggest that the low temperature component is emitted from a large fraction of the neutron star surface, while the high temperature component is emitted from a much smaller and hotter region. This double blackbody model, though, could be a two-step adaption for a wider temperature distribution which centrally peaks. Such a hot spot on the neutron star surface can be produced by several mechanisms. One of them is the bombardment of the polar cap regions by energetic particles accelerated in the magnetosphere backwards to the neutron star surface (Cheng, Ho & Ruderman 1986; Cheng & Zhang 1999). Another way to produce a hot spot on the stellar surface is by anisotropic heat transport (Page 1995). Since the heat conduction inside a neutron star is much more efficient in the direction along the magnetic field lines than that in the perpendicular direction, a complete model of cooling magnetic neutron star should lead to an anisotropic heat flow and hence produce hot spots on the stellar surface. In this scenario, one should expect the emission to be pulsed at the rotation period of the star as the hot spot goes across the line of sight. A pulsed X-ray flux as revealed by the putative periodic signals seen in XMM1 and XMM2 thus would support this scenario.

The pulsed fraction of the putative periodic signal is  $5 \pm 1\%$  in XMM1 and XMM2. The emission from young pulsars like the Crab is compatible with being 100% pulsed (Tennant et al. 2001), whereas the fraction of pulsed photons is  $\sim 7\%$  for the Vela pulsar and  $\sim 20 - 40\%$  in many of the other X-ray detected pulsars (e.g. Becker & Pavlov 2001; Becker & Aschenbach 2002; Kaspi et al. 2004). A low pulsed fraction, however, is not unexpected though. When the general relativistic effect is taken into account (Page 1995; Hui & Cheng 2004), the pulsations are found to be strongly suppressed and the pulsed fraction is highly dependent on the mass to radius ratio of the star, the orientation of the hot spot and the viewing angle geometry. This is due to the fact that the gravitational bending of light will make more than half of the stellar surface become visible at any instant and hence the contribution of the hot spot will be hampered. If the orientation of the hot spot is deviated from that of an orthogonal rotator and/or the star has a high

mass to radius ratio, then a very low amplitude pulsations is expected, which makes the periodicity search difficult.

The  $\dot{P}$  deduced for the candidate periodicity would be among the largest spin-down rates in the neutron star population. The largest known  $\dot{P}$  was inferred from SGR 1806-20,  $\dot{P} = (8-47) \times 10^{-11} \text{ s s}^{-1}$ , (Kouveliotou et al. 1998; Woods et al. 2002). If the identifications of  $P$  and  $\dot{P}$  are correct, it implies a non-steady spin-down behavior of RX J0822-4300. This phenomenon is not unobserved. There are two SGRs (SGR 1806-20 and SGR 1900+14) which show large changes in the spin-down torque up to a factor of  $\sim 4$  (Woods et al. 2002). Moreover, deviations from a steady spin-down were also observed in the other radio-quiet neutron stars such as in SNR PKS 1209-51/52 (Zavlin, Pavlov, & Sanwal 2004). However, the rotational dynamics cannot be determined without ambiguity here and further observations are needed to confirm and/or refine this putative periodicity.

An alternative proposal to explain the origin of X-rays from radio quiet compact objects in supernova remnants is accretion onto a neutron star (e.g. Pavlov et al. 2000). In this scenario, the observed luminosity  $L$  is powered by an accretion rate of  $\dot{M} = L/(\zeta c^2)$ .  $\zeta$  is the accretion efficiency which is expressed as  $\zeta = 0.2M_{1.4}R_6^{-1}$ . Equating the expression of  $\dot{M}$  with Bondi formula (i.e.  $\dot{M} = 4\pi G^2 M^2 \rho v^{-3}$ ), we can express the relation of the circumstellar baryon density as  $n = 8 \times 10^3 v_{100}^3 (0.2/\zeta) M_{1.4}^{-2} L_{33} \text{ cm}^{-3}$ , where  $v_{100}$  is the velocity of the neutron star in the unit of  $100 \text{ km s}^{-1}$  and  $L_{33}$  is the luminosity in the unit of  $10^{33} \text{ erg s}^{-1}$ . The offset of  $\sim 6.1$  arcmin from the optical expansion center, estimated distance ( $\sim 2.2$  kpc) and estimated age ( $\sim 3700$  years) suggest a transverse velocity of  $\sim 985 \text{ km s}^{-1}$ . Even we take  $L_{33} = 1$ , which is lower than the value inferred from the acceptable spectral fit  $L_{33} \sim 5$ , the expression of  $n$  implies a density of about 6 orders of magnitude higher than the expected value found by Petre et al. (1982).

It is therefore safe to reject the scenario that the observed X-rays are powered by accretion from circumstellar matter. The stringent optical limit also rules out the possibility that the accretion is from a massive companion. However, we cannot completely exclude the possibilities that the central object is accreting from a very close dwarf star or from a fossil disk (van Paradijs et al. 1995) which remained after the supernova explosion. For the first possibility, even though such a compact system is unlikely to remain bound in the disruption of the high mass progenitor ( $\leq 25M_{\odot}$  Canizares & Winkler 1981), a deeper search for optical/IR counterpart can still be beneficial.

As has been shown in this work, the properties of the compact object in Puppis-A are similar to those of other radio quiet neutron stars in many aspects (e.g. Cas A; Pavlov et al. 2000; Chakrabarty et al. 2001; Murray et al. 2002). Even though the nature of this class of object has not yet been completely resolved, their existence has already revolutionized the conventional notion of neutron stars and their environment. Since it is easier to detect and identify active radio/X-ray pulsars than the radio-quiet neutron stars which are only observable in X-ray and located in a patchy X-ray bright supernova remnant, it is plausible that they are more common than canonical pulsars. It is not unlikely to assume that the relatively small number of detected radio-quiet neutron stars is due to observational selection effects. In this sense, identifying the nature of this class, including RX J0822-4300, is very important.

Table 2.1: Details of the XMM-Newton and Chandra observations of RXJ0822-4300

Telescope	Instrument	Instrument Mode	Filter	Obs.ID	Start Date	Effective Exposure	Net Rate (cts s <sup>-1</sup> )
Chandra	HRC-I	Default	UVIS	749	1999-12-21	16 ks	0.21±0.01
Chandra	ACIS-S 2	Timed Exposure	OBF	750	2000-01-01	11 ks	0.71±0.01
Chandra	HRC-S	Imaging	UVIS	1851	2001-01-25	19 ks	0.32±0.01
XMM-Newton	MOS1	PrimeFullWindow	Medium	0113020101	2001-04-15	7.3 ks	0.50±0.01
XMM-Newton	MOS2	PrimeFullWindow	Medium	0113020101	2001-04-15	7.5 ks	0.52±0.01
XMM-Newton	PN	PrimeSmallWindow	Thin	0113020101	2001-04-15	16 ks	1.62±0.01
XMM-Newton	MOS1	PrimeFullWindow	Thick	0113020301	2001-11-08	7.5 ks	0.45±0.01
XMM-Newton	MOS2	PrimeFullWindow	Thick	0113020301	2001-11-08	6.2 ks	0.46±0.01
XMM-Newton	PN	PrimeSmallWindow	Thin	0113020301	2001-11-08	16 ks	1.63±0.01

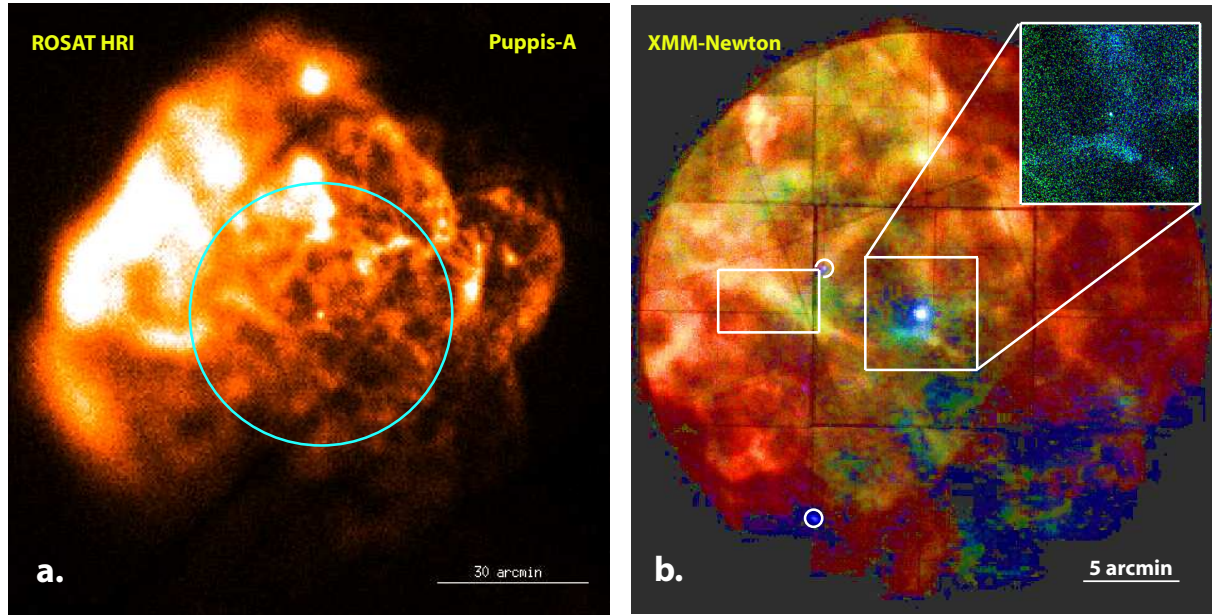


Figure 2.1: **a.** Composite ROSAT HRI image of the Puppis–A supernova remnant. The blue ring indicates the 30 arcmin central region which has been observed by XMM-Newton in April and November 2001. **b.** XMM-Newton MOS1/2 false color image of the inner 30 arcmin central region of Puppis–A (red: 0.3 – 0.75 keV, green: 0.75 – 2 keV and blue: 2 – 10 keV). The central source is RX J0822–4300. The inset shows the squared region as observed by the Chandra HRC-I. It is interesting to note that the region around RX J0822–4300 comprise mainly hard X-ray photons. The left white box indicates the region of the swirl-like structure interpreted by Winkler et al. (1989) as a second supernova in Puppis–A. The location of the northern and southern hard X-ray point sources are indicated by circles. The binning factors in the XMM and Chandra images are 4 arcsec and 0.6 arcsec, respectively. Adaptive smoothing with a Gaussian kernel of  $\sigma < 1$  pixel has been applied to the XMM-Newton and Chandra images. Top is north and left is east.

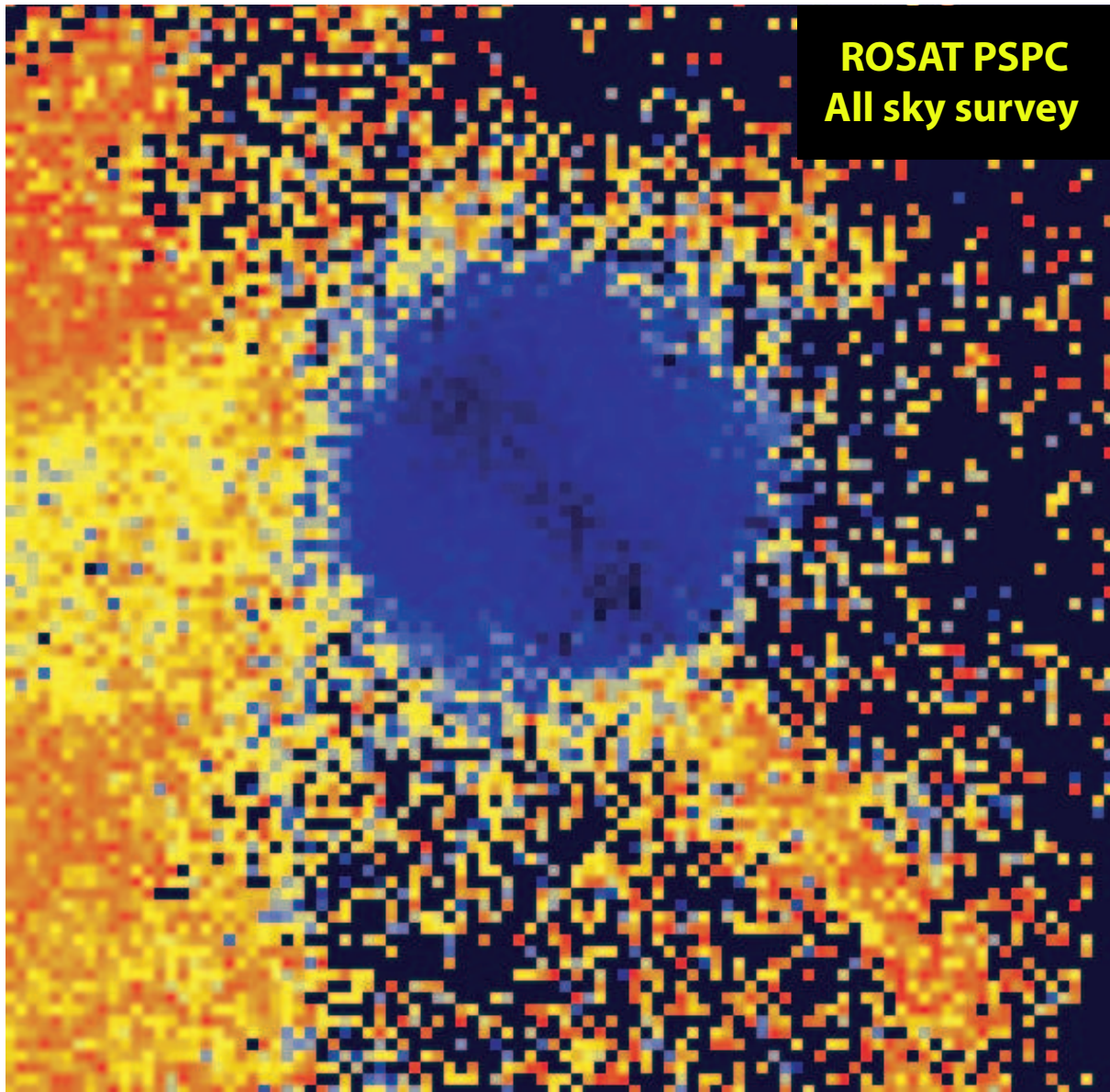


Figure 2.2: False color image of Puppis–A and parts of the Vela supernova remnant as seen in the ROSAT all-sky survey. Puppis–A appears solely in blue color (harder X-rays) while the soft emission from the Vela supernova remnant is represented by the red and yellow colors. The image clearly demonstrates the existence of the absorption belt which crosses Puppis–A from the south-west to north-east direction and which is associated with rim emission from the Vela supernova remnant.

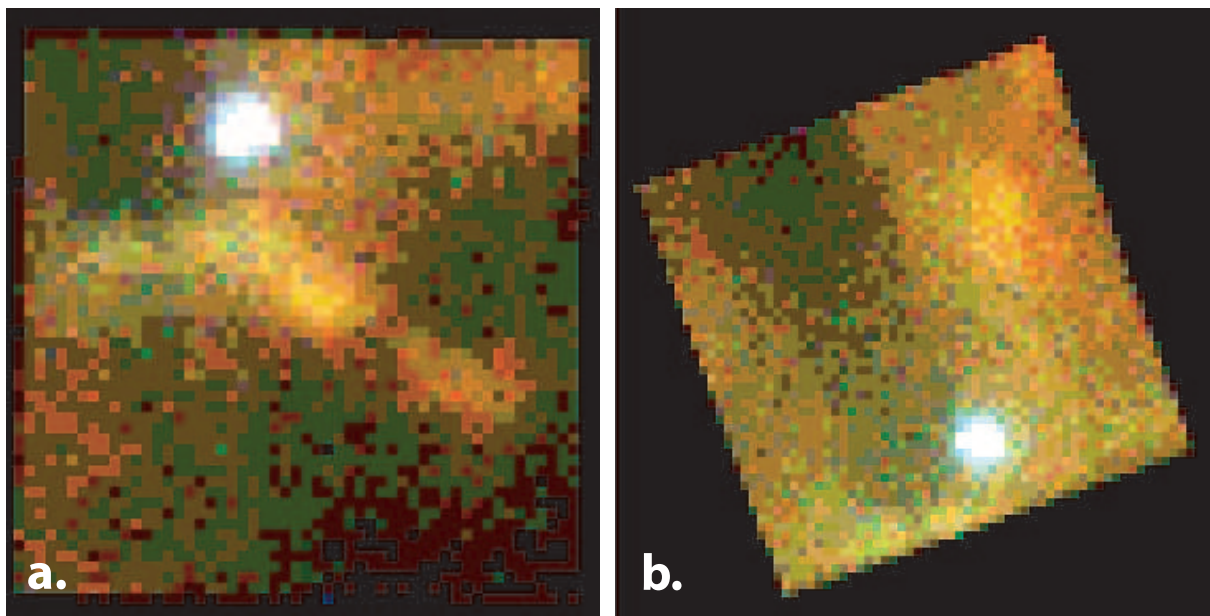


Figure 2.3: False color image (red: 0.3 – 0.75 keV, green: 0.75 – 2 keV and blue: 2 – 10 keV) of the  $4.4' \times 4.4'$  region around RX J0822-4300 as seen by XMM-Newton’s EPIC-PN detector during the observations in April 2001 (**a.**) and November 2001 (**b.**). The rim emission from Puppis–A near to the location of RX J0822–4300 is visible very well in **a.** Top is north and left is east.

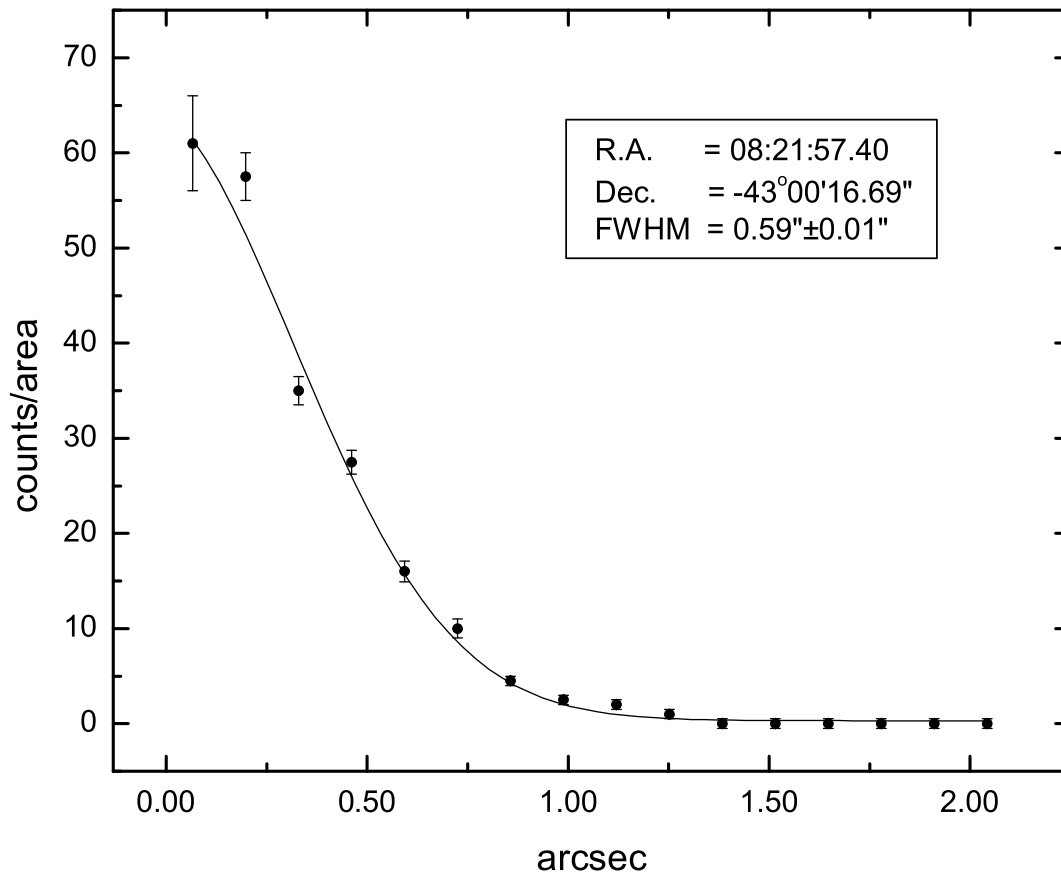


Figure 2.4: Chandra HRC-I brightness profile for RX J0822-4300. The solid curve represents the best-fit Gaussian model with the modeled PSF at 1.5 keV as a convolution kernel.



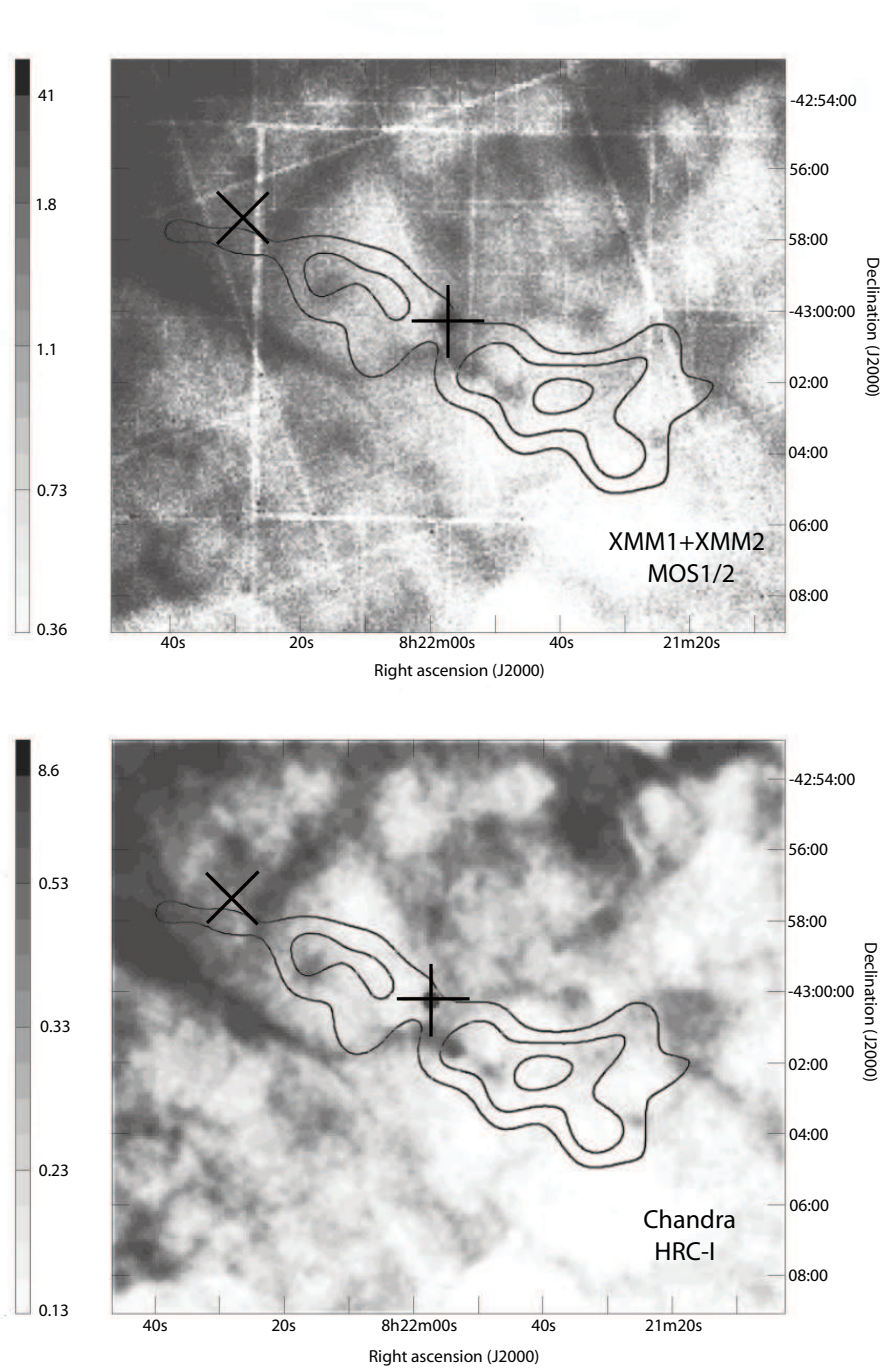


Figure 2.5: The contours depict a double-lobed feature of reduced  $\lambda 21$ -cm line emission (from Reynoso et al. 2003) superimposed on fluxed image of XMM-Newton MOS1/2 (*upper*) and Chandra HRC-I (*lower*) in gray scale. The cross shows the optical expansion center of Puppis–A as calculated by Winkler et al. (1988).

Table 2.2: Spectral Parameters of RX J0822-4300 inferred from data from XMM1 and XMM2.

Parameter	BB	BB+BB	BB+BB <sup>e</sup>	PL	BB+PL	BB+PL <sup>b</sup>	BB+PL <sup>c</sup>	BKPL	BREMSS
$N_H (10^{21} \text{ cm}^{-2})$	$2.67^{+0.09}_{-0.09}$	$4.54^{+0.49}_{-0.43}$	$6.38^{+0.21}_{-0.13}$	$9.26^{+0.14}_{-0.17}$	$8.57^{+0.88}_{-0.35}$	4.00	8.02	$7.62^{+0.17}_{-0.36}$	$5.76^{+0.11}_{-0.11}$
$\Gamma_1$	-	-	-	$4.29^{+0.02}_{-0.02}$	$4.67^{+0.14}_{-0.05}$	$2.51^{+0.11}_{-0.13}$	3.50	$3.61^{+0.05}_{-0.05}$	-
$\Gamma_2$	-	-	-	-	-	-	-	$5.29^{+0.20}_{-0.18}$	-
$T_1 (10^6 \text{ K})$	$4.32^{+0.04}_{-0.03}$	$2.61^{+0.30}_{-0.26}$	$1.87^{+0.02}_{-0.02}$	-	$4.43^{+0.05}_{-0.07}$	$3.80^{+0.06}_{-0.05}$	1.87	-	$9.57^{+0.18}_{-0.06}$
$T_2 (10^6 \text{ K})$	-	$5.04^{+0.28}_{-0.20}$	$4.58^{+0.03}_{-0.07}$	-	-	-	-	-	-
$R_1 (\text{ km})$	$1.23^{+0.03}_{-0.02}$	$3.29^{+1.12}_{-0.74}$	10	-	$0.80^{+0.06}_{-0.08}$	$1.59^{+0.06}_{-0.06}$	10	-	-
$R_2 (\text{ km})$	-	$0.75^{+0.12}_{-0.15}$	$1.09^{+0.04}_{-0.04}$	-	-	-	-	-	-
$N_{\text{bremss}} (10^{-2} \text{ cm}^{-5})$	-	-	-	-	-	-	-	-	$1.28^{+0.02}_{-0.02}$
$F_{X_{0.1-2.4\text{keV}}} (\text{ ergs cm}^{-2} \text{ s}^{-1})$	$5.82 \times 10^{-12}$	$9.67 \times 10^{-12}$	$2.04 \times 10^{-11}$	$1.77 \times 10^{-9}$	$2.60 \times 10^{-9}$	$1.18 \times 10^{-11}$	$2.18 \times 10^{-10}$	$3.45 \times 10^{-10}$	$2.40 \times 10^{-11}$
$F_{X_{0.5-10\text{keV}}} (\text{ ergs cm}^{-2} \text{ s}^{-1})$	$6.05 \times 10^{-12}$	$8.94 \times 10^{-12}$	$1.48 \times 10^{-11}$	$4.46 \times 10^{-11}$	$3.88 \times 10^{-11}$	$8.28 \times 10^{-12}$	$2.69 \times 10^{-11}$	$2.48 \times 10^{-11}$	$1.27 \times 10^{-11}$
Reduced $\chi^2$	1.82	1.20	1.28	1.91	1.21	1.42	3.77	1.22	1.20
D.O.F	467	465	466	467	465	466	467	465	467

The emitting areas inferred from the blackbody fits are calculated for the assumed distance of 2.2 kpc.

$F_{X_{0.1-2.4\text{keV}}}$  and  $F_{X_{0.5-10\text{keV}}}$  are unabsorbed fluxes in the energy range 0.1 – 2.4 keV and 0.5 – 10 keV, respectively.

<sup>a</sup>  $R_1$  fixed at 10 km radius.

<sup>b</sup>  $N_H$  fixed at  $4 \times 10^{21} \text{ cm}^{-2}$ .

<sup>c</sup>  $R_1$  and  $T_1$  fixed at 10 km and  $1.87 \times 10^6 \text{ K}$  respectively.

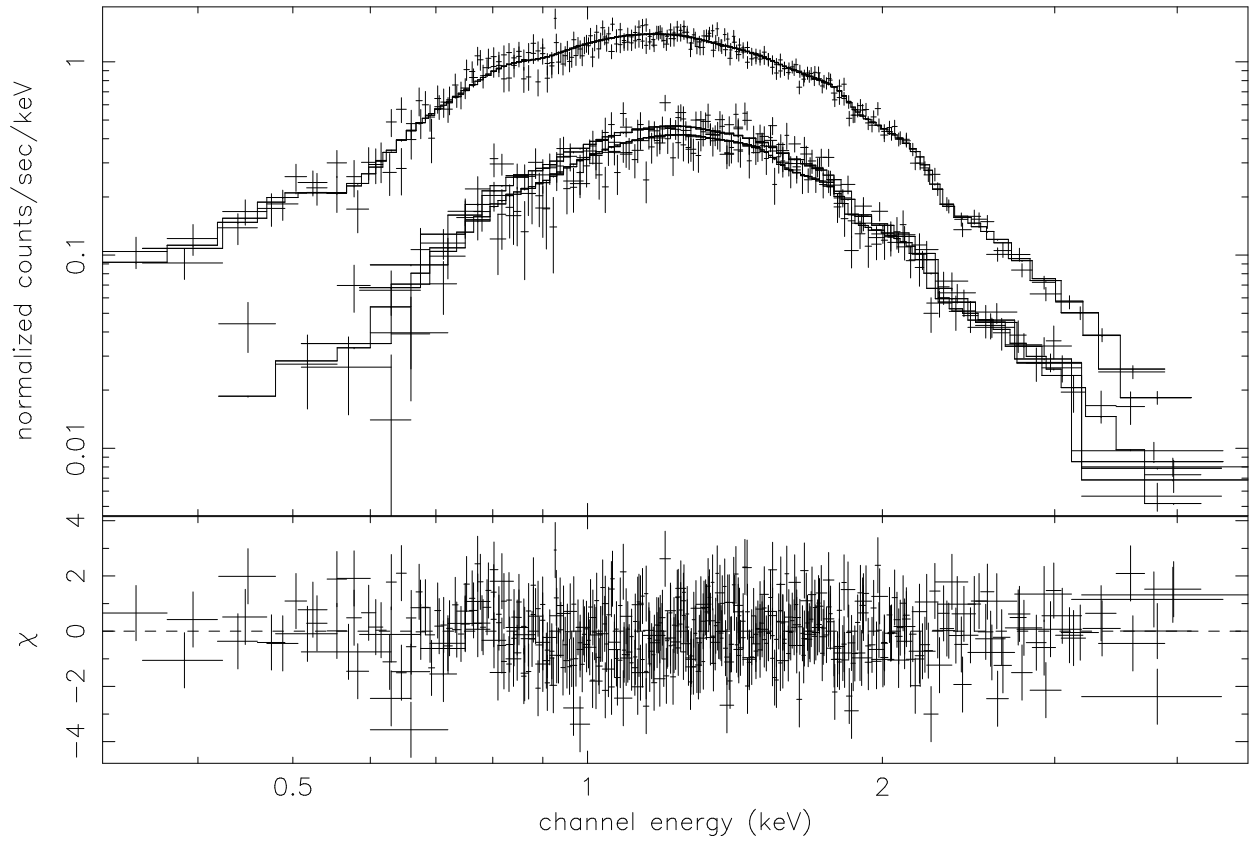


Figure 2.6: Energy spectrum of RX J0822–4300 as observed with the EPIC-PN (upper spectra) and MOS1/2 detectors (lower spectra) and simultaneously fitted to an absorbed two component blackbody model (*upper panel*) and contribution to the  $\chi^2$  fit statistic (*lower panel*).

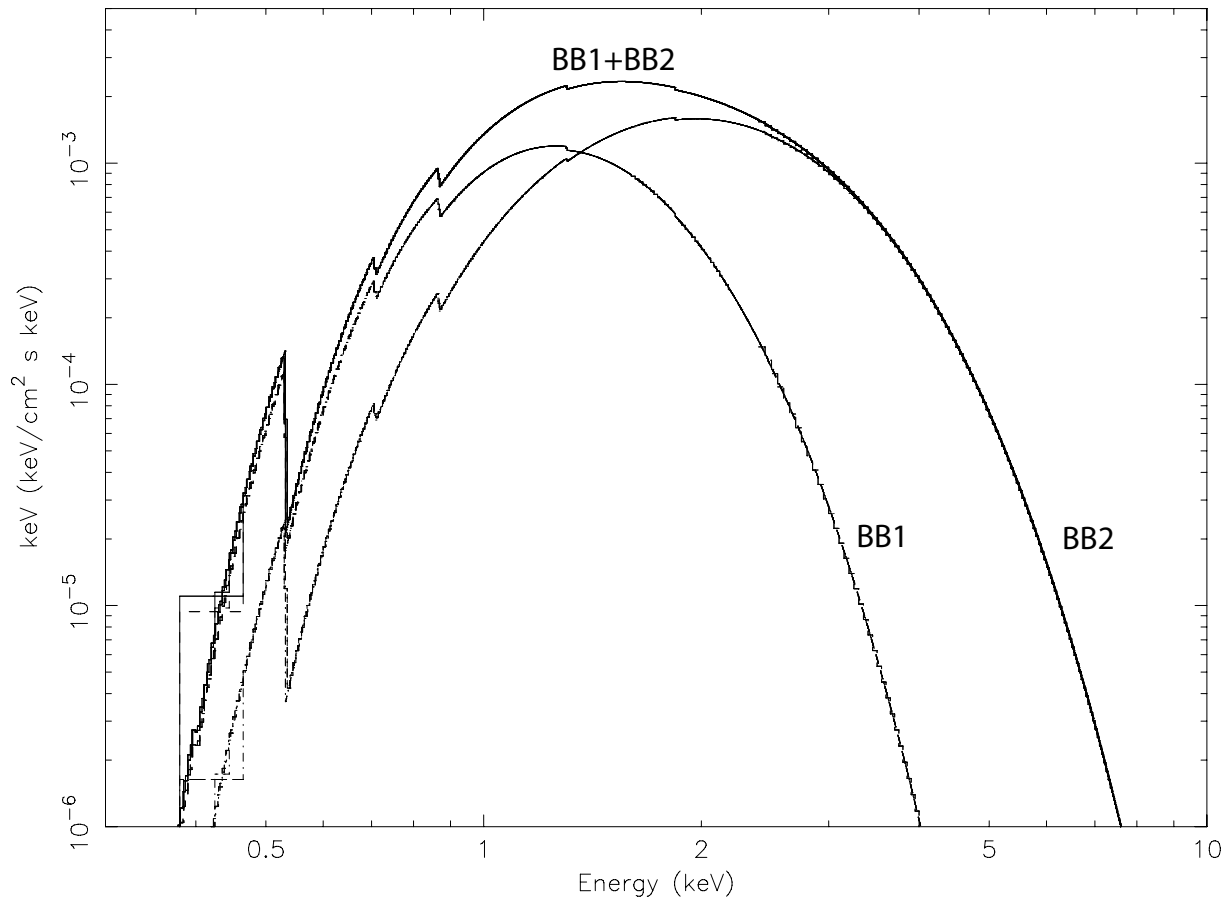


Figure 2.7: Components and combined model of double blackbody fitted to the spectral data of RX J0822-4300.

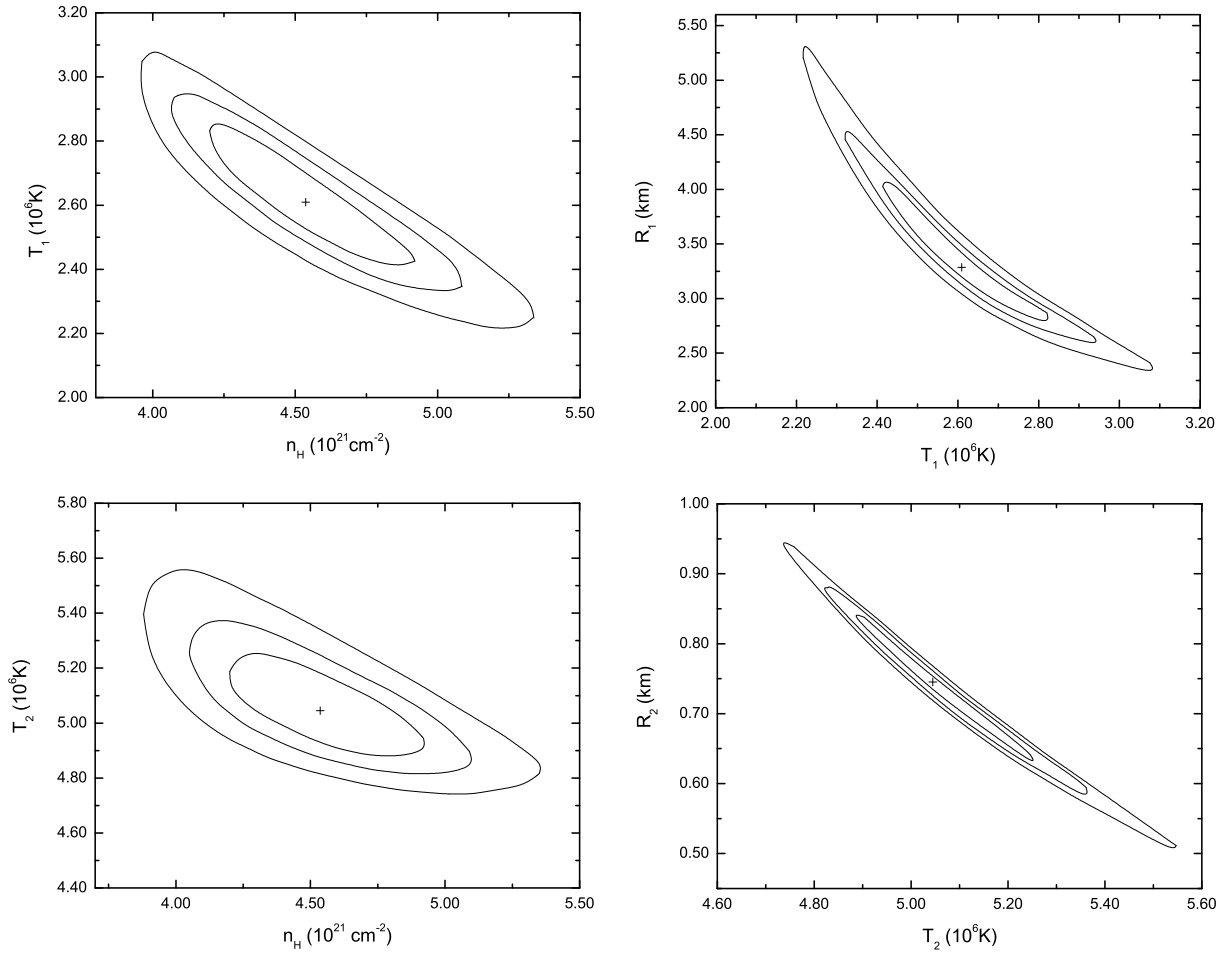


Figure 2.8:  $1\sigma$ ,  $2\sigma$  and  $3\sigma$  confidence contours for the double blackbody fit to the X-ray spectrum of RX J0822–4300.

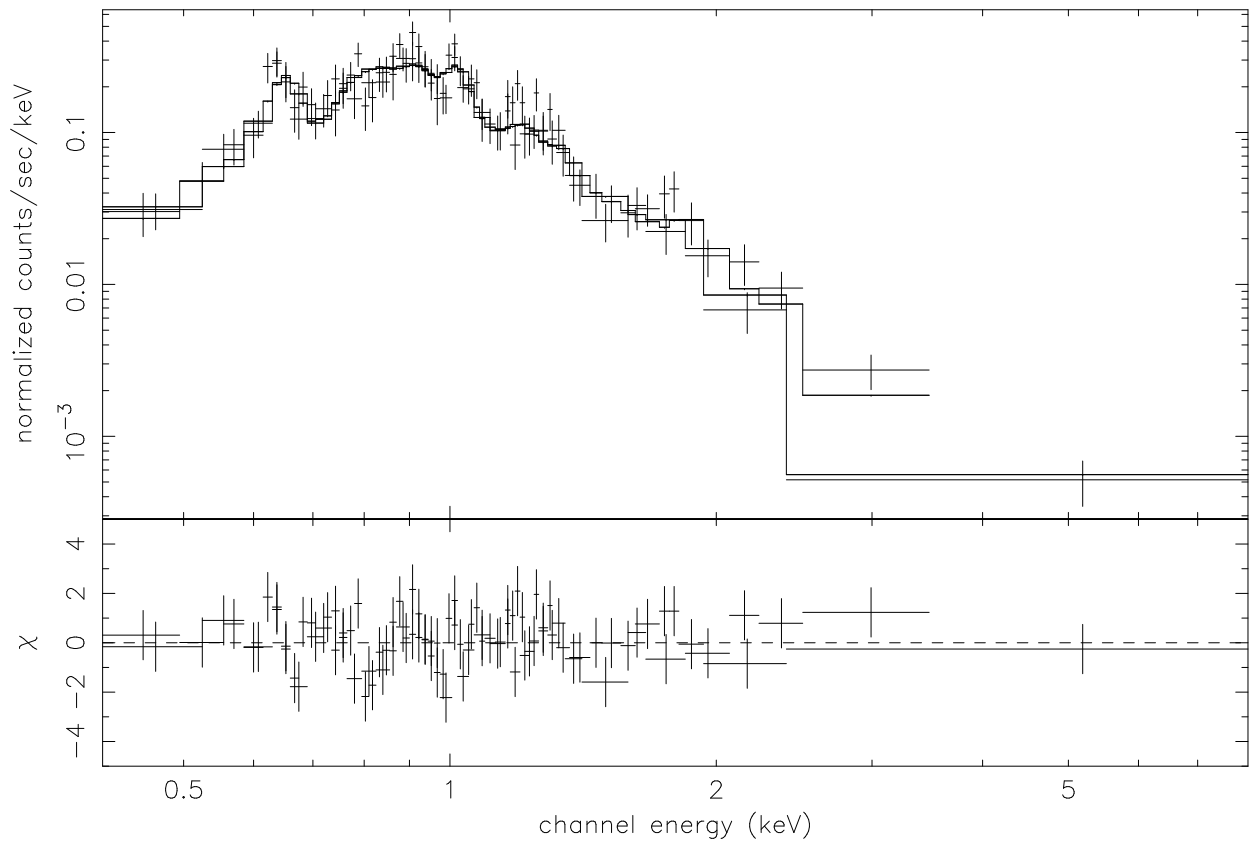


Figure 2.9: Energy spectrum of the rim emission underneath RX J0822-4300 as observed in April 2001 with the EPIC-MOS1/2 detector and simultaneously fitted to an absorbed non-equilibrium ionization collisional plasma model (*upper panel*) and contribution to the  $\chi^2$  fit statistic (*lower panel*).

Table 2.3: Observed fluxes of RX J0822–4300 inferred from observations at different epochs.

Observations	$F_X$ (0.1-2.4 keV) ergs cm <sup>-2</sup> s <sup>-1</sup>	$F_X$ (0.5-10 keV) ergs cm <sup>-2</sup> s <sup>-1</sup>	Start Date
XMM1	$3.37^{+0.28}_{-0.26} \times 10^{-12}$	$4.19^{+0.39}_{-0.36} \times 10^{-12}$	2001-04-15
XMM2	$3.38^{+0.30}_{-0.28} \times 10^{-12}$	$4.17^{+0.42}_{-0.37} \times 10^{-12}$	2001-11-08
Chandra ACIS	$3.34^{+0.40}_{-0.36} \times 10^{-12}$	$4.18^{+0.54}_{-0.50} \times 10^{-12}$	2000-01-01
ROSAT PSPC <sup>a</sup>	$\sim 3 \times 10^{-12}$	-	1991-04-16

<sup>a</sup> Flux observed by ROSAT according to PBW96

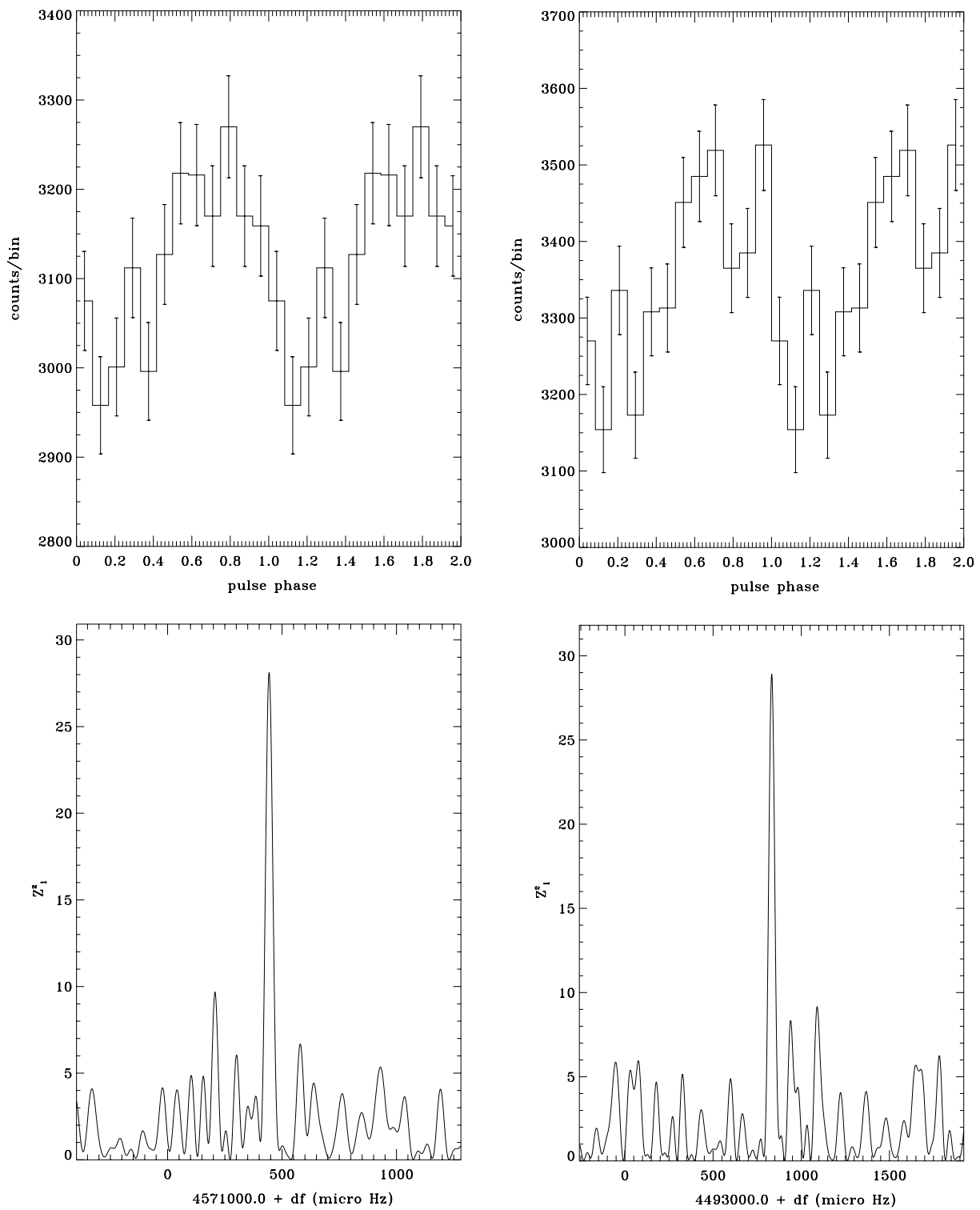


Figure 2.10: Pulse profiles and  $Z_1^2$ -distribution of the folded light curves as found in the XMM-Newton EPIC-PN data taken in April (left panel) and November 2001 (right panel).



# Chapter 3

## Probing the Proper Motion of the Compact Object in Puppis-A

This chapter is adopted from the refereed paper entitled “Probing the proper motion of the central compact object in Puppis-A with the Chandra high resolution camera” published in *Astronomy & Astrophysics* (Hui & Becker 2006c).

### 3.1 Introduction

The group of supernova remnant (SNRs) which are known to host a radio-quiet but X-ray bright central compact object (CCO) is a slowly growing one. Thanks to more sensitive X-ray observatories it currently includes Cas-A (CXOU J232327.9+584842; Tananbaum 1999), RX J0852.0–4622 (CXOU J085201.4–461753; Aschenbach 1998), RX J1713.7–3946 (RX J1713.4–3949; Pfeffermann & Aschenbach 1996), RCW 103 (1E 161348-5055; Tuohy & Garmire 1980), Puppis-A (RX J0822–4300; Petre et al. 1982; Petre, Becker, & Winkler 1996; Hui & Becker 2006), PKS 1209-51/52 (1E 1207.4–5209; Helfand & Becker 1984) and Kes 79 (CXOU J185238.6+004020; Seward et al. 2003; Gotthelf et al. 2005).

RX J0822–4300 was first noticed in one of the EINSTEIN HRI images of the Puppis-A supernova remnant (Petre et al. 1982). However, it appeared in this data only as a faint X-ray feature. It is not until the era of ROSAT when it became evident that RX J0822–4300 is the central compact stellar remnant which was formed in the supernova event (Petre, Becker, & Winkler 1996).

Recently, Hui & Becker (2006b) presented results from a detailed analysis of RX J0822-4300, which made use of all XMM-Newton and Chandra data available from it by beginning of 2005. The spectral analysis of XMM-Newton data revealed that the X-ray emission from RX J0822–4300 is in agreement with being of thermal origin. A double blackbody model with the temperatures  $T_1 = (2.35 - 2.91) \times 10^6$  K,  $T_2 = (4.84 - 5.3) \times 10^6$  K and the projected blackbody emitting radii  $R_1 = (2.55 - 4.41)$  km and  $R_2 = (600 - 870)$  m gave the best description of the observed point source spectrum among various spectral models tested. The X-ray images taken with the Chandra HRC-I camera allowed for the first time

to examine the spatial nature of RX J0822–4300 with sub-arcsecond resolution. Besides an accurate measurement of the source position, this observation constrained the point source nature of RX J0822–4300 down to  $0.59 \pm 0.01$  arcsec (FWHM) for the first time.

Despite the effort in searching for coherent radio pulsations, RX J0822–4300 has not been detected as a radio pulsar (Kaspi et al. 1996). Similar to many other CCOs, it has no optical counterpart down to a limiting magnitude of  $B \leq 25.0$  and  $R \leq 23.6$  (Petre, Becker, & Winkler 1996). Together with the lack of long term flux variation (Hui & Becker 2006b), all these evidences rule out many types of X-ray sources as a likely counterpart of RX J0822–4300, except a neutron star.

RX J0822–4300 is located about  $\sim 6$  arcmin distant from the optical expansion center of Puppis–A, which is at RA=08<sup>h</sup>22<sup>m</sup>27.45<sup>s</sup> and Dec=–42°57′28.6″ (J2000) (cf. Winkler & Kirshner 1985; Winkler et al. 1988). The age of the supernova remnant, as estimated from the kinematics of oxygen-rich filaments is  $\sim 3700$  years (Winkler et al. 1988). If these estimates are correct, RX J0822–4300 should have a proper motion of the order of  $\sim 100$  mas/yr to a direction away from its proposed birth place.

In this chapter, we test this hypothesis by making use of archival Chandra HRC-I data spanning an epoch of somewhat more than five years. The expected positional displacement for RX J0822–4300 in this time span is of the order of  $\sim 0.5$  arcsec. This is in the range of the Chandra accuracy given the possibility to correct for pointing uncertainties by using X-ray counterparts of stars with accurate position and which are serendipitously located in the field of view.

## 3.2 Observation and data analysis

Owing to the fact that there are only few bad pixels in the Chandra HRC-I and the pixel size of 0.13187 arcsec oversamples the point spread function (PSF) by a factor of  $\sim 5$ , the HRC-I appears to be the most suitable detector to perform astrometric measurements of X-ray sources.

Checking the Chandra archive for suitable data we found that by mid of 2006 RX J0822-4300, was observed twice with the HRC-I. The first observation was performed in 1999 December 21 (MJD 51533) for an exposure time of about 16 ksec. The second observation was done in 2005 April 25 (MJD 53485) for an on-source time of  $\sim 33$  ksec. In the April 2005 observation, the target was displaced only  $\sim 0.2$  arcmin off from the optical axis of the X-ray telescope. In the December 1999 data, it appears to be  $\sim 0.3$  arcmin off-axis which, in both cases, is small enough to have a negligible effect for the distortion of the PSF relative to an on-axis observation.

In order to increase the precision required for accurate astrometric measurements, systematic uncertainties need to be corrected. Apart from the aspect offset correction we also considered the errors introduced by determining the event positions. The later included corrections of the tap-ringing distortion in the position reconstruction and the correction of errors introduced by determining the centroid of the charge cloud. Instead of using the fully processed pipeline products, we started our data reduction with level-1 files to be

able to correct for these systematic effects. All the data processings were performed with CIAO 3.2.1. Details of the applied corrections are described in the following.

Instabilities in the HRC electronics can lead to a tap-ringing distortion in the position reconstruction of events. Correction has been applied to minimize this distortions in standard HRC level-1 processing which required to know the values of the amplitude scale factor (`AMP_SF`). Such values are found in the HRC telemetry and are different for each event. Unfortunately, they are often telemetered incorrectly. In order to fix this anomaly, we followed a thread in CIAO to deduce the correct values of `AMP_SF` in the level-1 event file from other HRC event data and applied these corrected values to minimize the distortion.

The de-gap correction was applied to the event files in order to compensate the systematic errors introduced in the event positions by the algorithm which determines the centroid of the charge cloud exiting the HRC rear micro-channel plate.

After correcting these systematic errors we generated the level-2 event lists files which were used thoroughly for the remaining analysis. We created HRC-I images of RX J0822-4300, for both epochs with a binning factor of 1 so that each pixel has a side length of 0.13187 arcsec.

To be able to correct for pointing uncertainties by using X-ray counterparts of stars which have their position known with high accuracy, we applied a wavelet source detection algorithm to the HRC-I images. Two X-ray point sources with a count rate of about 1% and 3% relative to that of RX J0822-4300 were detected serendipitously at about  $\sim 2.5$  arcmin and  $\sim 5.5$  arcmin distance from RX J0822-4300. Figure 3.1 shows a  $9.5 \times 7$  arcmin field surrounding RX J0822-4300 as seen with the HRC-I in April 2005. Both serendipitous sources, denoted as A and B, are indicated in this figure. Their X-ray properties are summarized in Table 3.1.

In order to determine their X-ray positions with higher accuracy than possible with the wavelet analysis, we fitted a 2-D Gaussian model with the modeled PSF as a convolution kernel to both sources A and B. These fits require some information on the source energy spectrum which is not available from the HRC-I data. We therefore checked the archival XMM-Newton data for both sources and found from an spectro-imaging analysis of MOS1/2 data (cf. Figure 1 in Hui & Becker 2006b) that the hardness-ratios of source A and B are comparable to that of RX J0822-4300 which has its energy peak at  $\sim 1.5$  keV. We therefore extract the Chandra HRC-I PSF model images at 1.5 keV with the corresponding off-axis angles from the CALDB standard library files (F1) by interpolating within the energy and off-axis grids using the CIAO tool `MKPSF`. The exposure maps were also generated at this energy by using `MKEXPMAP`.

The size of the  $1 - \sigma$  error circles of source A obtained by this method are 0.16 arcsec and 0.07 arcsec for the 1999 and 2005 observations, respectively. The relatively large error in the December 1999 observation is due to its shorter integration time and thus smaller photon statistics.

The large off-axis angle ( $\sim 5.5$  arcmin) of source B causes a marked blurring of the PSF (90% encircled energy radius  $\simeq 4$  arcsec). Such distortion makes the source appear to be very dispersed. Given the patchy and uneven supernova remnant emission this

source is surrounded by and the limited photon statistics we did not succeed in obtaining its coordinates more accurate than possible with the wavelet algorithm (which is  $\sim 0.2$  arcsec). This leaves source A as the only reference star to perform astrometric correction.

Correlating the source position of source A with the Two Micron All Sky Survey (2MASS) catalog (Skrutskie et al. 2006) identified the star with the source designation 08214628–4302037 as a possible optical counterpart. Since the next nearest optical source is located about 5 arcsec away from the X-ray position of source A, we adopt the 2MASS source 08214628–4302037 as its optical counterpart. The visual magnitudes of the object are  $J = 12.161 \pm 0.027$ ,  $H = 11.675 \pm 0.023$  and  $K = 11.558 \pm 0.024$ . Since its spectral type is not known with certainty, we adopted a typical X-ray-to-optical flux ratio of  $\log(F_x/F_{opt}) \simeq -2.46$  for stars from Krautter et al. (1999). Assuming a Raymond-Smith thermal plasma model with  $kT = 0.15$  keV,  $n_H = 4 \times 10^{21}$  cm $^{-2}$  (Hui & Becker 2006b) and solar abundances for the star’s spectrum we estimated with the aid of PIMMS (version 3.8a2) its HRC-I count rate to be  $\sim 3 \times 10^{-3}$  cts/s. This is in good agreement with the observed count rate of source A (cf. Table 3.1).

In order to use the optical identification of the serendipitous X-ray source A as a reference source for the offset correction, we have to check whether itself shows a proper motion. To investigate this, we correlated its 2MASS position with the UCAC2 catalog (Zacharias et al. 2003). We unambiguously found a source with the UCAC2 designation 13302738 as a counterpart of the X-ray source A. According to this catalog, this source has a proper motion of  $\mu_{RA} = -16.0 \pm 5.2$  mas/yr,  $\mu_{dec} = -1.7 \pm 5.2$  mas/yr.

We attempted to make an independent estimate by analysing the images from the first and the second Digitised Sky Surveys<sup>1</sup>. From the observation dates specified for the DSS-1 and DSS-2 images, we found that the epoches of these two images are separated by 5134 days. We took four bright stars within 1 arcmin neighbourhood of the X-ray source A as the references to align the frames of DSS-1 and DSS-2. None of these stars appeared to be saturated so that their positions could be properly determined by a 2-D Gaussian fit. We determined the offset between these two images from comparing the best-fit positions of the four reference stars in both frames. However, we found that the alignment error is at a level of  $\sim 0.5$  arcsec. This is close to the average positional discrepancy between DSS-1 and DSS-2 which is found to be  $\sim 0.6$  arcsec. The information provided by DSS-1/2 thus does not allow us to estimate the proper motion of our source of interest independently. In view of this, we can only resort on the findings in the UCAC2 catalog.

Under the assumption that the UCAC2 object 13302738 is indeed the optical counterpart of source A, we applied the aspect correction to the corresponding frames with the proper motion of the reference star taken into account. However, with only one comparison source available for the frame alignment, there are some limitations in our adopted method. Firstly, the roll angle between two frames cannot be determined independently with just one reference source. Hence, the accuracy of the current result is limited by the output of the star-tracking camera, the Pointing Control and Determination system (PCAD). Also, an independent estimate of the HRC-I plate scale cannot be made with only one reference

<sup>1</sup><http://ledas-www.star.le.ac.uk/DSSimage/>

source. The potential variation of the plate scale might introduce an extra error, though we consider this is negligible as the typical uncertainty of the HRC-I plate scale is at the order of  $\sim 0.05$  mas/pixel <sup>2</sup>.

The error circle of the UCAC2 object 13302738 is specified to be 0.015 arcsec. Including the uncertainty in the proper motion, the overall positional error of this astrometric source is increased with time which gives 0.016 arcsec and 0.037 arcsec in the December 1999 and April 2005 epoch respectively. The total error of the aspect corrections is calculated by combining the statistical error of the X-ray position of source A and the astrometric error of the UCAC2 object in quadrature. This yields a  $1 - \sigma$  error of 0.161 arcsec and 0.079 arcsec for the aspect correction of the December 1999 and April 2005 observation, respectively.

The position of RX J0822–4300 was determined by the same procedure we applied to obtain the position for source A. The fits provide us with the coordinates for RX J0822–4300 which are RA=08<sup>h</sup>21<sup>m</sup>57.389<sup>s</sup> and Dec=–43°00′16.90″ (J2000) in the 1999 observation and RA=08<sup>h</sup>21<sup>m</sup>57.343<sup>s</sup> and Dec=–43°00′17.18″ (J2000) in the April 2005 observation<sup>3</sup>. The  $1 - \sigma$  error of the position introduced by the PSF-fit is 0.01 arcsec in both epochs. In order to exclude any dependence of the deduced source positions on the aperture size of the selected source region, we repeated the fits for three different apertures with radii equal to 3 arcsec, 4 arcsec and 5 arcsec, respectively. We did not find any variation of the best-fitted parameters in these independent fittings.

### 3.3 Results and Discussion

The fitted X-ray positions of RX J0822–4300 are plotted for the observational epochs December 1999 and April 2005 in Figure 3.2. The size of the error circle for each position is determined by adding the error in correcting the aspect offset and the error of the position of RX J0822–4300 in quadrature. This gives 0.162 arcsec and 0.088 arcsec for the December 1999 and the April 2005 observations, respectively. The corresponding error circles are indicated in Figure 3.2.

Comparing the positions of RX J0822–4300 as deduced for the two observations in 1999 and 2005 we found that they are different by  $0.574 \pm 0.184$  arcsec. This is well consistent with the displacement estimated from the kinematic age of the SNR and the positional offset of RX J0822–4300 from the SNR’s optical expansion center (cf. section 3.1). The quoted error is  $1 - \sigma$  and combines the positional errors in both epochs in quadrature.

Given the epoch separation of 5.34 years for both Chandra HRC-I observations the observed proper motion of RX J0822–4300 is  $\mu = 107.49 \pm 34.46$  mas/yr. The position angle is PA=241°  $\pm$  24°. Taking the position inferred from the December 1999 observation and the position of the optical expansion center of Puppis–A (Winkler et al. 1988), a position

<sup>2</sup>[http://cxc.harvard.edu/cal/Hrma/optaxis/platescale/geom\\_public.html](http://cxc.harvard.edu/cal/Hrma/optaxis/platescale/geom_public.html)

<sup>3</sup>The best-fitting position in the 1999 observation has a 0.242 arcsec deviation from that inferred by Hui & Becker (2006b) which corrected the offset by simply using the calculator provided by the Chandra Aspect team [http://cxc.harvard.edu/cal/ASPECT/fix\\_offset/fix\\_offset.cgi](http://cxc.harvard.edu/cal/ASPECT/fix_offset/fix_offset.cgi)

angle of  $PA \simeq 243^\circ$  is implied. Such consistency suggests that RX J0822–4300 is indeed physically associated with Puppis–A and its actual birth place is not too far away from the SNR’s optical expansion center. Assuming that the distance of 2.2 kpc to Puppis–A is correct, the observed proper motion implies that RX J0822–4300 has a projected recoil velocity as high as  $1121.79 \pm 359.60$  km/s to the southwest. The inferred transverse velocity seems high compared with the average velocity,  $\sim 250$  km/s, of ordinary radio pulsars (Hobbs et al. 2005) though the large error prevents any constraining conclusions. We would like to mention, though, that there are several fast moving pulsars including PSRs B2011+38 and B2224+64 which have 2-D speeds of  $\sim 1600$  km/s (Hobbs et al. 2005).

The interesting association of Puppis–A and RX J0822–4300 provides a unique opportunity to observe the interaction between a compact stellar remnant and a SNR. Also, this system is a test-bed for studying the dynamics of the supernova explosion. Measuring the proper motion of RX J0822–4300 with higher accuracy than possible with the current data will make it possible to provide constraints for the SN explosion model which formed Puppis–A.

Although our result is a promising indication of a fast moving CCO in a SNR, we note that the deduced positional shift is only significant at a  $3.1\sigma$  level. Since the X-ray source A is rather faint, its relatively large positional error predominates in the error budget.

In this letter we have presented the first attempt to measure the proper motion of RX J0822–4300. In order to further constrain this measurement, one or more Chandra HRC-I observations can attain a much larger positional separation in a few years from today. Furthermore, a more accurate proper motion measurement for the optical counterpart of the reference source is also necessary.

After this work was accepted for publication in A&A letter, we became aware that a paper on the similar subject as presented here was submitted to ApJ by Winkler & Petre (2006). In their paper, though using the same dataset as we use, a much higher significance ( $9.4\sigma$  !) for the proper motion of RX J0822–4300 is claimed. They justify this by their inclusion of source B as a second reference star. In view of its large off-axis angle, thus blurred PSF and large error circle ( $\sim 0.2$  arcsec), we question their justification and doubt their error estimate being a realistic value, even their proper motion estimate is qualitatively similar with ours.

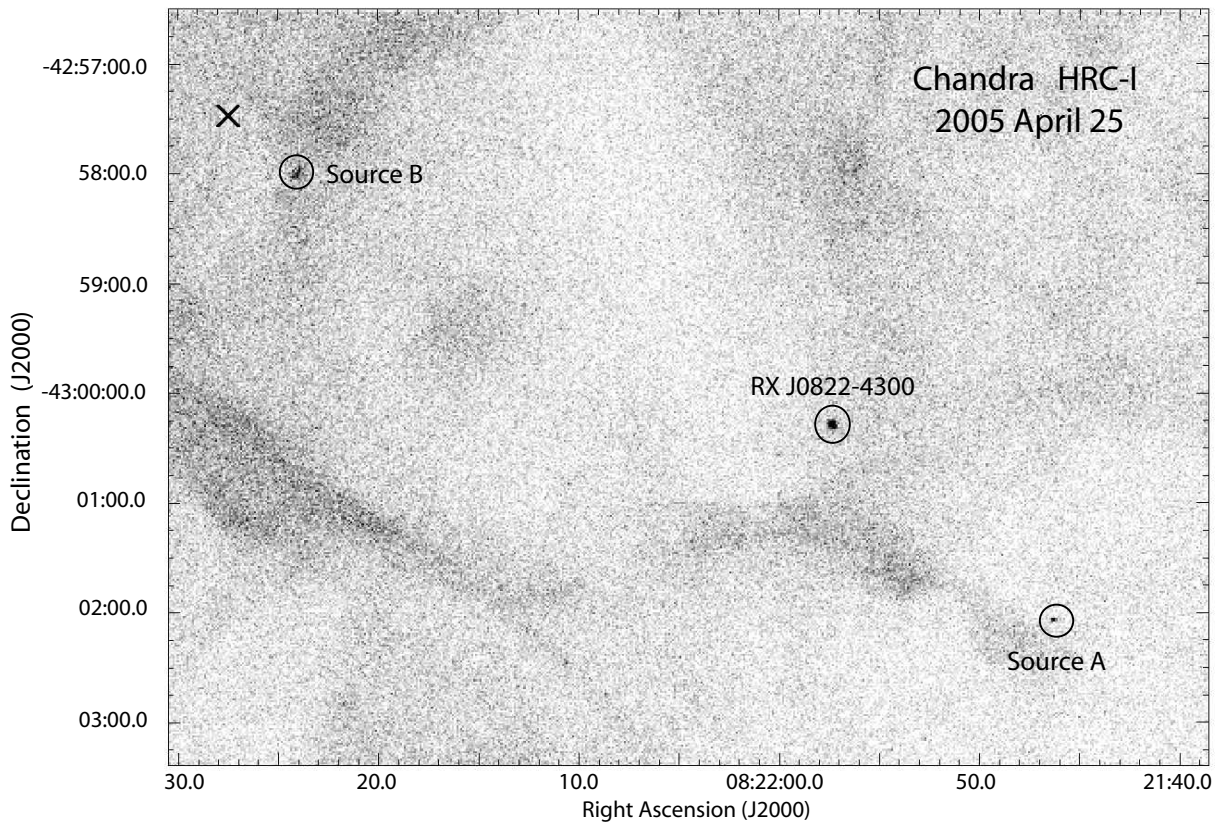


Figure 3.1: Part of the Chandra HRC-I image of the Puppis–A supernova remnant. Besides RX J0822–4300, there are two serendipitous point sources detected in the field of view. They are denoted as source A and B. The optical expansion center of Puppis–A as obtained by Winkler et al. (1988) is marked by a cross.

Table 3.1: X-ray properties of serendipitous sources around RX J0822–4300.

Source	X-ray position		Positional error <sup>a</sup>	Net count rate cts/s
	RA (J2000)	Dec (J2000)		
<b>1999 observation</b>				
A	08 <sup>h</sup> 21 <sup>m</sup> 46.339 <sup>s</sup>	–43°02′03.73″	0.16″	$(2.51 \pm 0.38) \times 10^{-3}$
B	08 <sup>h</sup> 22 <sup>m</sup> 23.924 <sup>s</sup>	–42°57′59.29″	0.20″	$(8.42 \pm 0.75) \times 10^{-3}$
<b>2005 observation</b>				
A	08 <sup>h</sup> 21 <sup>m</sup> 46.313 <sup>s</sup>	–43°02′03.46″	0.07″	$(3.20 \pm 0.30) \times 10^{-3}$
B	08 <sup>h</sup> 22 <sup>m</sup> 23.966 <sup>s</sup>	–42°57′59.70″	0.18″	$(7.47 \pm 0.48) \times 10^{-3}$

<sup>a</sup> The positional errors of sources A and B are given by the PSF fitting and the wavelet detection algorithm respectively.

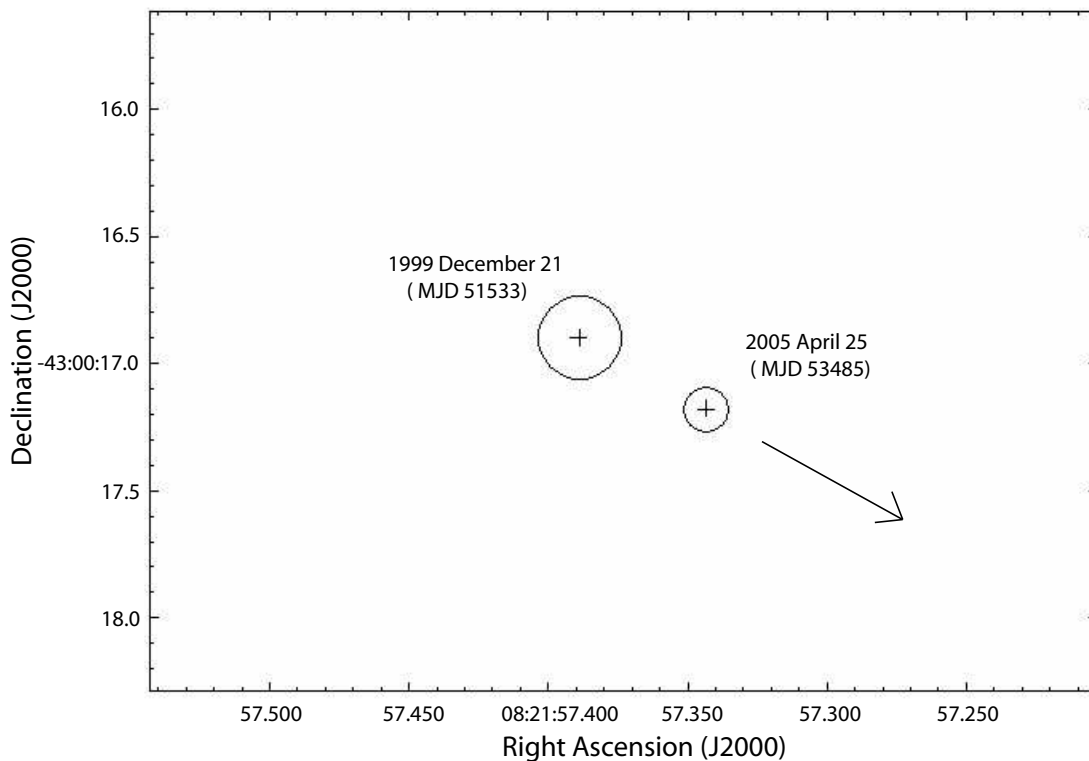


Figure 3.2: The best-fitted X-ray positions of RX J0822–4300 in two epochs are marked by crosses. The circles indicate the  $1 - \sigma$  error. The arrow shows the direction of proper motion inferred from both positions.



# Chapter 4

## XMM-Newton Observations of the Compact Object in RX J0852.0-4622

This chapter is adopted from the paper: “Exploring the Central Compact Object in the RX J0852.0-4622 Supernova Remnant with XMM-Newton” which is submitted to *Astronomy & Astrophysics* (Becker, Hui, Aschenbach & Iyudin 2006)

### 4.1 Introduction

A very fascinating result reflecting the advantage of wide-field spectro-imaging observations provided by ROSAT in its all-sky survey (RASS) is the discovery of the supernova remnant RX J0852.0-4622 by Aschenbach (1998). The remnant is located along the line of sight towards the south-east corner of the Vela supernova remnant (cf. Fig.4.1). Because the latter dominates the emission in the soft band, RX J0852.0-4622 is best visible in the RASS data at energies above  $\sim 1$  keV. The remnant has a circular shell-like shape with a diameter of 2 degrees. Although the distance to the remnant is uncertain, its free-expansion age ( $t \sim 3.4 \times 10^3 v_{5k}^{-1} d_{1kpc}$  yr, with  $v_{5k}$  as expansion velocity in units of 5000 km/s) suggests a remnant age much younger than that of Vela. Because of its suggested age, it is often denoted as *Vela-Junior*.

COMPTEL data suggest that the remnant has a 1.157 MeV  $\gamma$ -line from the radioactive isotope  $^{44}\text{Ti}$  associated with it (Iyudin et al. 1998). Together with ROSAT X-ray data, Aschenbach et al. (1999) suggested the remnant could be as young as  $\sim 680$  years and as close as  $\sim 200$  pc, which would make it the closest and youngest supernova remnant among the  $\sim 231$  galactic remnants known today (Green 2006).

However, reanalysis of COMPTEL data indicates that the detection of the  $^{44}\text{Ti}$  line in the direction of RX J0852.0-4622 is only significant at the level of  $\sim (2 - 4)\sigma$  (Schönfelder et al. 2000). Discarding the  $^{44}\text{Ti}$  line detection would leave the age and distance estimates significantly less constrained. ASCA observations have shown that the hydrogen column absorption of the remnant is about one order of magnitude larger than that of the Vela supernova remnant (Tsunemi et al. 2000; Slane et al. 2001) which would suggest that

## 60 4. XMM-Newton Observations of the Compact Object in RX J0852.0-4622

RX J0852.0-4622 is far behind Vela. On the other hand, the lack of strong variation in the column absorption across RX J0852.0-4622 further indicates that the remnant cannot be more distant than the Vela Molecular Ridge, i.e. 1 to 2 kpc (Slane et al. 2001).

The X-ray spectra from RX J0852.0-4622 as obtained by the ASCA GIS detector are well described by a power law model which indicates that the X-ray emission of RX J0852.0-4622 is likely to be predominately non-thermal (Tsunemi et al. 2000; Slane et al. 2001). Together with SN1006 and G347.3-0.5, RX J0852.0-4622 thus forms the exclusive group of non-thermal shell-type supernova remnants which are believed to be accelerators of cosmic rays. This is further supported by the recent detection of TeV  $\gamma$ -ray images by HESS which correlate well with the X-ray images (Aharonian et al. 2005).

Although the GIS spectra appear to be featureless and power law like, analysis of the spectrum of the north-western rim obtained by the ASCA SIS detector has shown a line feature at  $\sim 4.1$  keV, though its significance was low (Tsunemi et al. 2000; Slane et al. 2001). The recent study of the rim of RX J0852.0-4622 with XMM-Newton has confirmed the non-thermal nature of the remnant as well as the presence of an emission line feature at  $4.45 \pm 0.05$  keV (Iyudin et al. 2005). The authors suggest that the line (or lines) originate from the emission of Ti and Sc which might be excited by atom/ion or ion/ion high velocity collisions. This is in agreement with the width of the 1.157 MeV  $\gamma$ -ray line which indicates a large velocity of the emitting matter of  $\sim 15000$  km/s (Iyudin et al. 1998). Furthermore, the consistency of the X-ray line flux and the  $\gamma$ -ray line flux support the existence and the amount of Ti in RX J0852.0-4622 claimed by Iyudin et al. (1998). However, if the interpretation of Iyudin et al. (2005) is correct, only sub-Chandrasekhar type Ia supernova can produce such high ejecta velocity within the current knowledge of explosion model. On the other hand a sub-Chandrasekhar type Ia supernova would not leave a compact stellar-like object, in contrast to the observations. Apart from the 1.157 MeV line, the decay chain  $^{44}\text{Ti} \rightarrow ^{44}\text{Sc} \rightarrow ^{44}\text{Ca}$  also produces the hard X-ray lines at 67.9 keV and 78.4 keV. So far INTEGRAL observations have not found any evidence of these two lines (Renaud et al. 2006).

A central compact X-ray source CXOU J085201.4-461753 in RX J0852.0-4622 was first recognized as a  $5\sigma$  excess in the RASS data by Aschenbach et al. (1998). Its existence was finally confirmed with the detection of a hard, somewhat extended X-ray source in the ASCA data (Tsunemi et al. 2000; Slane et al. 2001). To conclusively identify this source as the compact remnant of the supernova explosion that created RX J0852.0-4622 was not possible because of the presence of two foreground stars (HD 76060 and Wray 16-30) which could be responsible for at least part of the central X-ray emission. On the other hand, BeppoSAX observations have revealed another hard X-ray source, SAX J0852.0-4615, which was not resolved in previous observations (Mereghetti 2001). Based on its harder X-ray spectrum and higher X-ray to optical flux ratio, the authors found SAX J0852.0-4615 to be more likely a neutron star candidate associated with RX J0852.0-4622.

A first Chandra observation of the central part of Vela-Jr was performed in October, 2000. The superior angular resolution of Chandra clearly resolved a point-like source, CXOU J085201.4-461753, and invalidated the association with the aforementioned foreground stars (Pavlov et al. 2001). Moreover, there was no source detected at the position

of SAX J0852.0–4615. In view of this, there is little doubt that CXOU J085201.4-461753, located only  $\sim 4$  arcmin off the geometric center of RX J0852.0-4622, is the compact remnant of the supernova explosion. This is further suggested by the  $f_x/f_{opt}$  ratio as the source has no optical counterpart known brighter than  $m_B > 22.5$ ,  $m_R > 21.0$  (Pavlov et al. 2001).

The first short 3 ksec Chandra observation provided only an accurate position for CXOU J085201.4-461753. Spectral analysis with this data were strongly hampered by low photon statistics and pile-up effect (Pavlov et al. 2001). A second 31.5 ksec Chandra observation performed in August, 2001, aimed for timing and spectral analysis and was set up in ACIS continuous clocking mode which provides 2.85 ms temporal resolution at the expense of spatial information in one dimension. In this data it was found that the spectrum of CXOU J085201.4-461753 can be well modeled by a single blackbody with a temperature of  $\sim 4.68 \times 10^6$  K and a projected emitting area with a blackbody radius of  $\sim 280$  m (Kargaltsev et al. 2002). From a timing analysis these authors reported two candidate periods of  $\sim 301$  and  $\sim 33$  ms, though the significance of these signals was rather low. Furthermore, no evidence for any long-term variability of the source flux was found (Kargaltsev et al. 2002).

Although there is no indication of diffuse nebular emission around the point source in X-rays (Pavlov et al. 2001; Kargaltsev et al. 2002), Pellizzoni, Mereghetti, & De Luca (2002) detected a faint and circular  $H_\alpha$  nebula with a diameter of  $\sim 6$  arcsec at the position of CXOU J085201.4-461753. These authors suggest that the nebula emission could be created by a bow shock which is driven by the relativistic wind of a neutron star.

Many previous studies favor the interpretation of CXOU J085201.4-461753 being a neutron star. It should be admitted, though, that the properties of this compact object are not tightly constrained and hence its nature cannot be resolved without ambiguity. It is further still on discussion whether this source is physically associated with RX J0852.0-4622. Answering this question can help us to constrain the nature of RX J0852.0-4622 in turn.

In this chapter, we present a first detailed study of CXOU J085201.4-461753 and its environment by making use all XMM-Newton data taken before 2005<sup>1</sup>. In section 4.2, we give a brief description of the performed observations. In section 4.3, we present the methods and results of our data analysis which are subsequently discussed in section 4.4.

## 4.2 Observations & Data Reduction

By early 2005 three observations have been targeted with XMM-Newton on CXOU J085201.4-461753. The basic information of the observations are summarized in Table 4.1. The huge collecting power and high spectral resolution of XMM-Newton provides us with data of much higher photon statistics than it was achieved with Chandra and other previous observatories.

<sup>1</sup>Tentative results on the analysis of parts of this data were already published by Becker & Aschenbach (2002).

CXOU J085201.4-461753 was first observed by XMM-Newton on April 27, 2001 for a duration of  $\sim 25$  ksec. The MOS1/2 and the PN cameras were operated in full-frame and extended full-frame mode, respectively. The medium filter was used in all instruments to block stray light and optical leakage from bright foreground stars. Since the accurate position of the central compact object was not known at the time of this first XMM-Newton observation, CXOU J085201.4-461753 got placed 2.3 arcmin off-axis. The point spread function at this off-axis angle is not much different from the on-axis one, but CXOU J085201.4-461753 got located right on a CCD gap in the PN-camera, causing a severe decrease in photon statistics and data quality. We therefore excluded this PN dataset from our analysis.

The second and third XMM-Newton observations of CXOU J085201.4-461753 were performed on May 21, 2003 and June 25, 2003 with total exposure times of  $\sim 43$  and  $\sim 17$  ksec, respectively. CXOU J085201.4-461753 was observed on-axis in both observations. The MOS1/2 cameras were setup in the same way as in the 2001 observation. The EPIC-PN camera was operated in small-window mode with a thin filter.

All the raw data were processed with version 6.1.0 of the XMM Science Analysis Software (XMMSAS). We created filtered event files for the energy range 0.3 – 10 keV and selected only those events for which the pattern was between 0 – 12 for the MOS cameras and 0 – 4 for the PN camera. We further cleaned the data by accepting only good time intervals (when the sky background was low) and removed all events potentially contaminated by bad pixels. The effective exposure times after data cleaning and the background corrected source count rates in the 0.3 – 10 keV band are summarized in Table 4.1.

## 4.3 Data Analysis

### 4.3.1 Spatial Analysis

A false color image of the merged MOS1/2 data from all three XMM-Newton observations is displayed in Figure 4.2. CXOU J085201.4-461753 is the brightest source in the field. It is located at the western edge of a faint  $\sim 9 \times 14$  arcmin wide diffuse and irregular shaped extended X-ray structure which emits mostly in the soft bands below  $\sim 2$  keV. The extended emission was already visible in ASCA images, but less resolved from and less discriminating the compact source because of ASCA's wide point spread function. The XMM-Newton observations provide for the first time a more detailed view of this field.

Apart from CXOU J085201.4-461753 we have detected 18 point-like sources serendipitously in the field of view. Their positions are given in Table 4.2. We have correlated these sources with the 30 radio sources discovered by Reynoso et al. (2006) within RX J0852.0-4622. We found that the nominal position of one of these radio sources coincides with the peak emission of the X-ray source 11. But cross-correlating all these 18 sources with SIMBAD and NED databases did not result in any identification within a circle of 30 arcsec radius around each source.

### 4.3.2 Spectral Analysis

As a compromise to select as much as possible events from CXOU J085201.4-461753 without the contamination from the surrounding remnant emission (see Figure 4.2) we extracted the source spectrum from a circular region of 20 arcsec radius. About 70% of all point source events are located within this region. Annular regions with radii of 22 and 35 arcsec, centered on CXOU J085201.4-461753, were used to extract the background spectra. The background corrected count rates are listed in column 6 of Table 4.1. Response files were computed for all datasets by using the XMMSAS tasks RMFGEN and ARFGEN. According to the XMMSAS task EPATPLOT, no dataset is affected by CCD pile.

In order to fit spectra from all three observation runs simultaneously we have grouped the energy channels of all spectra dynamically. For the MOS1/2 data of the April 2001 observation we grouped the data with  $\geq 30$  counts/bin. For the MOS1/2 and PN data of the May 2003 observation we used a grouping with  $\geq 100$  counts/bin and  $\geq 165$  counts/bin, respectively, whereas for the June 2003 observations the MOS1/2 and PN data were grouped with  $\geq 30$  counts/bin and  $\geq 50$  counts/bin respectively. The different grouping reflects the differences in photon statistics in the various datasets.

All the spectral fits were performed in the 0.3 – 10 keV energy range by using XSPEC 11.3.1. The spectral models tested include a single blackbody, a double blackbody, a power law, a combination of a blackbody and power law model as well as a broken power law and a thermal bremsstrahlung model. The parameters of all fitted model spectra are summarized in Table 4.3. The quoted errors are conservative and are  $1\sigma$  for 2 parameters of interest for single component spectral models and for 3 parameters of interest for multi-component models.

A single blackbody model gives a parameter set of  $T = (4.53 \pm 0.05) \times 10^6 K$ ,  $R = 0.29 \pm 0.01$  km (for a distance  $d = 1$  kpc) and  $N_H = 3.22_{-0.13}^{+0.14} \times 10^{21} \text{ cm}^{-2}$  ( $\chi^2_\nu = 1.21$  for 431 dof). These values are similar to those inferred from Chandra data by Kargaltsev et al. (2002). However, with a more than 3 times improved photon statistic we find that this simple model cannot describe the data beyond  $\sim 3$  keV and hence a single blackbody is not a valid description for the spectrum of CXOU J085201.4-461753. This is in contradiction to the results obtained by Kargaltsev et al. (2002) using Chandra data only.

Adding a second thermal component improves the fit and represents very well the observed spectrum up to  $\sim 7$  keV (see Figure 4.3). This thermal multi-component model yields a parameter set of  $N_H = 3.82_{-0.30}^{+0.36} \times 10^{21} \text{ cm}^{-2}$ ,  $T_1 = (2.98_{-0.47}^{+0.28}) \times 10^6 K$ ,  $R_1 = 0.36_{-0.03}^{+0.05}$  km,  $T_2 = (6.60_{-1.18}^{+3.02}) \times 10^6 K$  and  $R_2 = 59_{-43}^{+64}$  m ( $\chi^2_\nu = 1.08$  for 429 dof).  $R_1$  and  $R_2$  are given for a distance of 1 kpc. The  $F$ -test statistic indicates that the improvement of the goodness-of-fit for adding an extra thermal spectral component is significant at a confidence level of  $\geq 99\%$ . To further constrain the parameter space for this two component thermal model we calculated the  $\chi^2_\nu$  error contours which are shown in Figure 4.4. We would like to point out that the column density derived by us is consistent with the results from the spectral analysis of RX J0822–4300 by Iyudin et al. (2005).

We have also tested whether there is any thermal emission contributed from an emission area compatible with the entire neutron star surface. However, with  $R_1$  fixed to 10 km we

found that the goodness-of-fit decreased significantly to  $\chi^2_\nu = 1.46$  (for 430 dof).

Testing non-thermal emission models shows that a single power law model cannot fit the data ( $\chi^2_\nu = 2.18$  for 431 dof). However, a model combining a blackbody and a power law yields a goodness-of-fit which is comparable with that obtained with the double blackbody model ( $\chi^2_\nu = 1.09$  for 429 dof). The inferred slope of the power law component is  $\Gamma$  is  $4.21^{+0.30}_{-0.59}$ . A similar steep slope has also been observed in the X-ray spectrum of the central compact X-ray source RX J0822-4300 in Puppis-A (Hui & Becker 2006b). We point out that such a steep power law slope, a priori, cannot be considered to be *unphysical* as the nature of the central compact object is still uncertain. Compared with the double blackbody model the column density of the combined blackbody plus power law model,  $N_H = 7.63^{+0.72}_{-1.59} \times 10^{21} \text{ cm}^{-2}$ , is higher. However, we find it still within the limit of the total Galactic neutral hydrogen column density along the direction to CXOU J085201.4-461753 ( $\sim 10^{22} \text{ cm}^{-2}$ ; Dickey & Lockman 1990). The uncertainty in the source distance thus does not support to reject the blackbody plus power law model because of a larger  $N_H$  value.

We have also examined whether a thermal bremsstrahlung model, which physically implies that the central compact object is surrounded by a hot plasma, yields a viable description.  $\chi^2_\nu$  and  $N_H$  resulting from this model are similar to the values inferred from the broken power law and hence cannot be considered as an appropriate description of the source spectrum (c.f. Table 4.3).

From the October 2001 Chandra observation Kargaltsev et al. (2002) reported a marginal detection of a spectral feature at 1.68 keV with a width of  $\sim 100$  eV. The authors found that the shape of this feature is similar to that of an inverse P Cygni profile, suggesting a mass accreting neutron star. However, we have not found any significant feature around 1.68 keV in the spectra obtained by XMM-Newton. Figure 4.3b shows the contribution of the  $\chi^2$  statistics in the  $\sim 1.6 - 1.8$  keV range for the best-fitted double blackbody model. There is no evidence for any systematic residual in this region. In order to quantify this result we have fitted a Gaussian line of width 100 eV at 1.68 keV. A  $3\sigma$  upper limit of such a Gaussian line is  $8.27 \times 10^{-6} \text{ photons cm}^{-2} \text{ s}^{-1}$ , or  $2.23 \times 10^{-14} \text{ erg cm}^{-2} \text{ s}^{-1}$ .

### 4.3.3 Timing Analysis

The May and June 2003 observations were performed with the EPIC-PN camera operated in the small-window mode. The 5.7 ms temporal resolution provided by that mode enables us to search for coherent pulsations in these datasets. For the timing analysis we selected all events within 0.3 – 10 keV from a circle of 25 arcsec centered on the CXOU J085201.4-461753. This yields 15668 and 5974 events. The background contribution in each observation is about 15%.

The barycentric corrections of the arrival times were performed with the XMMSAS task BARYCEN. The position of CXOU J085201.4-461753 measured by Chandra, RA= $8^{\text{h}}52^{\text{m}}01^{\text{s}}.38$  and Dec= $-46^{\circ}17'53''.34$  (J2000), was used for barycentering photon arrival times in both datasets.

A FFT based period search did not reveal any strong signal of pulsed emission. Taking the candidate periods found by Kargaltsev et al. (2002),  $P = 300.8214531$  ms and  $P =$

32.92779028 ms, as initial trials, we carried out a detailed search around these periods by using the  $Z_m^2$  test where  $m$  is the numbers of harmonics included (Buccheri et al. 1983). We did not find any promising signals around these test periods either. A pulsed fraction upper limit  $p$  was computed using the May 2003 data according to

$$n_\sigma = \frac{p \sqrt{N_{tot}}}{\sqrt{p + \frac{d}{1-d} (1-p)}} \quad (4.1)$$

in which  $N_{tot}$  is the total number of detected source counts (12871 cts),  $p$  is the pulsed fraction (fraction between pulsed and total counts) and  $d$  is the duty cycle (fraction between pulsed and total time interval). Assuming a duty cycle of  $d = 0.5$  (sinusoidal modulation) we compute for  $n_\sigma = 3$  a pulsed fraction upper limit of  $p \sim 3\%$ .

## 4.4 Discussion

We have observed the neutron star CXOU J085201.4-461753 in the supernova remnant RX J0852.0-4622 with XMM-Newton. The XMM data have invalidated the interpretation that the nature of the diffuse and extended emission surrounding CXOU J085201.4-461753 is plerionic and powered by the young neutron star. The spectrum of CXOU J085201.4-461753 is best fitted by a double blackbody spectrum or a blackbody plus non-thermal spectral component. The fitted temperatures along with the small size of the emitting regions invalidate the interpretation that the thermal radiation is cooling emission from the entire neutron star surface. If the double black-body model indeed is the right description for the emission scenario of CXOU J085201.4-461753 it points towards emission from a  $\sim (4 - 6.5) \times 10^6$  K hot polar-region on the neutron star surface.

In the literature various models are proposed to produce hot-spots on the neutron star surface. Almost all magnetospheric emission models predict a bombardment of the polar cap regions by energetic particles accelerated in the magnetosphere backwards to the neutron star surface (cf. Cheng, Ho & Ruderman 1982; Harding & Muslimov 2002 and references therein). Though CXOU J085201.4-461753 is not known to be a radio pulsar it still could be possible that the hot polar caps are heated by particle bombardment while the radio emission itself is undetected due to an unfavorable beaming geometry. This is not an unlikely scenario. The opening angle of a radio beam is inversely proportional to the square-root of the pulsar's rotation period so that the radio beams of slow rotating pulsars can easily miss the observers line of sight and thus keep undetected.

The heat transport in neutron stars is accomplished by electrons. A strong magnetic field thus is expected to have an essential impact on the neutron star cooling as it channels the heat along the magnetic field lines and suppresses it perpendicular to it. Neutron star cooling with a full treatment of the strong magnetic field thus should lead to an anisotropic heat flow and subsequently to an anisotropic surface temperature distribution, with the polar-cap regions getting hotter than the surface temperature of the equatorial regions. This scenario has been modeled recently by Geppert et al. (2004; 2006).

## 66 4. XMM-Newton Observations of the Compact Object in RX J0852.0-4622

---

Independent of these scenarios there exists the possibility that CXOU J085201.4-461753 is accreting from fall-back matter or a residual disk and that the accreting matter causes the hot-spots on the surface.

The low pulsed fraction upper limit is not in disagreement with any of these scenarios. When general relativistic effects are taken into account (Page 1995; Hui & Cheng 2004), pulsations are found to be strongly suppressed and the pulsed fraction is highly dependent on the mass to radius ratio of the star, the orientation of the hot spot and the viewing angle geometry. This is due to the fact that the gravitational bending of light will make more than half of the stellar surface become visible at any instant and hence the contribution of the hot spot will be strongly reduced. If the orientation of the hot spot differs from that of an orthogonal rotator and/or the star has a high mass to radius ratio, then very low amplitude pulsations are expected.

Anyway, future data to be taken in forthcoming observations will further explore the emission models and hopefully detect the neutron star's rotation period.



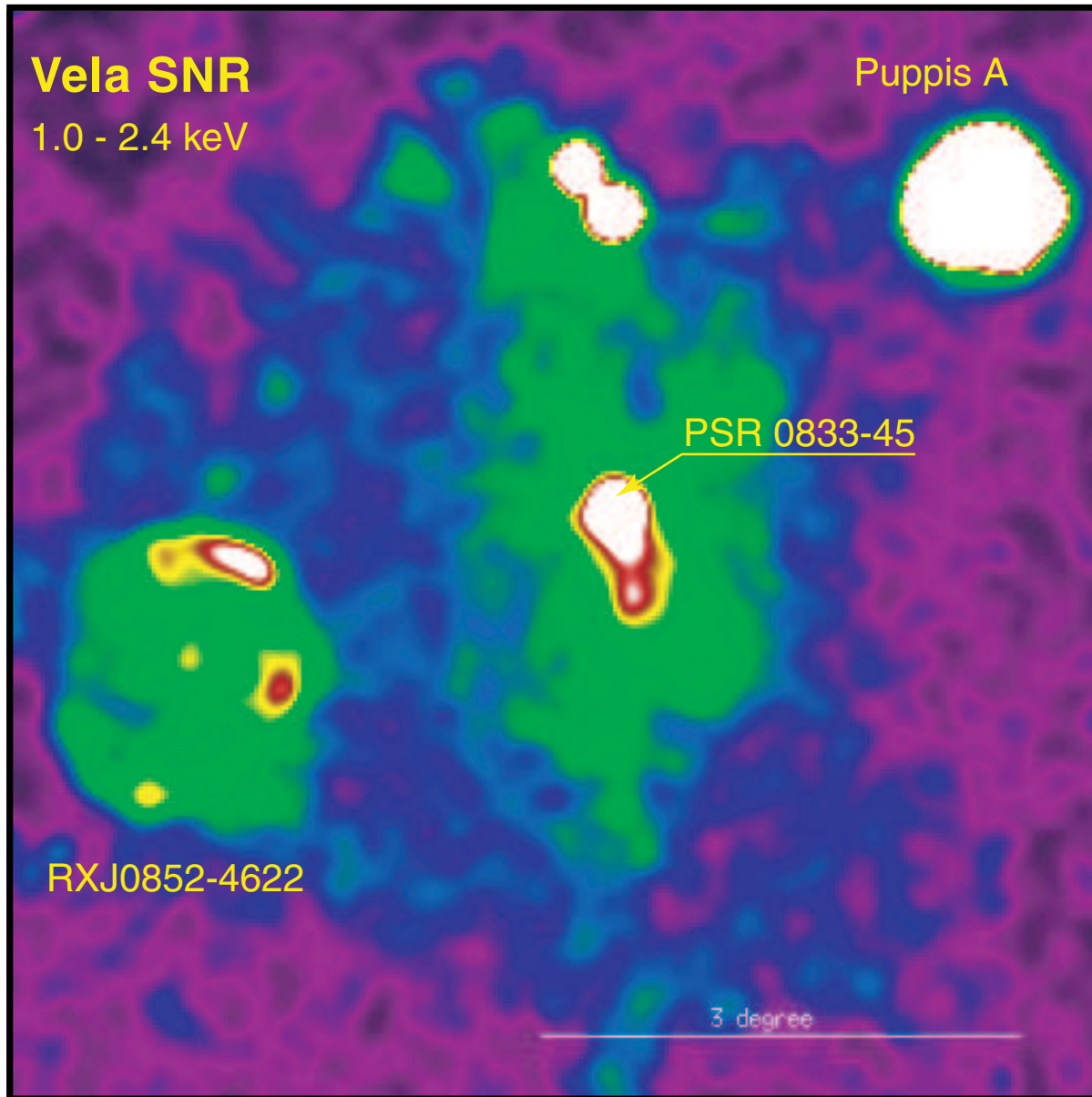


Figure 4.1: *Vela and friends*: The two supernova remnants Puppis-A and RX J0852.0-4622 are both located at the edge of the Vela supernova remnant. Emission from the central compact source CXOU J085201.4-461753 is clearly visible in the ROSAT all-sky survey image near to the center of RX J0852.0-4622.

Table 4.1: Details of XMM-Newton observations of CXOU J085201.4-461753. In the April 2001 observation CXOU J085201.4-461753 got placed right on a PN CCD gap. We therefore don't give a counting rate.

Detector	Instrument Mode	Filter	Start Date	Effective Exposure	Net Rate (cts s <sup>-1</sup> )
<b>Obs. ID: 0112870601</b>					
MOS1	Full Frame	Medium	2001-04-27	8 ksec	0.146 ± 0.004
MOS2	Full Frame	Medium	2001-04-27	8 ksec	0.149 ± 0.004
PN	Extended Full Frame	Medium	2001-04-27	6 ksec	
<b>Obs. ID: 0147750101</b>					
MOS1	Full Frame	Medium	2003-05-21	38 ksec	0.155 ± 0.002
MOS2	Full Frame	Medium	2003-05-21	38 ksec	0.156 ± 0.002
PN	Small Window	Thin	2003-05-21	25 ksec	0.477 ± 0.005
<b>Obs. ID: 0147750201</b>					
MOS1	Full Frame	Medium	2003-06-25	12 ksec	0.156 ± 0.004
MOS2	Full Frame	Medium	2003-06-25	12 ksec	0.154 ± 0.004
PN	Small Window	Thin	2003-06-25	8 ksec	0.472 ± 0.008

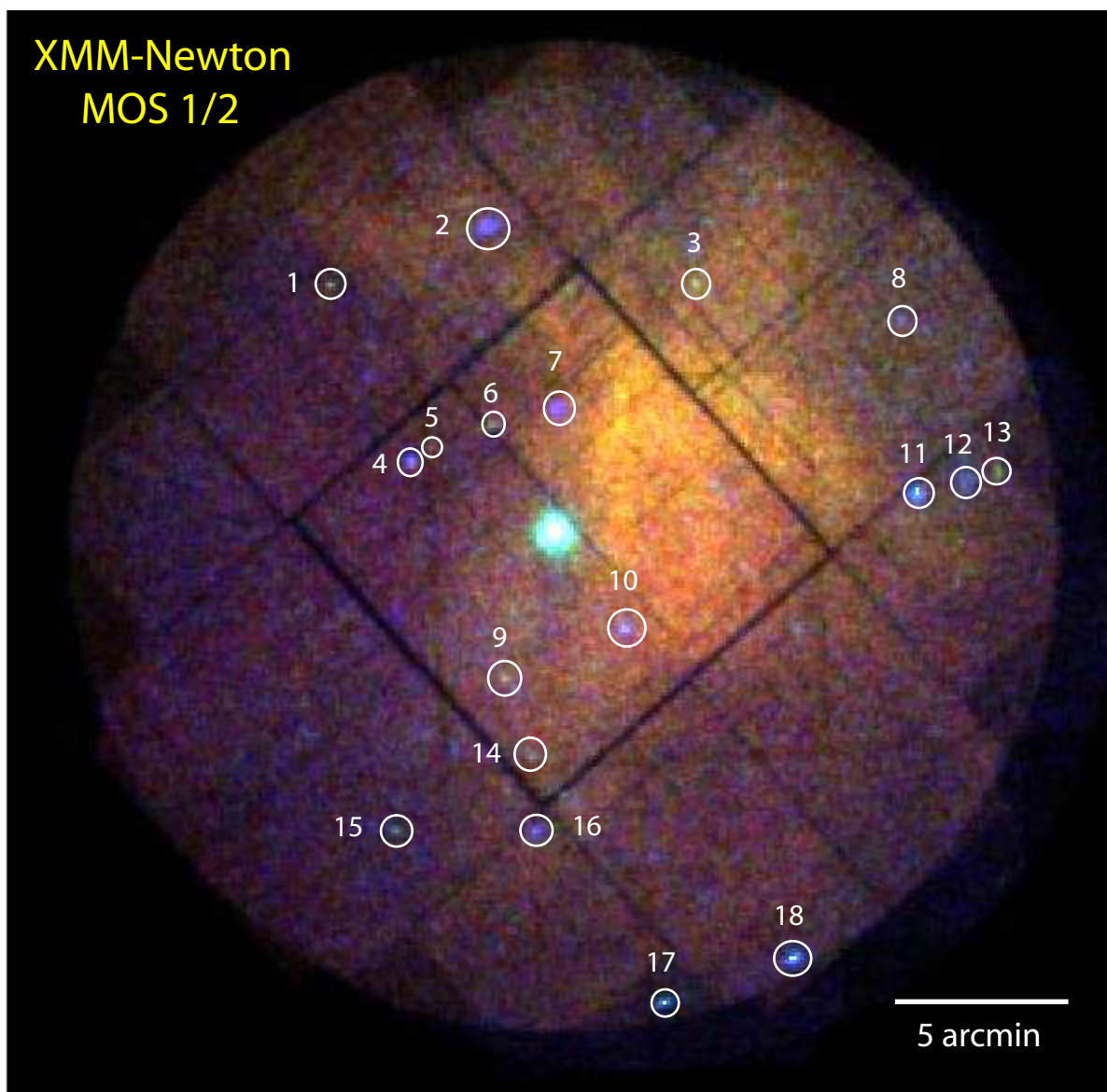


Figure 4.2: XMM-Newton MOS1/2 false color image of the inner 30 arcmin central region of RX J0852.0-4622 (red: 0.3 – 0.75 keV; green: 0.75 – 2 keV and blue: 2 – 10 keV). The central bright source is CXOU J085201.4-461753. 18 other point-like sources, marked by circles, are detected in the field of view (cf. Table 4.2). The binning factor of this image is 4 arcsec.

## 70 4. XMM-Newton Observations of the Compact Object in RX J0852.0-4622

Table 4.2: Faint X-ray sources detected serendipitously within RX J0852.0-4622.

Source	RA (J2000)	Dec (J2000)	$\delta$ RA	$\delta$ Dec
	h:m:s	d:m:s	arcsec	arcsec
1	08:52:39.037	-46:10:50.08	0.45	0.31
2	08:52:12.931	-46:09:06.68	0.37	0.25
3	08:51:38.185	-46:10:46.41	0.38	0.26
4	08:52:25.433	-46:15:57.23	0.45	0.32
5	08:52:22.510	-46:15:28.37	0.50	0.48
6	08:52:11.708	-46:14:46.48	0.40	0.28
7	08:52:01.231	-46:14:18.78	0.31	0.21
8	08:51:04.275	-46:11:53.72	0.45	0.32
9	08:52:09.804	-46:22:04.49	0.38	0.26
10	08:51:49.975	-46:20:41.32	0.35	0.24
11	08:51:01.452	-46:16:47.83	0.30	0.23
12	08:50:53.378	-46:16:21.35	0.48	0.32
13	08:50:47.810	-46:16:09.15	0.45	0.33
14	08:52:04.977	-46:24:20.52	0.44	0.30
15	08:52:27.994	-46:26:25.81	0.78	0.28
16	08:52:04.651	-46:26:28.66	0.49	0.33
17	08:51:43.459	-46:31:22.22	0.50	0.28
18	08:51:22.030	-46:30:08.20	0.39	0.25

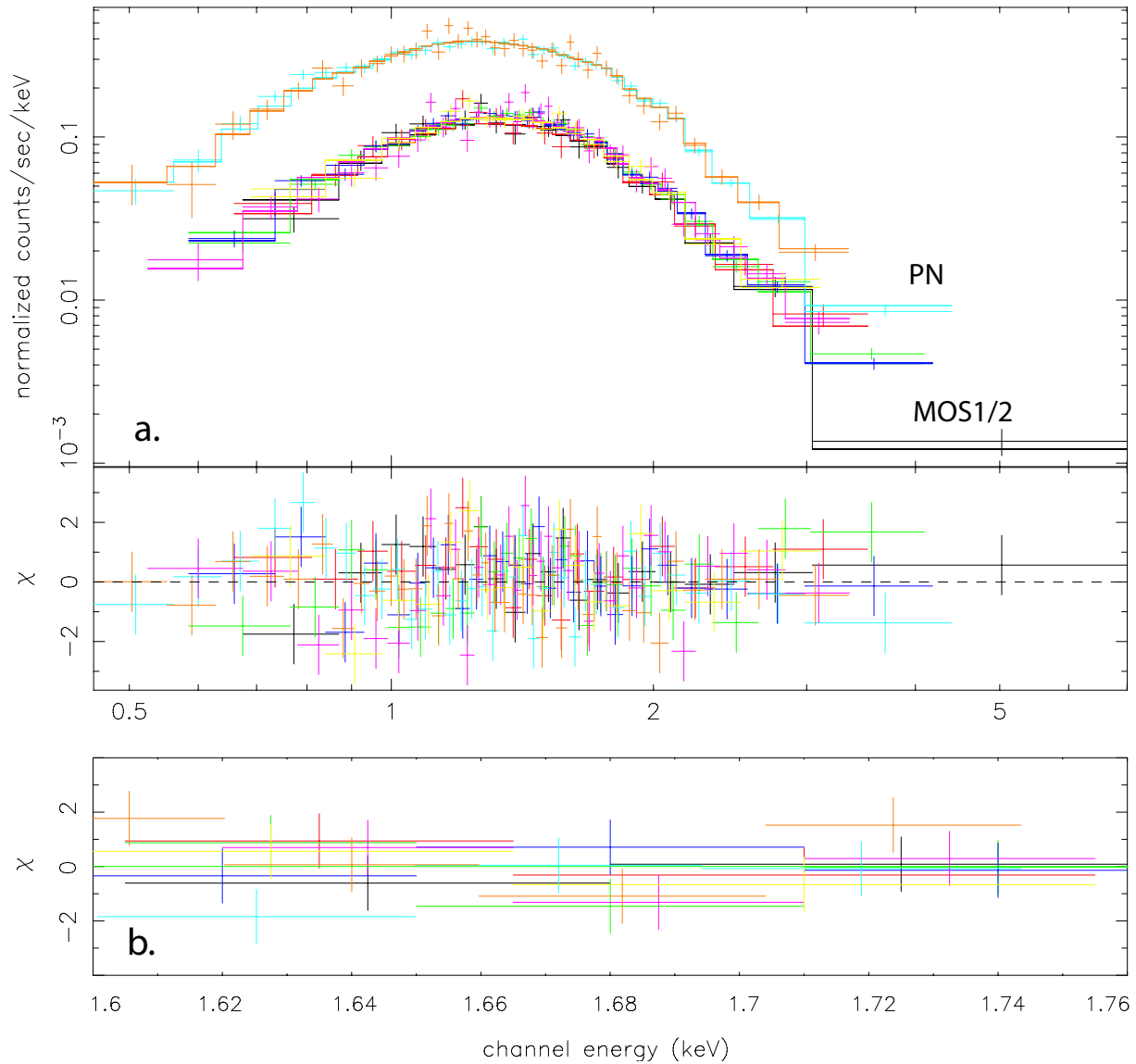


Figure 4.3: **a.** Energy spectra of CXOU J085201.4-461753 observed with the EPIC-PN (upper spectra) and the MOS1/2 detectors (lower spectra) with the best-fitting absorbed two component blackbody model (*upper panel*), and the contribution to the  $\chi^2$  fit statistic (*lower panel*). **b.** Details of the  $\chi^2$  fit distribution of the absorbed two component blackbody model in the  $\sim 1.6 - 1.8$  keV energy range. No line feature is indicated in the fit residuals.

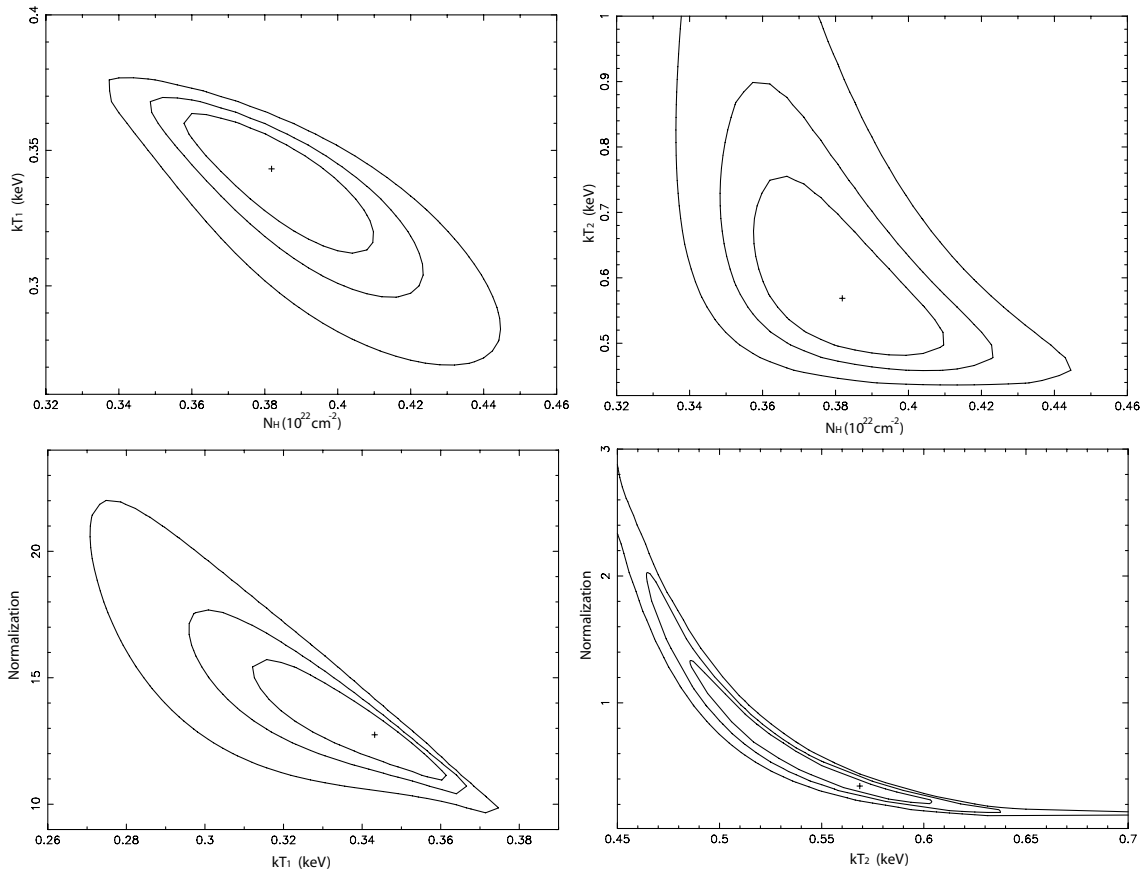


Figure 4.4:  $1\sigma$ ,  $2\sigma$  and  $3\sigma$  confidence contours for the double blackbody fit to the X-ray spectrum of CXOU J085201.4-461753.

Parameter	BB	BB+BB	BB+BB (fix $R_1$ at 10 km)	PL	BB+PL	BKPL	BREMSS
$N_H$ ( $10^{21} \text{ cm}^{-2}$ )	$3.215^{+0.135}_{-0.132}$	$3.819^{+0.356}_{-0.295}$	$9.212^{+0.313}_{-0.553}$	10.994	$7.633^{+0.718}_{-1.594}$	$7.422^{+0.421}_{-0.519}$	$6.821^{+0.146}_{-0.156}$
$\Gamma_1$	-	-	-	4.407	$4.208^{+0.298}_{-0.590}$	$3.050^{+0.170}_{-0.213}$	-
$\Gamma_2$	-	-	-	-	-	$5.139^{+0.238}_{-0.188}$	-
$T_1$ ( $10^6 \text{ K}$ )	$4.533^{+0.048}_{-0.049}$	$3.983^{+0.281}_{-0.466}$	$1.358^{+0.022}_{-0.042}$	-	$4.248^{+0.114}_{-0.147}$	-	$9.874^{+0.201}_{-0.178}$
$T_2$ ( $10^6 \text{ K}$ )	-	$6.599^{+3.023}_{-1.177}$	$4.171^{+0.054}_{-0.066}$	-	-	-	-
$R_1$ (km)	$0.285^{+0.009}_{-0.008}$	$0.357^{+0.052}_{-0.034}$	10	-	$0.300^{+0.034}_{-0.021}$	-	-
$R_2$ (km)	-	$0.059^{+0.064}_{-0.043}$	$0.408^{+0.018}_{-0.014}$	-	-	-	-
$F_{X_{0.5-10\text{keV}}}$ ( $\text{ergs cm}^{-2} \text{ s}^{-1}$ )	$1.905 \times 10^{-12}$	$2.113 \times 10^{-12}$	$9.916 \times 10^{-12}$	$1.720 \times 10^{-11}$	$6.324 \times 10^{-12}$	$5.426 \times 10^{-12}$	$4.162 \times 10^{-12}$
Reduced $\chi^2$	1.208	1.083	1.460	2.177	1.094	1.200	1.207
D.O.F	431	429	430	431	429	429	431

Table 4.3: Spectral model parameters of CXOU J085201.4-461753 derived from XMM-Newton data; models: blackbody (BB), two blackbodies (BB+BB), power law (PL), blackbody plus power law (BB+PL), broken power law (BKPL), bremsstrahlung (BREMSS).

#### 74 4. XMM-Newton Observations of the Compact Object in RX J0852.0-4622



# Chapter 5

## Radio and X-ray Nebulae associated with PSR J1509-5850

This chapter is adopted from the refereed paper entitled “Radio and X-ray Nebulae associated with PSR J1509-5850” published in *Astronomy & Astrophysics* (Hui & Becker 2007b)

### 5.1 Introduction

It is generally believed that a significant fraction of the rotational energy of a pulsar leaves the magnetosphere in the form of a magnetized pulsar wind consisting of electromagnetic radiation and high energy particles. In view of this, it is energetically important to study the physical properties of this wind. When the relativistic wind particles interact with the shocked interstellar medium, the charged particles will be accelerated in the shock and hence synchrotron radiation from radio to X-ray is generated. In order to obtain a better understanding of the interaction nature, multiwavelength studies of the pulsar wind nebulae are deeply needed. X-ray and radio observations have recently revealed a number of pulsar wind nebulae. However, there is only a handful of shocked emission detected in both the X-ray and radio regimes (c.f. see Hui & Becker 2006a and references therein).

PSR J1509–5850 was discovered by Manchester et al. (2001) in the Parkes Multibeam Pulsar Survey. The pulsar has a rotation period of  $P = 88.9$  ms and a period derivative of  $\dot{P} = 9.17 \times 10^{-15}$  s s<sup>-1</sup>. These spin parameters imply a characteristic age of  $1.54 \times 10^5$  yrs, a dipole surface magnetic field of  $B_{\perp} = 9.14 \times 10^{11}$  G and a spin-down luminosity of  $5.1 \times 10^{35}$  ergs s<sup>-1</sup> (c.f. Table 5.1). The radio dispersion measure yields a distance of about 3.81 kpc based on the galactic free electron model of Taylor & Cordes (1993). Using the model of Cordes & Lazio (2002) the dispersion measure based distance is estimated to be 2.56 kpc. The proper motion of this pulsar is not yet known. Recently, a brief X-ray study of the field of PSR J1509–5850 was presented by Kargaltsev et al. (2006). The authors have reported that a trail-like pulsar wind nebula associated with PSR J1509–5850 was observed in a Chandra observation. The X-ray nebula is found to be extended in the

south-west direction.

In this chapter, we report on the discovery of a possible radio counterpart of the X-ray trail associated with PSR J1509–5850 and provide a detailed X-ray analysis of the trail. In section 5.2 we describe the observations and the data analysis and in section 5.3 we summarize and discuss our results.

## 5.2 Observations and data analysis

PSR J1509–5850 was observed with Chandra in 2003 February 9–10 (Obs ID: 3513) with the Advanced CCD Imaging Spectrometer (ACIS). The pulsar is located on the back-illuminated (BI) ACIS-S3 chip which has a superior quantum efficiency among the spectroscopic array. Standard processed level-2 data were used. The effective exposure is about 40 ks.

Chandra observation has revealed an X-ray trail associated with PSR J1509–5850. The X-ray image of the  $4 \times 4$  arcmin field near to PSR J1509–5850 is shown in Figure 5.1. The binning factor of the image is 0.5 arcsec. Adaptive smoothing with a Gaussian kernel of  $\sigma < 3$  arcsec has been applied to the image. The trail appears to have a length of  $\sim 2$  arcmin. From a Digitized Sky Survey (DSS) image, 25 bright field stars are found in the field of view of Figure 5.1. We subsequently identified the magnitudes of these stars from the USNO-A2.0 catalog (Monet et al. 1998), which are within the range of  $B \sim 10 - 18$ . Their positions are plotted as white circles in Figure 5.1.

For the spectral analysis, we extracted the spectrum of PSR J1509–5850 from a circle of 4 arcsec radius (encircled energy  $\sim 99\%$ ) centered on the pulsar position. To minimize the possible contamination from the field stars, the spectrum from the trail was extracted within a box of  $25 \times 95$  arcsec, oriented along the direction of the trail emission. Even with this consideration, there are still two stars with magnitude  $B = 17$  and  $B = 16.4$  located on the trail (cf. Fig. 5.1) and unavoidably lie in the extraction region. Without the knowledge of the extinctions, we are not able to estimate the possible contribution in X-ray from these two stars. The background spectra were extracted from the low count regions nearby. After background subtraction, there are  $\sim 100$  net counts and  $\sim 270$  net counts extracted from the pulsar and the trail in 0.3 – 8 keV respectively. Response files were computed by using the CIAO tools MKRMF and MKARF. The spectra were dynamically binned so as to have at least 10 counts per bin for the pulsar and 30 counts per bin for the trail. All the spectral fitting were performed in the energy range of 0.3 – 8 keV by using XSPEC 11.3.1. The degradation of the ACIS quantum efficiency was corrected by XSPEC model ACISABS. All the quoted errors are  $1 - \sigma$  and were computed for 1 parameter in interest.

For the X-ray emission from PSR J1509–5850, we found that it can be modeled with an absorbed power-law fairly well ( $\chi_\nu = 0.68$  for 8 D.O.F.). This model yields a column density of  $N_H = 8.0^{+2.3}_{-2.1} \times 10^{21} \text{ cm}^{-2}$ , a photon index of  $\Gamma = 1.0^{+0.2}_{-0.3}$  and a normalization at 1 keV of  $5.1^{+1.3}_{-1.6} \times 10^{-6} \text{ photons keV}^{-1} \text{ cm}^{-2} \text{ s}^{-1}$ . The best-fitted model results in an unabsorbed flux of  $f_X = 5.9 \times 10^{-14} \text{ ergs cm}^{-2} \text{ s}^{-1}$  in the energy range of 0.5 – 8 keV. The dispersion based

distance implies a luminosity of  $L_X = 4.8 \times 10^{31}$  and  $1.0 \times 10^{32}$  erg s<sup>-1</sup> for  $d=2.6$  and  $3.8$  kpc respectively. Although a blackbody model can give a compatible goodness-of-fit ( $\chi_\nu = 0.82$  for 8 D.O.F.), it infers a rather high temperature ( $T \sim 1.7 \times 10^7$  K) and a small projected blackbody radius ( $R \sim 10$  m). We hence regard this model as not physically reasonable to describe the X-ray spectrum of PSR J1509–5850. We note that the characteristic age indicates that PSR J1509–5850 belongs to the class of middle-aged pulsars. Their spectra typically consist of a soft thermal component, a harder thermal component from the heated polar caps as well as contribution from the non-thermal emission (cf. Becker & Aschenbach 2002). However, the small number of collected photons and the high column density does not support any fitting with multicomponent models.

We have tested the hypothesis that the trail emission is originated from the interaction of pulsar wind and ISM by fitting an absorbed power-law model to the trail spectrum. The model yields an acceptable goodness-of-fit ( $\chi_\nu = 0.73$  for 9 D.O.F.). The best fitting spectral model is displayed in Figure 5.2. This model yield a column density of  $N_H = 8.2_{-3.7}^{+9.3} \times 10^{21}$  cm<sup>-2</sup>, a photon index of  $\Gamma = 1.3_{-0.4}^{+0.8}$  and a normalization at 1 keV of  $1.9_{-1.9}^{+4.3} \times 10^{-5}$  photons keV<sup>-1</sup> cm<sup>-2</sup> s<sup>-1</sup>. We note that the column density agrees with that inferred from the pulsar spectrum. The unabsorbed flux deduced for the best-fitted model parameters are  $f_X = 1.6 \times 10^{-13}$  erg s<sup>-1</sup> cm<sup>-2</sup> in the energy range of 0.5 – 8 keV. The dispersion based distance implies a luminosity of  $L_X = 1.3 \times 10^{32}$  and  $2.7 \times 10^{32}$  erg s<sup>-1</sup> for  $d=2.6$  and  $3.8$  kpc, respectively.

We have searched for a possible radio counterpart for the X-ray nebula with the Sydney University Molonglo Sky Survey data (SUMSS) (Bock et al. 1999). We have discovered a long radio trail apparently associated with PSR J1509–5850. The radio image of the  $11 \times 11$  arcmin field near to PSR J1509–5850 is displayed in Figure 5.3. The radio feature has a length of  $\sim 7$  arcmin. Radio contours were calculated at the levels of 7, 23, 39, 54 and 70 mJy/beam. These contours were overlaid on the image of the Chandra ACIS-S3 chip in Figure 5.4. It is interesting to note that the radio trail starts exactly from the position of PSR J1509–5850 and has the same orientation as that of the X-ray trail. These facts support the interpretation that this extended radio feature is the radio counterpart of the X-ray trail and is indeed physically associated with PSR J1509–5850.

There are two clumpy structures observed along the radio trail (see Figure 5.3). The northern clump has its emission center at RA=15<sup>h</sup> 09<sup>m</sup> 14.35<sup>s</sup>, Dec=-58° 54′ 50.7″ (J2000) with a radius of  $\sim 1.5$  arcmin. The southern clump has its emission center at RA=15<sup>h</sup>09<sup>m</sup>06.33<sup>s</sup>, Dec=-58° 58′ 34.7″ (J2000) with a radius of  $\sim 1$  arcmin. While the southern clump is unidentified in SIMBAD and NED, the northern clump, which locates  $\sim 4$  arcmin away from PSR J1509–5850, has been proposed to be a supernova remnant candidate MSC 319.9-0.7 (Whiteoak & Green 1996). Comparing the X-ray and the radio data in Figure 5.4, we found that there is some faint X-ray emission near to the location of MSC 319.9-0.7. The emission does not appear to be the continuation of the trail associated with PSR J1509–5850. It cannot be excluded that this faint emission is related to MSC 319.9-0.7. However, the limited photon statistics does not allow any final conclusion.

### 5.3 Discussion & Conclusion

In this chapter, we report the detection of a possible radio counterpart of the X-ray trail associated with PSR J1509–5850 and present a first detailed X-ray study of the X-ray trail. Apart from the radio trail, we have found that there are two clumpy structures located on the trail. While the smaller one is still unidentified, the larger one, which is located  $\sim 4$  arcmin away from PSR J1509–5850, is identified as a SNR candidate MSC 319.9-0.7.

Despite the proximity of MSC 319.9-0.7, it seems unlikely that it is the birth place of PSR J1509–5850. Assuming this shell-like SNR candidate is in a Sedov phase, the radius of the shocked shell emission can be estimated by (Culhane 1977):

$$R_s = 2.15 \times 10^{-11} \left( \frac{E}{n} \right)^{\frac{1}{5}} t^{\frac{2}{5}} \text{pc} \quad (5.1)$$

where  $t$ ,  $E$  and  $n$  are the time after the explosion in units of years, the released kinetic energy in units of ergs and the ISM number density in units of  $\text{cm}^{-3}$  respectively. Taking the typical values of  $E = 10^{51}$  ergs and  $n = 1 \text{ cm}^{-3}$  and  $t$  to be the characteristic age of PSR J1509–5850, we estimate that a SNR associated with PSR J1509–5850 should have a radius of  $R_s \sim 40$  pc. However, MSC 319.9-0.7 only has a radius of  $\sim 1.1 - 1.7$  pc for  $d = 2.6 - 3.8$  kpc. Thus, the discrepancy between the expected  $R_s$  and the observed value which with a factor of  $\sim 30$  is not likely to be reconciled by the uncertainty of the dispersion based distance. On the other hand, the characteristic age of the pulsar can be older than its actual age if its initial spin period was close to its current period. However, to reconcile such discrepancy would require  $t$  to be smaller by a factor of  $\sim 4000$  which is not likely. Moreover, associating MSC 319.9-0.7 with PSR J1509–5850 would leave the origin of the southern part of the radio trail unexplained. Thus, with the current knowledge of parameters it seems most reasonable for us to interpret MSC 319.9-0.7 as a background source.

Following the discussion in Hui & Becker (2006a), we apply a simple one zone model (Chevalier 2000; Cheng, Tamm, & Wang 2004) to model the X-ray emission properties of the pulsar wind nebula. Since the proper motion of PSR J1509–5850 is not yet known, we assume the pulsar is in supersonic motion on the basis that the nebula resembles a bow-shock morphology. For the supersonic motion, the termination shock radius  $R_{ts}$  is determined by the balance of the ram pressure between the relativistic pulsar wind particles and the ISM at the head of the shock (cf. Cheng et al. 2004):

$$R_{ts} \simeq \left( \frac{\dot{E}}{2\pi\rho_{ISM}v_p^2c} \right)^{1/2} \sim 3 \times 10^{16} \dot{E}_{34}^{1/2} n^{-1/2} v_{p,100}^{-1} \text{cm} \quad (5.2)$$

where  $v_{p,100}$  is the velocity of the pulsar in units of  $100 \text{ km s}^{-1}$ ,  $\dot{E}_{34}$  is the spin-down luminosity of the pulsar in units of  $10^{34} \text{ erg s}^{-1}$ , and  $n$  is the number density of the ISM in units of  $\text{cm}^{-3}$ . In all the following estimation, we assume PSR J1509–5850 has a transverse velocity comparable to the average velocity,  $\sim 250 \text{ km s}^{-1}$ , of ordinary radio pulsars (Hobbs

et al. 2005). For a ISM density of  $1 \text{ cm}^{-3}$ , equation 5.2 implies a termination radius of  $R_{ts} \sim 8.6 \times 10^{16} \text{ cm}$ .

The X-ray trail is found to be  $\sim 2$  arcmin long. For the dispersion based distance in the range of  $\sim 2.6 - 3.8$  kpc, the trail has a length of  $l \sim (4.7 - 6.8) \times 10^{18} \text{ cm}$ . For the assumed pulsar velocity of  $\sim 250 \text{ km s}^{-1}$ , the timescale for the passage of the pulsar over the length of its X-ray trail,  $t_{\text{flow}}$ , is estimated to be  $\sim 6000 - 8600$  years. The magnetic field in the shocked region can be estimated by assuming  $t_{\text{flow}}$  to be comparable to the synchrotron cooling timescale of electrons:

$$\tau_{\text{syn}} = \frac{6\pi m_e c}{\gamma \sigma_T B^2} \simeq 10^5 \left( \frac{h\nu}{\text{keV}} \right)^{-\frac{1}{2}} B_{\mu G}^{-\frac{3}{2}} \text{yrs} \quad (5.3)$$

where  $\gamma$  is the Lorentz factor of the wind, taken to be  $10^6$  (cf. Cheng et al. 2004),  $\sigma_T$  is the Thompson cross section, and  $B_{\mu G}$  is the magnetic field in the shocked region in unit of micro gauss. The inferred magnetic field in the shocked region is  $\sim 5 - 7 \mu G$ . For comparison, the magnetic field strength in the ISM is estimated to be  $\sim 2 - 6 \mu G$  (cf. Beck et al. 2003, and references therein).

The X-ray luminosity and spectral index depend on the inequality between the characteristic observed frequency  $\nu_X^{\text{obs}}$  and the electron synchrotron cooling frequency  $\nu_c$  (see Chevalier 2000 and references therein):

$$\nu_c = \frac{18\pi e m_e c}{\sigma_T^2 \tau_{\text{syn}}^2 B^3} \quad (5.4)$$

which is estimated to be  $\nu_c = (1.3 - 1.8) \times 10^{17} \text{ Hz}$ . Since in general  $\nu_X^{\text{obs}} > \nu_c$ , this suggests the X-ray emission is in a fast cooling regime. Electrons with the energy distribution,  $N(\gamma) \propto \gamma^{-p}$ , are able to radiate their energy in the trail with photon index  $\alpha = (p + 2)/2$ . The index  $p$  due to shock acceleration typically lies between 2 and 3 (cf. Cheng et al. 2004 and reference therein). This would result in a photon index  $\alpha \simeq 2.0 - 2.5$ . In view of the large error of the observed photon index  $\Gamma = 1.3_{-0.4}^{+0.8}$ , we cannot firmly conclude the emission scenario simply based on the photon index. We note that the photon index can still be possibly in the fast cooling regime within the  $1\sigma$  uncertainty. With this consideration and  $\nu_X^{\text{obs}} > \nu_c$ , we adopted the fast cooling scenario in the following discussion. With the assumed value  $p = 2.2$ , the calculated photon index  $\alpha = 2.1$  which is marginally within the  $1\sigma$  uncertainty of the observed value.

In a fast cooling regime, the luminosity per unit frequency is given by (cf. Cheng et al. 2004):

$$L_\nu = \frac{1}{2} \left( \frac{p-2}{p-1} \right)^{p-1} \left( \frac{6e^2}{4\pi^2 m_e c^3} \right)^{\frac{p-2}{4}} \epsilon_e^{p-1} \epsilon_B^{\frac{p-2}{4}} \gamma^{p-2} R_{ts}^{-\frac{p-2}{2}} \dot{E}^{\frac{p+2}{4}} \nu^{-\frac{p}{2}} \quad (5.5)$$

Assuming the energy equipartition between the electron and proton, we take the fractional energy density of electron  $\epsilon_e$  to be  $\sim 0.5$  and the fractional energy density of the magnetic field  $\epsilon_B$  to be  $\sim 0.01$ . We integrate equation 5.5 from 0.5 keV to 8 keV and result

in a calculated luminosity of  $\sim 6 \times 10^{32}$  ergs  $s^{-1}$ . With the reasonable choice of parameters stated above, the luminosity estimated by this simple model is found to be the same order as the observed value.

It is obvious that the radio nebula is significantly longer than its X-ray counterpart (cf. Fig. 5.4). This is not unexpected. Considering a scenario of constant injection of particles with a finite synchrotron cooling time, the number of particles that can reach at a further distance from the pulsar should decrease with increasing frequency. This is because the synchrotron cooling timescale decrease with frequency. This would result in a fact that the synchrotron nebular size decreases with frequency.

To further constrain the physical properties of the pulsar wind nebula associated with PSR J1509–5850, multi-wavelength observations are badly needed. Since SUMSS data have a rather poor spatial resolution which has a typical beam size of  $\sim 45$  arcsec, there might be details of the nebular emission remain unresolved. In particular, it is important to better resolve the nebular emission from the contribution of the SNR candidate MSC 319.9-0.7. In view of this, high resolution radio observations (e.g. ATCA) are required. In the X-ray regime, although the Chandra observation has already provided us with a high resolution image of the nebula, the photon statistics is not sufficient to tightly constrain the spectral properties. Owing to the superior collecting power, observations with XMM-Newton are expected to put a strict constraint on the emission nature of the nebula as well as the pulsar itself.

Apart from the radio and X-ray observations, a complete study of pulsar wind nebula should also include TeV observations (e.g. HESS). It is generally believed that the TeV photons are resulted from inverse Compton scattering of soft photon field by the relativistic particles in the nebulae. The seed soft photons are possibly contributed by the cosmic microwave background (Cui 2006). However, there is only a handful of pulsar wind nebulae detected in TeV regime so far (see Cui 2006), a larger sample is needed for differentiating the aforementioned interpretation from its competing scenario (e.g. neutral pion decay).

From the above discussion, one should note that the pulsar's transverse velocity is an important parameter in studying the shock physics. And hence measuring the proper motion of PSR J1509–5850 is badly needed. Moreover, although the orientation of the trail suggests PSR J1509–5850 is likely moving in the direction of northeast, it is not necessary for the trail to be aligned with the pulsar velocity. PSRs J2124-3358 and B2224+65 are the examples that the X-ray trails are misaligned with the direction of the pulsars' proper motion (Hui & Becker 2006a, 2007a).

Table 5.1: Pulsar parameters of PSR J1509–5850 (from Manchester et al. 2005)

Right Ascension (J2000)	15 <sup>h</sup> 09 <sup>m</sup> 27.13 <sup>s</sup>
Declination (J2000)	−58° 50′ 56.1″
Pulsar Period, $P$ (s)	0.088921760489
Period derivative $\dot{P}$ ( $10^{-15}$ s s <sup>−1</sup> )	9.1698
Age ( $10^5$ yrs)	1.54
Surface dipole magnetic field ( $10^{12}$ G)	0.914
Epoch of Period (MJD)	51463
Dispersion Measure (pc cm <sup>−3</sup> )	137.7
Dispersion based distance (kpc)	~ 2.6 – 3.8
Spin-down Luminosity ( $10^{35}$ ergs s <sup>−1</sup> )	5.1

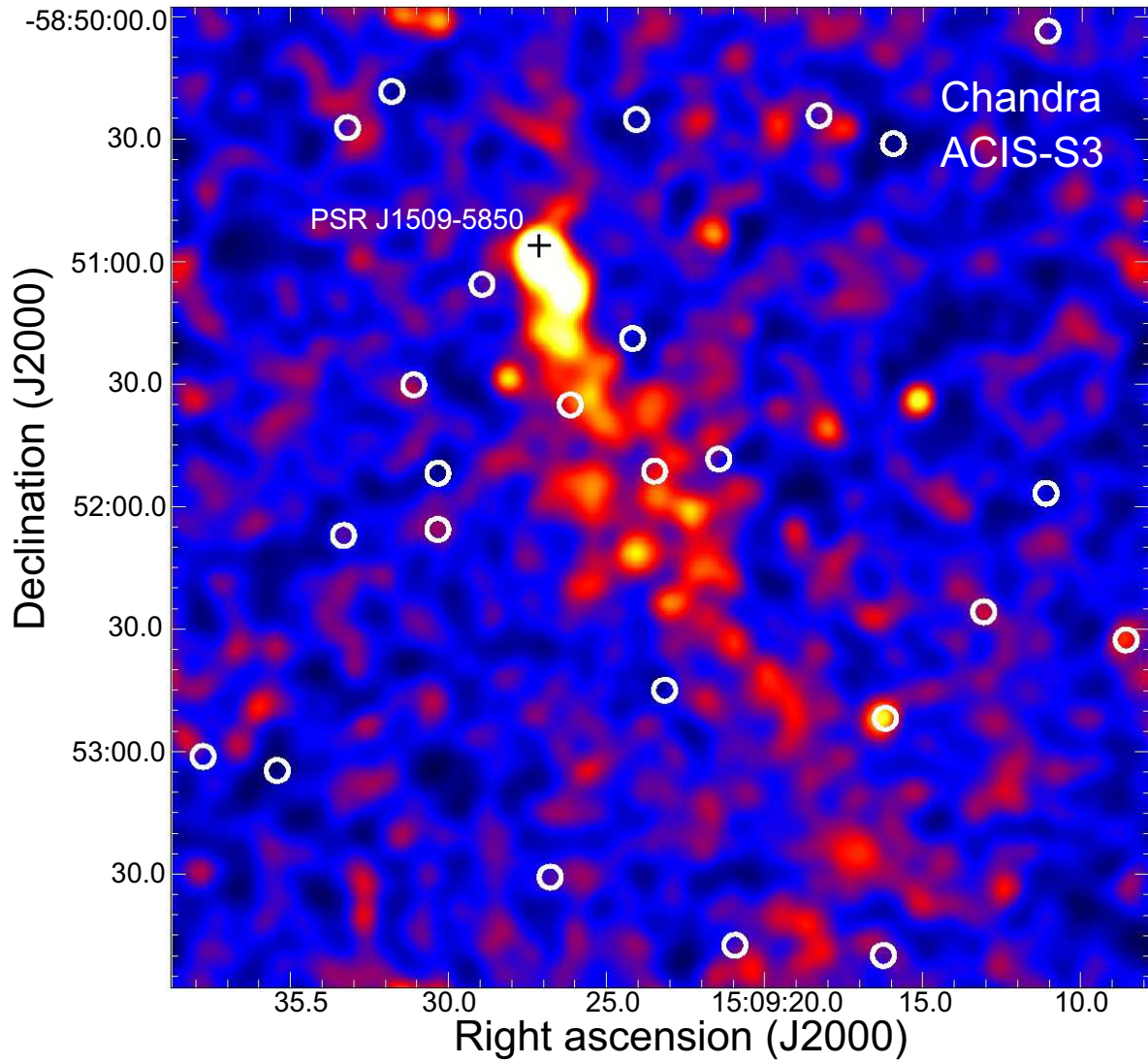


Figure 5.1: Chandra’s  $4 \times 4$  arcmin view of PSR J1509–5850 and its X-ray trail in the energy band 0.3–8 keV. The pulsar position is indicated by the black cross. The white circles indicate the positions of field stars identified in the DSS image.



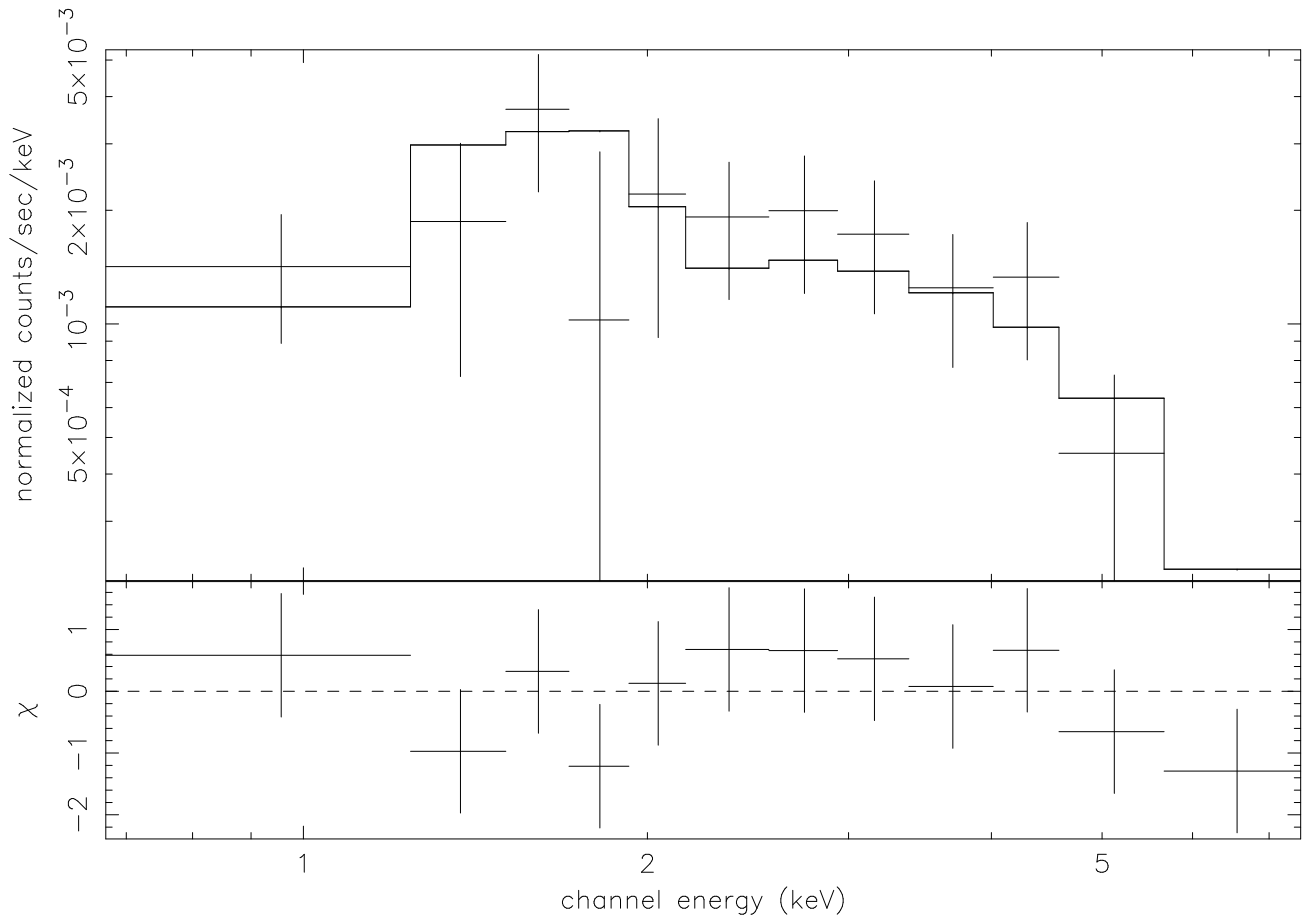


Figure 5.2: Energy spectrum of the X-ray trail of PSR J1509–5850 as observed with the Chandra ACIS-S3 detector and fitted to an absorbed power-law model (*upper panel*) and contribution to the  $\chi^2$  fit statistic (*lower panel*).

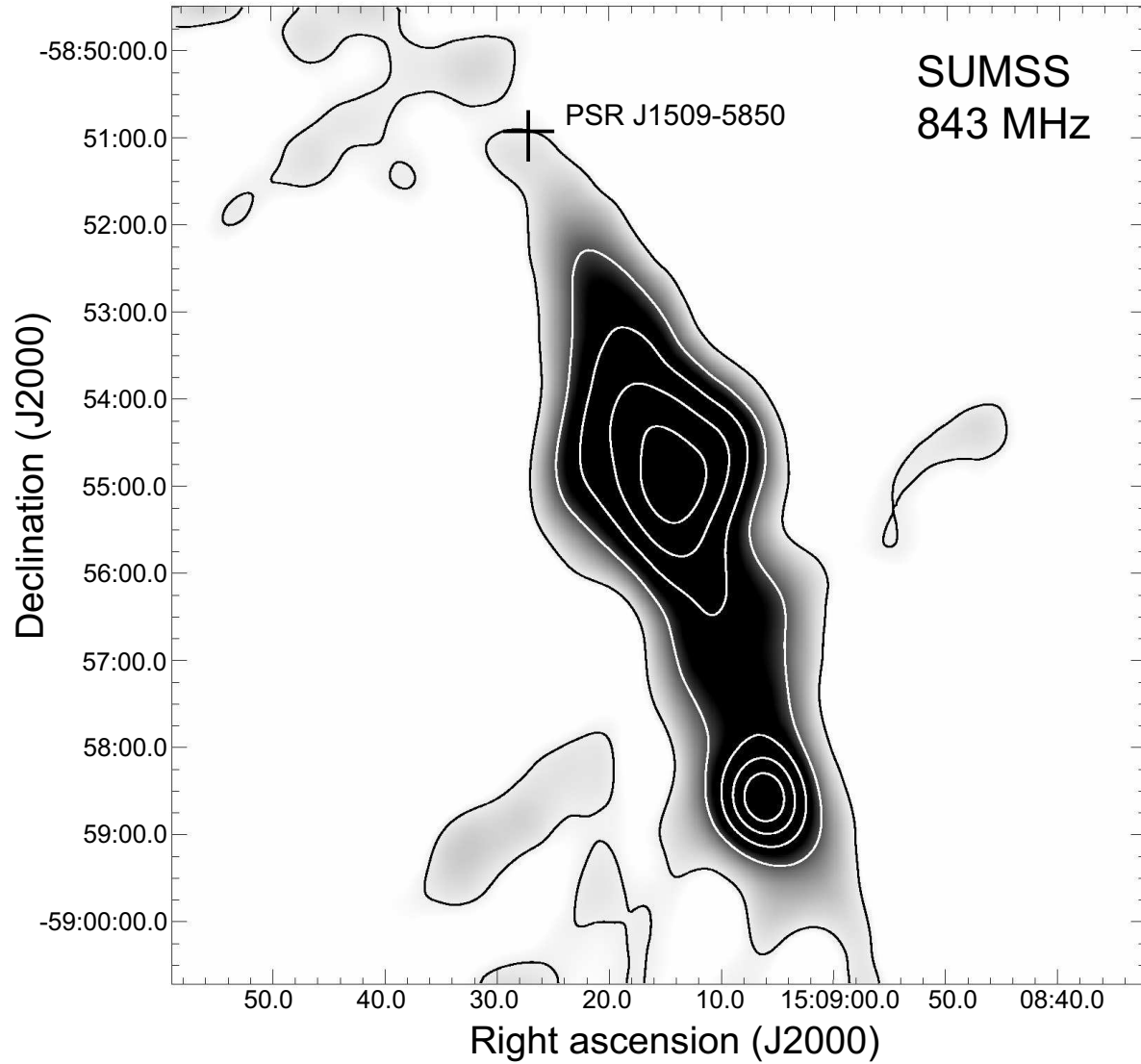


Figure 5.3: The 843 MHz SUMSS image of a field of  $11 \times 11$  arcmin around PSR J1509-5850. The pulsar position is indicated by the black cross. The  $\sim 7$  arcmin long radio feature is found to have the same orientation as the X-ray trail. The contour levels are 7, 23, 39, 54 and 70 mJy/beam. Two clumps are observed along the trail. The larger clump, near to the center of this image, on the trail is identified as the SNR candidate MSC 319.9-0.7.

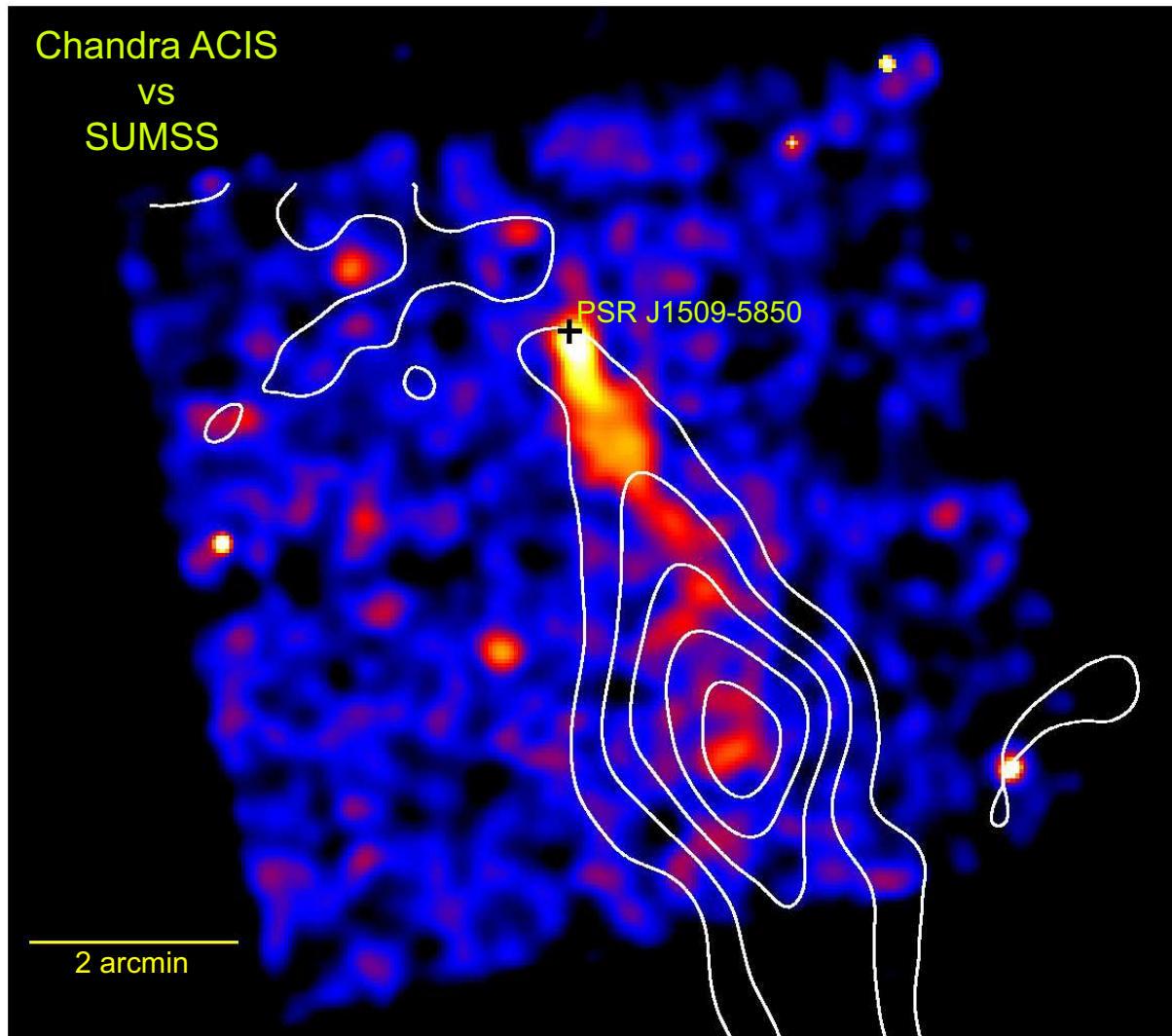


Figure 5.4: The X-ray image of the Chandra ACIS-S3 chip with the radio contour lines from SUMSS data (cf. Figure 5.3) overlaid. The X-ray image is binned with a pixel size of 2.5 arcsec and adaptively smoothed with a Gaussian kernel of  $\sigma < 7.5$  arcsec. We note that there is a faint X-ray feature near to the location of the SNR candidate MSC 319.9-0.7. Top is north and left is east.



# Chapter 6

## Discovery of an X-ray Nebula associated with PSR J2124-3358

This chapter is adopted from the refereed paper entitled “Searches for diffuse X-ray emission around millisecond pulsars: An X-ray nebula associated with PSR J2124-3358” published in *Astronomy & Astrophysics* (Hui & Becker 2006a).

### 6.1 Introduction

Diffuse plerionic emission is often a special marker of young and powerful pulsars if their spin-down energy is in excess of  $\sim 10^{36}$  erg/s. Extended diffuse emission associated with older and less powerful pulsars, however, is rare and so far only seen in Geminga (Caraveo et al. 2003), PSR B1929+10 (Becker et al. 2006), PSR B2224+65 (Romani et al. 1997; Chatterjee & Cordes 2002) and the millisecond pulsars (MSPs) PSR B1957+20 (Stappers et al. 2003), J0437-4715 (Bell et al. 1995), and J2124–3358 (Gaensler, Jones & Stappers 2002). While all three MSPs have bright bow-shock nebulae detected in  $H_\alpha$ , diffuse X-ray emission associated with it could be detected only from the black widow pulsar PSR B1957+20 in a recent Chandra observation (Stappers et al. 2003). Comparable deep observations of almost all X-ray bright MSPs, however, have been performed by XMM-Newton in previous years. These XMM-Newton data thus provides us a valuable data base to search for diffuse and extended emission components from these MSPs as well.

In this chapter we report on a search for diffuse X-ray emission to be associated with the MSPs PSR J2124–3358, J0437-4715, J0030+0451 and J1024-0719. All these pulsars have comparable spin parameters (cf. Table 6.1) so that differences in their emission properties are most likely cause by differences in the pulsar-ISM interaction/local environment rather than by differences in their total energy output.

PSRs J2124-3358 and J1024-0719 were both discovered during the Parkes 436 MHz survey of the southern sky (Bailes et al. 1997). PSR J0030+0451 was discovered at 430 MHz during the Arecibo Drift Scan Search (Somers 2000) and independently in the Bologna sub-millisecond pulsar survey (D’Amico 2000), whereas PSR J0437-4715 was discovered in

the Parkes southern sky survey (Johnston et al. 1993). PSR J0437-4715 was the first MSP of which pulsed X-ray emission was detected (Becker & Trümper 1993). X-ray emission from PSR J2124-3358 and J1024-0719 was reported by Becker & Trümper (1998, 1999) in ROSAT HRI data whereas the X-ray counterpart of PSR J0030+0451 was discovered in the final ROSAT PSPC observation (Becker et al. 2000). A  $H_\alpha$  bow shock is seen around PSR J0437-4715 (Bell et al. 1995). However, its X-ray counterpart was not detected by ROSAT and Chandra (Becker & Trümper 1999, Zavlin et al. 2002). Gaensler, Jones & Stappers (2002) discovered an  $H_\alpha$ -emitting bow shock nebula around PSR J2124-3358. This bow shock is very broad and highly asymmetric about the direction of the pulsar's proper motion. The asymmetric shape might be caused by a significant density gradient in the ISM, bulk flow of ambient gas and/or anisotropies in the pulsar's relativistic wind (Gaensler, Jones & Stappers 2002). Observation of PSR J0030+0451, performed with the ESO NTT in La Sila, did not detect diffuse  $H_\alpha$  emission associated with it (A. Pellizzoni priv. com.).

## 6.2 Observations and data analysis

The pulsars PSR J2124-3358, J0030+0451, J1024-0719 and J0437-4715 were observed by XMM-Newton in 2002 April 14-15, in 2001 June 19-20, in 2003 December 2 and in 2002 October 9, respectively. In all observations the MOS1/2 cameras were operated in full-frame mode while the PN camera was setup to work in the fast-timing mode. The PN fast-timing mode provides only limited spatial information so that these data are not used in the present analysis. To block stray light and optical leakage from bright foreground stars we operated the MOS1/2 cameras with the thin filters during the observations of PSRs J0030+0451, J1024-0719 and J0437-4715 while PSR J2124-3358 was observed by using a medium filter. Events were selected for the energy range 0.25 – 10 keV and standard correction procedures were applied to reduce the data (e.g. Becker et al. 2006). Filtering the data for times of excessive background from soft proton flares was done using conservative thresholds in view of the planned search for diffuse and extended X-ray emission. The effective exposure time after data reduction turns out to be 40 ksec for PSR J2124-3358, 14 ksec for J0030+0451, 65 ksec for J1024-0719 and 55 ksec for J0437-4715.

A vignetting corrected image of the field of PSR J2124-3358 as seen by the XMM-Newton's MOS1/2 CCDs is shown in Figure 6.1a. The binning factor in this image is 6 arcsec. Adaptive smoothing with a Gaussian kernel of  $\sigma < 4$  pixels has been applied to the image. X-ray contours are calculated and overlaid on the image. The contour lines are at the levels of  $(4.2, 5.2, 7.6, 13, 28, 63) \times 10^{-6}$  cts  $s^{-1}$  arcsec $^{-2}$ . It can be seen that the X-ray source which is coincident with the pulsar position has an asymmetric source structure of  $\sim 0.5$  arcmin extent, with its orientation to the northwest. Systematic effects which could cause an adequate distortion of the instrument's point spread function (PSF) are not known for XMM-Newton. We are therefore prompted to interpret this elongated structure in terms of a pulsar X-ray trail. The net count rate of the diffuse emission in a  $30 \times 35$  arcsec box centered at RA(J2000)=21<sup>h</sup>24<sup>m</sup>42.69<sup>s</sup>, Dec= $-33^\circ 58' 16.06''$  and oriented

along the extended feature is estimated to be  $(1.25 \pm 0.16) \times 10^{-3}$  cts s<sup>-1</sup>. For this estimate we determined the background from a low count region close to PSR J2124–3358. For comparison, the pulsar emission is estimated to have a net count rate of  $(1.07 \pm 0.01) \times 10^{-2}$  cts s<sup>-1</sup> in a circle of 18 arcsec radius centered at the pulsar position. The signal-to-noise of this elongated feature is  $\sim 4$  in the energy range 0.25 – 5 keV.

PSR J2124–3358 was observed by Chandra with the back-illuminated ACIS-S3 chip in the focus of the XRT. The observation took place on 2004 December 19-20 for an exposure time of  $\sim 30$  ksec. An image made from this data with 0.5 arcsec binning and adaptive smoothing applied (using a Gaussian kernel with  $\sigma < 1.5$  pixel) is shown in Figure 6.1b. Arc-like diffuse emission which is within the pulsar’s H $\alpha$  nebula is clearly detected. Its net count rate is estimated to be  $(1.28 \pm 0.23) \times 10^{-3}$  cts s<sup>-1</sup> in a box of  $10 \times 20$  arcsec centered at RA(J2000)=21<sup>h</sup>24<sup>m</sup>43.17<sup>s</sup>, Dec=–33°58′33.53″. With the aid of PIMMS, the pileup fraction of the ACIS-S3 data was found to be less than 0.2%, i.e. is negligible. The signal-to-noise of this feature is  $\sim 5$  in the energy range of 0.3 – 8 keV.

Since the PSF width of XMM-Newton is about 10 times that of Chandra, it blurred most of the detailed structure seen in the Chandra data. However, it should be noted that the overall direction of the feature in the Chandra image is consistent with the orientation of the trail detected by XMM-Newton.

In order to investigate a possible contribution to the diffuse X-ray emission by nearby stars we investigated the Digitized Sky Survey data (DSS) for the sky region around PSR J2124–3358. There are four field stars (labeled as A, B, C and D in Figure 6.1a and Table 6.2) in the 1.5 arcmin neighborhood of PSR J2124–3358. From the USNO catalogue, we identified the magnitudes of these stars. None of them is found to match the position of the diffuse elongated X-ray structure seen in the XMM-Newton and Chandra data. It can be seen in Figure 6.1a that the positions of stars B and C coincide with two faint X-ray sources which are disconnected with the trail emission of PSR J2124–3358 though.

To examine the nature of the faint X-ray nebular emission by a spectral analysis we make use of the XMM-Newton data and extract the energy spectrum from within a  $30 \times 35$  arcsec box. Using a box rather than a circular selection region allows to avoid the emission from the pulsar and excludes any potential contamination from the field stars B and C. However, we estimate that the wing of the XMM-Newton PSF centered at the pulsar position still contributes  $\sim 20\%$  to the total counts inside the box. The background spectrum was extracted from a source free region near to PSR J2124–3358. In total, 92 and 67 source counts are available from the trail in the MOS1 and MOS2 detectors, respectively. Response files were computed by using the XMMSAS tasks RMFGEN and ARFGEN. The spectra were dynamically binned so as to have at least 10 counts per bin.

In the Chandra data we selected the energy spectrum of the diffuse emission from a box of size  $10 \times 20$  arcsec. Owing to the narrow PSF of Chandra the contamination of pulsar emission in this box is negligible. The background spectrum was extracted from a low count region near to the diffuse feature. In total 46 source counts are contributed from the Chandra data. Response files were computed by using tools MKRMF and MKARF of CIAO. The spectrum was binned to have at least 8 counts per bin. The degradation of

quantum efficiency of ACIS was corrected by applying the XSPEC model ACISABS.

We hypothesize that the diffused emission should be originated from the interaction of pulsar wind and the ISM. Synchrotron radiation from the ultra-relativistic electrons is generally believed to be the emission mechanism of the pulsar wind nebula, which then is characterized by a power-law spectrum. With a view to test this hypothesis, we fitted an absorbed power-law model to the nebular spectrum with XSPEC 11.3.1 in the 0.25 – 10 keV energy range. With a column density of  $5 \times 10^{20} \text{ cm}^{-2}$  as obtained from spectral fits to the pulsar emission, we found that the model describes the observed spectrum fairly well ( $\chi^2_\nu = 0.79$  for 26 D.O.F.). The photon index is  $\alpha = 2.2 \pm 0.4$  and the normalization at 1 keV is  $(2.94 \pm 0.48) \times 10^{-6} \text{ photons keV}^{-1} \text{ cm}^{-2} \text{ s}^{-1}$  ( $1 - \sigma$  error for 1 parameter in interest). In view of the low photon statistic we tested for a possible dependence of the fitted model parameters against the background spectrum. All deviations found in repeating the fits with different background spectra were within the  $1 - \sigma$  confidence interval quoted above. The unabsorbed fluxes and luminosities deduced for the best fit model parameters and the energy ranges 0.1–2.4 keV and 0.5–10 keV are  $f_X = 1.8 \times 10^{-14} \text{ ergs s}^{-1} \text{ cm}^{-2}$ ,  $L_X = 1.3 \times 10^{29} \text{ ergs s}^{-1}$  and  $f_X = 1.2 \times 10^{-14} \text{ ergs s}^{-1} \text{ cm}^{-2}$ ,  $L_X = 8.9 \times 10^{28} \text{ ergs s}^{-1}$ , respectively. The best fitting spectral model is displayed in Figure 6.2.

Motivated by the extended source structure seen in PSR J2124–3358 we have also inspected the XMM-Newton data of PSRs J0030+0451, J1024–0719 and J0437-4715 in order to search for extended tail-like X-ray emission. There is no evidence for any extended emission around these pulsars. In order to deduce an upper limit for an X-ray trail in these sources we have estimated the net count rates for the regions of  $30 \times 35$  arcsec right behind the corresponding directions of each pulsar’s proper motion. The net count rate for any diffuse emission in these regions is  $(3.1 \pm 1.5) \times 10^{-4} \text{ cts s}^{-1}$ ,  $(3.1 \pm 0.7) \times 10^{-4} \text{ cts s}^{-1}$  and  $(2.5 \pm 0.9) \times 10^{-4} \text{ cts s}^{-1}$  for PSRs J0030+0451, J1024–0719 and J0437-4715, respectively. The quoted errors are  $1 - \sigma$  confidence intervals. Assuming a Crab-like spectrum (i.e.  $\alpha = 2$ ) and taking the values of column density inferred from the pulsar spectral fits ( $1 \times 10^{20} \text{ cm}^{-2}$  for J0030+0451,  $2 \times 10^{20} \text{ cm}^{-2}$  for J1024–0719 and  $3 \times 10^{19} \text{ cm}^{-2}$  for J0437-4715), we calculated the  $3 - \sigma$  limiting fluxes from the above count rates. For PSRs J0030+0451, J1024–0719 and J0437-4715, the limiting fluxes in 0.5–10 keV are estimated to be  $6.9 \times 10^{-15} \text{ ergs s}^{-1} \text{ cm}^{-2}$ ,  $4.9 \times 10^{-15} \text{ ergs s}^{-1} \text{ cm}^{-2}$  and  $4.2 \times 10^{-15} \text{ ergs s}^{-1} \text{ cm}^{-2}$ , respectively.

### 6.3 Discussion & Conclusion

Basic characteristics of the X-ray bow shocks detected around rotation-powered pulsars are summarized in Table 6.3. PSR J2124–3358 is a new candidate to this group. Its tail is found to have an extent of  $\sim 0.5$  arcmin. Adopting the distance of  $\sim 250$  pc, the tail has a length of  $l \sim 1.1 \times 10^{17} \text{ cm}$ . For the pulsar’s proper motion velocity of  $58 \text{ km s}^{-1}$  (Manchester et al. 2005), the timescale,  $t_{\text{flow}}$ , for the passage of the pulsar over the length of its X-ray trail is estimated to be  $\sim 600$  yrs. According to the discussion in Becker et al. (2006) on the trail emission of PSR B1929+10 we estimate the magnetic field



in the shocked region by assuming  $t_{\text{flow}}$  to be comparable to the electron lifetime of the synchrotron emission. This yields  $\sim 30\mu\text{G}$  for the inferred magnetic field strength in the emitting region. The magnetic field strength in the ISM is estimated to be  $\sim 2 - 6\mu\text{G}$  (cf. Beck et al. 2003 and references therein). Taking into account that the magnetic field in the termination shock might be compressed (e.g. Kennel & Coroniti 1984), our estimation is approximately consistent if the compression factor is  $\sim 7$ .

Following Becker et al. (2006), we apply a simple one zone model (Chevalier 2000) to estimate the spectral behavior and the X-ray luminosity of the nebular emission. The X-ray luminosity and spectral index depend on the inequality between the characteristic observed frequency  $\nu_X^{\text{obs}}$  and the electron synchrotron cooling frequency  $\nu_c$  which is estimated to be  $1.6 \times 10^{17}$  Hz. Since in general  $\nu_X^{\text{obs}} > \nu_c$ , we concluded that the emission is in a fast cooling regime. Electrons with the energy distribution,  $N(\gamma) \propto \gamma^{-p}$ , are able to radiate their energy in the trail with photon index  $\alpha = (p + 2)/2$ . The index  $p$  due to shock acceleration typically lies between 2 and 3 (cf. Cheng, Taam, & Wang 2004 and references therein). Taking  $p = 2.35$  yields  $\alpha^{\text{th}} \simeq 2.2$  which is in accordance with the result from the observed value  $\alpha^{\text{obs}} = 2.2 \pm 0.4$ . Assuming the energy equipartition between the electron and proton (Cheng, Taam, & Wang 2004), we take the fractional energy density of electron  $\epsilon_e$  to be  $\sim 0.5$  and the fractional energy density of the magnetic field  $\epsilon_B$  to be  $\sim 0.01$ . Assuming a number density of ISM to be  $1 \text{ cm}^{-3}$ , the distance of the shock from the pulsar is estimated to be  $\sim 3.6 \times 10^{16}$  cm. With these estimates, the calculated luminosity,  $\nu L_\nu$ , is given as  $\sim 10^{29}$  ergs  $\text{s}^{-1}$  which is well consistent with the observed values of  $1.3 \times 10^{29}$  ergs  $\text{s}^{-1}$  (0.1-2.4 keV) and  $8.9 \times 10^{28}$  ergs  $\text{s}^{-1}$  (0.5-10 keV).

Although the general properties of the X-ray trail in PSR B2224+65 are not in contradiction with properties observed in other pulsars there are still ambiguities which are not completely resolved. First, one should notice that the trail is misaligned with the direction of the pulsar's proper motion. As reported by Gaensler, Jones, & Stappers (2002), the head of the  $H_\alpha$  bow shock is found to be highly asymmetric about the pulsar's velocity vector with the apparent nebular symmetry axis deviated from the velocity vector by  $\sim 30^\circ$ . Even though the misalignment of the X-ray trail seems to agree with the asymmetry of the  $H_\alpha$  nebula, deeper observations by XMM-Newton and Chandra are required in order to constrain the physical properties of this interesting nebula in higher detail.

Table 6.1: Pulsar Parameters of PSRs J0030+0451, J2124-3358, J1024-0719 and J0437-4715 (from Manchester et al. 2005)

Pulsar	PSR J0030+0451	PSR J2124-3358	PSR J1024-0719	PSR J0437-4715
Right Ascension (J2000)	00 <sup>h</sup> 30 <sup>m</sup> 27.432 <sup>s</sup>	21 <sup>h</sup> 24 <sup>m</sup> 43.862 <sup>s</sup>	10 <sup>h</sup> 24 <sup>m</sup> 38.700 <sup>s</sup>	04 <sup>h</sup> 37 <sup>m</sup> 15.787 <sup>s</sup>
Declination (J2000)	+04° 51' 39.7"	-33° 58' 44.257"	-07° 19' 18.915"	-47° 15' 08.462"
Pulsar Period, $P$ (ms)	4.865453207369	4.9311148591481	5.1622045539088	5.7574518310720
Period derivative $\dot{P}$ ( $10^{-20}$ s s <sup>-1</sup> )	1.0	1.33	1.85	1.87
Age ( $10^9$ yrs)	7.71	5.86	4.41	4.89
Surface dipole magnetic field ( $10^8$ G)	2.23	2.60	3.13	3.32
Epoch of Period (MJD)	50984.4	50288.0	51018.0	51194.0
Dispersion Measure (pc cm <sup>-3</sup> )	4.3328	4.6152	6.491	2.6469
Dispersion based distance (pc)	230	250	350	140
Spin-down Luminosity ( $10^{33}$ ) ergs s <sup>-2</sup>	3.43	4.38	5.3	3.87

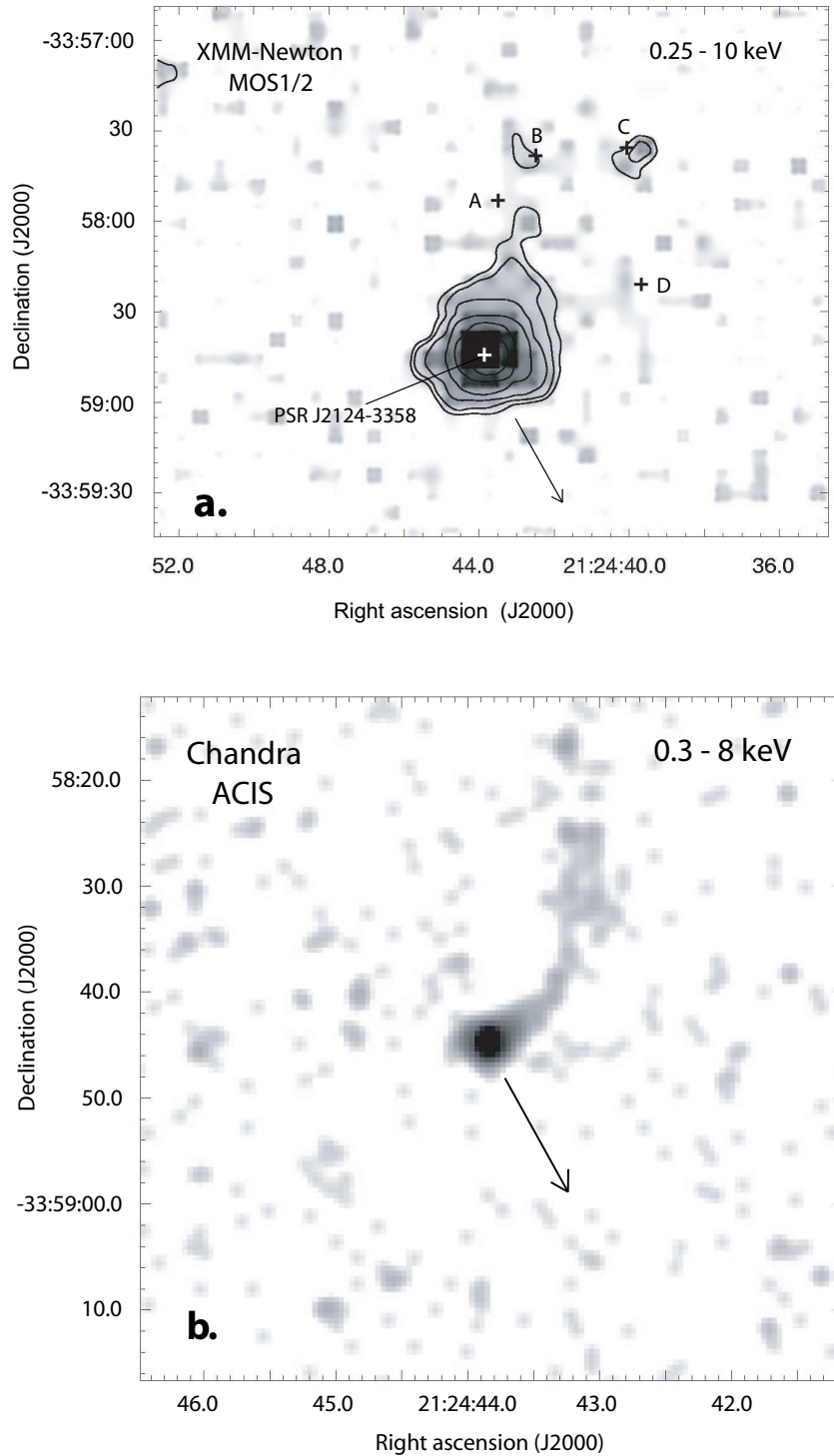


Figure 6.1: a) XMM-Newton MOS1/2 image of PSR J2124–3358 with overlaid contours. The pulsar proper motion is indicated by an arrow. The position of bright stars located in the 1.5 arcmin neighborhood of PSR J2124–3358 are indicated. b) PSR J2124–3358 as seen by the ACIS detector aboard Chandra.

Table 6.2: Identifications of the stars around the X-ray trail of PSR J2124-3358.

Stars <sup>a</sup>	USNO catalogue ID	Magnitude: <i>R</i>	Magnitude: <i>B</i>
A	U052543254607	17.1	18.7
B	U052543254423	18.0	20.2
C	U052543253997	16.7	17.4
D	U052543253910	13.5	15.5

a. See Figure 6.1a.

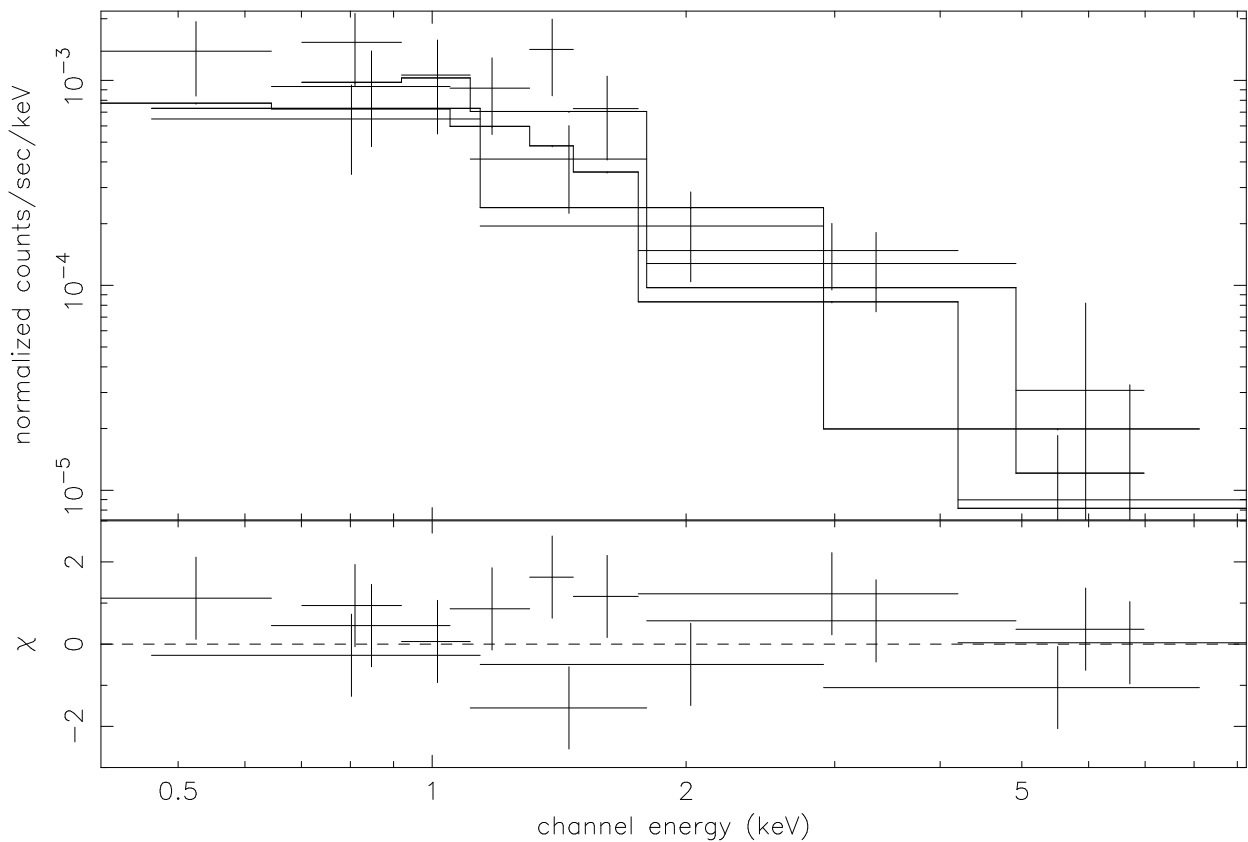


Figure 6.2: Energy spectrum of the X-ray trail of PSR J2124-3358 as observed with MOS1/2 and ACIS-S3 detectors and simultaneously fitted to an absorbed power-law model (*upper panel*) and contribution to the  $\chi^2$  fit statistic (*lower panel*).

Table 6.3: Properties of rotation-powered pulsars with X-ray/ $H_\alpha$  bow shocks.

PSR	Other Name/ associated SNR	$\dot{E}$ erg s <sup>-1</sup>	$L_X^{diff}$ (0.5–10 keV) <sup>a</sup> erg s <sup>-1</sup>	$\tau_{spin-down}$ years	$H_\alpha$ bow shock	X-ray trail	Radio nebula	Reference
Young pulsars								
J0537-6910	LMC: N157B	$4.8 \times 10^{38}$	$3.5 \times 10^{36}$	$5.0 \times 10^3$	-	d	-	1,2
B1757-24	Duck	$2.6 \times 10^{36}$	$4.6 \times 10^{32}$	$1.6 \times 10^4$	-	d	d	3
B1853+01	W44	$4.3 \times 10^{35}$	$5.7 \times 10^{32}$	$2.0 \times 10^4$	-	d	d	4
J1747-2958	Mouse	$2.5 \times 10^{36}$	$5.3 \times 10^{34}$	$2.6 \times 10^4$	-	d	d	5
B1951+32	CTB80	$3.7 \times 10^{36}$	$2.5 \times 10^{33}$	$1.1 \times 10^5$	d	d	d	6,7,8
Middle age and old pulsars								
B0740-28		$1.4 \times 10^{35}$	-	$1.6 \times 10^5$	d	-	-	9
B0633+17	Geminga	$3.2 \times 10^{34}$	$8.9 \times 10^{28}$	$3.4 \times 10^5$	-	d	-	10
B2224+65	Guitar	$1.2 \times 10^{33}$	$3.7 \times 10^{31}$	$1.1 \times 10^6$	d	?	-	11,12
B1929+10		$3.9 \times 10^{33}$	$8.3 \times 10^{29}$	$3.1 \times 10^6$	-	d	?	13
Millisecond pulsars								
B1957+20		$1.1 \times 10^{35}$	$1.9 \times 10^{31}$	$2.2 \times 10^9$	d	d	-	14
J0437-4715		$3.9 \times 10^{33}$	-	$4.9 \times 10^9$	d	-	-	15,16
J2124-3358		$4.4 \times 10^{33}$	$10^{29}$	$5.9 \times 10^9$	d	d	-	17,18

a. The X-ray luminosities of the diffuse emission are taken from the corresponding reference and recalculated into energy band of 0.5–10 keV for easy comparison. References: (1) Wang & Gotthelf 1998; (2) Wang et al. 2001; (3) Kaspi et al. 2001; (4) Petre et al. 2002; (5) Gaensler et al. 2004; (6) Migliazzo et al. 2002; (7) Moon et al. 2004; (8) Li et al. 2005; (9) Jones et al. 2002; (10) Caraveo et al. 2003; (11) Romani et al. 1997; (12) Chatterjee & Cordes 2002; (13) Becker et al. 2006; (14) Stappers et al. 2003; (15) Bell et al. 1995; (16) Zavlin et al. 2002; (17) Gaensler et al. 2002; (18) This letter; and Manchester et al. 2005 otherwise.



# Chapter 7

## X-ray emission properties of the old pulsar PSR B2224+65

This chapter is adopted from the refereed paper "X-ray emission properties of the old pulsar PSR B2224+65" published in *Astronomy & Astrophysics* (Hui & Becker 2007a).

### 7.1 Introduction

High energy radiation properties of rotation-powered pulsars are known to approximately correlate with their spin-down age. X-rays from young pulsars with age less than  $\sim 10^5$  years are believed to be dominated by magnetospheric emission, characterized by a power-law spectrum and narrow pulse profiles. For middle-aged pulsars in the age bracket between  $\sim 10^5 - 10^6$  years the pulsars' X-radiation is dominated by cooling emission from the hot stellar surface. This class of pulsars is observed to have composite spectra consisting of a soft thermal component, a harder thermal component from heated polar caps as well as some non-thermal emission. The thermal and non-thermal contributions in the emission of younger and middle-aged pulsars has already been well disentangled and studied by previous X-ray observatories (for recent reviews see e.g. Becker & Aschenbach 2002; Kaspi et al. 2004 and references therein).

Old neutron stars with ages  $> 10^6$  years have already cooled down to less than five hundred thousand degrees so that the thermal emission from their surface has faded from view for X-ray observatories. Recently, the much improved sensitivity of the XMM-Newton and Chandra observatories enabled a series of comprehensive studies to probe and identify the origin of the X-radiation from old rotation-powered pulsars. Until now, results have been presented for the pulsars B0950+08, B0823+26, J2043+2740 (Becker et al. 2004), B0628-28 (Becker et al. 2005), B0943+10 (Zhang, Sanwal & Pavlov 2005), B1133+16 (Kargaltsev, Pavlov & Garmire 2006) and for PSR B1929+10 (Becker et al. 2006). For all old pulsars which were observed with sufficient photon statistics the X-ray emission turned out to be dominated by non-thermal emission originating in the pulsar's magnetosphere. X-ray pulses, if detected, often show narrow features.

A very interesting member in this class of old pulsars is PSR B2224+65. The proper motion of PSR B2224+65,  $\mu_{\text{RA}}=144$  mas/yr and  $\mu_{\text{Dec}}=112$  mas/yr, is among the highest observed by now (Manchester et al. 2005). The pulsar's interaction with the ISM produces a magnificent bow shock nebula which was discovered in  $\text{H}\alpha$  by Cordes et al. (1993). Because the shape of this nebula resembles that of a guitar the nebula got dubbed *Guitar Nebula*. The pulsar has a period of about 0.68 s and a period derivative of  $9.55 \times 10^{-15}$  s/s, implying a spin-down luminosity of  $\dot{E} = 1.19 \times 10^{33}$  erg/s and a spin-down age of somewhat more than one million years. The distance to PSR B2224+65 is not very well constrained. The radio dispersion measure based distance in the Cordes & Lazio (2002) Galactic free electron density model is 1.86 kpc. However, Chatterjee & Cordes (2004) found by modeling the head of the Guitar Nebula that the pulsar distance could be as close as 1 kpc. For this work we adopt the distance of 1 kpc as suggested by Chatterjee & Cordes (2004). The ephemeris of this pulsar as adopted from Manchester et al. (2005) are summarized in Table 7.1.

In this chapter, we present a detailed X-ray study of PSR B2224+65 and its environment based on archival Chandra data. Brief results from this observation were already reported by Wong et al. (2003) and Zavlin & Pavlov (2004). The structure of this chapter is as follows. In section 7.2 we describe the observations and data analysis and in section 7.3 we summarize the results which for the pulsar are discussed in the context of the outer-gap model.

## 7.2 Observations and data analysis

PSR B2224+65 was observed by the Chandra satellite in 2000 October 21-22 (Obs ID: 755) with the Advanced CCD Imaging Spectrometer (ACIS). The pulsar is located on the back-illuminated (BI) ACIS-S3 chip which has a superior quantum efficiency among the spectroscopic array. Standard processed level-2 data were used in our study. The effective exposure is found to be  $\sim 50$  ksec. The frame time of 3.2 sec does not support a timing analysis of PSR B2224+65 to search for X-ray pulsations.

The Chandra image of the  $4 \times 4$  arcmin field around PSR B2224+65 is shown in Figure 7.1. The binning factor of the image is 0.5 arcsec. Adaptive smoothing with a Gaussian kernel of  $\sigma < 2$  pixels has been applied to better make visible faint diffuse emission. The X-ray point source is clearly seen at the radio pulsar position. The inset in Figure 7.1 shows the  $\text{H}\alpha$  image observed by the Wide Field Planetary Camera 2 (WFPC2) on the Hubble Space Telescope (HST). This image shows the Guitar Nebula. Romani et al. (1997) reported on a  $4 - \sigma$  detection of diffuse X-ray emission associated with the  $\text{H}\alpha$  nebula in ROSAT HRI data. However, we found no evidence for any diffuse X-ray emission within the corresponding region of the Chandra image. Rather than an extended X-ray feature which has a length of  $\sim 2$  arcmin but which deviates from the pulsar's direction of proper motion by  $\sim 118^\circ$  is observed. The signal-to-noise ratio of this feature in the energy range 2–8 keV is about 6. We further compute the brightness profile of the feature. From the raw image with bin size of 0.5 arcsec, we estimate counts in eight consecutive boxes of



$20 \times 10$  arcsec oriented along the feature. The first box is centered at RA= $22^h 25^m 48.609^s$ , Dec= $+65^\circ 35' 45.15''$  (J2000). The vignetting corrected brightness profile in the energy band 0.3 – 8 keV is shown in Figure 7.2. The feature was already noticed by Wong et al. (2003). Inspecting the radio data from the NRAO/VLA Sky Survey (NVSS) archive (Condon et al. 1998) did not reveal a radio counterpart of it.

In their brief analysis, Wong et al. (2003) claimed that the X-ray emission at the pulsar position is likely to be from a shocked nebula. In order to investigate whether there is extended nebular emission around PSR B2224+65, we have examined the spatial nature of the emission by fitting a convolved 2-D Gaussian to the sub-image around the pulsar position with the point spread function (PSF) as the convolution kernel. The model PSF at 1.5 keV is created by using the CIAO tool MKPSF. The best-fitted result yields a FWHM of  $0.55 \pm 0.03$  arcsec ( $1-\sigma$  error) which is in agreement with the expected width of the Chandra PSF for a point source observed on-axis.

For a spectral analysis of the pulsar emission we extracted events from a circle of 3 arcsec radius (encircled energy  $\sim 99\%$ ) centered on the radio pulsar position. The spectrum from the extended X-ray feature was extracted from a box of  $132 \times 15$  arcsec, oriented along the direction of this feature. In total,  $\sim 80$  counts for the pulsar and  $\sim 370$  counts for the feature were selected in the energy band 0.3 – 8 keV. Even though the photon statistics is on the smaller size it is sufficient to provide us with interesting insights on the radiation emission nature of the pulsar and the unidentified X-ray feature.

Response files were computed by using the CIAO tools MKRMF and MKARF. According to the photon statistics, the spectra were dynamically binned so as to have at least 8 counts per bin for the pulsar and at least 30 counts per bin for the extended feature. The background spectrum for the spectral analysis of the pulsar is extracted from a circle near to the pulsar of 3 arcsec at RA= $22^h 25^m 53.893^s$ , Dec= $+65^\circ 35' 34.79''$  (J2000). For the analysis of the extended feature, the background spectrum is extracted from a low count region of  $18 \times 15$  arcsec centered at RA= $22^h 25^m 49.113^s$ , Dec= $+65^\circ 36' 08.84''$  (J2000). In the energy band 0.3 – 8 keV, the net count rates for the pulsar and the feature are estimated to be  $(1.53 \pm 0.18) \times 10^{-3}$  cts/s and  $(5.59 \pm 0.34) \times 10^{-3}$  cts/s respectively. With the aid of PIMMS, the pileup fraction of the ACIS-S3 data is estimated to be  $\leq 0.7\%$  which is negligible. All spectral fits were performed in the 0.3–8 keV energy range by using XSPEC 11.3.1. The degradation of the ACIS quantum efficiency was corrected by the XSPEC model ACISABS. The parameters of all fitted model spectra are summarized in Table 7.2. All the quoted errors are  $1-\sigma$  and were computed for 1 parameter in interest.

For the pulsar PSR B2224+65 we found that among the tested models a single power-law model describes the observed spectrum best ( $\chi^2_\nu = 0.70$  for 6 D.O.F.). This model yields a column density of  $N_H < 0.9 \times 10^{21}$  cm $^{-2}$ , a photon index of  $\Gamma = 1.58^{+0.43}_{-0.33}$  and a normalization at 1 keV of  $(2.28^{+0.75}_{-0.39}) \times 10^{-6}$  photons keV $^{-1}$  cm $^{-2}$  s $^{-1}$ . The best-fitted power-law spectrum and residuals are shown in Figure 7.3.

The unabsorbed fluxes deduced for the best-fitting power-law model are  $f_X = 9.3 \times 10^{-15}$  ergs cm $^{-2}$  s $^{-1}$  and  $f_X = 1.6 \times 10^{-14}$  ergs cm $^{-2}$  s $^{-1}$  in the 0.1–2.4 keV and 0.5–10 keV energy bands, respectively. The luminosities in these bands are  $L_X = 1.1 d_{1\text{kpc}}^2 \times 10^{30}$  ergs s $^{-1}$  and  $L_X = 2.0 d_{1\text{kpc}}^2 \times 10^{30}$  ergs s $^{-1}$ .  $d_{1\text{kpc}}$  denotes the distance to PSR B2224+65 in units

of 1 kpc. The conversion efficiency,  $L_X(0.1-2.4 \text{ keV})/\dot{E}$ , is found to be  $0.9d_{1\text{kpc}}^2 \times 10^{-3}$ . For a distance close to 1 kpc as suggested by Chatterjee & Cordes (2004), this is in good agreement with the relation  $L_X(0.1-2.4 \text{ keV}) \approx 10^{-3}\dot{E}$  found by Becker & Trümper (1997) for rotation powered pulsars

We have also considered the possibility of a purely thermal emission scenario. However, fitting a blackbody yields a reduced  $\chi_\nu^2$  of 2.06 for 6 D.O.F. which invalidates this model. Although the small number of counts does not support any fitting with multicomponent models, we were still able to estimate the upper limit for the polar cap temperature and surface temperature by adding a blackbody component to the best-fitting power-law model. We computed the confidence contours of the blackbody normalization versus the temperature. They are shown in Figure 7.4. Assuming a dipolar magnetic field, the conventional size of a polar cap is defined by the last open field lines. The radius of the polar cap area is given as  $r_{\text{pc}} = R(2\pi R/cP)^{1/2}$ , where  $R$  is the neutron star radius,  $c$  is the speed of light and  $P$  is the rotation period of the pulsar. For PSR B2224+65, the rotation period of 0.68 s implies a polar cap of radius  $r_{\text{pc}} = 175 \text{ m}$ . With this estimate we set a  $1 - \sigma$  polar cap temperature upper limit of  $T_{\text{pc}}^\infty < 1.3 \times 10^6 \text{ K}$  by assuming contribution from one polar cap only. This corresponds to a  $1 - \sigma$  upper limit on the bolometric luminosity of  $L_{\text{bol}}^{\text{pc}} < 6.5 \times 10^{29} \text{ ergs s}^{-1}$ . Zavlin & Pavlov (2004) have estimated a  $1 - \sigma$  upper limit on the bolometric luminosity of  $L_{\text{bol}}^{\text{pc}} < 9.1 \times 10^{29} \text{ ergs s}^{-1}$  by adopting a hydrogen polar cap model. However, such models have many free parameters of which most are unknown for PSR B2224+65 (e.g. magnetic inclination, viewing angle). In view of this, the applicability of this model is restricted and a simple blackbody model regarded to provide us with a more conservative upper limit. If we assume that the thermal emission is emitted from the whole neutron star surface of 10 km radius we compute a surface temperature upper limit to be  $T_s^\infty < 6.1 \times 10^5 \text{ K}$  ( $3 - \sigma$ ). This limit is of the same order as those found for the other old X-ray detected pulsars (see Becker et al. 2004, 2005, 2006).

For the linearly extended feature we found that the spectrum is best-fitted by a single power-law model ( $\chi_\nu^2 = 0.79$  for 9 D.O.F.). This suggests a non-thermal origin of its emission. The model inferred column absorption is found to be  $N_H < 2.25 \times 10^{21} \text{ cm}^{-2}$ . The photon index is  $\Gamma = 0.90_{-0.24}^{+0.35}$  and the normalization at 1 keV is  $(5.66_{-1.31}^{+3.56}) \times 10^{-6} \text{ photons keV}^{-1} \text{ cm}^{-2} \text{ s}^{-1}$ . The best-fitted power-law spectrum and residuals are shown in Figure 7.5. The unabsorbed fluxes of the extended feature deduced for the best-fitted model parameters and the energy ranges 0.1–2.4 keV and 0.5–10 keV are  $f_X = 2.1 \times 10^{-14} \text{ ergs cm}^{-2} \text{ s}^{-1}$  and  $f_X = 1.0 \times 10^{-13} \text{ ergs cm}^{-2} \text{ s}^{-1}$ , respectively. The corresponding luminosities in the 0.1–2.4 keV and 0.5–10 keV bands are  $L_X = 2.5d_{1\text{kpc}}^2 \times 10^{30} \text{ ergs s}^{-1}$  and  $L_X = 1.2d_{1\text{kpc}}^2 \times 10^{31} \text{ ergs s}^{-1}$ , respectively. Fitting the spectrum of the X-ray feature with the blackbody model does not yield an acceptable goodness-of-fit ( $\chi_\nu^2 = 1.50$  for 9 D.O.F.). We have also tried to fit the spectrum with a thermal bremsstrahlung model. However, the model implies a temperature as high as 200 keV and hence can be rejected simply because it is not physical.

## 7.3 Discussion & Conclusion

According to our analysis, the observed X-rays of PSR B2224+65 are of non-thermal origin, suggesting a magnetospheric radiation dominated emission scenario. To model the detected X-ray spectrum with a blackbody model yields no acceptable results. A distinct extended X-ray feature of 2 arcmin size is observed to start at the pulsar position. Its X-ray spectrum is very hard and no counterpart of it is found in H $\alpha$  nor in NVSS radio data. Comparing the energy spectra of PSR B2224+65 and of the extended feature it is obvious that the X-ray emission of the later is much harder. We found that neither a blackbody nor a thermal bremsstrahlung model yields a valid description for its observed spectrum. This contradicts to the findings reported by Wong et al. (2003) who fitted the emission from the extended feature with a blackbody. That the X-ray feature is not aligned with the pulsar's proper motion does not a priori invalidate its association with the pulsar. Markwardt & Ögelman (1995) reported the ROSAT PSPC observation of a highly extended jet-like feature associated with the Vela pulsar which also is found to be entirely misaligned with the pulsar's proper motion vector. The recent discovery of the X-ray trail associated with the millisecond pulsar PSR J2124–3358 is another example (Hui & Becker 2006a). Such asymmetry might be caused by e.g. the inhomogeneities of the surrounding ISM or anisotropies in the pulsar wind and/or bulk flow of ambient gas (see also Gaensler, Jones & Stappers 2002). The fact that the feature starts exactly at the position of PSR B2224+65 argues against an interpretation as random ISM feature. Deeper future observations though are badly needed to further study this unique system.

Same as PSR B2224+65 the X-ray emission of many old pulsars are found to be described by power-law spectral models (Becker et al. 2004, 2005, 2006) suggesting that their X-ray emission is largely dominated by non-thermal emission processes. This is further supported by the fact that the pulse profiles of this class of pulsars are not sinusoidal as it would be expected from spin-modulated thermal emission (cf. Becker et al. 2004, 2005, 2006). For B1133+16 (Kargaltsev et al. 2006) and B0943+10 (Zhang et al. 2005), Owing to the limited photon statistics, their spectra can be fitted equally well by both blackbody and power-law models. While we cannot discriminate whether the X-ray emission are thermal or non-thermal in these cases, we have not taken these two pulsars in the following discussion.

According to Cheng & Zhang (1999; hereafter CZ99), the non-thermal X-rays from pulsars are synchrotron radiation of electron-positron pairs which are created in the strong magnetic field near the neutron star surface by curvature photons. These photons are emitted by charged particles on their way from the outer-gap to the stellar surface. The fractional size of the outer-gap,  $f_0$ , is defined as the ratio between the mean vertical separation of the gap boundaries in the plane spanned by the rotation axis and the magnetic axis to the light cylinder radius. CZ99 estimated the fractional gap size as  $f_0 = 5.5P^{26/21}B_{12}^{-4/7}$  and determined the existence of the outer-gap by the criteria  $f_0 < 1$ . We calculated the  $f_0$  for six recently studied old pulsars and tabulated them in Table 7.3. Five out of six pulsars have  $f_0 > 1$  which indicates that all but one of these old pulsars do not have outer-gaps in the framework of this model. Rather then, the CZ99-model predicts that if there is

any X-ray emission from these old pulsars, it should be thermal. This is obviously not in agreement with the observations, showing the limitation of this model.

A point, however, which has not been considered in this model is that the fractional gap size should depend on the inclination angle  $\alpha$  of the magnetic axis vs. the rotational axis. As mentioned by Zhang et al. (2004), the active region of the outer-gap should begin at the null charge surface ( $\Omega \cdot B = 0$ ) which is at the radial distance  $r_{in}$  from the star. Since the fractional size reaches a minimum at  $r_{in}$ , it is more reasonable to determine whether the gap exist by the criteria  $f(r_{in}, \alpha) < 1$  rather than by  $f_0 < 1$ . Especially for larger magnetic inclination angles the null charge surface is expected to move closer to the star, i.e.  $f(r_{in}, \alpha)$  decreases with increasing  $\alpha$ . Using Equation 36 in Zhang et al. (2004) we calculated the variation of  $f(r_{in}, \alpha)$  with  $\alpha$  for several X-ray detected old pulsars and plotted the result in Figure 7.6. Interestingly, for PSRs B0950+08, B0823+26, B0628-28 and B1929+10, the inclination angles deduced from fitting the rotating vector model to the radio polarization angle swing (Everett & Weisberg 2001; Becker et al. 2005) are all in the region  $f(r_{in}, \alpha) < 1$  (c.f. Figure 7.6 & Table 7.3). The emission geometry for the PSR B2224+65 is currently unknown which prevents us to discuss whether the outer-gap can sustain in this pulsar.

Whether the outer-gap model is of any general meaning for the description of the X-ray emission from old pulsars can only be constrained by observations. It is necessary to obtain the light curves and the spectra from a much larger sample than currently available. By now it seems rather speculative to assume that those X-ray detected old pulsars, by chance, all have their inclination angles in that range for which the outer-gap model predicts non-thermal emission.

Table 7.1: Proper-motion corrected ephemeris<sup>a</sup> of PSR B2224+65.

Right Ascension (J2000)	22 <sup>h</sup> 25 <sup>m</sup> 52.424 <sup>s</sup>
Declination (J2000)	+65° 35' 34.08"
Pulsar Period, $P$ (s)	0.682538228276
Period derivative $\dot{P}$ ( $10^{-15}$ s s <sup>-1</sup> )	9.55
Age ( $10^6$ yrs)	1.13
Surface dipole magnetic field ( $10^{12}$ G)	2.58
Epoch of Period (MJD)	49303.00
DM (pc cm <sup>-3</sup> )	36.079
DM based distance <sup>b</sup> (kpc)	1.86
Spin-down Luminosity ( $10^{33}$ ergs s <sup>-2</sup> )	1.19

<sup>a</sup>Manchester et al. (2005).<sup>b</sup>According to Cordes & Lazio (2002).

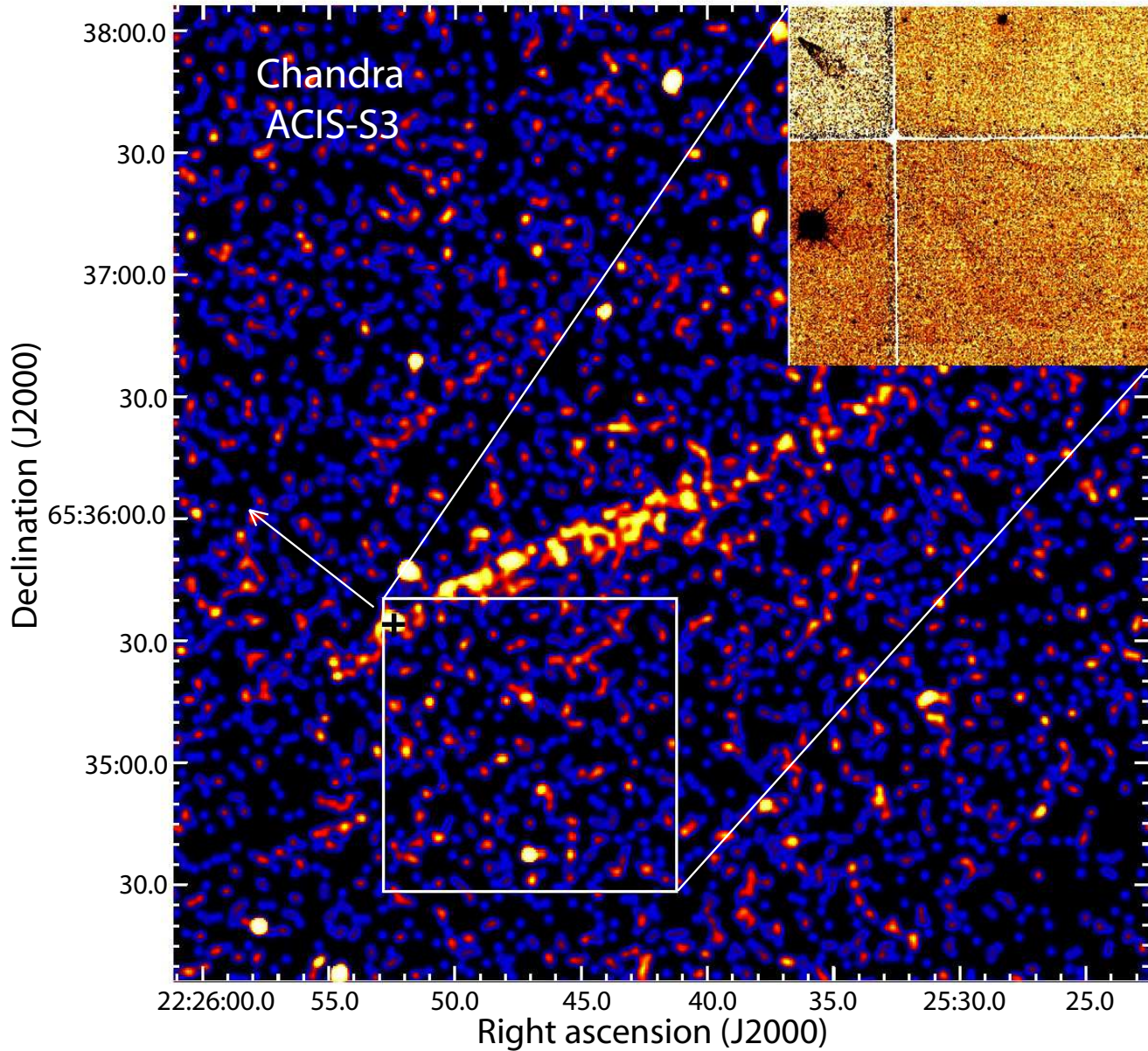


Figure 7.1: Chandra ACIS-S3 image in the energy band 0.3 – 8 keV of the field around PSR B2224+65 smoothed with an adaptive Gaussian filter. The black cross and white arrow indicate the radio pulsar position and the pulsar’s proper motion direction. The inset shows the H $\alpha$  image of the Guitar Nebula as seen by HST WFPC2.

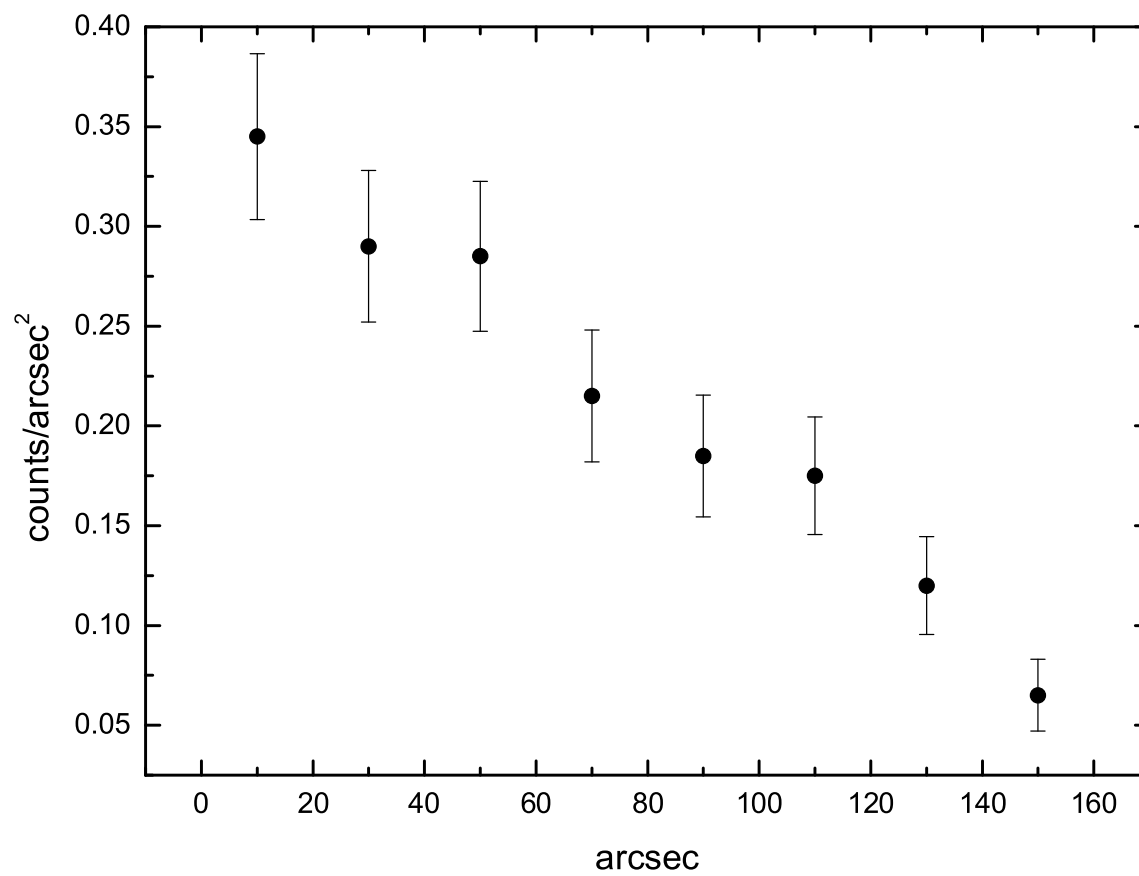


Figure 7.2: Vignetting corrected brightness profile in the energy band 0.3 – 8 keV of the extended feature associated with PSR B2224+65.

Table 7.2: Spectral parameters inferred from fitting the Chandra observed spectrum of PSR B2224+65 and X-ray feature.

Model <sup>a</sup>	$\chi^2_\nu$	D.O.F.	$N_H$ $10^{21} \text{ cm}^{-2}$	$\Gamma / kT$	Normalization <sup>b</sup>
PSR B2224+65					
PL	0.70	6	$\leq 0.90$	$1.58^{+0.43}_{-0.33}$	$2.28^{+0.75}_{-0.39} \times 10^{-6}$
BB	2.07	6	0.00	0.46	$1.46 \times 10^{-2}$
Extended X-ray feature					
PL	0.79	9	$\leq 2.25$	$0.90^{+0.35}_{-0.24}$	$5.66^{+3.56}_{-1.31} \times 10^{-6}$
BB	1.50	9	$\leq 0.62$	$0.91^{+0.15}_{-0.14}$	$7.17^{+4.82}_{-2.68} \times 10^{-3}$
BREMSS	0.86	9	$1.47^{+1.44}_{-1.02}$	$199.36^{+0.64}_{-199.36}$	$2.46^{+0.38}_{-0.99} \times 10^{-5}$

<sup>a</sup> PL = power-law; BB = blackbody; BREMSS = Thermal bremsstrahlung

<sup>b</sup> The entry in this column depends on the model in interest. For the power-law model, the unit of the normalization constant is photons  $\text{keV}^{-1} \text{ cm}^{-2} \text{ s}^{-1}$ . For the blackbody model, the normalization is  $(R_{km}/D_{10})^2$ , where  $R_{km}$  is the source radius in km and  $D_{10}$  is the distance to the source in unit of 10 kpc. For the thermal bremsstrahlung model, the normalization constant is expressed as  $(3.02 \times 10^{-15}/4\pi D^2) \int n_e n_I dV$  where  $D$  is the source distance in cm and  $n_e$  and  $n_I$  are the electron and ion densities in  $\text{cm}^{-3}$ .



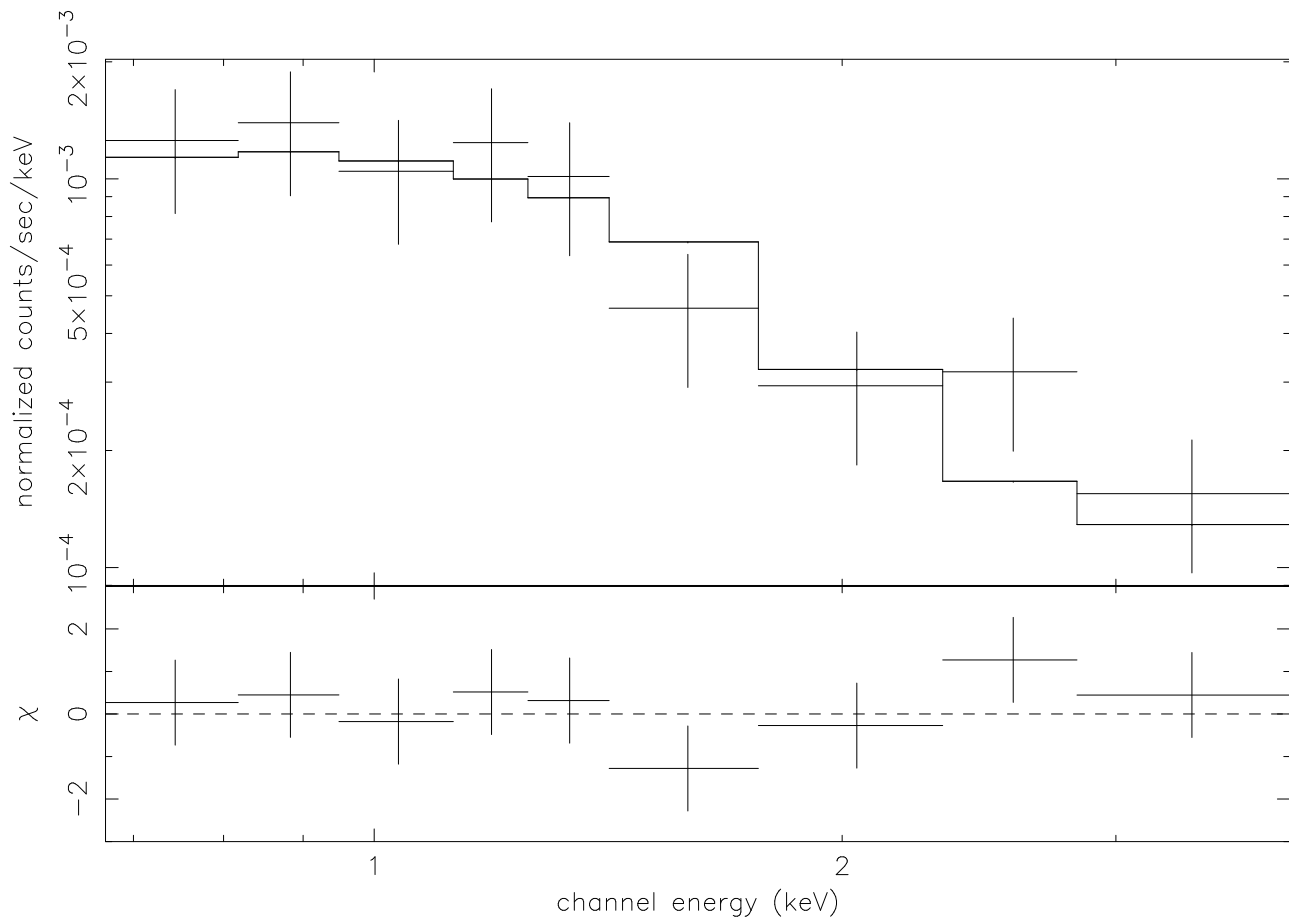


Figure 7.3: Energy spectrum of PSR B2224+65 as observed with the Chandra ACIS-S3 detector and fitted to an absorbed power-law model (*upper panel*) and contribution to the  $\chi^2$  fit statistic (*lower panel*).

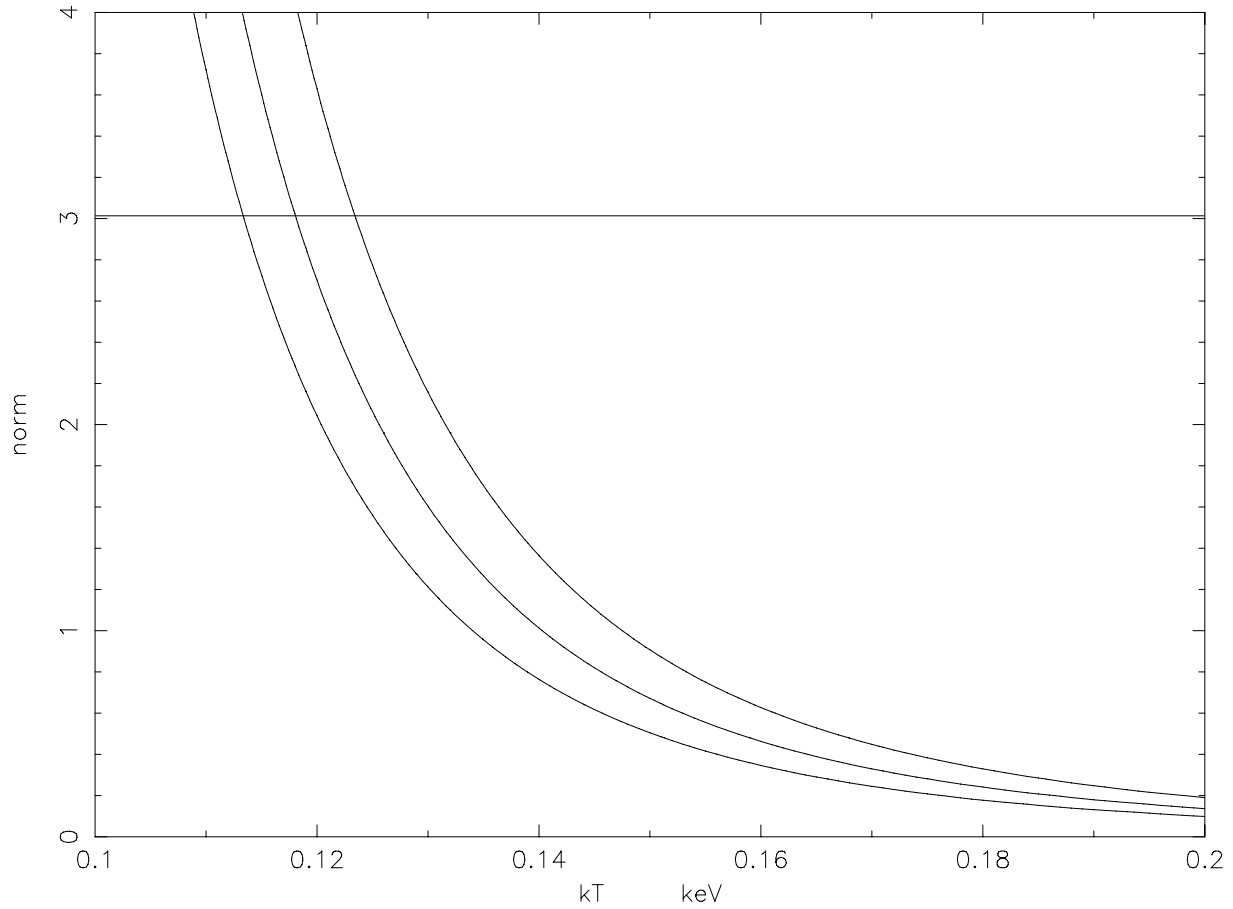


Figure 7.4: Portion of the  $1\sigma$ ,  $2\sigma$  and  $3\sigma$  confidence contours showing the blackbody normalization versus temperature for a blackbody model added on the best-fitted power law model. The horizontal line at a normalization of 3.06 corresponds to a polar cap radius of 175 m and a pulsar distance of 1 kpc as suggested by Chatterjee & Cordes (2004).

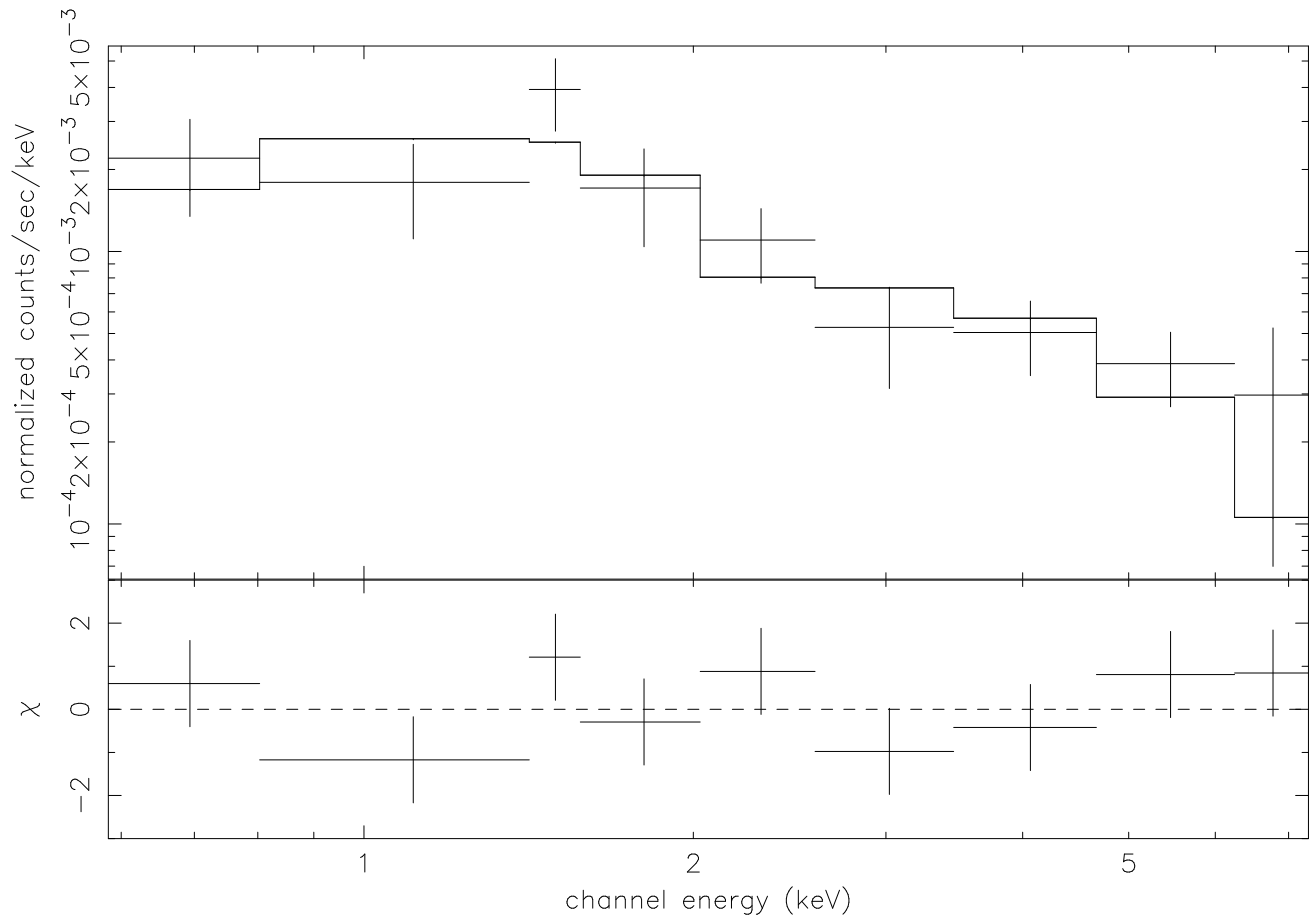


Figure 7.5: Energy spectrum of extended feature detected in the field of PSR B2224+65, as observed with Chandra ACIS-S3 detector and fitted to an absorbed power-law model (*upper panel*) and contribution to the  $\chi^2$  fit statistic (*lower panel*).

Table 7.3: The calculated  $f_0$  and  $f(r_{in}, \alpha_{\text{RVM}})$  of old pulsars according to CZ99 and Zhang et al. (2004) respectively.

PSR	$P$ (s)	$B$ ( $10^{12}G$ )	$\alpha_{\text{RVM}}$ (degree) <sup>a</sup>	$f_0 = 5.5P^{26/21}B_{12}^{-4/7}$	$f(r_{in}, \alpha_{\text{RVM}})$
B2224+65	0.68	2.58	-	1.99	-
B1929+10	0.23	0.51	35.97	1.31	0.62
B0628-28	1.24	3.02	70	3.82	0.58
B0950+08	0.25	0.25	74.6	2.18	0.23
B0823+26	0.53	0.98	81.1	2.54	0.12
J2043+2740	0.096	0.35	-	0.55	-

<sup>a</sup> The magnetic inclination angles  $\alpha_{\text{RVM}}$  are deduced from fitting the rotating vector model (RVM) to the radio polarization angle swing.  $\alpha_{\text{RVM}}$  of B0628-28 is taken from Becker et al. (2005). Others are adopted from Everett & Weisberg (2001).

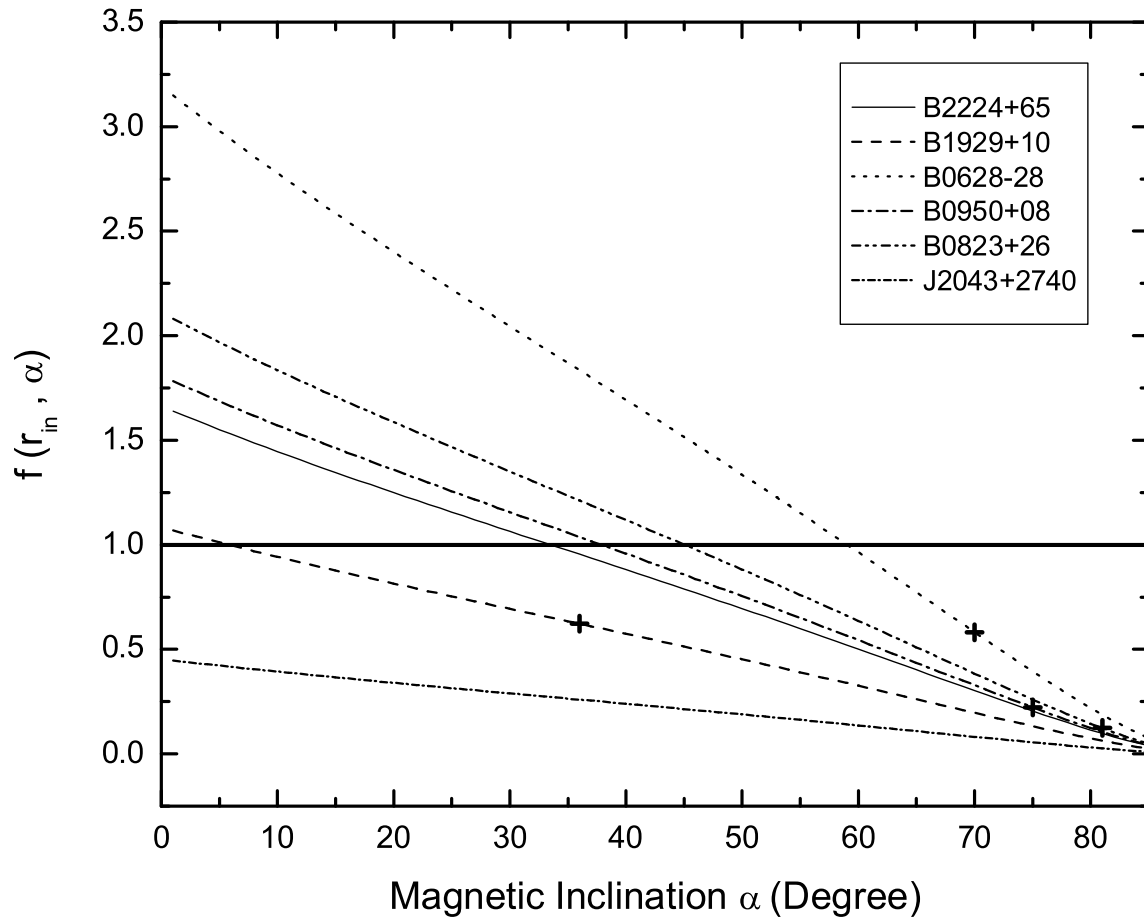


Figure 7.6: Variation of the fractional size of the outer-gap at the null charge surface with magnetic inclination angle for old pulsars. The crosses indicate the calculated  $f(r_{in}, \alpha_{RVM})$  for the pulsars with measured magnetic inclination angle (cf. Table 7.3).



# Chapter 8

## Chandra observation of the old pulsar PSR B1929+10

This chapter is adopted from the paper entitled “Resolving the bow-shock nebula around the old pulsar PSR B1929+10 with multi-epoch Chandra observations” which was submitted to *Astronomy & Astrophysics* at the time of thesis submission (Hui & Becker 2007c). The recent published version can be found in 2008, *Astronomy & Astrophysics*, volume 486 page 485.

### 8.1 Introduction

In the 90’s of the last century a series of powerful X-ray observatories were launched to space. Among many great results on various aspects in astrophysics they allowed a first detailed study of the X-ray emission properties of rotation-powered pulsars as a class (cf. Becker & Trümper 1997; Becker & Pavlov 2001 for a review). Most old<sup>1</sup> radio pulsars, though, were still too faint for a detailed study by these satellites (cf. Sun et al. 1993; Manning & Willmore 1994; Becker & Trümper 1997; Saito 1998). Old pulsars are clearly in the domain of the XMM-Newton and Chandra observatories. Observations of PSR B0950+08, B0823+26, J2043+2740 (Becker et al. 2004; Zavlin & Pavlov 2004), B0628-28 (Becker et al. 2005), B0943+10 (Zhang, Sanwal & Pavlov 2005), B1133+16 (Kargaltsev, Pavlov & Garmire 2006), B1929+10 (Becker et al. 2006) and B2224+65 (Hui & Becker 2007a) have finally allowed a first detailed view to the emission properties of old pulsars as a class. Surprisingly, the X-ray emission from old pulsars seems to be largely dominated by non-thermal radiation processes. Thermal components (e.g. account for the emission from hot polar caps) are not required to model the X-ray spectra of these pulsars. Further support for an emission scenario dominated by non-thermal radiation is found by the observed temporal emission properties. Pulse profiles, if detected with sufficient photon

---

<sup>1</sup>In standards of high energy astronomy rotation-powered pulsars are called young, middle aged and old if their spin-down age is of the order of few times  $10^3 - 10^4$  yrs,  $10^5 - 10^6$  yrs and  $\geq 10^6$  yrs, respectively. This classification is diffuse, though, with a smooth transition in between the different groups.

statistics, show multiple components and narrow features. This is indicative of strongly beamed emission which further invalidates the heated polar cap scenario as the main source of X-ray emission in old pulsars. The pulsed fractions in old pulsars are in the range of  $\sim 30 - 50\%$ .

In addition to the pulsar emission which is originating within the co-rotating magnetosphere extended trail-like X-ray emission was observed from PSR B1929+10 (Becker et al. 2006) and PSR B2224+65 (Hui & Becker 2007a) on a scale of several arc-minutes. In the case of PSR B1929+10 the X-ray emission in the trail is interpreted as synchrotron emission produced in the shock between the pulsar wind and the surrounding medium (see the discussion in Becker et al. 2006 for details). Owing to the moderate (15" Half Energy Width) spatial resolution of XMM-Newton, details of the nebular emission associated with PSR B1929+10 might have been remained unresolved. With a ten times improved angular resolution Chandra data can thus be essential to further constrain the properties of the nebula very near to the pulsar.

In this chapter we present a detailed analysis of multi-epoch Chandra observations of the field around PSR B1929+10<sup>2</sup>. According to its X-ray emission properties this source can be considered to be prototypical of an old pulsar (Becker et al. 2006). With a pulse period of  $P = 226.5$  ms and a period derivative of  $\dot{P} = 1.16 \times 10^{-15}$ , its characteristic age is determined to be  $\sim 3 \times 10^6$  years. These spin parameters imply a spin-down luminosity of  $\dot{E} = 3.9 \times 10^{33}$  erg s<sup>-1</sup> and a magnetic field at the neutron star magnetic poles of  $B_{\perp} \sim 5 \times 10^{11}$  G. With a radio dispersion measure of 3.178 pc cm<sup>-3</sup>, the NE2001 Galactic free electron density model of Cordes & Lazio (2002) predicts a distance of 170 pc. However, the recent astrometric measurements by Chatterjee et al. (2004) yielded a precise proper motion and parallax determination that translates into an accurate distance measurement of  $d = 361_{-8}^{+10}$  pc and a proper motion of  $V_{\perp} = 177_{-5}^{+4}$  km s<sup>-1</sup>. The ephemerides of PSR B1929+10 which we made use of in this paper are listed in Table 8.1.

In section 8.2 we describe the observations and data analysis, in section 8.3 we summarize the results and provide a discussion relative to the results obtained by XMM-Newton.

## 8.2 Observations and data analysis

Data analysis is restricted to the energy range 0.5 – 8.0 keV. All energy fluxes, however, are computed for the 0.5 – 10 keV band for better comparison with the results based on XMM-Newton data (Becker et al. 2006).

PSR B1929+10 was observed with Chandra in 2005 December 04 (Obs ID: 6657) and 2006 May 28 (Obs ID: 7230) with the Advanced CCD Imaging Spectrometer (ACIS). In both observations, PSR B1929+10 was located on the back-illuminated (BI) ACIS-S3 chip with an off-axis angle of  $\sim 0.1$  arcmin. Standard processed level-2 data were used. The effective exposures are  $\sim 21$  ks and  $\sim 25$  ks for the observations in 2005 December and 2006 May, respectively.

<sup>2</sup>A brief X-ray study of PSR B1929+10 with Chandra was recently presented by Misanovic, Pavlov & Garmire (2006).



### 8.2.1 Spatial analysis

With a view to obtain a better statistics for the the analysis, we combined both datasets to produced better images. Prior to the merging, aspect offsets for each observations, which is a function of the spacecraft roll angle, have been carefully checked and corrected.

The X-ray images of the  $4 \times 4$  arcmin field centered on PSR B1929+10 as well as a close-up of the central  $1 \times 1$  arcmin regions are shown in Figure 8.1 for both epochs. A compact nebula which has an arc-like morphology resembling somewhat a bow-shock is clearly detected around PSR B1929+10. The signal-to-noise ratio of this compact features is  $\sim 6.7$  in the energy band of  $0.5 - 8$  keV. X-ray contours were calculated at the levels of  $(6.1 - 26) \times 10^{-6}$  counts arcsec $^{-2}$  s $^{-1}$ . These contours were overlaid on the image in Figure 8.1b.

To further examined the extent of the compact nebula, we computed the radial profile from the raw image. It was calculated from a set of concentric rings centered at the pulsar position, each with a width of 0.5 arcsec. The radial profile is shown in Figure 8.2. In contrast with the expected point source model of a FWHM  $\simeq 0.5$  arcsec, we found that fitting a Gaussian model to the radial profile resulted in a FWHM of  $1.13 \pm 0.02$  arcsec ( $1\sigma$  error). Also, it apparently extended up to  $\sim 5$  arcsec before it falls to the background level of  $0.19 \pm 0.01$  cts/arcsec $^{-2}$  ( $1\sigma$  error).

We have also compared the individual fields from both epochs in order to search for the possible morphological variability of the compact nebula. Limited by the photon statistics from the individual datasets, no final conclusion can be drawn. In addition to the features near to the pulsar a clumpy structure (which is labeled as C in Figure 8.1b) is observed. There are only  $\sim 24$  net counts from this clump which does not allow a more detailed analysis on it. The signal-to-noise ratio of this clump is estimated to be  $\sim 2$  and thus is still in agreement with being background fluctuation.

In Figures 8.1a no prominent structure resembling the X-ray trail seen by ROSAT and XMM-Newton opposite to the pulsar's proper motion direction can be identified (cf. Figure 2 in Becker et al. 2006). We have further examined the Chandra images by smoothing the raw data with a kernel of  $\sigma < 6$  arcsec which is comparable with the FWHM of XMM-Newton's PSF. The smoothed images are displayed in Figure 8.3. Comparing the image with the contours calculated from XMM-Newton MOS1/2 data, a faint trail-like feature is noticed. However, the background contribution of this feature is estimated to be  $\sim 60\%$ . The unabsorbed X-ray flux of a 1 arcmin circular trail region near to the pulsar as detected by XMM-Newton is  $f_X = 5.3 \times 10^{-14}$  erg/s/cm $^2$  within the 0.5–10 keV band (Becker et al. 2006). The low significance of the trail in the two Chandra observations thus is in agreement with Chandra's lower sensitivity. We therefore will not further consider the X-ray trail emission in this paper and forward the interested reader to Becker et al. (2006) for a detailed discussion of its emission properties.

### 8.2.2 Spectral analysis

Although the spectrum from PSR B1929+10 has already been constrained tightly using XMM-Newton data (Becker et al. 2006) it is still essential for us to re-examine its spectral properties with Chandra since it better resolves the pulsar emission from the compact surrounding nebular component.

We extracted the pulsar spectrum in both data sets from a circle of 2 arcsec radius (encircled energy  $\sim 95\%$ ), centered on the pulsar, and fitted both simultaneously. The background spectrum was extracted from a source free region within a 10 arcsec radius centered at R.A.=19<sup>h</sup>32<sup>m</sup>14.107<sup>s</sup>, Dec.=10°59′51.57″ (J2000). After background subtraction,  $593 \pm 24$  and  $682 \pm 26$  net counts were available for the spectral analysis. These values imply the net counting rates of  $(2.84 \pm 0.11) \times 10^{-2}$  cts/s and  $(2.77 \pm 0.11) \times 10^{-2}$  cts/s for the observations in 2005 December and 2006 May respectively.

Response files were computed by using the tools MKRMF and MKARF in CIAO 3.4. Utilizing the most updated calibration data, CALDB 3.4.1, the generated response files have corrected the degradation of quantum efficiency in the ACIS CCD accordingly. Each spectrum was dynamically binned so as to have at least 30 counts per bin. To better constrain the spectral properties, we fitted the spectra obtain from both observations simultaneously. All the spectral fittings were performed in 0.5 – 8 keV by using XSPEC 11.3.2.. The parameters of all fitted model spectra are summarized in Table 8.2. All the quoted errors are 1 –  $\sigma$  and were computed for 1 parameter of interest.

Among the single component models which were tested we found that a power-law model fits the data best ( $\chi^2_\nu = 0.89$  for 36 D.O.F.). This model yields a column density of  $N_H = 2.40_{-0.34}^{+0.36} \times 10^{21}$  cm<sup>-2</sup>, a photon index of  $\Gamma = 2.91_{-0.13}^{+0.16}$  and a normalization at 1 keV of  $8.12_{-0.90}^{+1.04} \times 10^{-5}$  photons keV<sup>-1</sup> cm<sup>-2</sup> s<sup>-1</sup>. These best-fit values are well consistent with those obtained by XMM-Newton (see Table 3 in Becker et al. 2006). The best-fit power-law spectrum and residuals are shown in Figure 8.4. We have also computed the error contours to demonstrate the relative parameter dependences of the photon index vs. the hydrogen column density and plotted this in Figure 8.5. The unabsorbed flux deduced for the best fit power-law model parameters is  $f_X = 2.5 \times 10^{-13}$  ergs s<sup>-1</sup> cm<sup>-2</sup> within 0.5 – 10 keV. At a distance of 361 pc it implies a luminosity of  $L_X = 3.9 \times 10^{30}$  ergs s<sup>-1</sup>.

As for the XMM-Newton data it is obvious that the single power-law model already describes the observed pulsar spectrum very well. Hence, the justification of including an additional thermal component is absent. In the Chandra data, we found that fitting with a power-law plus blackbody model does not yield a reasonable solution if one let both blackbody radius and temperature be free parameters. It resulted in a blackbody radius of  $R = 25.81_{-25.81}^{+18.34}$  m which is about 12 times smaller than the size of a classic polar cap (i.e.  $r_{pc} = R(2\pi R/cP)^{1/2} \sim 300$  m). We quantified the statistical significance for adding this extra component to the power-law model with the  $F$ -test which suggest that inclusion of this thermal components is only required at a confidence level of 26%.

We have also examined the possible contributions from a classic polar cap and the neutron star surface by fixing the blackbody radius at  $R = 300$  m and  $R = 10$  km respectively. These fits resulted in temperatures of  $T \sim 8.7 \times 10^5$  K and  $T \sim 5.6 \times 10^5$  K.  $F$ -test sug-

gests that adding these thermal components to the power-law model is only significant at a confidence level  $< 62\%$ . Due to the better photon-statistics this number was even smaller in the XMM-Newton data (Becker et al. 2006). This low significance is also reflected by the relative contribution of the thermal component in the total energy flux observed by Chandra. For any thermal polar-cap contribution  $\sim 12\%$  is the  $1\sigma$  limit.

For the spectral model consisting of two blackbody components, we found that the best-fitted model parameters also agree well with those inferred from the XMM-Newton spectra (Becker et al. 2006). Despite the acceptable value of the goodness-of-fit, the inferred blackbody radii are too small to be considered as a reasonable description. Moreover, the pulsar spectrum obtained by XMM-Newton, which covered a wider energy bandwidth, has already shown that such model cannot describe the data beyond  $\sim 5$  keV (see Becker et al. 2006).

Since the arc-like nebula is resolved by Chandra for the first time, it is instructive to examine its energy spectrum, albeit the photon statistics is small. We extracted the nebular spectra from the regions in accordance with its observed morphology. For the sake of consistency, we adopted the same extraction region in both datasets. It consists of an annular region centered on the pulsar position with inner and outer radii of 2 arcsec and 5 arcsec, a circular region with a radius of 2.2 arcsec centered at R.A.= $19^{\text{h}}32^{\text{m}}14.006^{\text{s}}$ , Dec.= $+10^{\circ}59'25.63''$  (J2000), as well as an ellipse centered at R.A.= $19^{\text{h}}32^{\text{m}}13.329^{\text{s}}$ , Dec.= $+10^{\circ}59'30.12''$  (J2000) of a 4 arcsec semi-major axis and 8 arcsec semi-minor axis with the major axis oriented  $25^{\circ}$  east from the north.

The background spectra were extracted from each dataset within a nearby source free region of a 10 arcsec radius circle centered at R.A.= $19^{\text{h}}32^{\text{m}}15.470^{\text{s}}$  and Dec.= $+10^{\circ}59'29.01''$  (J2000). After background subtraction, there were  $29 \pm 5$  and  $41 \pm 7$  net counts extracted from the arc-like feature, implying the net counting rates of  $(1.29 \pm 0.26) \times 10^{-3}$  cts/s and  $(1.65 \pm 0.28) \times 10^{-3}$  cts/s for the observations in 2005 December and 2006 May respectively. Within the  $1\sigma$  errors of these count rates, no variability can be firmly concluded on the basis of these two observations. The response files were computed in the same manner as those for the pulsar spectra. Each spectrum was dynamically binned so as to have at least 10 counts per bin. In order to obtain a better statistic, we analyzed both spectra simultaneously.

We hypothesized that the nebular emission originates from the interaction of pulsar wind and the ISM. Synchrotron radiation from the ultra-relativistic electrons is generally believed to be the emission mechanism of the pulsar wind nebula, which is characterized by a power-law spectrum. We tested this hypothesis by fitting an absorbed power-law model to the nebular spectra. We fixed the column density at the value inferred from the best-fitted power-law model for the pulsar spectrum, namely  $N_H = 2.4 \times 10^{21} \text{ cm}^{-2}$ . We found that the model described the observed spectrum reasonably well ( $\chi_{\nu} = 0.88$  for 6 D.O.F.). The best-fit power-law spectrum and residuals are shown in Figure 8.6. This model yields a photon index of  $\Gamma = 2.00^{+0.32}_{-0.30}$  and a normalization at 1 keV of  $3.63^{+0.78}_{-0.74} \times 10^{-6}$  photons  $\text{keV}^{-1} \text{ cm}^{-2} \text{ s}^{-1}$ . The unabsorbed flux deduced for the best-fitted model parameters are  $f_X = 1.7 \times 10^{-14} \text{ erg s}^{-1} \text{ cm}^{-2}$  in the energy range of 0.5 – 10 keV. The pulsar distance of 361 pc implies a luminosity of  $L_X = 2.7 \times 10^{29} \text{ erg s}^{-1}$ .

We have checked the robustness of all the spectral parameters quoted in this paper by incorporating background spectra extracted from different source-free regions. We found that within the  $1\sigma$  errors the spectral parameters inferred from independent fittings are all consistent with each other.

### 8.3 Discussion

Complementing the XMM-Newton observation, we have studied PSR B1929+10 and its surrounding medium with Chandra which provides us data with sub-arcsecond resolution. So far three distinct components have been resolved, namely the pulsar itself, the X-ray trail opposite to the pulsars proper motion direction as well as the arc-like nebula surrounding the pulsar. The flux contributions from these components and the corresponding X-ray conversion efficiencies are summarized in Table 8.3.

For PSR B1929+10, we found that the spectral properties inferred from our analysis are in good agreement with the results obtained by XMM-Newton which did not allow the pulsar emission to be separated from the compact nebular component. The consistency is not unexpected even in the presence of the diffuse compact nebulae which contributes only  $\sim 7\%$  to the observed energy flux (see Table 8.3). Thus, the non-thermal emission scenario of PSR B1929+10 is confirmed. Hui & Becker (2007a) had argued that it is possible to sustain particle acceleration regions in PSR B1929+10's outer-magnetosphere (so-called outer-gap) if the inclination of the magnetic axis with respect to the rotational axis is taken into account. This inference is supported by the ability of the outer-gap model in reproducing the observed X-ray pulse profile and its phase shift relative to the radio pulse (see Fig. 16 Becker et al. 2006). However, such model is not without difficulty in explaining the observed properties of PSR B1929+10.

In the outer-gap model, the non-thermal X-rays result from the back-flowing charge particles from the outer gap (Cheng & Zhang 1999). When the primary electrons/positrons leave the outer-gap, they will emit curvature photons which are subsequently converted into secondary pairs in the presence of the strong magnetic field. Synchrotron photons will then be emitted by these secondary electrons/positrons. If these photons are energetic enough, they will further be converted into pairs which again lose their energy via synchrotron radiation. Therefore, an electromagnetic cascade is developed. Based on this model, Cheng & Zhang (1999) argued that the X-ray photon index resulting from such cascades should be  $\leq 2$ . This is obviously not in agreement with the observed photon index for PSR B1929+10 which is as steep as  $2.91^{+0.16}_{-0.13}$ . Observations of five other old pulsars: B1133+16 (Kargaltsev, Pavlov & Garmire 2006), B0943+10 (Zhang, Sanwal & Pavlov 2005), B0628-28 (Becker et al. 2005), B0823+26 (Becker et al. 2004) and J2043+2740 (Becker et al. 2004), also found the photon indices steeper than 2. This gives the outer-gap emission model a challenge. Re-examination of the model is thus required.

The morphology and the orientation of the arc-like nebula with respect to the pulsar's proper motion direction suggest a bow-shock nature. This is first well-defined bow-shock morphology observed among all old pulsars. A bow-shock nebula can be produced by a

pulsar in supersonic motion. In this case, the termination shock radius  $R_s$  is determined by the balance of the ram pressure between the relativistic pulsar wind particles and the ISM at the head of the shock (cf. Becker et al. 2006):  $R_s \simeq (\dot{E}/2\pi\rho_{ISM}v_p^2c)^{1/2} \sim 10^{16} \dot{E}_{34}^{1/2} n^{-1/2} v_{p,100}^{-1} \text{cm}$ , where  $v_{p,100}$  is the velocity of the pulsar in units of  $100 \text{ km s}^{-1}$ ,  $\dot{E}_{34}$  is the spin-down luminosity of the pulsar in units of  $10^{34} \text{ erg s}^{-1}$ , and  $n$  is the number density of the ISM in units of  $\text{cm}^{-3}$ . A density of  $1 \text{ cm}^{-3}$  implies a shock radius of  $R_s \sim 6 \times 10^{15} \text{ cm}$ . The stand-off angle  $\theta_s$  between the pulsar and edge of the shock in the forward direction is related to  $R_s$  by  $\theta_s = R_s \cos i/D$ , where  $D$  is the distance to the pulsar and  $i$  is the inclination angle between the proper motion and the plane of the sky. Taking the FWHM resulted from Gaussian fitting to the radial profile (i.e.  $1.13 \text{ arcsec}$ ) as the lower limit of  $\theta_s$ ,  $i < 15^\circ$  is implied, which suggests the pulsar travels in a direction very close to the sky plane.

The arc-like structure apparently elongates behind the direction of the proper motion by  $\sim 0.25 \text{ arcmin}$ . The time taken by the pulsar to pass through the arc-like structure is about  $\sim 150 \text{ years}$ . Following the discussion of Hui & Becker (2007b), we estimated the magnetic field in this shocked region by equating the passage time to the synchrotron cooling timescale  $\tau_{\text{syn}} = 6\pi m_e c / \gamma \sigma_T B^2$ .  $\simeq 10^5 (h\nu/\text{keV})^{-0.5} B_{\mu G}^{-3/2} \text{ yr}$ , where  $\gamma$  is the Lorentz factor of the wind, taken to be  $10^6$  (cf. Cheng et al. 2004),  $\sigma_T$  is the Thompson cross section, and  $B_{\mu G}$  is the magnetic field in the shocked region in unit of micro gauss. This implies a magnetic field of  $\sim 75 \mu G$ . Comparing this estimate to the typical strength in the ISM of  $\sim 2 - 6 \mu G$  (cf. Beck et al. 2003, and references therein), a very high compression factor of  $\sim 13 - 38$  in this shock region has been inferred.

The arc-shaped morphology of this newly resolved nebula is similar to that of Geminga (Caraveo et al. 2003). However, there is a main difference between these two cases. While the arc-like nebula of Geminga is rather symmetric with respect to the direction of proper motion, asymmetry is indicated in the case of PSR B1929+10 (see Fig. 1b). Asymmetric X-ray nebula was firstly observed in the field around PSR J2124-3358 (Hui & Becker 2006a). Its X-ray trail was found to be deviated from the pulsar's proper motion vector. As suggested by Hui & Becker 2006a, its asymmetric shape might be a result of the anisotropic pulsar wind and/or inhomogeneities in the surrounding ISM.

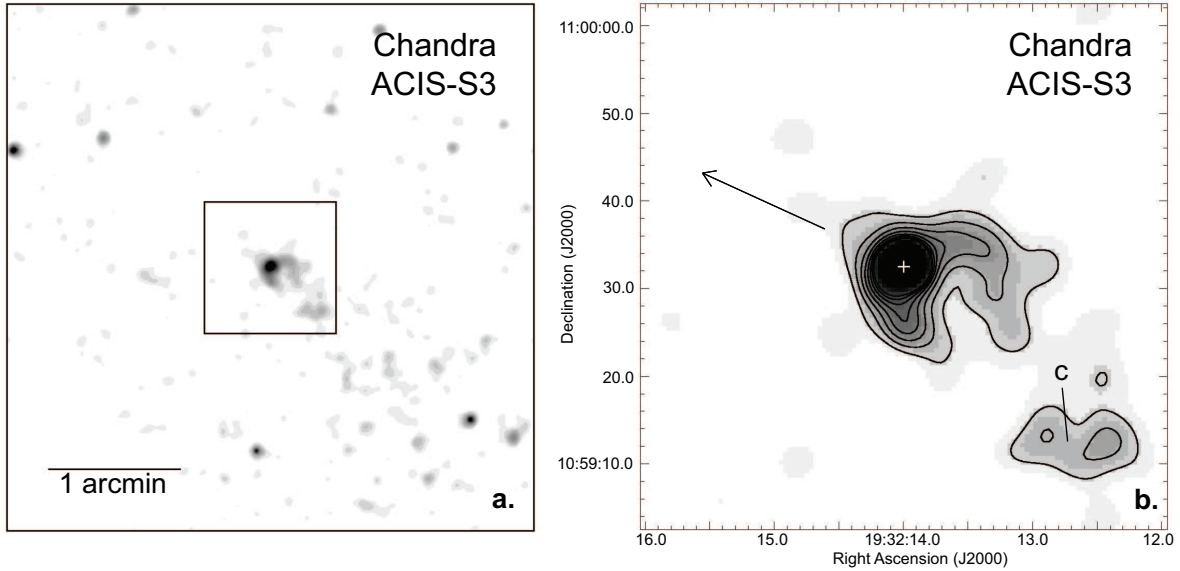


Figure 8.1: **(a)**  $4 \times 4$  arcmin image centered on PSR B1929+10 in the energy band of  $0.5 - 8$  keV. Top is north and left is east. The image is created by merging both Chandra observations. It is binned with a factor of 0.5 arcsec and adaptively smoothed with a kernel of  $\sigma < 2$  arcsec. **(b)** The close-up view of the central  $1 \times 1$  arcmin region as illustrated in **a**. The proper motion corrected pulsar position is indicated by the white cross. An arc-like feature associated with the pulsar is observed. The proper motion direction of the pulsar is illustrated by the arrow. Contour lines at the levels of  $(6.1 - 26) \times 10^{-6}$  counts arcsec $^{-2}$  s $^{-1}$  are overlaid.

Table 8.1: Ephemerides of PSR B1929+10 <sup>a</sup>

Right Ascension (J2000)	$19^{\text{h}}32^{\text{m}}13.983^{\text{s}} \pm 0.002^{\text{s}}$
Declination (J2000)	$+10^{\circ} 59' 32.41'' \pm 0.07''$
First date for valid parameters (MJD)	52929
Last date for valid parameters (MJD)	53159
Pulsar rotation period (s)	0.2265182954
Period derivative $\dot{P}$ ( $10^{-15}$ s s $^{-1}$ )	1.164739
Characteristic age ( $10^6$ yrs)	3.09
Surface dipole magnetic field ( $10^{12}$ G)	0.5129
Dispersion Measure (pc cm $^{-3}$ )	3.178
Distance (pc)	$361_{-8}^{+10}$
Spin-down Luminosity ( $10^{33}$ ) ergs s $^{-1}$	3.89

<sup>a</sup>Adopted from Becker et al. (2006)

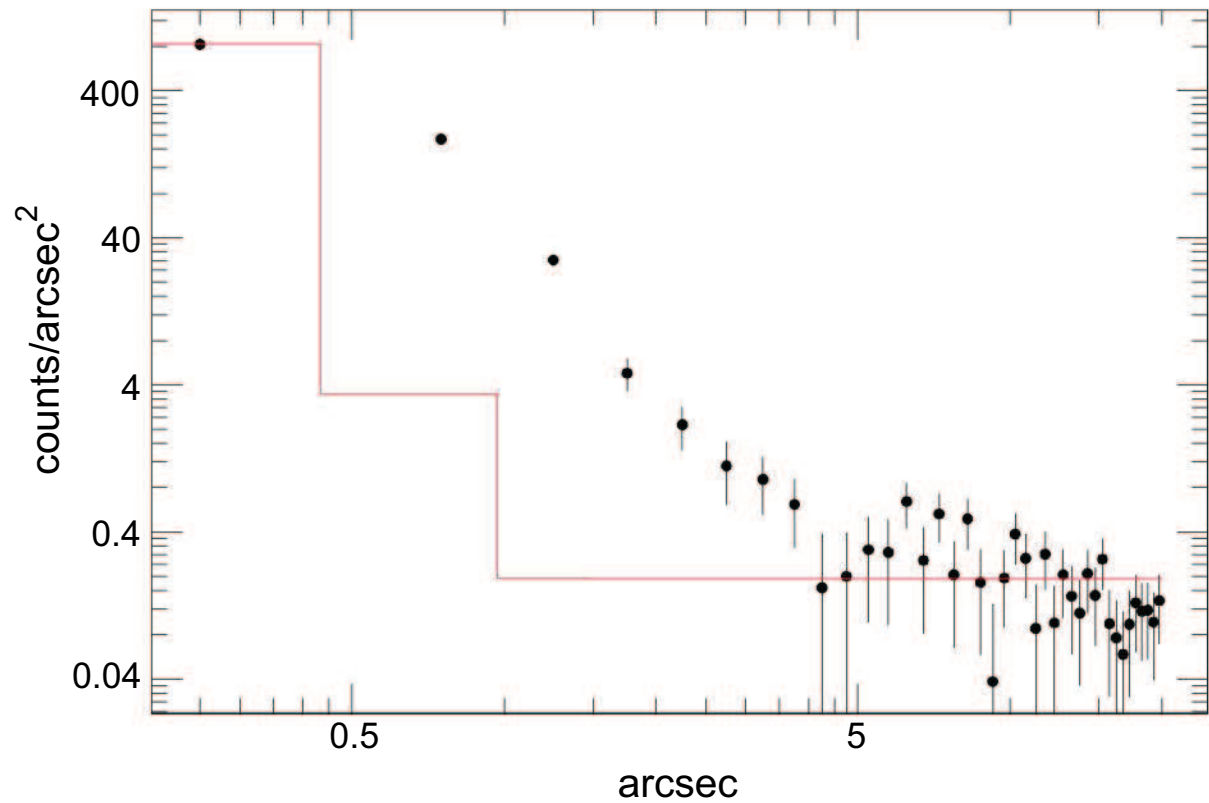


Figure 8.2: Radial profile centered at the proper motion corrected pulsar position. The profile is computed from the merged raw Chandra image. The solid line represents the addition of a PSF model normalized at the peak value of the image and a constant background at the level of 0.2 counts/arcsec<sup>2</sup>.

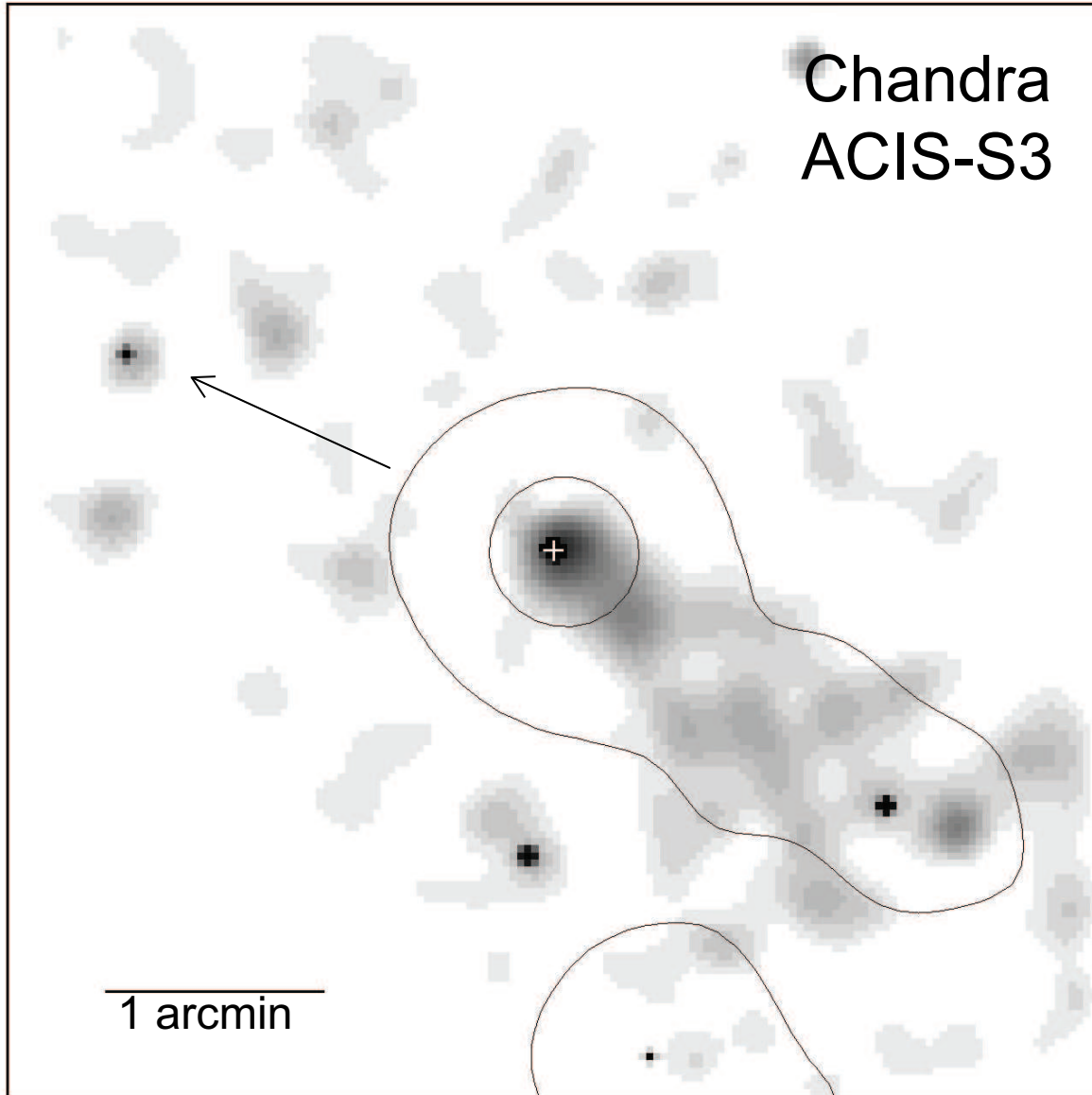


Figure 8.3:  $5 \times 5$  arcmin region around PSR B1929+10 in the energy band of  $0.5 - 8$  keV. The image is produced with a binning factor of 2 arcsec and adaptively smoothed with a kernel of  $\sigma < 6$  arcsec. Top is north and left is east. The contours calculated at the level of 0.09 and 0.44 counts  $\text{arcsec}^{-2}$  from the XMM-Newton's MOS1/2 image in the energy band  $0.2 - 10$  keV are overlaid on both images to illustrate the correspondence. The proper motion corrected pulsar position is indicated by the white cross. The proper motion direction of the pulsar is illustrated by the arrow in the images.



Table 8.2: Spectral parameters inferred from fitting the Chandra observed spectra of PSR B1929+10 and the associated extended feature.

Model <sup>a</sup>	$\chi^2_\nu$	D.O.F.	$N_H$ $10^{21} \text{ cm}^{-2}$	$\Gamma^b / kT$	Normalization at 1 keV <sup>c</sup> photons $\text{keV}^{-1} \text{ cm}^{-2} \text{ s}^{-1}$	Radius <sup>d</sup> m
PSR B1929+10						
PL	0.89	36	$2.40^{+0.36}_{-0.34}$	$2.91^{+0.16}_{-0.13}$	$8.12^{+1.04}_{-0.90} \times 10^{-5}$	-
BB	2.00	36	< 0.04	$0.36^{+0.01}_{-0.01}$	-	$29^{+2}_{-2}$
PL+BB	0.93	34	$1.40^{+1.09}_{-1.40}$	$2.48^{+0.52}_{-1.09}/0.29^{+0.05}_{-0.29}$	$4.60^{+6.29}_{-3.42} \times 10^{-5}$	$25.81^{+18.34}_{-25.81}$
PL+BB	0.92	35	$2.44^{+0.60}_{-0.39}$	$2.91^{+0.16}_{-0.16}/0.07^{+0.03}_{-0.07}$	$8.17^{+1.09}_{-0.94} \times 10^{-5}$	300
PL+BB	0.90	35	$2.72^{+1.06}_{-0.55}$	$2.97^{+0.27}_{-0.17}/0.05^{+0.01}_{-0.05}$	$8.67^{+2.25}_{-1.22} \times 10^{-5}$	10000
BB+BB	0.91	34	< 0.70	$0.71^{+0.21}_{-0.13}/0.27^{+0.03}_{-0.05}$	-	$5.37^{+3.43}_{-2.30}/42.32^{+22.74}_{-4.47}$
Arc-like feature						
PL	0.88	6	2.40	$2.00^{+0.32}_{-0.30}$	$3.63^{+0.78}_{-0.74} \times 10^{-6}$	-

<sup>a</sup> PL = power-law; BB = blackbody

<sup>b</sup> The entry in this column depends on the model in interest. It is the temperature  $kT$  in keV or the photon index  $\Gamma$

<sup>c</sup> The normalization constant for the power-law model.

<sup>d</sup> The radius of the blackbody emitting area is calculate for an assumed pulsar distance of 361 pc.

Table 8.3: Unabsorbed fluxes, luminosities and the conversion efficiencies of PSR B1929+10 and the nebular components in 0.5 – 10 keV

Component	$f_X$ ergs $\text{s}^{-1} \text{ cm}^{-2}$	$L_X^a$ ergs $\text{s}^{-1}$	$L_X/\dot{E}$
PSR B1929+10	$2.5 \times 10^{-13}$	$3.9 \times 10^{30}$	$1.0 \times 10^{-3}$
Trail-like feature <sup>b</sup>	$5.3 \times 10^{-14}$	$8.3 \times 10^{29}$	$2.1 \times 10^{-4}$
Arc-like feature	$1.7 \times 10^{-14}$	$2.7 \times 10^{29}$	$6.9 \times 10^{-5}$

<sup>a</sup> Luminosities are calculated at the assumed pulsar distance of 361 pc

<sup>b</sup> Adopted from Becker et al. (2006)

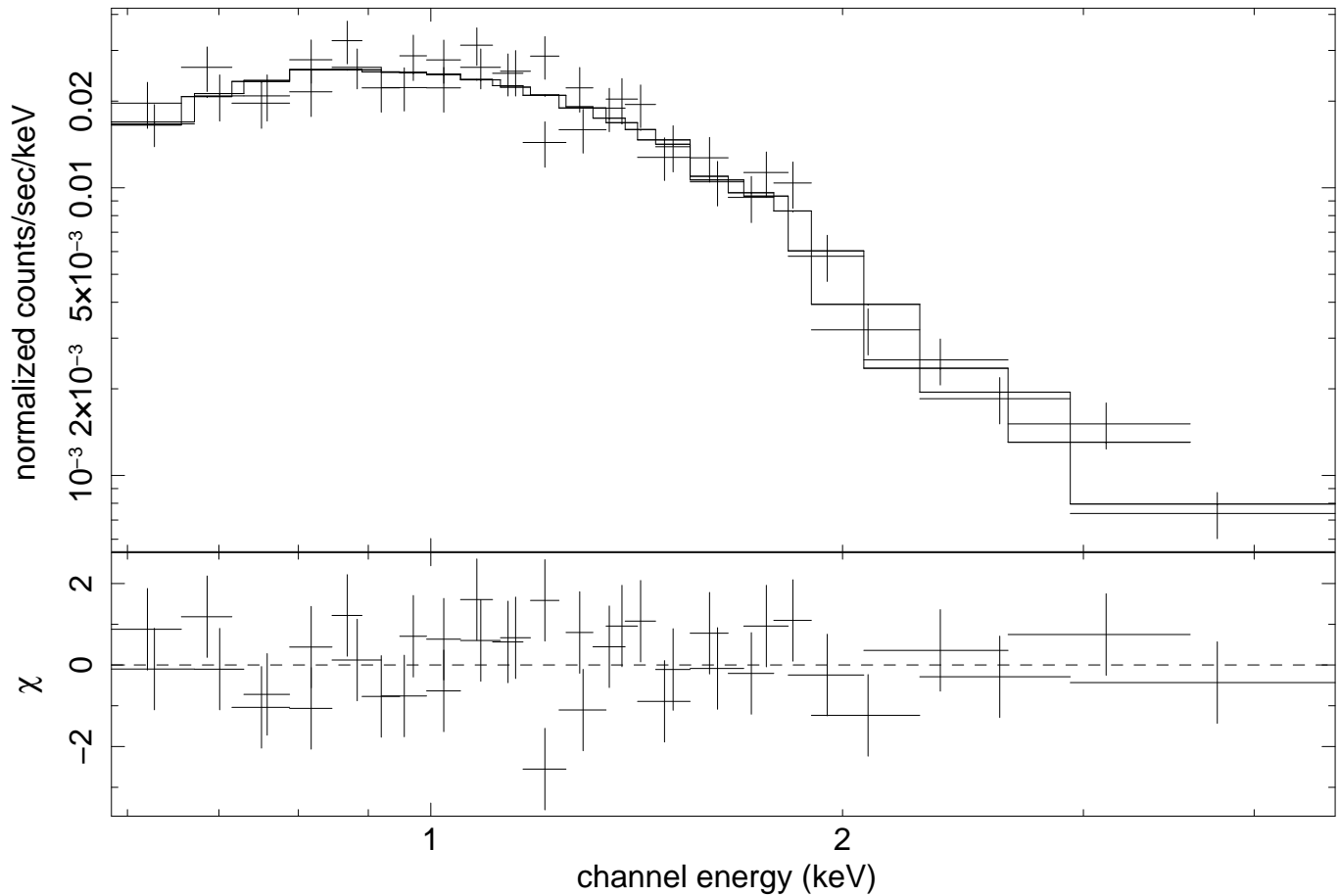


Figure 8.4: Energy spectra of PSR B1929+10 as observed with the Chandra ACIS-S3 detector on 04 Dec 2005 and 28 May 2006 and simultaneously fitted to an absorbed power-law model (*upper panel*) and contribution to the  $\chi^2$  fit statistic (*lower panel*).

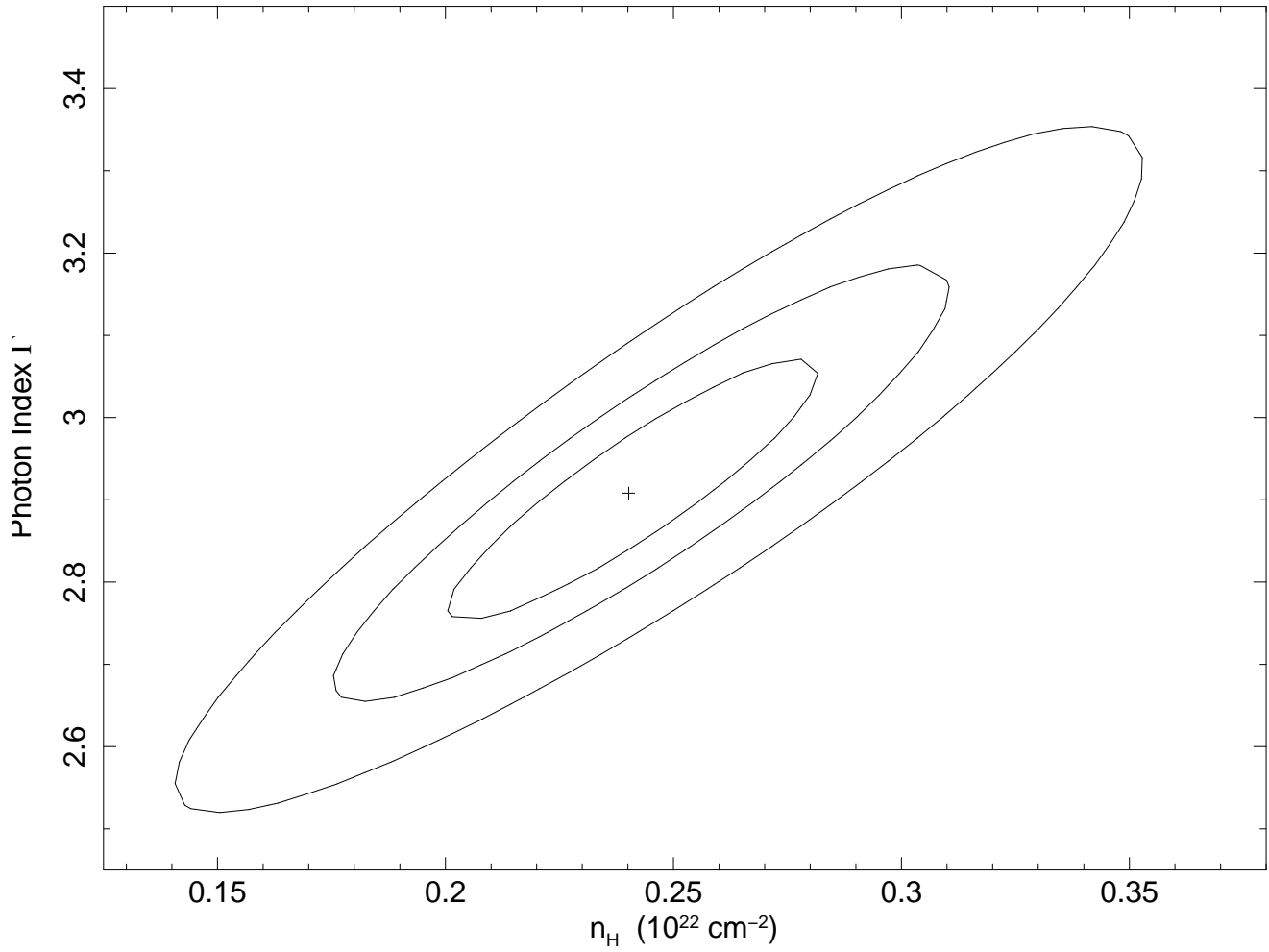


Figure 8.5:  $1\sigma$ ,  $2\sigma$  and  $3\sigma$  confidence contours calculated for 1 parameter of interest for the power-law model fitted to the spectrum of PSR B1929+10.

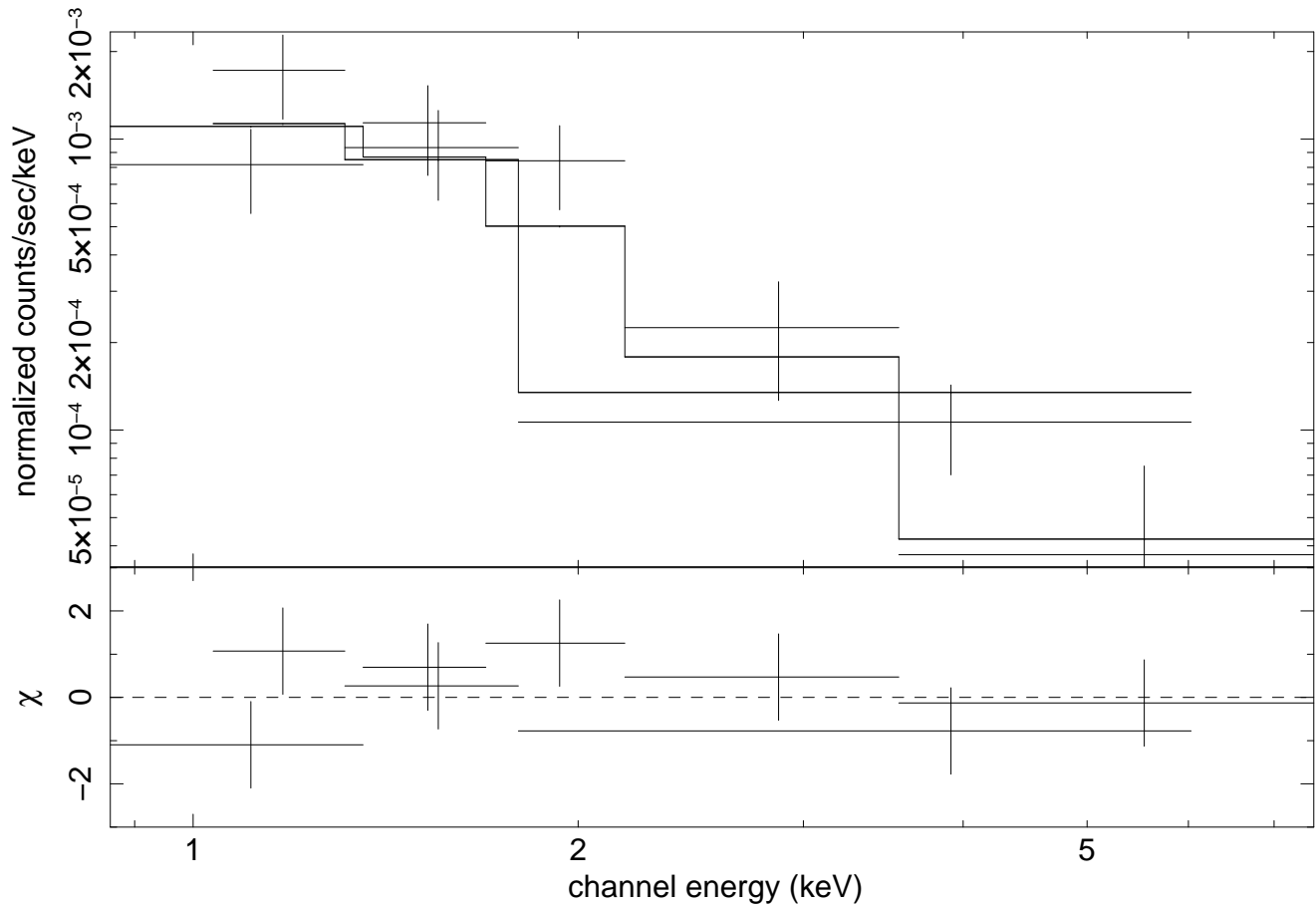


Figure 8.6: Energy spectra of the arc-like structure associated with PSR B1929+10 as observed by the Chandra ACIS-S3 detector on 04 Dec 2005 and 28 May 2006 and simultaneously fitted to an absorbed power-law model (*upper panel*) and contribution to the  $\chi^2$  fit statistic (*lower panel*).

# Chapter 9

## Searches for X-ray counterparts of millisecond pulsars in M28

This chapter is adopted from the paper entitled “A search for X-ray counterparts of the millisecond pulsars in the globular cluster M28 (NGC 6626)” which is submitted to *Astronomy & Astrophysics* (Becker, Hui & Bégin 2007).

### 9.1 Introduction

About 10% of the 1765 known radio pulsars are millisecond pulsars (MSPs). The majority of them<sup>1</sup>, currently 134, are located within 24 globular clusters (GCs) which, because of their extreme stellar core density, lead to dynamical interactions that apparently play a significant role in the formation of MSPs. The first MSP discovered in a globular cluster was PSR J1824–2452A in M28 (Lyne et al. 1987). Its inferred pulsar parameters make it the youngest ( $P/2\dot{P} = 3.0 \times 10^7$  yrs) and most powerful ( $\dot{E} = 2.24 \times 10^{36}$  erg s<sup>-1</sup>) pulsar among all known MSPs. A recently performed deep radio survey of M28 which was designed to search for more cluster pulsars led to the discovery of ten new MSPs (Bégin 2006). Together with the previously discovered PSR J1824–2452A, four pulsars in M28 are found to be solitary. The others are in binaries. Two pulsars are found to be in highly eccentric binary systems with eccentricities of  $e = 0.847$  and  $0.776$ , respectively, and companion masses of at least  $0.26 M_{\odot}$  and  $0.38 M_{\odot}$  (Bégin 2006). M28 is now the globular cluster with the third largest population of known MSPs pulsars, after Terzan 5 and 47 Tucanae (Camilo et al. 2000, Ransom et al. 2005, Stairs et al. 2006).

In this chapter, we report on a re-analysis of Chandra ACIS-S data from the globular cluster M28. It was performed to search for X-ray counterparts of the newly discovered MSPs. The re-analysis builds partly on the analysis of the M28 Chandra data which was published by Becker et al. (2003).

---

<sup>1</sup><http://www2.naic.edu/~pfreire/GCpsr.html>

## 9.2 Observations and Data Analysis

M28 was observed by the Chandra ACIS-S three times for approximately equal observing intervals of about 13 ksec between July and September 2002. These observations were scheduled so as to be sensitive to time variability on time scales up to weeks. The observations were made using 3 of the *CXO* Advanced CCD Imaging Spectrometer (ACIS) CCDs (S2,3,4) in the faint timed exposure mode with a frame time of 3.241 s. Standard *Chandra* data processing has applied aspect corrections and compensated for spacecraft dither. Level 2 event lists were used in our analyses. Events in pulse invariant channels corresponding to  $\approx 0.2$  to 8.0 keV were selected for the purpose of finding sources. Increased background corrupted a small portion of the third data set reducing its effective exposure time from 14.1 ksec to 11.4 ksec although no results were impacted by the increased background.

The optical center of the cluster at  $\alpha_{2000} = 18^{\text{h}}24^{\text{m}}32.89\text{s}$  and  $\delta_{2000} = -24^{\circ}, 52'11.4''$  (Shawl and White 1986) was positioned 1 arcmin off-axis to the nominal aim point on the back-illuminated CCD, ACIS-S3, in all 3 observations. A circular region with 3.1''-radius, corresponding to twice the half-mass radius of M28, centered at the optical center was extracted from each data set for analysis. No correction for exposure was deemed necessary because the small region of interest lies far from the edges of the S3 chip.

Applying a wavelet source detection algorithm, the X-ray position of PSR J1824–2452A was measured separately using the three data sets and the merged data. The set-averaged position is the same as that derived using the merged data set and was found to be in agreement with the pulsar’s radio position. The result is summarized in Table 8.1. The root-mean-square (rms) uncertainty in the pulsar position, based on the 3 pointings, is 0.042'' in right ascension and 0.029'' in declination. The radio position and proper motion of the pulsar, as measured by Rutledge et al. (2003), places the pulsar at the time of the observation only  $\Delta_{\alpha} = 0.083''$ ,  $\Delta_{\delta} = -0.042''$  away from the best-estimated X-ray position. In what follows the X-ray positions of all sources have been adjusted to remove this offset.

In addition to the 37.6 ksec of ACIS-S data we reanalyzed about 100 ksec of HRC data which were available from M28 in the Chandra archive. Part of this data were taken in 2002 October 11. and were used by Rutledge et al. (2003) to investigate the temporal X-ray emission properties of PSR J1824–2452A. The second half of the HRC-S data was taken more recently, in 2006 May 27. & 28., for the purpose of Chandra on-board clock calibration. However, both HRC data sets were taken in *timing mode* and hence suffer from very high background as in this mode all photons which are registered in the detector are transmitted to the ground to allow a correction for the detectors timing bug (cf. Tenant et al. 2001). As far as the detection of faint sources is concerned the available ACIS-S data supersede the HRC data in sensitivity, albeit more than 60% shorter in exposure time. We therefore did not further consider the HRC data for the search of X-ray counterparts of the newly discovered MSPs.

Amongst the many interesting results we obtained from the ACIS-S observation and which were reported already in detail in Becker et al. (2003), this data detected 46 X-ray sources in a field of 4 arcmin near to the pulsar PSR J1824–2452A. 12 of these sources

are located within the 14.4 arcsec cluster core radius. The properties of these sources along a detailed spectral analysis for the brightest among them was published in Becker et al. (2003) so that we can omit to repeat all details of our previous analysis here again. To briefly summarize few basic findings in the following, though, might be convenient for the reader.

The brightest source in the ACIS-S data (#26 in Table 3 of Becker et al. 2003), which is also the one with the softest spectrum, was identified as a candidate LMXB in quiescence, whereas all the other sources in the field turned out to have rather hard X-ray spectra. Source #19 (cf. Table 3 of Becker et al. 2003 and Figure 9.1 below), which emits the hardest X-rays, is the millisecond pulsar PSR J1824–2452A. Several of the other X-ray sources seen in M28 were found to show variability on time scales of hours to weeks and are still unidentified.

The superior  $\sim 1$  arcsec angular resolution of Chandra not only allowed us to resolve PSR J1824–2452A from nearby sources which in the ROSAT HRI were only seen as diffuse unresolved emission, it furthermore provided the first uncontaminated, phase-averaged, spectrum from the brightest among all millisecond pulsars. This spectrum was found to be best described by a power law with photon index  $1.2^{+0.15}_{-0.13}$ . PSR J1824–2452A thus has a very hard X-ray spectrum which made it to detect the pulsar up to  $\sim 20$  keV with RXTE (Mineo et al. 2004). Exciting to note and most interesting, however, is the evidence of an emission line feature centered at  $\sim 3.3$  keV in the pulsar spectrum (cf. Fig. 2 in Becker et al. 2003). This line feature can be interpreted as cyclotron emission from a corona above the pulsar’s polar cap if the magnetic field is different from a centered dipole configuration. The significance of the feature, however, is at the edge of detectability which prevents any final conclusion and clearly calls for confirmation in a further deeper observation.

Figure 9.1 shows the central region of M28 as seen by Chandra ACIS-S3 between July and September 2002. The image was created with a spatial binning of 0.5 arcsec. Positions of PSR J1824–2452A and nine newly discovered millisecond pulsars <sup>2</sup> are indicated (cf. Table 9.2). Inspecting the data for possible emission from the newly discovered MSPs shows that there is some faint unresolved X-ray emission near to the center of M28 (cf. Figure 9.1) which is coincident with the locations of four of the new MSPs: PSR J1824-2452G, J1824-2452J, J1824-2452I and J1824-2452E. The position of the eclipsing binary millisecond pulsar PSR J1824–2452H reported by Bégin (2006) is found to be  $\sim 0.2$  arcmin north from the position of CXC 182431-245217 which is source #18 reported in Becker et al. (2003). Follow-up observations, however, had found that the position of PSR J1824–2452H in agreement with CXC 182431-245217 (Ransom 2007). The identification of this X-ray source as a pulsar is further supported by the similarity of its hardness ratio with that of PSR J1824–2452A and the lack of variability (cf. Table 3 in Becker et al. 2003). By measuring the counts within a circle of 2 arcsec (encircled energy  $\sim 95\%$ ) at the MSP source positions, we have determined the counting rates and upper limits for the 10 out of 11 pulsars in M28. The results are listed in Table 9.2 together with the a summary of the millisecond pulsar parameters (Bégin 2006).

<sup>2</sup>The position of PSR J1824–2452K is not available in Bégin (2006)

Because of the low ACIS-S instrument background, the counts obtained from the location of the MSPs J1824-2452G, J1824-2452I and J1824-2452J suggest that there is significant emission from these sources, albeit unresolved and at the edge of sensitivity in the available data. This suggests, however, that in a deeper Chandra ACIS-S observation it will be possible to resolve and detect the emission from all these new pulsars and to obtain spectral information from them. The pulsar PSR J1824–2452H (respectively CXC 182431-245217) is detected with a signal-to-noise ratio of 2.88. Determining its counting rate yields  $(2.9 \pm 0.9) \times 10^{-4}$  cts/s, corresponding to an 0.2 – 8.0 keV X-ray luminosity of  $1.2 \times 10^{31}$  erg/s for an assumed power-law spectrum with a photon-index of 2, a source distance of 5.5 kpc and a column absorption of  $0.18 \times 10^{22}$  cm<sup>-2</sup>. Albeit this is only a rough luminosity estimate, the X-ray conversion concluded from it is  $3.6 \times 10^{-4}$ .

### 9.3 Discussion

Since the *Einstein* era it has been clear that globular cluster contain various populations of X-ray sources of very different luminosities (Hertz & Grindlay 1983). The stronger sources ( $L_x \approx 10^{36} - 10^{38}$  erg s<sup>-1</sup>) were seen to exhibit X-ray bursts which led to their identification as low-mass X-ray binaries (LMXBs). The nature of the weaker sources, with  $L_x \leq 3 \times 10^{34}$  erg s<sup>-1</sup>, however, was more open to discussion (e.g., Cool et al. 1993; Johnston & Verbunt 1996). Although many weak X-ray sources were detected in globulars by ROSAT (Johnston & Verbunt 1996; Verbunt 2001), their identification has been difficult due to low photon statistics and strong source confusion in the crowded globular cluster fields. It was therefore clear that Chandra with its sub-arcsecond angular resolution would contribute tremendously to the investigation of globular clusters. The results which have been published on this subject so far has shown that these expectations were justified. Among the results we obtained on M28 (Becker et al. 2003) important work has been done on Terzan 5 (Heinke et al. 2006) and of 47 Tuc = NGC 104. From the latter, Grindlay et al. (2001) reported the detection of 108 sources within a region corresponding to about 5 times the 47 Tuc core radius. Nineteen of the soft/faint sources were found to be coincident with radio-detected millisecond pulsars (Bogdanov et al. 2006) and Grindlay et al. (2001a, 2002) concluded that more than 50 percent of all the unidentified sources in 47 Tuc are MSPs. This conclusion is in concert with theoretical estimates on the formation scenarios of short-period (binary) pulsars in globular clusters (e.g. Rasio, Pfahl & Rappaport 2000).

Some of the unresolved excess of X-ray emission from within the central part of M28 that we reported in Becker et al. (2003) is likely due to point sources that were just below the 38-ksec sensitivity limit. The recent discovery of the new MSPs, which are partly in positional agreement with this excess emission, strongly support the conjecture. We also know from Chandra observations of 47 Tuc that the soft emission from millisecond pulsars, like those found in that cluster, tend to be below the sensitivity limit of the previous Chandra M28 observation because of the higher absorption towards M28. Hence it is quite likely that a deeper exposure will reveal more, faint, X-ray sources which might turn out to be millisecond pulsars as well. Apart from resolving the diffuse emission, a



second deeper observation will add significant information to those faint sources for which a detailed spectral modeling was precluded by limited photon statistics in the existing 38-ksec ACIS-S data.

As all these MSPs in M28 are virtually located at the same distance from us detecting them will allow one to investigate their relative X-ray efficiency,  $L_x/\dot{E}$ , unbiased by distance uncertainties. Grindlay et al. (2002) found that the dependence of  $L_x$  on  $\dot{E}$  for 47 Tuc MSPs may be  $L_x \propto \dot{E}^{0.5}$ , i.e. significant flatter than the  $L_x/\dot{E} = 10^{-3}$  observed for pulsars located in the galactic plane (cf. Becker & Trümper 1997). The 47 Tuc MSPs were found to be consistent with the X-radiation being emitted from heated polar caps. Whether this will be the dominating X-ray emission process of the newly discovered MSPs in M28 and whether their X-ray efficiency will be consistent with  $L_x \propto \dot{E}^{0.5}$  or with  $L_x/\dot{E} = 10^{-3}$  will be a question one can address with data of higher photon statistics.

Several of the other sources we detected previously in M28 exhibit variability on time scales of weeks. Our M28 X-ray survey also found a large number of objects that were bright in only a single observation. Some of these latter objects were bright because they flared during the observation (i.e., not only were they bright in one observation, they were bright for only part of the observation). We suspect that these sources are flare stars (RS CVn or BY Dra). There were a few additional sources seen in the HRC observation of M28 by Rutledge et al. (2004) —performed only a few weeks after the ACIS-S observations. These sources either turned on at, or in between, the two observations. As long as each star is only seen to flare in one observation then all that we know is that the total population is larger than the number that we have seen in the previous 38-ksec observation. However, if one sees the same flare stars more than once it will allow one to better estimate the total source population.

Table 9.1: PSR J1824–2452A positions (J2000)

Date	Position	
2002 July 4	18 24 32.015	–24 52 10.81
2002 Aug 8	18 24 32.016	–24 52 10.76
2002 Sep 9	18 24 32.009	–24 52 10.83
average	18 24 32.013	–24 52 10.80
rms (arcsec)	0.042	0.029
merged data	18 24 32.013	–24 52 10.80
radio (8/02)	18 24 32.008	–24 52 10.76

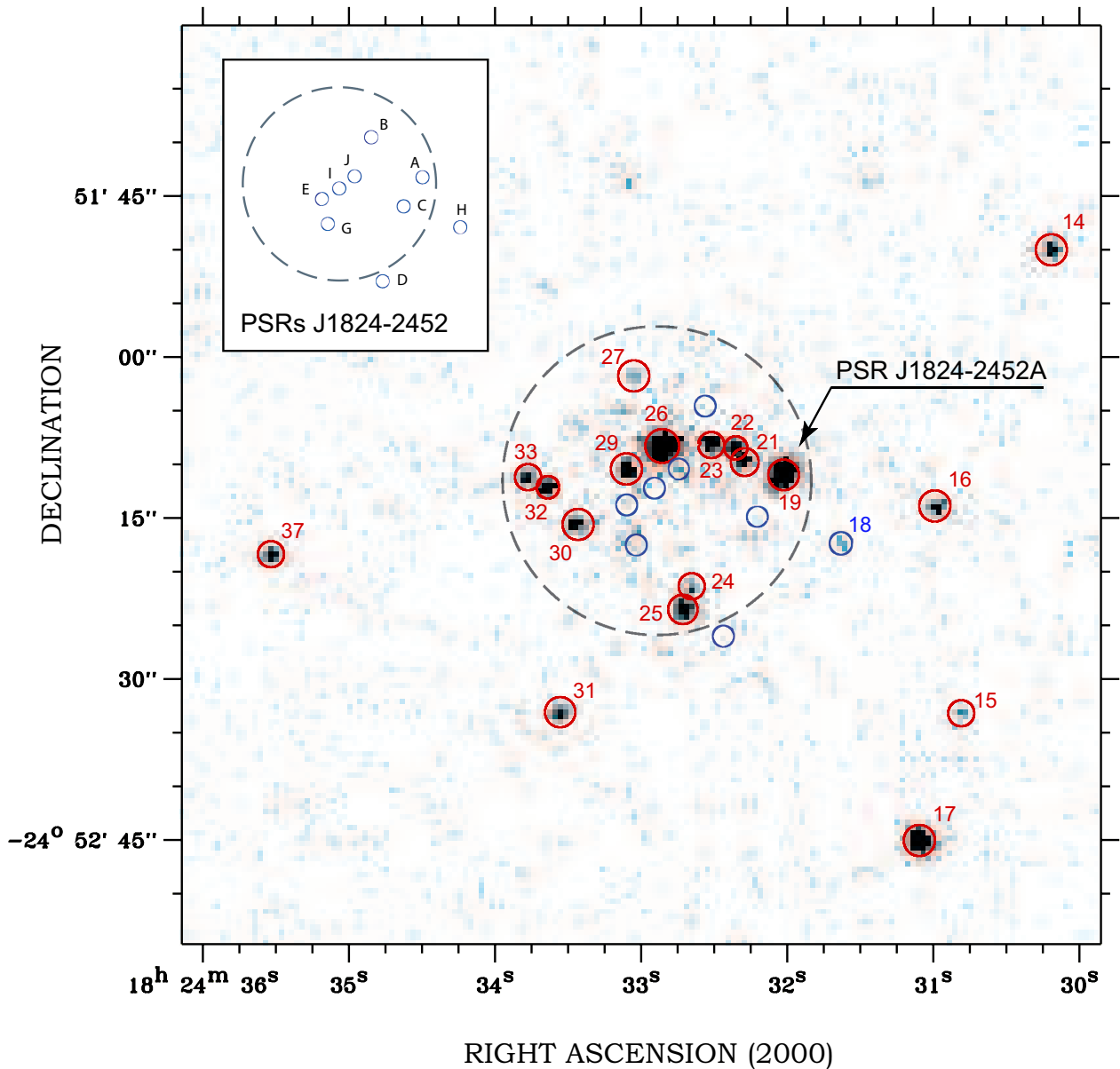


Figure 9.1: *Chandra* ACIS-S3 image of the central region of M28. The positions of the recently discovered new ms-pulsars are indicated by blue circles. Most are located within or near to the core-radius (dashed circle). One of the new ms-pulsars is placed outside the field shown in this plot. The binary millisecond pulsar PSR J1824–2452H is in agreement with source #18 reported in Becker et al. (2003). There is faint (only partly resolved) emission near to the center of the cluster which is in agreement with the location of the new pulsars PSR J1824–2452J, J1824–2452I and J1824–2452E. The inset helps to locate the different MSPs.

Table 9.2: Basic properties of millisecond pulsars located in the globular cluster M28 and their counting rates in Chandra ACIS-S data. The position of J1824-2452H is the Chandra X-ray position while for the other pulsars it is the radio timing position from Bégin (2006).

Name	Ra H:M:S	Dec D:M:S	P $10^{-3}$ s	$\dot{E}$ $10^{34}$ erg/s	$B_{\perp}$ $10^9$ G	ACIS-S net counts	rate cts/s
J1824-2452A	18 24 32.007	-24 52 10.49	3.0543	22.243		1100	2.63e-2
J1824-2452B	18 24 32.545	-24 52 04.29	6.5466		< 0.4	3	7.89e-5
J1824-2452E	18 24 33.089	-24 52 13.57	5.4191		< 0.8	5	1.32e-4
J1824-2452F	18 24 31.812	-24 49 25.03	2.4511	2.5198	< 0.5	1	2.63e-5
Binary pulsars:							
J1824-2452G	18 24 33.025	-24 52 17.32	5.90905	3.4228	< 1.6	17	4.47e-4
J1824-2452H	18 24 31.591	-24 52 17.49	4.62941	3.2586	< 1.1	11	2.89e-4
J1824-2452I	18 24 32.9	-24 52 12.00	3.93180			12	3.16e-4
J1824-2452J	18 24 32.733	-24 52 10.18	4.03968		< 0.6	22	5.78e-4
Eccentric binary pulsars:							
J1824-2452C	18 24 32.192	-24 52 14.66	4.15828	9.3416	< 1.2	3	7.89e-5
J1824-2452D	18 24 32.422	-24 52 25.90	79.8354	7.6183	$\sim 91.0$	2	5.26e-5



# Chapter 10

## Conclusions & Discussions

In the chapter, I would like to summarize the results reported in the previous chapters and discuss their impacts on our understanding of the nature of neutron stars. The prospects of further studies in these subjects would also be mentioned.

### 10.1 The nature of central compact objects in supernova remnants

Among many different manifestations of neutron stars, the one of the central compact objects (CCOs) is among the most enigmatic class. In this thesis, we have examined the physical properties of two CCOs located in the supernova remnants Puppis-A as well as Vela-Junior. These CCOs are generally accepted as the young neutron stars formed in core-collapsed supernova explosions. However, their emission properties are found to be very different from those observed in young canonical pulsars in many aspects.

While the X-ray emission of young rotation-powered pulsars are generally dominated by magnetospheric emission which is characterized by a power-law spectrum, the X-ray spectra of these CCOs can be well-modeled with a double blackbody model or a blackbody plus a steep power-law model with photon index  $> 3$ . Utilizing the superior spatial resolution of Chandra, we found no evidence of any plerionic emission, which are typically powered by Crab-like pulsars, around the CCO in Puppis-A down to an accuracy of sub-arcsecond. Moreover, making use of two Chandra HRC-I observations with an epoch separation of somewhat more than five years we have probed the proper motion of this CCO. This is the first case that a CCO's proper motion being measured directly. Our result suggests that the transverse velocity of this object is at a magnitude of  $\sim 1000$  km/s which is about 4 times higher than the average velocity observed in ordinary pulsars.

Our spectral analysis of the CCOs suggest the presence of high temperature hot spots on the stellar surfaces. Under a favorable viewing geometry, low-amplitude periodic signals produced by the rotating hot spots can possibly be observed. Searching for possible pulsations, we have revealed an interesting periodicity candidate from the CCO in Puppis-A. A periodic signal at  $\sim 0.22$  s has been marginally detected. Although the significance of

the detection is rather low, the signal is found with comparable properties (e.g. pulsed fraction, shape of the pulse profile, signal strength) in two independent XMM-Newton observations which were taken about 7 months apart from each other. The period derivative calculated from the separation of the epochs of the two XMM-Newton observations is  $\dot{P} = (2.112 \pm 0.002) \times 10^{-10} \text{ s s}^{-1}$ . This is comparable with  $\dot{P} = (0.8 - 4.7) \times 10^{-10} \text{ s s}^{-1}$  which is the largest spin-down rate known for a neutron star and has been observed in the soft gamma-ray repeater (SGR) SGR 1806-20 (Kouveliotou et al. 1998; Woods et al. 2002). If the periodic signal found in RX J0822-4300 is confirmed it suggests a non-steady spin-down behavior for this source as well as making it joining the exclusive group of SGR 1806-20 and SGR 1900+14 which both show large changes in the spin-down torque up to a factor of  $\sim 4$  (Woods et al. 2002).

Similar to the other SGRs in quiescence, a recent XMM-Newton observation of SGR 1627-41 has found that its spectrum is rather soft (Mereghetti et al. 2006). Both, a steep power-law and a high temperature blackbody model are able to fit the SGR spectrum. This is similar to the spectral behavior seen in many CCOs. Taken this similarity and the putative periodicity together it may suggest that the CCO in Puppis-A resembles a SGR in some way. This makes the further examination of the rotational dynamics of this CCO extremely interesting. An identification of a CCO with the group of magnetars would be a milestone in neutron star research. The recent XMM-Newton observations of the CCO in the SNR RCW 103 indicate that it could also be a peculiar magnetar (de Luca et al. 2006; Li 2007). This demonstrates indeed that such association is not too speculative.

On the other hand, Li (2007) has also pointed out that fallback disk accretion can be the other possible origin for the CCOs' X-ray emission. During the core collapse of massive stars, a considerable amount of the stellar material can fall onto the collapsed stellar remnants. The existence of fallback disks can be examined by optical/IR observations since the irradiation of the debris disks by the CCOs is expected to result in IR excess. Wang et al. (2007) has searched for the optical/IR counterparts of a number of CCOs in supernova remnants, including Puppis-A. No conclusive evidence of fallback disks around these CCOs have been reported.

We would also like to point out that the class of CCO only has a sample size of about ten objects. In order to improve our knowledge of them, the sample size has to be enlarged. Systematic searches have been conveyed to look for extended X-ray sources as supernova remnant candidates in the ROSAT all-sky survey (RASS) data base (Busser 1998; Schaudel 2002). A number of diffuse structures have already been identified as promising X-ray counterparts of supernova remnants (Schaudel 2002). For those having compact features identified within the diffuse X-ray emission, observations with Chandra can possibly detect point sources as new neutron star candidates. We have identified one promising candidate in the supernova remnant G67.7+1.8. It was firstly noticed in a ROSAT PSPC image (Fig. 10.1) by matching the geometric center of the remnant with the peak emission in the diffuse X-ray structures. We have subsequently observed the source with Chandra. Figure 10.2 shows the false color image of the SNR as obtained by the ACIS-I detector. Using the wavelet source detection algorithm, we have detected 36 point-like sources in the field of view. Four point sources (labeled with # 9, 10, 11, 35 in Fig. 10.2) are located within 1.5

arcmin from the geometrical center of G67.7+1.8, they all appear to be harder than the surrounding remnant emission. Hence they are considered to be the likely CCO candidates associated with this SNR. Detailed analysis of these X-ray sources will be published soon.

## 10.2 Emission mechanism of non-recycled old pulsars

Although rotation-powered pulsars have been studied for 40 years, we have to admit that the exact high energy emission mechanism is still uncertain. After a debate of more than 20 years, even the location of the emission site remain unclear. There are two main streams in this years long debate: 1) The polar cap model that suggests the high energy emission originated near the magnetic poles in the the inner magnetosphere. 2) The outer-gap model suggests the high energy emission originated in the outer magnetosphere. The recent observations of non-recycled old pulsars have raised challenges for these models. Their observational properties are summarized in Table 10.1.

Most of these old pulsars were too faint for a detailed study by previous X-ray observatories. Owing to the improved sensitivity of XMM-Newton and Chandra, a series of comprehensive studies of these faint sources have finally allowed a first detailed view of their emission nature. Surprisingly, the X-ray emission from old pulsars seems to be largely dominated by non-thermal radiation processes. Thermal components (e.g. account for the emission from hot polar caps) are not required to model the X-ray spectra of these pulsars. Further support for an emission scenario dominated by non-thermal radiation is found by the observed temporal emission properties. Pulse profiles, if detected with sufficient photon statistics, show multiple components and narrow features. This is indicative of strongly beamed emission which further invalidates the heated polar cap scenario as the main source of X-ray emission in old pulsars.

In this thesis, we have discussed the possibility of the particle acceleration regions to be sustained in the outer magnetospheres of these old pulsars when the inclination of the magnetic axis with respect to the rotational axis is taken into account. This inference is supported by the ability of the outer-gap model in reproducing the observed X-ray pulse profile and its phase shift relative to the radio pulse in the case of PSR B1929+10 (see Fig. 16 in Becker et al. 2006). However, such model is not without difficulty in explaining the observed X-ray properties of this class of pulsars.

In the outer-gap model, the non-thermal X-rays result from the back-flowing charge particles from the outer gap (Cheng & Zhang 1999). When the primary electrons/positrons leave the outer-gap, they will emit curvature photons which are subsequently converted into secondary pairs in the presence of the strong magnetic field. Synchrotron photons will then be emitted by these secondary electrons/positrons. If these photons are energetic enough, they will further be converted into pairs which again lose their energy via synchrotron radiation. Therefore, an electromagnetic cascade is developed. Based on this model, Cheng & Zhang (1999) argued that the X-ray photon index resulting from such cascades should be  $\leq 2$ . This is obviously not in agreement with the observed photon index for the spectra of old pulsars. Observations of six old pulsars: PSRs B1929+10 (Becker et al. 2006;

Hui & Becker 2007d), B1133+16 (Kargaltsev, Pavlov & Garmire 2006), B0943+10 (Zhang, Sanwal & Pavlov 2005), B0628-28 (Becker et al. 2005), B0823+26 (Becker et al. 2004) and J2043+2740 (Becker et al. 2004), found the photon indices steeper than 2 (see Table 10.1). This gives the outer-gap emission model a challenge. Re-examination of the model is thus still required.

### 10.3 High energy emission of pulsar wind nebulae

One of the remarkable achievement by Chandra is that the sample size of pulsar wind nebulae is significantly enlarged. Such triumph is due to the superior spatial resolution of the observatory. Now we know that extended X-ray emission have been observed around pulsars at different ages, from young pulsars of a few thousand years old to the millisecond pulsars at the order of billion years old (see Table 6.3).

We have conveyed searches for diffused X-ray emission around a number of pulsars. One of the most interesting results is the discovery of an X-ray trail associated with PSR J2124–3358. This is the first time that extended emission from a solitary millisecond pulsar is detected. We found that the observed X-rays from the nebula are in line with the emission originating from accelerated charged particles in the post-shock flow. However, in contrast to the typical X-ray trails associated with pulsars, the X-ray nebula of PSR J2124–3358 appears to be highly asymmetric and significantly deviated from the direction of the pulsar’s velocity. We argued that the asymmetric morphology might be caused by a significant density gradient in the interstellar medium, bulk flow of ambient gas and/or anisotropies in the pulsar’s relativistic wind. This argument suggests that pulsar wind nebula can be used as a probe for the physical properties of the interstellar medium as well as the shock region. As an example, we have demonstrated that the passage time of the pulsar across the trail can be taken as an estimate of the synchrotron cooling timescale and hence the local magnetic field in the shock can be calculated.

Besides X-rays, the interaction between the highly relativistic magnetized wind and the surrounding medium will also produce the synchrotron emission in the radio band. The synchrotron lifetime of the emitting particles at the radio band is much larger than that in X-ray. While the X-rays of the nebula are resulted from the freshly injected charged particles from the pulsar, the radio counterpart allows us to probe early epochs of pulsar injection. Therefore, it is important to study the structure and the spectral properties of pulsar wind nebulae across the whole electromagnetic spectrum, from radio to high energy, to obtain a better understanding of the interaction nature as well as the integrated injection history of the pulsars. In this thesis, we reported the discovery of a possible radio counterpart of the X-ray nebula associated with PSR B1509–5850. Also, we have recently searched for radio counterparts of a group of X-ray pulsar wind nebulae, including PSR J2124–3358, by using the Australia Telescope Compact Array (ATCA) for aperture synthesis. A brief analysis at the beginning stage does not reveal any extended radio emission associated with PSR J2124–3358, though a more detail study is still needed to confirm the result.



The synchrotron photons produced by the relativistic electrons/positrons in the pulsar wind nebulae have been expected to be up-scattered by the same leptons to produce TeV  $\gamma$ -rays through the inverse Compton process. Other soft photon sources (e.g. cosmic microwave background radiation, starlight) can also be boosted to TeV photons by these leptons. Once the TeV photons interact with the Earth's atmosphere, relativistic electron-positron pairs will be produced. The Cerenkov radiation from these energetic leptons can be observed on the ground. Since the High Energy Stereoscopic System (HESS) were fully employed in December 2003, a large number of new TeV sources have been discovered. One interesting class of these very high energy (VHE) gamma-ray sources are pulsar wind nebulae. While radio and X-ray observations probe the extreme ends of the electron energy distributions in the pulsar wind nebulae, HESS has made a ground breaking contribution by adding spectral information on electron energies between radio and X-rays (de Jager 2008). This stresses the importance of multi-wavelength observations.

## 10.4 Millisecond pulsars in globular clusters

The physical properties of the millisecond pulsars (MSPs) in globular clusters (GCs) are found to be very different from those in the open field. As an example, the X-ray emission of MSPs in the open field were found to have a non-thermal component (Becker & Trümper 1997, 1999; Zavlin 2006). On the other hand, X-ray study of the MSPs in 47 Tuc suggested their emission spectra are consistent with blackbody models (Grindlay et al. 2002). While the pulsars located in the open field generally obey the  $L_X \propto \dot{E}$  relation (Becker & Trümper 1997), the MSPs in 47 Tuc have found to obey a significantly flatter relation of  $L_X \propto \dot{E}^{0.5}$  (Grindlay et al. 2002). It is interesting to notice that, although these two type of MSPs have similar spin parameters, their emission properties are so different from each other.

One clue to explain the differences is the fact that the MSPs in a GC reside in an environment with a much higher stellar density than those in the galactic field. Therefore, the stellar interaction in GCs is more frequent. MSPs in the GCs can thus possibly change their companion a few times throughout their lives. As the accretion might affect the magnetic field structure at the neutron star surface (Cheng 2008), this would result in a much more complicated field structure of the MSPs in the GCs than the case in the galactic plane. In a complicated magnetic field, Ruderman & Cheng (1988) argued that high energy curvature photons will be emitted and subsequently converted into pairs to quench the charge depletion region. This can explain the absence of non-thermal emission in the globular cluster MSPs. Cheng & Taam (2003) attempted to explain the relation between  $L_X$  and  $\dot{E}$  for the MSPs in 47 Tuc by recognizing the current flows to the polar cap is limited by the Goldreich-Julian current which is proportional to  $\dot{E}^{0.5}$  (see Chapter 1). This naturally explains the thermal X-ray luminosities by polar cap heating.

Searching and studying MSPs in GCs not only provide us with the knowledge of the pulsars themselves, but also enable us to probe the interactions inside the GCs. Therefore, extensive surveys are necessary. Traditional pulsar searches are based on radio timing observations. These studies have successfully expanded the populations of the GC MSPs

(e.g. Manchester et al. 2001). During the time this thesis is written, there are 129 MSPs from 24 GCs. However, one should be aware of some limitations of timing observations. For example, it is difficult to detect pulsars with short periods and/or with large dispersion measure. Also, a fraction of GC MSPs can possibly be bounded in very tight binaries which have the orbital period as short as a few hours. This fact has further complicated the pulsar searches. Parameters, including the positions, are inferred from minimizing the pulse arrival-time residuals. Since the signals from the GC MSPs are typically weak, the fitted parameters can possibly suffer from large errors. As an example, the position of the eclipsing binary MSP PSR J1824–2452H in M28 was firstly reported by Bégin (2006). It was found to have a  $\sim 0.2$  arcmin offset from a more accurate radio timing solution reported by Ransom (2007, priv. com.) which was found to be in agreement with the position of a previously unidentified X-ray source in the GC (Becker et al. 2003). The identification of this X-ray source as a pulsar is further supported by its hardness ratio and the lack of the long-term variability (Becker, Hui & Bégin 2007). It is interesting to notice that the X-ray emission of PSR J1824–2452H has already been detected about four years before the radio pulsations be detected. This suggests that combining X-ray imaging with radio timing can be an efficient way for searching pulsars. With the aid of X-ray spectro-imaging analysis, not only the pulsar positions can be constrained independently, but also their emission properties. It is possible that a substantial populations of GC MSPs be firstly identified through X-ray studies, though the detections of periodicities are needed to confirm the identifications unambiguously.

## 10.5 Future prospects

After 40 years studies of neutron stars, there are still a lot questions remain not answered. In the previous sections, we have pointed out and discuss some questions raised by the studies presented in this thesis. Here we will briefly discuss the feasibilities of the future astronomical facilities in answering these questions.

In X-rays, our knowledge of the neutron stars are so far limited to the spatial, spectral and temporal information. In order to broaden our horizon, new windows in the neutron star researches have to be explored. X-ray polarimetry is one of the promising window to be utilized in exploring the nature of neutron stars. Since neutron stars are highly magnetized objects, radiation emitted in such strong magnetic fields is expected to be polarized. While radio and optical astronomers have already used polarimetry extensively to study the emission properties of pulsars (e.g. constraining the radio emission site from the S-shape polarization swing across the pulse phase), significant X-ray polarization was so far only detected in the Crab Nebula (Weisskopf et al. 1976). Here we would like to point out the potential use of X-ray polarimetry in answering some of the aforementioned questions.

We have already mentioned that the X-ray spectroscopy suggests the presence of hot spots on the surface of CCOs. This can possibly be due to the bombardment of the back-flow particles in the magnetosphere or from the anisotropic heat transport inside the

neutron stars. No matter which scenario is indeed the case, the observed properties should be related to the high magnetic field. This implies that the X-ray from the hot spot should be strongly polarized (Weisskopf et al. 2008). In searches for the periodic signals produced by the hot spots when the star rotates, we have revealed a periodicity candidate from the CCO in Puppis-A with a small pulsed fraction of  $\sim 5\%$ . Such low pulsed fraction is not unexpected. This is due to the fact that the gravitational light bending will make more than half of the stellar surface become visible at any time and decrease the relative contribution of the hot spot. However, the degree of the polarization of the emission from hot spots, which is likely come from the magnetic pole, should be very different from the rest of the stellar surface. Therefore, restricting the periodicity searches in a particular range of polarization degree should make the searches easier. As aforementioned, examination of the rotational dynamics of CCOs can lead to a deeper insight of their properties as well as their relations with the other classes of neutron stars. Hence, development of X-ray polarimeter with sufficient temporal resolution can provide the key to unlock the mystery of CCOs.

X-ray polarimetry can also possibly settle the decades-long debate on the origin of the pulsed non-thermal X-ray emission from the pulsars. As the pulsar rotates, the position angle of the linear polarization varies with the pulse phase. Since the location and geometry of the emission site suggested by the polar cap model and the outer-gap model are entirely different (cf. Cheng 2008; Harding 2008), their predicted patterns of the position angle variation should be different from each other. Therefore, phase-resolved polarimetric measurements in X-rays can discriminate among the competing models.

Polarization detector for X-rays has been proposed to be installed in the X-ray Evolving Universe Spectroscopy Mission (XEUS) which is ESA's potential follow-on mission to XMM-Newton (see Becker 2008 and references therein). While we still have to wait for more than a decade for the launch of XEUS, there are a number of upcoming missions in the near future.

After the successful launch of the  $\gamma$ -ray satellite, Astro-rivelatore Gamma a Immagini Leggero (AGILE), on 23 April 2007, the other  $\gamma$ -ray detector, the Gamma-ray Large Area Space Telescope (GLAST), is prepared to be launched at the end of 2007/the beginning of 2008. AGILE and GLAST are capable to image  $\gamma$ -ray emission in the energy bands of 0.03-30 GeV and 0.03-300 GeV respectively. The spectral cut-offs predicted by different emission models fall into these ranges (see Chapter 1). Polar cap model predicts a very sharp cut-off at a few GeV through the magnetic pairs attenuation. On the other hand, in the context of the outer-gap model, the cut-off is determined by photon-photon pair production which is found to have weaker energy dependence than magnetic pair production, and a cut-off at a few tens of GeV is expected (cf. Smith 2008). Therefore, observations with GLAST/AGILE can judge which prediction is indeed the case or request the existing theories to be revised.

In the coming decades, all-sky surveys will be conveyed from radio to X-rays. These surveys will attain unprecedented sensitivities and take the astronomers to leap further. In the radio band, projects like the LOw Frequency ARray (LOFAR) and the Square Kilometer Array (SKA) will enable a full census of radio-emitting neutron stars in our galaxy (see Kramer 2008). As an example, a feasibility study of the SKA galactic census

suggested  $\sim 20000 - 30000$  pulsars, including  $\sim 1000$  MSPs which can possibly be detected in the blind surveys (Kramer 2008). The unbiased sample of pulsars can be used as a tool to probe the physical properties of the galaxy, such as the electron density, magnetic field as well as the gravitational potential. In X-rays, eROSITA will be launched in 2011 and will extend the successful ROSAT all-sky survey up to 15 keV (Becker 2008). It will be equipped with 7 Wolter-I telescopes, each with 54 mirror shells. Each of the telescopes will carry an individual CCD detector which is an advanced version of the EPIC-PN camera on XMM-Newton. At 1 keV, the effective area of the 7 eROSITA telescopes is about a factor of two larger than one of the XMM-Newton telescope. With such huge collecting power, the all-sky survey with eROSITA is expected to expand the population of X-ray emitting neutron stars considerably.

With all the upcoming missions, our journey of neutron stars exploration can be continued across the whole electromagnetic spectrum. Exciting discoveries are certainly lying ahead!

Table 10.1: Physical properties of non-recycled old pulsars

PSR	$P$ sec	$B$ $10^{12}\text{G}$	$\dot{E}$ $10^{32}\text{erg/s}$	$d$ kpc	$\alpha$ degree	$\Gamma_X$	$L_{X,0.1-2.4}$ $10^{30}\text{erg/s}$	$L_{X,0.5-10}$ $10^{30}\text{erg/s}$	no. of pulse 0.2-10 keV	pulse width 0.2-10 keV	$r_{in}(\alpha)^e$ $10^8\text{cm}$	$f(r_{in}, \alpha)^e$	ref.
B1133+16 <sup>d</sup>	1.19	2.09	0.85	0.36	51.3	$2.51^{+0.36}_{-0.33}$	0.34	0.15	-	-	13.8	1.5	1,2,3
B0943+10 <sup>d</sup>	1.10	1.98	1.0	0.63	-	$2.6^{+0.7}_{-0.5}$	0.58	0.22	-	-	-	-	4
B0628-28	1.24	3.02	1.45	1.45	70	$2.63^{+0.23}_{-0.15}$	23.7	8.42	2	180°, 45°	5.37	0.58	5
B0823+26	0.53	0.98	4.57	0.34	98.9	$2.50^{+0.90}_{-0.45}$	0.23	0.10	1	288°	0.57	0.12	6,7
B0950+08	0.25	0.25	5.62	0.26	105.4	$1.92^{+0.14}_{-0.12}$	0.17	0.18	2	108°, 180°	0.70	0.23	6,7
B2224+65	0.68	2.58	11.9	1	-	$1.58^{+0.43}_{-0.33}$	1.11	1.95	-	-	-	-	8,9
B1929+10	0.23	0.51	38.9	0.36	35.97	$2.72^{+0.12}_{-0.09}$	13.4	4.11	2	273°, 44°	4.1	0.62	7,10,11
J2043+2740	0.096	0.35	562	1.8	-	$3.1^{+1.1}_{-0.6}$	27.9	4.27	-	-	-	-	6

References: (1) Kargaltsev et al. 2006; (2) Briskin et al. 2002; (3) Lyne & Manchester 1988; (4) Zhang et al. 2005; (5) Becker et al. 2005; (6) Becker et al. 2004; (7) Everett & Weisberg 2001; (8) Hui & Becker 2006; (9) Chatterjee & Cordes 2004; (10) Becker et al. 2006; (11) Chatterjee et al. 2004

<sup>a</sup> Distances are taken from the corresponding literature. Otherwise, the dispersion measure based distances computed by using the electron density model NE2001 of Cordes & Lazio (2002) are adopted.

<sup>b</sup> The magnetic inclination angles of B1133+16 and B0628-28 are taken from Lyne & Manchester (1988) and Becker et al. (2005) respectively. Others are adopted from Everett & Weisberg (2001).

<sup>c</sup> The X-ray luminosities are taken from the corresponding literature and recalculated into energy bands of 0.1 – 2.4 keV and 0.5 – 10 keV.

<sup>d</sup> Owing to the limited photon statistics, B1133+16 and B0943+10 can be fit equally well by both blackbody and power-law models.

<sup>e</sup>  $r_{in}(\alpha)$  and  $f(r_{in}, \alpha)$  are the locations of the inner boundary of the outer-gap from the center of the star and the fractional gap size respectively.

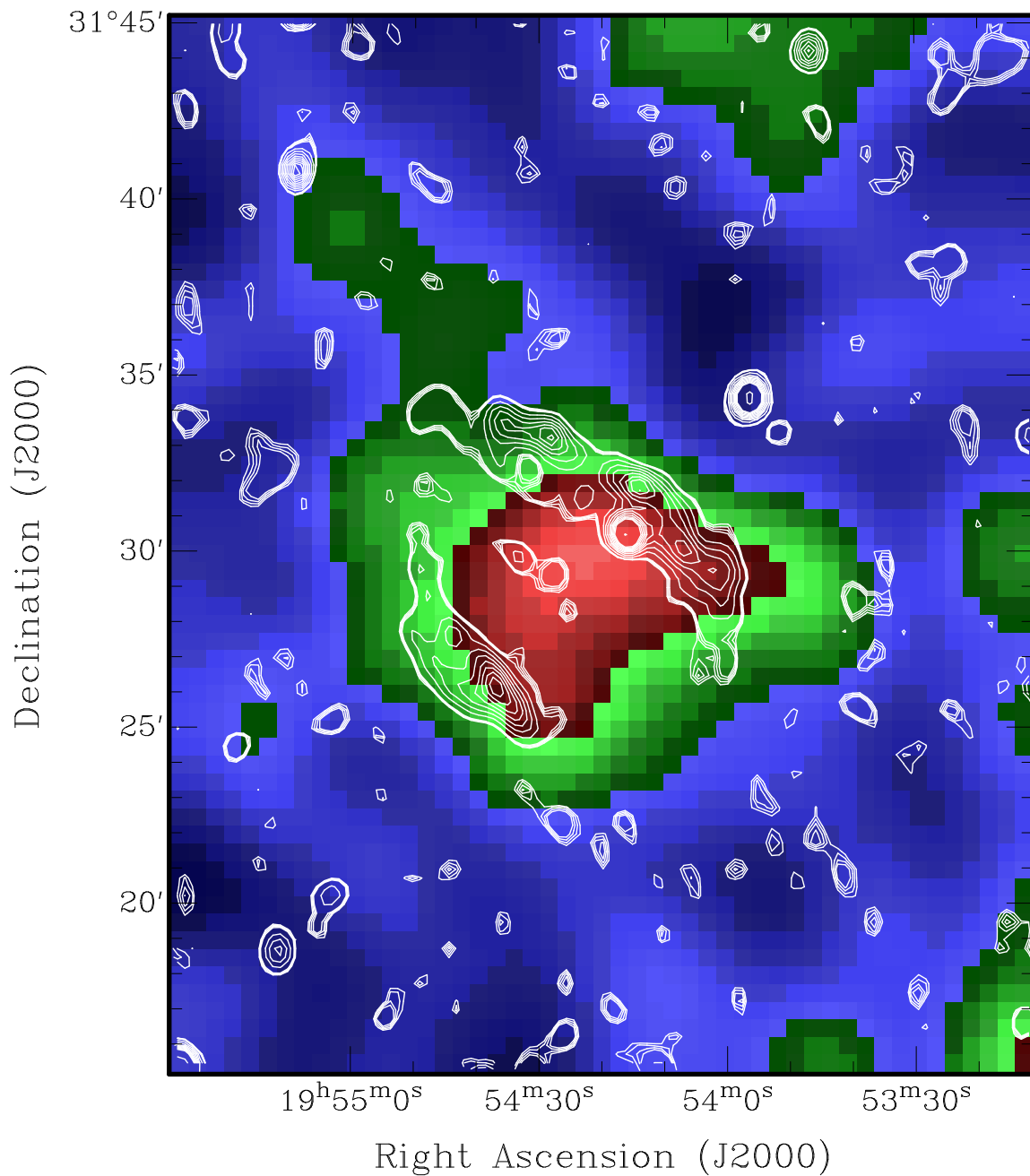


Figure 10.1: ROSAT PSPC image of G67.7+1.8 overlaid with contours from the NVSS survey data. The remnant appears center-filled in X-rays and has a bilateral radio arc-like structure. The peak of the central X-ray emission is found to be rough matching the geometric center of the remnant

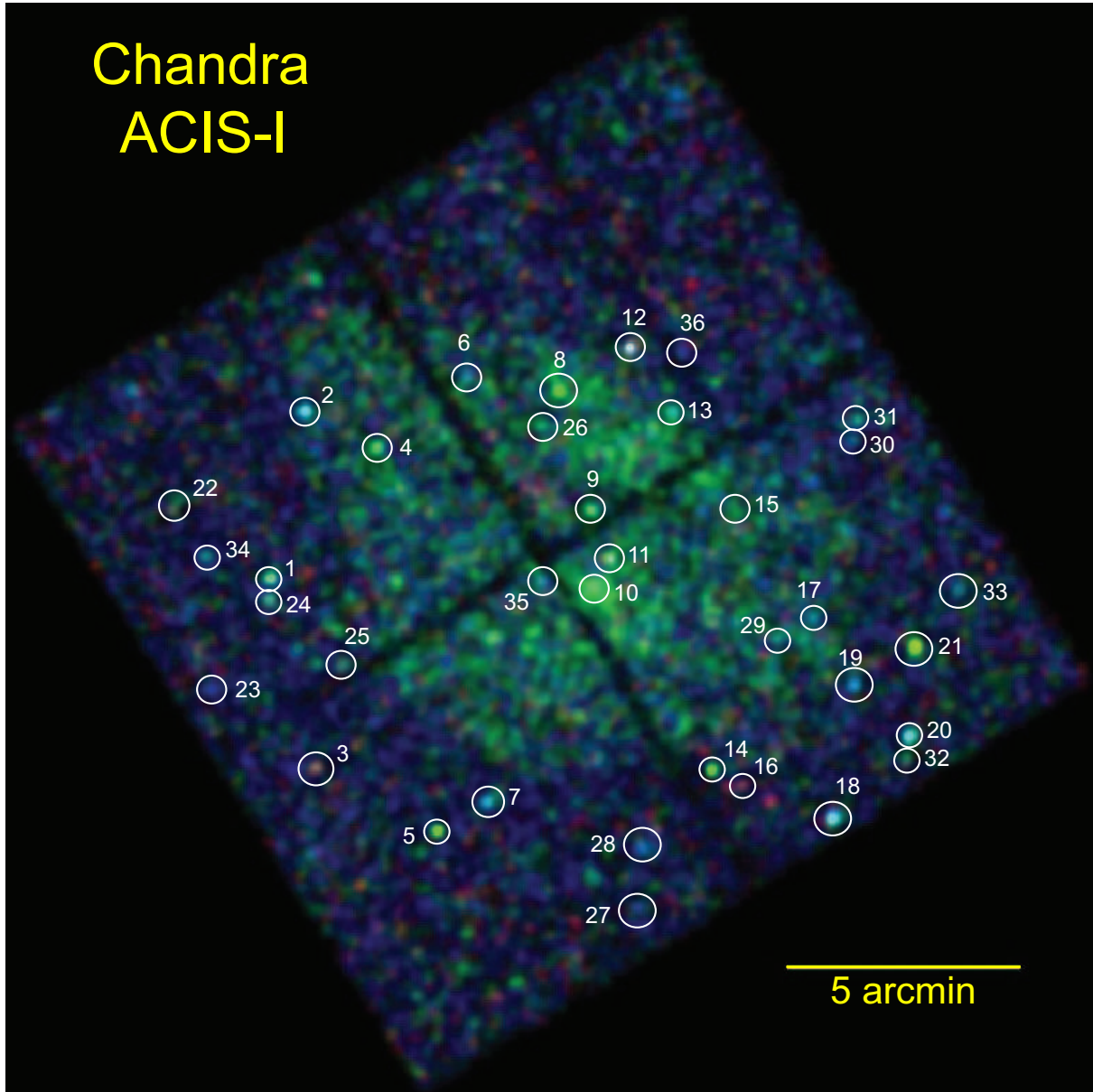


Figure 10.2: Chandra ACIS-I false color image of G67.7+1.8 (red: 0.3-0.75 keV, green: 0.75-2 keV, blue: 2-8 keV). The binning factor of this image is  $2''$  and is adaptively smoothed by a Gaussian kernel of  $\sigma < 6''$ .





# Bibliography

- Aharonian, F., Akhperjanian, A. G., Bazer-Bachi, A. R., et al. 2005, *A&A*, 437, L7
- Arons, J. 1983, *ApJ*, 266, 215
- Arons, J., & Scharlemann, E. T. 1979, *ApJ*, 231, 854
- Aschenbach, B., 1994, in *New Horizon of X-ray Astronomy – First Results from ASCA*, eds Makino, F., and Ohashi, T., Frontier Science Series No 12., p103ff
- Aschenbach, B., 1998, *Nature*, 396, 141
- Aschenbach, B., Iyudin, A., Schönfelder, V., 1999, *A&A*, 350, 997
- Baade, W., & Zwicky, F., 1934, *Phys. Rev.*, 45, 138
- Backer, D. C., Kulkarni, S. R., Heiles, C., Davis, M. M., & Goss, W. M. 1982, *Nature*, 300, 615
- Backer, D. C., & Sallmen, S. 1997, *ApJS*, 114, 1539
- Bailes, M., Johnston, S., Bell, J. F., et al. 1997, *ApJ*, 481, 386
- Baym, G., & Pethick, C. 1975, *Annu. Rev. Nucl. Part. Sci.*, 25, 75
- Baym, G., & Pethick, C. 1979, *Annu. Rev. Astron. Astrophys.*, 17, 415
- Beck, R., Shukurov, A., Sokoloff, D., & Wielebinski, R. 2003, *A&A*, 411, 99
- Becker, W. 2008, to appear in Springer Lecture notes on “Pulsars and Neutron stars: 40 years after the discovery”, eds. W. Becker, 2008, in press
- Becker, W., & Aschenbach, B. 2002, in *Proceedings of the WE-Heraeus Seminar on Neutron Stars, Pulsars and Supernova remnants*, eds. W. Becker, H. Lesch & J. Trümper, MPE-Report 278, 64, (available from astro-ph/0208466)
- Becker, W., Hui, C. Y., Aschenbach, B., & Iyudin, A. 2006, submitted to *A&A*, (available from astro-ph/0607081)
- Becker, W., & Hui, C. Y. 2007, submitted to *A&A*, (available from arXiv:0705.0119)
- Becker, W., Jessner, A., Kramer, M., Testa, V., & Howaldt, C. 2005, *ApJ*, 633, 367
- Becker, W., Kramer, M., Jessner, A., et al. 2006, *ApJ*, 645, 1421
- Becker, W., Pavlov, G. G. 2001, in *The Century of Space Science*, eds. J. Bleeker, J. Geiss & M. Huber, Kluwer Academic Publishers, p721 (available from astro-ph/0208356).
- Becker, W., Swartz, D., Pavlov, G., Elsner, R., Grindlay, J., et al., 2003, *ApJ*, 594, 798
- Becker, W., & Trümper, J. 1993, *Nature*, 365, 528
- Becker, W., & Trümper, J. 1997, *A&A*, 326, 682
- Becker, W., & Trümper, J. 1999, *A&A*, 341, 803
- Becker, W., & Trümper, J. 1998, *IAU Circular* 6829
- Becker, W., Trümper, J., Lommen, A. N., & Backer, D. C. 2000, *ApJ*, 545, 1015

- Becker, W., Weisskopf, M. C., Tennant, A. F., Jessner, A., Dyks, J., Harding, A. K., & Zhang, S. N. 2004, *ApJ*, 615, 908
- Bégin, S., Thesis submitted to the Faculty of Physics, University of British Columbia, 2006
- Bell, J.F., Bailes, M., Manchester, R. N., Weisberg, J. M., & Lyne, A. G. 1995, *ApJ*, 440, L81
- Bertsch, D. L., et al. 1992, *Nature*, 357, 306
- Bhattacharya, D., & van den Heuvel, E. P. J. 1991, *PhR*, 203, 1
- Bock, D. C.-J., Large, M. I., & Sadler, Elaine M. 1999, *AJ*, 117, 1578
- Bogdanov, S., Grindlay, J.E., Heinke, C.O., Camilo, F., Freire, P.C.C., Becker, W., 2006, *ApJ*, 646, 1104
- Brazier, K. T. S., & Johnston, S. 1999, *MNRAS*, 305, 671
- Brown, G. E. 1996, *Supernova Explosions, Black Holes and Nucleon Stars*, in Proceedings of the Nuclear Physics Conference — INPC 95, ed by S. Zuxum & X. Jincheng (World Scientific, Singapore, 1996), 623
- Buccheri, R., et al. 1983, *A&A*, 128, 245
- Burke, B. E., et al. 1997, *IEEE Trans. Elec. Devices*, 44, 1633
- Busser, J.-U. 1998, PhD thesis, Munich
- Camilo, F. 2003, in *ASP Conf. Ser. 302, Radio Pulsars*, ed. M. Bailes, D. J. Nice, & S. Thorsett (San Francisco: ASP), 145
- Camilo, F., Lorimer, D.R., Freire, P., et al., 2000, *ApJ*, 535, 975
- Camilo, F., Ransom, S. M., Halpern, J. P. et al., 2006, *Nature*, 442, 892
- Canizares, C. R., & Winkler, P. F., Jr. 1981, *ApJ*, 246, L33
- Caraveo, P. A., Bignami, G. F., DeLuca, A., Mereghetti, S., Pellizzoni, A., Mignani, R., Tur, A., & Becker, W. 2003, *Science*, 301, 1345
- Chadwick, J. 1932, *Nature*, 129, 312
- Chakrabarty, D., Pivovarov, M. J., Hernquist, L. E., Jeremy, S. H., & Narayan, R. 2001, *ApJ*, 548, 800
- Chatterjee, S., & Cordes, J.M. 2002, *ApJ*, 575, 407
- Chatterjee, S., & Cordes, J.M. 2004, *ApJ*, 600, L51
- Chatterjee, S., Cordes, J. M., Vlemmings, W. H. T., Arzoumanian, Z., Goss, W. M., & Lazio, T. J. W. 2004, *ApJ*, 575, 407
- Cheng, K. S. 2008, to appear in Springer Lecture notes on “Pulsars and Neutron stars: 40 years after the discovery”, eds. W. Becker, 2008, in press
- Cheng, K. S., Ho, C. & Ruderman, M. A. 1986, *ApJ*, 300, 500
- Cheng, K. S., & Taam, R. E. 2003, *ApJ*, 598, 1207
- Cheng, K. S., Taam, R. E., & Wang, W., 2004, *ApJ*, 617, 480
- Cheng, K. S., & Zhang, L. 1999, *ApJ*, 515, 337
- Chevalier, R. A. 2000, *ApJ*, 539, L45
- Condon, J. J., Cotton, W. D., Greisen, E. W., Yin, Q. F., Perley, R. A., Taylor, G. B., & Broderick, J. J. 1998, *AJ*, 115, 1693
- Contopoulos, I., Kazanas, D., & Fendt, C. 1999, *ApJ*, 511, 351
- Cool, A.M., Grindlay, J.E., Krockenberger, M., & Bailyn, C.D., 1993, *ApJ*, 410, L103
- Cordes, J. M., & Lazio, T. J. W., 2002, (astro-ph/0207156)

- Cordes, J. M., Romani, R. W., & Lundgren, S. C. 1993, *Nature*, 362, 133
- Cui, W. 2006, (astro-ph/0608042)
- Culhane, J. L.: 1977, in D. N. Schram (ed.), *Supernovae*, D. Reidel Publishing Co., Dordrecht, Holland, p. 29
- D'Amico 2000, N., in *Pulsar Astronomy - 2000 and Beyond*, 202th ASP Conf. Ser., ed. M. Kramer, N. Wex & R. Wielebinski (San Francisco:ASP), 27
- Daugherty, J. K., & Harding, A. K. 1996, *ApJ*, 458, 278
- Davis, J. E. 2001, *ApJ*, 562, 575
- Davis, J. E. 2002, HEAD meeting in Albuquerque,
- De Jager, O. C. 2008, to appear in Springer Lecture notes on "Pulsars and Neutron stars: 40 years after the discovery", eds. W. Becker, 2008, in press
- De Jager, O. C., Swanepoel, J. W. H., & Raubenheimer, B. C. 1989, *A&A*, 221, 180
- De Luca, A., Caraveo, P. A., Mereghetti, S., Negroni, M., & Bignami, G. F. 2005, *ApJ*, 623, 1051
- De Luca, A., et al. 2006, *Science*, 313, 814
- den Herder, et al. 2001 *A&A*, 365, L7
- Duncan, R. C., & Thompson, C. 1992, *ApJ*, 392, L9
- Everett, J. E., & Weisberg, J. M. 2001, *ApJ*, 553, 341
- Fishman, G. J., Harnden, F. R., Jr., & Haymes, R. C. 1969, *ApJ*, 156, L107
- Flowers, E., Ruderman, M., & Sutherland, P. 1976, *ApJ*, 205, 541
- Fritz, G., Henry, R. C., Meekins, J. F., Chubb, T. A., & Friedman, H. 1969, *Science*, 164, 709
- Fruchter, A. S., Bookbinder, J., Garcia, M. R., & Bailyn, C. D. 1992, *Nature*, 359, 303
- Gaensler, B. M., Bock, D. C.-J., & Stappers, B. W. 2000, *ApJ*, 537, L35
- Gaensler, B. M., & Slane, P. 2006, *Ann. Rev. Astron. & Astrophys.*, 44, 17
- Gaensler, B. M., van der Swaluw, E., Camilo, F., Kaspi, V. M., Baganoff, F. K., Yusef-Zadeh, F., & Manchester, R. N. 2004, *ApJ*, 616, 383
- Gaensler, B. M., Jones, D. H., & Stappers, B. W. 2002, *ApJ*, 580, L137
- Gallant, Yves A. et al. 2006, (astro-ph/0611720)
- Geppert, U., Küker, M., Page, D., 2004, *A&A*, 426, 26
- Geppert, U., Küker, M., Page, D., 2006, *A&A*, 457, 937
- Giacconi, R., Gursky, H., Kellogg, E., Schreier, E., & Tananbaum, H. 1971, *ApJ*, 167, L67
- Giacconi, R., Gursky, H., Paolini, F. R., & Rossi, B. B., 1962, *Phy. Rev.*, 9, 439
- Gold, T. 1968, *Nature*, 218, 731
- Goldreich, P., & Julian, W. H. 1969, *ApJ*, 157, 869
- Gotthelf, E. V., Halpern, J. P., & Seward, F. D. 2005, *ApJ*, 627, 390
- Gotthelf, E. V., & Kulkarni, S. R. 1997, *ApJL*, 490, L161
- Green D.A., 2006, 'A Catalogue of Galactic Supernova Remnants (2006 April version)', Mullard Radio Astronomy Observatory, Cavendish Laboratory, Cambridge, United Kingdom
- Grindlay, J.E., Camilo, F., Heinke, C.O., Edmonds, P.D., Cohn, H., Lugger, P., 2002, *ApJ*, 581, 470
- Grindlay, J.E., Heinke, C., Edmonds, P.D., & Murray, S.S., 2001a, *Science*, 290, 2292

- Grindlay, J.E., Heinke, C.O., Edmonds, P.D., Murray, S.S., Cool, A. M. 2001, *ApJ*, 563, 53
- Gudmundsson, E. H., Pethick, C. J., & Epstein, R. I., 1983, *ApJ*, 272, 286
- Haberl, F., in *Astrophysics and Space Science*, eds D. Page, R. Turolla & S. Zane, astro-ph/0609066
- Haberl, F. 2008, to appear in Springer Lecture notes on “Pulsars and Neutron stars: 40 years after the discovery”, eds. W. Becker, 2008, in press
- Halpern, J. P., & Holt, S. S. 1992, *Nature*, 357, 222
- Harding, A.K. 2008, to appear in Springer Lecture notes on “Pulsars and Neutron stars: 40 years after the discovery”, eds. W. Becker, 2008, in press
- Harding, A.K., Muslimov, A.G., 2001, *ApJ*, 556, 987
- Harding, A.K., Muslimov, A.G., 2002, *ApJ*, 568, 862
- Hayakawa, S., & Matsuoka, M., 1964, *PThP*, 30, 204
- Heinke, C.O., Wijnands, R., Cohn, H.N., et al., 2006, *ApJ*, 651, 1098
- Helfand, D. J., & Becker, R. H. 1984, *Nature*, 307, 215
- Hessels, J. W. T., Ransom, S. M., Stairs, I. H., Freire, P. C. C., Kaspi, V. M., & Camilo, F. 2006, *Science*, 311, 1901
- Hewish, A., Bell, S. J., Pilkington, J. D., Scott, P. F., & Collins, R. A. 1968, *Nature*, 217, 709
- Hirovani, K. 2005, *Ap&SS*, 297, 81
- Hobbs, G., Lorimer, D. R., Lyne, A. G., & Kramer, M. 2005, *MNRAS*, 360, 974
- Horowitz, C. J., Pèrez-García, M. A., Berry, D. K., & Piekarewicz, J. 2005, *Phys. Rev. C*, 72, 035801
- Hoyle, F., Narlikar, J. V., & Wheeler, J. A. 1964, *Nature*, 203, 914
- Hui, C. Y., & Cheng, K. S. 2004, *ApJ*, 608, 935
- Hui, C. Y., & Becker, W. 2006a, *A&A*, 448, L13
- Hui, C. Y., & Becker, W. 2006b, *A&A*, 454, 543
- Hui, C. Y., & Becker, W. 2006c, *A&A*, 457, L33
- Hui, C. Y., & Becker, W. 2007a, *A&A*, 467, 1209
- Hui, C. Y., & Becker, W. 2007b, *A&A*, 470, 965
- Hui, C. Y., & Becker, W. 2007c, submitted to *A&A*, (available from arXiv:0707.0800)
- Iaria, R., Di Salvo, T., Burderi, L., & Robba, N. R. 2001, *ApJ*, 548, 883
- Iyudin, A. F., Aschenbach, B., Becker, W., Dennerl, K., & Haberl, F. 2005, *A&A*, 429, 225
- Iyudin, A. F., Schönfelder, V., Bennet, K., et al. 1998, *Nature*, 396, 142
- Jansen, F., et al. 2001, *A&A*, 365, L1
- Johnston, H.M., & Verbunt, F., 1996, *A&A*, 312, 80
- Johnston, S., Lorimer, D. R., Harrison, P. A., et al. 1993, *Nature*, 361, 613
- Jones, D.H., Stappers, B.W., & Gaensler, B.M. 2002, *A&A*, 389, L1
- Kargaltsev, O., et al. 2006, AAS HEAD meeting 9
- Kargaltsev, O., Pavlov, G. G., & Garmire, G. P. 2006, *ApJ*, 636, 406
- Kargaltsev, O., Pavlov, G. G., Sanwal, D., & Garmire, G. P. 2002, *ApJ*, 580, 1060
- Kaspi, V. M. 2004, *Young Neutron Stars and Their Environments*, IAU Symposium no. 218, eds F. Camilo and B. M. Gaensler. San Francisco, CA: Astronomical Society of the Pacific, 2004., p.231

- Kaspi, V. M., Gotthelf, E. V., Gaensler, B. M., & Lyutikov, M. 2001, ApJ, 562, L163
- Kaspi, V. M., Roberts, M.S.E., Harding, A., 2004, astro-ph/0402136
- Kaspi, V. M., Manchester, R. N., Johnston, S., Lyne, A. G., & Amico, N. D' 1996, AJ, 111, 2028
- Kawai N., Saito Y., 1999, Proc. 3rd INTEGRAL Workshop, Taormina, Astroph. Lett. & Comm. 38, 1
- Kennel, C. F., & Coroniti, F. V. 1984, ApJ, 283, 694
- Kirsch, M.G.F., Becker, W., Benlloch-Garcia, S., et al., in *X-Ray and Gamma-Ray Instrumentation for Astronomy XIII*, eds Flanagan, K.A. & Siegmund, O.H.W., SPIE, Volume 5165, 85, 2004
- Kouveliotou, C. et al. 1998, Nature, 393, 235
- Kramer, M. 2008 to appear in Springer Lecture notes on "Pulsars and Neutron stars: 40 years after the discovery", eds. W. Becker, 2008, in press
- Krautter, J, Zickgraf, F.-J., Appenzeller, I., et al. 1999, A&A, 350, 743
- Kulkarni, S. R., Phinney, E. S., Evans, C. R., & Hasinger, G. 1992, Nature, 359, 300
- Lattimer, J. M., & Prakash, M. 2001, ApJ, 550, 426
- Lattimer, J. M., & Prakash, M. 2004, Science, 304, 536
- Li, X. D. 2007, ApJ, 666, L81
- Li, X. H., Lu, F. J., & Li, T. P. 2005, ApJ, 628, 931
- Manchester, R. N. 2004, Science, 304, 542
- Manchester, R. N., Hobbs, G. B., Teoh, A., & Hobbs, M. 2005, AJ, 129, 1993 (for recent update, please refer to <http://www.atnf.csiro.au/research/pulsar/psrcat>)
- Manchester, R. N., et al., 2001, MNRAS, 328, 17
- Manning, R. A., & Willmore, A. P. 1994, MNRAS, 266, 635
- Markwardt, C. B., & Ögelman, H. 1995, Nature, 375, 40
- McLaughlin, M. A., Lyne, A. G., Lorimer, D. R., et al. 2006, Nature, 439, 817
- McLaughlin, M. A., Rea, N., Gaensler, B. M., et al. 2007, ApJ in press (arXiv:0708.1149)
- Mereghetti, S. 1998, Mem. Soc. Astron. Italiana., 69, 819
- Mereghetti, S., 2001, ApJ, 548, L213
- Mereghetti, S., et al. 2006, A&A, 450, 759
- Mewe, R., Gronenschild, E. H. B. M., & van den Oord, G. H. J. 1985, A&AS, 62, 197
- Migliazzo, J. M., Gaensler, B. M., Backer, D. C., Stappers, B. W., van der Swaluw, E., & Strom, R. G. 2002, ApJ, 567, L141
- Mineo, T., Cusumano, G., Massaro, E., Becker, W., Nicastro, L., 2004, A&A, 423, 1045
- Misanovic, Z., Pavlov, G. G., & Garmire, G. P. 2006, AAS HEAD meeting 9
- Monet, D. B. A., Canzian, B., Dahn, C., et al. 1998, VizieR Online Data Catalog, 1252, 0
- Moon, D.-S., Lee, J.-J., Eikenberry, S. S., et al. 2004, ApJ, 610, L33
- Mori, K., Chonko, J.C.; Hailey, C.J., 2005, ApJ, 631, 1082
- Murray, S. S., et al. 1997, Proc. SPIE, 3114, 11
- Murray, S. S., Ransom, S. M., Juda, M., Hwang, U. & Holt, S. S. 2002, ApJ, 566, 1039
- Muslimov, A. G., & Tsygan, A. I. 1992, MNRAS, 255, 61
- Oppenheimer, J. R., & Volkoff, G. M. 1939, Phy. Rev., 55, 374
- Pacini, F. 1967, Nature, 216, 567

- Page, D. 1995, *ApJ*, 442, 273
- Pavlov, G. G., Sanwal, D., Garmire, G. P., & Zavlin, V. E. 2002, in Slane P. O., & Gaensler B. M., eds, *ASP Conf. Ser. Vol. 271, Neutron Stars in Supernova Remnants*. Astron. Soc. Pac., San Francisco, p. 247
- Pavlov, G.G., Sanwal, D., Kiziltan, B., G.Garmire, 2001, *ApJ*, 559, 131
- Pavlov, G. G., Zavlin, V. E., Aschenbach, B., Trümper, J., & Sanwal, D. 2000, *ApJ*, 531, L53
- Pavlov, G. G., Zavlin, V. E., & Trümper, J. 1999, *ApJ*, 511, L45
- Pellizzoni, A., Mereghetti, S., & De Luca, A. 2002, *A&A*, 393, L65
- Pethick, C. J., & Ravenhall, D. G., 1995, *Annu. Rev. Nucl. Part. Sci.*, 45, 429
- Petre, R., Becker, C. M., & Winkler, P. F. 1996, *ApJ*, 465, L43
- Petre, R., Canizares, C. R., Kriss, G. A., & Winkler, P. F., Jr. 1982, *ApJ*, 258, 22
- Petre, R., Kuntz, K. D., & Shelton, R. L. 2002, *ApJ*, 579, 404
- Pfeffermann, E., & Aschenbach, B. 1996, in *Roentgenstrahlung from the Universe*, ed. H. H. Zimmermann, J. Trümper, & H. Yorke (MPE Rep. 263, Garching: MPE), 267
- Popov, S. B. 2006, (astro-ph/0610593)
- Prakash, M. 2007, *J. Phys. G: Nucl. Part. Phys*, 34, S253
- Prakash, M., Ainsworth, T. L., & Lattimer, J. M. 1988, *Phys. Rev. Lett.*, 61, 2518
- Ransom, S.M., 2007, private communication
- Ransom, S.M., Hessels, J.W.T., Stairs I.H., et al., 2006, *AAS*, 207, 3205
- Ransom, S.M., Hessels, J.W.T., Stairs I.H., et al., 2006, *Science*, 307, 892
- Rasio, F.A., Pfahl, E.D. & Rappaport, S., 2000, *ApJ*, 532, 47
- Rees, M. J., & Gunn, J. E. 1974, *MNRAS*, 167, 1
- Renaud, M., Vink, J., Decourchelle, A., Lebrun, F., Terrier, R., & Ballet, J. 2006, *NewAR*, 50, 540
- Reynolds, S. P., Borkowski, K. J., Gaensler, B. M. et al. 2006, *ApJ*, 639, L71
- Reynoso, E. M., Dubner, G. M., Goss, W. M., & Arnal, E. M. 1995, *AJ*, 110, 318
- Reynoso, E. M., Dubner, G., Giacani, E., Johnston, S., & Green, A. J., 2006, *A&A*, 449, 243
- Reynoso, E. M., Green, A. J., Johnston, S., Dubner, G. M., Giacani, E. B., & Goss, W. M. 2003, *MNRAS*, 345, 671
- Richards, D. W., & Comella, J. M. 1969, *Nature*, 222, 551
- Romani, R.W., Cordes, J.M., & Yadigaroglu, I.-A. 1997, *ApJ*, 484, L137
- Ruderman, M. A. & Cheng, K. S. 1988, *ApJ*, 335, 306
- Ruderman, M. A., & Sutherland, P. G. 1975, *ApJ*, 196, 51
- Rutledge, R.E., Fox, D.W., Kulkarni, S.R., et al., 2004, *ApJ*, 613, 52
- Saito, Y. 1997, Ph.D. thesis, Univ. Tokyo
- Sanwal, D.; Pavlov, G. G.; Zavlin, V. E.; Teter, M. A., 2002, *ApJ*, 574L, 61
- Schaudel, D., Becker, W., Voges, W., Aschenbach, B., Reich, W., & Weisskopf, M. 2002, *Neutron Stars in Supernova Remnants*, *ASP Conference Series*, Vol. 271, eds Patrick O. Slane and Bryan M. Gaensler. San Francisco: ASP, 2002., p.391
- Schönfelder, V., Bloemen, H., Collmar, W., et al. 2000, *AIP Conf. Proc*, AIP, 510, 54
- Seward, F. D., & Harnden, F. R., Jr. 1982, *ApJ*, 256, L45

- Seward, F. D., Harnden, F. R., Jr., & Helfand, D. J. 1984, ApJ, 287, L19
- Seward, F. D., Slane, P. O., Smith, R. K., & Sun, M. 2003, ApJ, 584, 414
- Seward, F. D., & Wang, Z. R. 1988, ApJ, 332, 199
- Skrutskie, M.F., Cutri, R.M., Stiening, R., et al. 2006, AJ, 131, 1163
- Slane, P., Hughes, J.P., Edgar, J., et al., 2001, ApJ, 548, 814
- Smith, D. 2008, to appear in Springer Lecture notes on “Pulsars and Neutron stars: 40 years after the discovery”, eds. W. Becker, 2008, in press
- Somer, A. 2000, in Pulsar Astronomy - 2000 and Beyond, 202th ASP Conf. Ser., ed. M. Kramer, N. Wex & R. Wielebinski (San Francisco:ASP), 17
- Staelin, D. H., & Reifenstein, E. C. 1968, Science, 162, 1481
- Stairs, I.H., Bègin, S., Ransom, S., et al., AAS Meeting 209, 2006
- Stappers, B. W., Gaensler, B. M., Kaspi, V. M., van der Klis, M., & Lewin, W. H. G. 2003, Science, 299, 1372
- Strüder, L., et al. 2001, A&A, 365, L18
- Sturrock, P. A. 1971, ApJ, 164, 529
- Sun, X., Trümper, J., Dennerl, K., & Becker, W. 1993, IAU Circ., 5895, 2
- Swanepoel, J. W. H., de Beer, C. F., & Loots, H. 1996, ApJ, 467, 261
- Tananbaum, H. 1999 IAU Circ., 7246
- Taylor, J. H., & Cordes, J. M 1993, ApJ, 411, 674
- Tennant, A.F., Becker, W., Juda, M., et al., 2001, ApJ, 554L, 173
- Thompson, C. 2000, in ASP Conf. Ser. 202, Pulsar Astronomy-2000 and Beyond, ed. M. Kramer, N. Wex, & N. Wielebinski (IAU Colloq. 177; San Francisco: ASP), 669
- Thompson, C., & Duncan, R. C. 1996, ApJ, 473, 322
- Tiengo, A., & Mereghetti, S. 2007, ApJ, 657, L101
- Tolman, R. C., 1934, *Relativity, Thermodynamics and Cosmology*
- Trümper, J. 2008, to appear in Springer Lecture notes on “Pulsars and Neutron stars: 40 years after the discovery”, eds. W. Becker, 2008, in press
- Tsuruta, S. 2008, to appear in Springer Lecture notes on “Pulsars and Neutron stars: 40 years after the discovery”, eds. W. Becker, 2008, in press
- Tsunemi, H., Miyata, E., Aschenbach, B., Hiraga, J., Akutsu, D., 2000, PASJ, 52, 887
- Tuohy, I. R., & Garmire, G. P. 1980, ApJ, 239, L107
- Turner, M.J.L., et al. 2001, A&A, 365, L27
- Usov, V. V., & Melrose, D. B. 1995, AuJPh, 48, 571
- van Paradijs, J., Taam, R. E., & van den Heuvel, E. P. J. 1995, A&A, 299, L41
- Verbunt, F. 2001, A&A, 368, 137
- Walter, F. M., Wolk, S. J., & Neuhäuser, R., 1996, Nature, 379, 233
- Wang, Q.D., & Gotthelf, E.V. 1998, ApJ, 494, 623
- Wang, Q.D., Gotthelf, E.V., Chu, Y.-H., & Dickel, J.R. 2001, ApJ, 559, 275
- Wang, Z.X., Kaplan, D.L., & Chakrabarty, D. 2007, ApJ, 655, 261
- Weber, F., Negreiros, R., & Rosenfield, 2008 to appear in Springer Lecture notes on “Pulsars and Neutron stars: 40 years after the discovery”, eds. W. Becker, 2008, in press
- Weisskopf, M.C., 2004, Proceedings of the SPIE, Volume 5488, pp. 25

- Weisskopf, M. C., Cohen, G. G., Kestenbaum, H. L., Long, K. S., Novick, R., & Wolff, R. S. 1976, *ApJ*, 208, L125
- Weisskopf, M. C. et al. 2008 to appear in Springer Lecture notes on “Pulsars and Neutron stars: 40 years after the discovery”, eds. W. Becker, 2008, in press
- Whiteoak, J. B. Z., & Green, A. J. 1996, *A&AS*, 118, 329
- Winkler, P. F., Canizares, C. R., Clark, G. W., Markert, T. H., Kalata, K., & Schnopper, H. W. 1981, *ApJ*, 246, L27
- Winkler, P. F., & Kirshner, R. P. 1985, *ApJ*, 299, 981
- Winkler, P. F., Kirshner, R. P., Hughes, J. P., & Heathcote, S. R. 1989, *Nature*, 337, 48
- Winkler, P. F., & Petre, R. 2006 (astro-ph/0608205 ver. 1)
- Winkler, P. F., Tuttle, J. H., Kirshner, R. P., & Irwin, M. J. 1988, in Roger, R. S., & Landecker, T., eds, *Supernova Remnants and the Interstellar Medium*. Cambridge Univ. Press, Cambridge, p. 65
- Wong, D. S., Cordes, J. M., Chatterjee, S., Zweibel, E. G., Finley, J. P., Romani, R. W., Ulmer, M. P. 2003, *IAU Symposium 214: High Energy Processes and Phenomena in Astrophysics*, Eds. Li, X. D., Trimble, V., & Wang, Z. R., 135
- Woods, P. M., et al. 2002, *ApJ*, 576, 381
- Yakolev, D. G., Gnedin, O. Y., Kaminker, A. D., Levenfish, K. P., & Potekhin, A. Y. 2004, *AdSpR*, 33, 523
- Zacharias, N., Urban, S. E., Zacharias, M. I., et al., 2003, *VizieR Online Data Catalog*, 1289, 0
- Zavlin, V. E. 2006, *ApJ*, 638, 951
- Zavlin, V. E., & Pavlov, G. G. 2004, *ApJ*, 616, 452
- Zavlin, V.E., Pavlov, G.G., Sanwal, D., Manchester, R.N., Trümper, J., Halpern, J.P., & Becker, W. 2002, *ApJ*, 569, 894
- Zavlin, V. E., Pavlov, G. G., & Sanwal, D. 2004, *ApJ*, 606, 444
- Zavlin, V.E., Pavlov, G.G., Shibano, Y.A., 1996, *A&A*, 315, 141
- Zavlin, V. E., Trümper, J., & Pavlov, G. G. 1999, *ApJ*, 525, 959
- Zel’dovich, Ya. B. & Guseynov, O. H. 1965, *ApJ*, 144, 840
- Zhang, B., & Harding, A. K. 2000, *ApJ*, 532, 1150
- Zhang, B., Sanwal, D., & Pavlov, G. G. 2005, 624, L109
- Zhang, C. M., & Kojima, Y., 2006, *MNRAS*, 366, 137
- Zhang, L., & Cheng, K. S. 1997, *ApJ*, 487, 370
- Zhang, L., Cheng, K. S., Jiang, Z. J., & Leung, P. 2004, *ApJ*, 604, 317
- Zombeck, M. V., Chappell, J. H., Kenter, A. T., Moore, R. W., Murray, S. S., Fraser, G. W., & Serio, S. 1995, *Proc. SPIE*, 2518, 96



# Acknowledgments

I would like to take this opportunity to thank the many people who made this thesis possible. The first person I would like to thank is my research supervisor, Dr. Werner Becker. With his enthusiasm, inspiration, encouragement and continuous guidance, this three-years journey of research has become one of the most memorable and enjoyable experience in my life. I would also like to thank Ms. Christa Ingram for helping me in every aspect of my daily life, especially for helping me to go through the complicated process of applying my wife's visa.

I would also like to give my special thanks to Prof. K. S. Cheng of the University of Hong Kong. Not only for his enlightening discussion in pulsar physics, but also for his encouragement and support of pursuing my PhD study in MPE.

I would also like to thank the Max-Planck-Institut für extraterrestrische Physik and Prof. Günther Hasinger for providing me the financial support as well as a pleasant environment so that I can carry out my researches and finish this thesis. Acknowledgments would be also given to the Croucher Foundation for supporting me to participate in the 7<sup>th</sup> Pacific Rim Conference on Stellar Astrophysics as well as the out-bound ticket from Hong Kong to Munich.

I cannot end without thanking my family, whose constant encouragement and love I have relied throughout my time in Germany. I am very grateful for the company of my beloved wife, Chow Wai, throughout my PhD period. Without her love and patience, the life during these periods would surely be more difficult. I also feel a deep sense of gratitude for my parents. Even though they are not with me in Germany, their "action-at-a distance" has always kept me warm.

Lastly, I would like to express my sincere gratitude to my mathematics teacher in high school, Mr. T. H. Ho, for showing me the fun of science and mathematics. Here I would like to wish he can recover very soon.



# Curriculum Vitae

## Hui Chung Yue

Date of birth: 04 May 1975

Place of birth: Hong Kong (China)

Citizenship: Hong Kong (China)

Gender: Male

Marital Status: Married

### Education

Institution	From	To	Subject	Qualifications
LMU / MPE	2004	2007	Physics	PhD (Dr. rer. nat.)
The University of Hong Kong	2001	2003	Physics	Master of Philosophy
The University of Hong Kong	1998	2001	Physics	Bachelor of Science
Hong Kong Academy for Performing Arts	1996	1998	Theatrical Art	Advance Diploma
Hong Kong Academy for Performing Arts	1994	1996	Theatrical Art	Diploma

### Honors & Awards

Croucher Foundation Postdoctoral Fellowship	2007-2009
The International Max-Planck Research School (IMPRS) Fellowships	2004-2007
Croucher Foundation Honorary Scholarships	2004-2007
Marie Curie Fellowships for Early Stage Research Training	2004-2005
Postgraduate Studentships from The University of Hong Kong (HKU)	2001-2003
William Faid Memorial Prize in Physics	2000-2001
Li Po Kwai Scholarships	1999-2001
Lam Chi Him Memorial Prize in Physics	1999-2000
Dean's Honors List (Faculty of Science, HKU)	1998-2001